SAPIENZA
UNIVERSITÀ DI ROMA

Experimental study of anomalous diffusion and quantum correlations in an all optical quantum walk

Facoltà di Scienze Matematiche Fisiche e Naturali

Dottorato di Ricerca in Fisica – XXXIII Ciclo

Candidate

Andrea Geraldi

ID number 1556731

Thesis Advisor

Prof. Paolo Mataloni

2020/2021

Thesis defended on Tuesday 06, July 2021
in front of a Board of Examiners composed by:

Prof. Dario Gerace (chairman)

Prof. Stefano Lupi

Prof. Miriam Vitiello

Referees: Prof. Massimo Palma, Prof. Dagmar Bruß

Experimental study of anomalous diffusion and quantum correlations in an all optical quantum walk

Ph.D. thesis. Sapienza – University of Rome

This thesis has been typeset by LaTeX and the Sapthesis class.

Author's email: andrea.geraldi@uniroma1.it andreageraldi.ag@gmail.com

Τὰ εἰς ἑαυτόν

Contents

Chapter 1

Introduction

Since its introduction in the first years of XX century, the theory of Quantum Mechanics (QM) not only paved the way for a complete reinterpretation of several physical phenomena, but has been also able to predict many other ones, most of the time completely counterintuitive in the sense of a classical-physics-guided approach to the nature. Examples of this can be found in the quantum tunneling effect, in the Pauli exclusion principle linked to the indistinguishability of the (fermionic) particles, in the superposition of different states of a system and, as a prime example, in the entanglement between two subsystems [1].
The ability of QM to clearly explain an increasingly amount of physical phenomena, makes it one of the most accurate theories ever created. Such an accuracy allows to perform an extremely important step: QM ceases to be a theory only useful to explain phenomena and it starts to be used in a practical way. In such sense, among other possible applications of QM to practical problems, its use in information and communication tasks, in the field known as Quantum Information (QI), has became ever and ever more relevant and it is turning out to be one of the most intriguing utilizations of QM.
QI deals with codification, manipulation, transport and communication of information by means of a quantum system. The uncertainty principle lying at the base of QM could put a stop to the idea of using this theory for information purposes; indeed, the probabilistic nature of QM governing, among other things, the output of a measure performed on a quantum system, could be seen like a clue of the impossibility to use a quantum system to encode a well defined information. It turns out that it holds the opposite: such peculiarities of QM lie at the base of innovative ways to manipulate information. Moreover, it also allows to reach tasks otherwise unattainable when working with classical physics as, for instance, 100% secure communication.
Despite QM is mature enough to be used in a practical sense, many questions remain open. For instance, the link with other theories, as general relativity, is nowadays hindered despite many efforts have been done in this direction. Also, when focusing solely on the QM theory, many questions remain without answer. For instance, the measurement procedure is still not completely understood, as well as the collapse of the wavefunction. For this reason, QM still remains a active field for fundamental research. Besides, its study is increasingly relevant to understand the ever new phenomena arising thanks to technology improvements. In this sense, it is absolutely imperative to explore new paths branching out from QM theory.
The present thesis work tries to follow this path, reporting on the last findings about a particular topic of QM and QI, i.e. Quantum Walks, a particular model which is able to describe the movement of quantum particles among the sites of

a discretized space. Its relevance is straightforward: the miniaturization process, which is basically ever present during the improvement of each technology, will bring to deal with the nano-scale of the matter, in which quantum mechanical effects are dominant over classical ones. The capability to understand how quantum particles move or how they spread, for instance, inside a material, or how they exchange information between them is of relevant importance in this sense. In particular, when facing real systems, most of the times very far from being ideal, the difficulty to describe exactly the system itself could bring to hypercomplex problems. In this perspective, Quantum Walks could furnish an easy framework to model such systems, overcoming the difficulties arising from a direct application of QM to them. Of course, the present thesis work doesn't aim to be complete in this sense. Such a goal, which comprises a non trivial mapping between the real system and the Quantum Walk model, is far to be reached. Nonetheless, each finding in this direction is a step ahead to its achievement. With this thesis work, such a step wants to be performed, not aiming to report a complete model or to say a final word on such topic.
After all, it is impossible to pose a concluding point on the research itself.

Chapter 2

Quantum Walks

This chapter reports on the theoretical and experimental background necessary to understand this thesis work.
In section 2.1, we briefly describe the relevant elements of the second quantization formalism, which is used later in the text. It is worth noting that this section does not aim to provide a complete and exhaustive description of quantum theory, for the comprehension of which we suggest the following books [2, 3, 4, 5].
In section 2.2 the basic idea of Quantum Walk is introduced, together with an overview of the latest results achieved so far.
Subsection 2.2.1 addresses the motivations behind this thesis work, showing the usefulness of the Quantum Walk in describing and modelling some energy transport phenomena.
Section 2.3 describes the model of the Quantum Walk, highlighting differences and analogies with the the classical random walk model.
In section 2.4 we describe different types of disorder that can be introduced along the Quantum Walk evolution, such as static or dynamic, as well as the new disordering technique adopted in the present work to reproduce particular types of evolution.
Finally, in section 2.5 we deal with the description of the experimental implementations of Quantum Walk that have been used to experimentally test the theoretically predicted behaviors that we set out to study.

2.1 Second quantization formalism

We briefly recall here the results of the second quantization formalism relative to the electromagnetic field. Such a formalism is based on the notion of the Fock states, or number states, which are the basis kets describing the system under investigation. A Fock state $|\psi\rangle_F$ describes a system S composed by quantum particles in terms of the number n_i of particles characterized by a given set i of features. Fock states live in the Fock space, which is mathematically described as the direct sum of the tensor product of single particle Hilbert spaces

$$F_\nu(\mathcal{H}) = \bigoplus_{n=0}^{\infty} \hat{\mathcal{S}}_\nu \mathcal{H}^{\otimes n}$$

where $\hat{\mathcal{S}}_\nu$ is the operator which symmetrizes or antisymmetrizes the state depending on the fermionic ($\nu = -$) or bosonic ($\nu = +$) nature of the particles.
Let's consider the orthonormal basis states $\{|\psi_i\rangle\}_{i=1,2,\dots}$ of the single particle Hilbert space. The state of a system composed by k indistinguishable particles, which for

simplicity we consider to be in a single product state, can be written as the tensor product of k states, symmetrized through the action of the symmetrization operator

$$|\psi\rangle = \hat{\mathcal{S}}_\nu |\psi_i\rangle \otimes |\psi_j\rangle \otimes \cdots |\psi_l\rangle = \hat{\mathcal{S}}_\nu |\psi_i, \psi_j, \cdots, \psi_l\rangle \tag{2.1}$$

which represents the state of k particles in which the first particle is in the state $|\psi_i\rangle$, the second one in the state $|\psi_j\rangle$, the $k-$th one in the state $|\psi_l\rangle$. The order in the writing identifies the particle number, i.e. the state in the $n-$th position corresponds to the state of the $n-$th particle. The states of the particles are not necessarily different one with respect to the others. In the last equality we omitted the tensor product symbol for the sake of semplicity.
A convenient way to rewrite the state (2.1) is through a Fock state expressed by means of the occupation number, namely the number n_i of particles in the same state $|\psi_i\rangle$

$$|n_1, n_2, \cdots\rangle_F \equiv \hat{\mathcal{S}}_\nu |\psi_1\rangle^{n_1} |\psi_2\rangle^{n_2} \cdots . \tag{2.2}$$

where the ordering is no more relevant. The occupation number state automatically takes care of the symmetrization of the wavefunction. Such states are a useful basis of the Fock space and, of course, linear superposition of different Fock states can exist. For each different value of the generic occupation number n_i a basis state is obtained. In the following, we will add a subscript F to a ket each time it will be necessary to indicate that we are working with states belonging to the Fock space. In the case of a system composed by photons, the general state $|\psi_i\rangle$ represents a wavefunction characterized by the set i of features which comprises, for instance, the momentum $\vec{k}$ of the particle, the wavelength λ, the value of its orbital angular momentum (OAM), the polarization state $\vec{\pi}$ and the temporal delay of one particle with respect to the others (as we will see later, this is a fundamental property in the description of the Hong-Ou-Mandel effect [6]). Because of the fact that in the present work we deal with photons, in the following we will use the term particles to refer to photons.
Consider a pair of Fock states $|n_i\rangle, |m_j\rangle$. It holds

$$\langle n_i | m_j \rangle = \delta_{ij} \delta_{n,m}$$

i.e. the occupancy number states form an orthonormal basis. Such states are modified by means of the creation and destruction operators $\hat{a}_i^\dagger$ and $\hat{a}_i$, defined through their action on a generic Fock state vector

$$\begin{aligned} \hat{a}_i^\dagger |n_i\rangle &= \sqrt{n_i + 1}\, |n_i + 1\rangle \\ \hat{a}_i |n_i\rangle &= \sqrt{n_i}\, |n_i - 1\rangle . \end{aligned}$$

Due to this rules, a normalized state of N indistinguishable particles, namely N particles of the same nature featured by the very same features set i, can be written as

$$(\hat{a}_i^\dagger)^N |0\rangle_F = \frac{1}{\sqrt{N!}} |N_i\rangle .$$

Note that, in the second quantization formalism, the operator $\hat{\mathcal{S}}_\nu$ is no more needed. Indeed, when the creation and destruction operators act on a second quantized state, expressed through the occupation number, the simmetrization or antisimmetrization of the wavefunction is automatically retrieved because of Eq.

(2.2). For this reason, the second quantization formalism shows its extreme useful applicability when two or more indistinguishable photons are present in the system. If one has to account for only one photon, or more than one distinguishable photons, then the second quantization formalism is equivalent to the first quantization one. In the following, when dealing with the evolution of a single particle, we will explicit the mapping between the second and first quantization kets.
The evolution of a generic quantum state $|\psi\rangle$, in both first or second quantization, can be described by a unitary operator $\hat{U}$, which contains all the information about the evolution. Of course, in the second quantization formalism, the operator has to be expressed by means of creation and destruction operators. The evolution of a state $|\psi\rangle$ from a certain time t_0 to an other t_1 can be written as

$$|\psi\rangle_{t_1} = e^{-\frac{i}{\hbar}\hat{H}(t_1-t_0)}\,|\psi\rangle_{t_0} = \hat{U}\,|\psi\rangle_{t_0}$$

with $\hat{U} = \mathrm{e}^{-\frac{i}{\hbar}\hat{H}(t_1-t_0)}$ where $\hat{H}$ is the hamiltionian governing the evolution.

2.2 Basic idea and applications

The very first idea of a Quantum Walk (QW) was developed by Aharonov, Davidovich, and N. Zagury in their paper *Quantum Random Walk* in 1993 [7]. In their description, the characterizing elements of QWs were the indetermination and superposition principles, typical of quantum mechanics, which allow the walker to be in more than one site per time, which of course is not possible for a classical walker. To explain how the QW actually works, it is convenient to compare it with its classical counterpart, the Classical Random Walk (CRW).
In the simplest CRW model, a classical walker moves between the sites of a discretized line starting its walk in a given site x_0. In a QW the same happens, but the quantum walker is represented by a wave function $\langle x|\psi(x_0)\rangle$ centered around x_0 with a finite width.
In CRW, the walker is furnished with a coin, which he tosses to determine where to move, for instance to the left if the output is head or to the right if it is tail. In QW, the quantum walker is provided with a quantum coin, represented by a quantum system of dimension two, for example the spin if the walker is a quantum particle. The quantum coin can not only be in one of the two states head or tail, as the classical one, but in principle in any linear combination of them. At each step of the walk, both in CRW and QW, the coin is tossed, namely its state is changed. In the classical case, it will change its state in head or tail in a mutually exclusive way. In the quantum framework, in the easiest case, it will change in a balanced linear superposition of them.
The walkers then look at the coin. The classical one moves right or left accordingly. The quantum one, instead, has to make a choice, and here quantumness really starts playing a role. Indeed, a measurement over the state of the coin has to be performed. If a head-tail basis is chosen for the measurement, the evolution will be exactly the same as in the classical case, because the walker will move right or left in a mutually exclusive way. Conversely, by measuring the state of the coin in a rotated basis, with basis states represented by a linear superposition of head and tail, interference effects change the probability to go left or right and, eventually, the whole probability distribution at each step of the evolution. Another way to understand such a behaviour is that the walker, when the coin state is measured in a rotated basis, actually goes in a linear superposition of right and left movements which, of course, would be impossible for a classical walker. Such a superposition creates interference

effects along the evolution, thus greatly changing the final probability distribution. It has been shown by Einstein in [8] that, in CRW, the probability to find the walker, for instance a particle, at a given distance x from the initial position after a time t of the evolution is represented by a gaussian probability distribution centered in the starting site x_0. Moreover, the square of the width of the distribution grows linearly with time, a behavior usually referred to as diffusive. As we will show later, in a QW, quantum effects give birth to several different spreading regimes.

From its first introduction, several changes have been introduced on top of the CRW and QW models. For instance, it is possible to insert a probability distribution for the length of the step performed by the the walker, such that it can perform longer or shorter steps than the usual one, eventually resulting in the movement in a continuous site space instead of a discrete one. Such kind of conditions brings to the so called (Quantum) Lévy Flights or (Quantum) Lévy Walks, which have been extensively studied [9, 10].
One of the most important change that can be imposed on both models is probably the introduction of two different approaches to the walker evolution, resulting in the discrete and continuous time models [11]. Let's focus on the first one. It basically consists on the model presented above which, in the quantum case, is called Discrete Time QW (DTQW) because of the fact that the time parameter, corresponding to the step number t, is discretized and the walker can only moves instantaneously from a site to another one, with no dynamics happening during the movement. In this framework, the equation governing the whole evolution is

$$|\psi\rangle_{t+1} = \hat{U} |\psi\rangle_t$$

where $\hat{U}$ is the unitary evolution operator acting on both the coin and walker states encoded in $|\psi\rangle$. This approach is extremely useful to model, for instance, coherent excitation and energy transport in photosynthetic and solid state systems [12, 13, 14, 15, 16]. The evolution of the walker can also be studied by introducing a degree of classicality, namely an amount of decoherence [17]. This reduces the interference effects, which is the main difference between CRW and QW. Moreover, disordering techniques can be used to modify the evolution of the walker without loosing its coherence during the walk [18, 19].
Let's now focus on the second approach. In the case of CRW, the continuous time version of it is achieved by inserting a continuous probability distribution over the waiting times of the walker. This means that the walker waits for a random time before taking a step, resulting in a continuum of the times in which it can move. For the quantum case, the model of Continuous Time QW (CTQW) has been introduced for the first time in [20] by Farhi, trying to introduce the solution of a continuous time Markov chain, of which the CTQW is a particular realization. In this approach, a continuous time application of the evolution operator, which in this case is represented by a Hamiltonian operator, characterizes the evolution. This means that the walker can move at any time by following the equation [21, 22]

$$i\frac{\partial\psi(x,t)}{\partial t} = -\gamma\left[\psi(x+1,t) - 2\psi(x,t) - \psi(x-1,t)\right]$$

where γ is the jumping rate from one site to its neighbour.
Despite the differences in the two formulations, i.e. discrete and continuous walks, many efforts have been done to link one to the other. In the classical case, discrete CRW are linked to continuous time ones by a limit process. On the contrary, in the quantum case, a relevant difference between DTQW and CTQW holds, making it

difficult to directly link the two approaches: in the discrete version a coin is needed, in the continuous one it is not. This difficulty has been overcame only in 2006 by Strauch, who showed that the two models are linked under a limit operation, considering particular working conditions [21]. A later work by Childs showed that it is possible for a DTQW to simulate a CTQW, working with the so called ϵ-approximation. We will not go more deeply in this topic, as it is not the main task of this work. Despite this, it is important to be aware of the link between DTQW and CTQW because of the fact that, under some approximations, the findings in one of the model can be translated in the other one.
Beyond this main separation, many other modifications can be superimposed to both models. For instance, one can study the effect of different coin operators acting during the evolution [23, 24], or how a multidimensional coin affects the evolution of the walker [25, 26]. Moreover, modifications can be performed on top of the line along which the particle moves. For instance, one can impose same boundary conditions on the sides of the line, turning it into a circle, or can impose absorbing or reflecting barriers [27], which corresponds, respectively to a finite line in presence or absence of losses. Moreover, one can enlarge the space in which the walker moves, and think about several graph structures in two, three or even higher dimensions [28].
Despite all these modifications, the most studied model of QW remains the one in which the walker moves on a discretized and infinite line. The reason for this is the relevance of such a simple model for quantum information tasks as well as the possible experimental implementation [29, 30, 31, 32, 33]. First of all, it is useful to build quantum walks on more sophisticated graphs, thus acting as a building block for all the studies about QWs. Secondly, it is useful to understand applicability of QW to algorithm developments and third, it is a suitable platform to test the effective quantumness of quantum computers [11]. For all these reasons, several efforts have been done in order to deeply understand the features of the evolution as, for instance, the infinite time limit shape of the probability distribution. In this sense, DTQW has been analytically solved by means of different techniques. For instance, a Schrodinger approach considering Fourier transform has been used by Nayak [34], followed by Ambainis et al. [27, 35] to compute the probability distribution as the number of the step approaches infinity, demonstrating some relevant theorems. A different approach, based on a combinatorial computation, has been used by Carteret et al. [36, 37] . This approach considers the number of paths leading to a given site x^* starting from an initial site x_0. In this sense, it can be seen as a discretized version of path integral method. It has been shown that these two approaches are equivalent [37].

Many authors studied the link between CRW and QW, aiming to understand the computational properties of both type of random walks. This has been usually done by means of decoherence, which allows to reduce a QW into a CRW. For a long time decoherence has been thought as a limiting effect, because it was linked to the loss of quantum information. In recent years, Mohseni et al. showed that decoherence can be useful in some natural processes, which have their rate increased thanks to interaction with environment, which generally decreases the coherence of a quantum system [14]. Moreover, the effect of decoherence has been studied in both cases of DTQW and CTQW [38, 39] and it has been shown that it can be useful in quantum algorithm development. Decoherence is not the only tool that has been used to study the quantum to classical transition. Indeed, the insertion of completely random disorder along the QW evolution showed that, after avearaging over many realization of the disorder, the evolution resembles the classical one, characterized

by a diffusive spread [40, 41].

A question naturally arise: why QW, after all the studies that has been performed on them, are still a so extensively studied research field? One answer can be found in their possible algorithmic employment. CRWs have been proved to be useful in many stochastic algorithms used, for instance, in optimization problems. For this reason, a huge interest borned in the study of algorithmic properties of QWs. The development of quantum algorithms as well as the proof that QWs are a computationally universal model, has increased the efforts in QW studies. By an algorithmic point of view, DTQWs have been used for the oracle determination in research problems. For instance, a QW based algorithm to search elements among a set of them has been developed [42]. After this, several algorithms aimed to solve searching problems in more than one dimension have been developed [43, 44]. Also CTQW have a huge relevance in quantum algorithms. As an example, Farhi and Gutmann in [20] described a CTQW based algorithm to traverse a graph in polynomial time instead of an exponential time. Recently, Caruso and Dalla Pozza showed that QWs can be useful in the solution of the open problem of quantum state discrimination [45].
A huge speedup in QW studies has been given by the paper from Childs [46] and Lovett [47]. In the first one, the universality of CTQW computation model has been proved. This implied that any algorithm implementable on a quantum computer can be also implementable by quantum gates in the model under investigation. In the second one, the universality of DTQW has been proved.
For all these reasons, it is clear that the study of QW, along with all its possible modification, is of fundamental relevance. Its wide applicability makes it a powerful tool not only for quantum information theory but also for quantum computation and simulation tasks.

2.2.1 Natural phenomena simulation

Simulations of classical and quantum systems has ever been relevant to understand their properties. In his 1982 paper, Feynman observed that only a quantum computer could simulate, or better, imitate, the nature, because of the fact that nature is quantum and resources needed to compute and store information about probability distribution increases exponentially with the size of the physical portion of nature we aim to simulate. In this sense, quantum simulation become more and more relevant, and many studies, both experimental and theoretical, have been performed to deepen the knowledge on this topic. For instance, complex phenomena have been simulated by means of CTQW, as fermion statistics [48], Rabi model [49], dynamics in topological insulators [50], relativistic Majorana equation [51], Fano interference [52] and NOON states bloch oscillations [53]. Moreover, QWs have been used to study transport phenomena in biomolecules [54], evolution in solid-state systems [55], formation of molecular states [56], topological invariants [57, 58] and edge states [59, 60]. Following this path, a novel use of CTQW has been used by Mohseni et al. to model the energy transport phenomena in photosynthetic processes, considering the effect of the environment on the interference effects [14]. Their findings show that QWs are a suitable model to describe energy transport phenomena. The present thesis covers findings within this particular field of study. In fact, as explained later, in the present work we explore the possibility to reproduce the spread of an energy packet resembling the ones which can be found in several natural energy transport phenomena, which in many cases present some particular characteristics, i.e. a non linear dependence of the spread of the energy excitation over time.

2.3 Classical and Quantum Random Walk

In this section, we will describe in detail the model of the CRW and QW, focusing on the case in which the classical or quantum particle moves among the sites of a discretized line. Sometimes, we will refer to the particle as walker.
The basic idea of a QW is the very same as CRW, modified according to quantum mechanics. Let us briefly recall the model of CRW. In this model, a (classical) walker moves among the sites of a 1D space and, at each step of the walk, it randomly jumps to its left or right, respectively with a probability p and $q = 1 - p$, as shown in Fig. 2.1, with no dynamics happening during the movement.

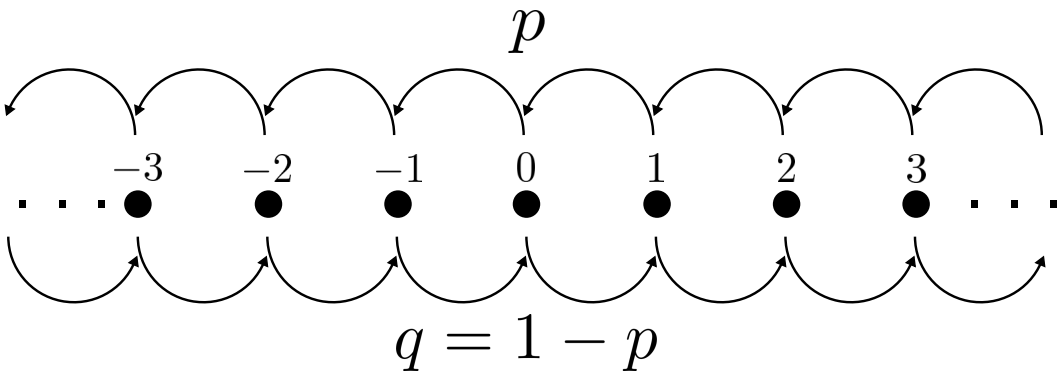

Figure 2.1. Sites of a discretized line represented as black circles. In CRW, the walker, which without loss of generality starts from site 0, jumps to its left or right at each step with probability p and $q = 1 - p$, respectively.

It is easy to generalize the model to higher dimensions. For instance, the walker can move in a 2D discretized space as a grid, according to four values of probability $p_{\rightarrow}, p_{\leftarrow}, p_{\uparrow}, p_{\downarrow}$ where the subscript denotes the direction of the movement.
The decision to go left or right can be modelled as the toss of a (rigged) coin and can then be described as a Bernoulli process. Because of the fact that the walker moves by shifting its position of the same fixed amount at each step, i.e. ± 1 and that, without loss of generality, it starts the walk in site 0, at even (odd) step numbers it can be only found in even (odd) sites. The movement of the walker can be expressed by means of a random variable $X_t = \pm 1$, representing the direction taken by the particle at each step, or time interval, t, each of them independent and identically distributed. The position reached by the walker after T steps when it starts in $x_0 = 0$ is

$$x_T = X_1 + X_2 + \cdots + X_T.$$

We can define the Bernoulli variable Y_t as

$$Y_t = \begin{cases} 1, & X_t = 1 \\ 0, & X_t = -1 \end{cases}$$

which can be expressed as

$$Y_t = \frac{1}{2}(X_t + 1).$$

The variable Y_t models the toss of the coin at each step t.
Because Y_t is a Bernoulli variable, we can define the variable $Z_T = \sum_{t=1}^{T} Y_t =$

$\frac{1}{2}(x_T + T)$ which is distributed according to the binomial distribution. We can then compute the probability to find the particle in site x after T steps as

$$P(x_T = x, t = T | x_0 = 0) = P(Z_T = \frac{1}{2}(x_T + T) = \frac{1}{2}(x + T)) =$$
$$= \begin{cases} \binom{T}{\frac{T+x}{2}} p^{\frac{T+x}{2}} q^{\frac{T-x}{2}}, & \frac{1}{2}(x+T) \in \mathbb{N} \cup 0 \\ 0, \quad \text{otherwise.} \end{cases}$$

Basically, the distribution can be easily derived by counting the number of paths bringing to each site x after T steps. In Fig. 2.2 we report the simulation of a CRW with $p = q = \frac{1}{2}$ for 30 steps and 10^5 trials.

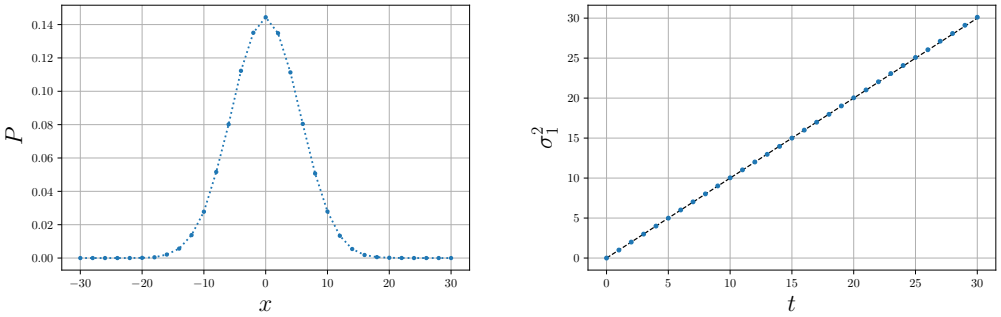

Figure 2.2. Left: walker probability distribution at step 30 considering 10^5 repetitions of the walk. **Right**: variance behaviour as a function of the step (dots) superimposed to a perfectly linear behaviour (black dashed line).

For a high number of steps, the Binomial probability distribution approaches a Gaussian one. The bell shaped distribution is typical of classical mass and energy transport phenomena, as, for instance, the Brownian motion of a particle. When computing the variance of the probability distribution as a function of the step number, namely

$$\sigma_1^2(t) = \sum_{x=-t}^{t} x^2 \cdot P(x,t) - \left(\sum_{x=-t}^{t} x \cdot P(x,t) \right)^2 \tag{2.3}$$

it is easy to see that it grows linearly with the time t (see right image in Fig. 2.2), namely

$$\sigma_1^2(t) \propto t.$$

This can be derived considering that Z_T follows the binomial distribution, thus the expected value $E[Z_T] = Tp$ and the variance is $V[Z_T] = Tpq$. Thus, the variance of x_T, which corresponds to σ_1^2, reads $V[x_T] = 4Tpq$, which is linear in the number of the step T. This behaviour is known as *diffusive* and it features several natural phenomena. One can add several modification to the basic model of CRW, for example by giving the walker the chance to perform jumps of different length at each step, or to wait for some time before deciding to move again, or by furnishing it with some memory of the past walk, as in the elephant walk [61], and so on. Several studies have been performed on this topic, see for instance [9].

When focusing on the quantum counterpart of CRW, namely the QW, the walker and coin became quantum, but the basic idea remains untouched. Indeed, the walker again moves between the sites of an infinite discretized line, but in general he will be found in a linear superposition of all the possible site states [11, 62]. The walker state is written as a linear combination of the position, or site, kets $|x\rangle_p$, with $x \in \mathbb{Z}$, which form an orthonormal basis of an infinite-dimensional Hilbert space $\mathcal{H}_p$. In the following we will omit the subscript p unless it is necessary. Because of the fact that at each step the walker can move only to adjacent sites, for a given time t of the evolution, which we recall corresponds to the step number, it is possible to restrict the dimension of the Hilbert space to $2t+1$ by considering only the possible states in which the walker can be found, i.e. $\{-t, -t+2, \ldots, t-2, t\}$.
As in the classical case, the movement of the walker is conditioned to the state of an other system, in this case a quantum coin. In the present work, we will restrict our attention to coins living in a two dimensional Hilbert space $\mathcal{H}_c$, but more general treatments can be done, exploiting dimensionality larger than 2 [11]. The usual basis states of the coin is represented by the kets $|0\rangle_c, |1\rangle_c$, playing the role of head and tail.
With this elements, it is possible to write the state of the whole system composed by the walker and the coin at a given step t as

$$|\psi\rangle_t = \sum_{x=-t}^{t} \alpha_{x,0} |x\rangle |0\rangle_c + \alpha_{x,1} |x\rangle |1\rangle_c$$

with $\alpha_{x,0}, \alpha_{x,1} \in \mathbb{C}$ provided that $\sum_{x=-t}^{t} |\alpha_{x,0}|^2 + |\alpha_{x,1}|^2 = 1$.
The evolution of the complete system *walker* $\otimes$ *coin* is described by two operators: a coin operator $\hat{C}$, which changes the state of the coin, and a shift operator $\hat{S}$, which moves the walker depending on the state of the coin.

Let's consider the state of both coin and walker $|\psi\rangle_t$ at a certain evolution time t. One step of the evolution in terms of $\hat{C}$ and $\hat{S}$ can be written as

$$|\psi\rangle_{t+1} = \hat{S} \cdot \hat{C} |\psi\rangle_t = \hat{U} |\psi\rangle_t . \tag{2.4}$$

The shift operator $\hat{S}$ is usually written as

$$\hat{S} = \sum_x |x-1\rangle \langle x| \otimes |0\rangle_c \langle 0|_c + |x+1\rangle \langle x| \otimes |1\rangle_c \langle 1|_c$$

which represents a conditional shift depending on the state of the coin, while the $\hat{C}$ operator is usually written as an Hadamard operator acting on the coin state and an identity operator acting on the walker

$$\hat{C} = \hat{\mathbb{I}} \otimes \frac{1}{\sqrt{2}} (|0\rangle_c \langle 0|_c + |0\rangle_c \langle 1|_c + |1\rangle_c \langle 0|_c - |1\rangle_c \langle 1|_c)$$

which, applied to a coin state $|0\rangle_c$ or $|1\rangle_c$, generates a balanced superposition of both basis states.
A typical representation of a QW is reported in Fig. 2.3. Here, each vertical line represents a site of the line that the walker can reach. The walker moves from top to bottom, such that different rows correspond to different steps.

The diagonal lines represent paths that the walker can travel, linking adjacent sites. The coin operator, embedded in each vertical line, changes the state of the coin whenever the walker reaches a new position. In this representation, the two different paths bringing at the same site represent the two basis states of the coin.

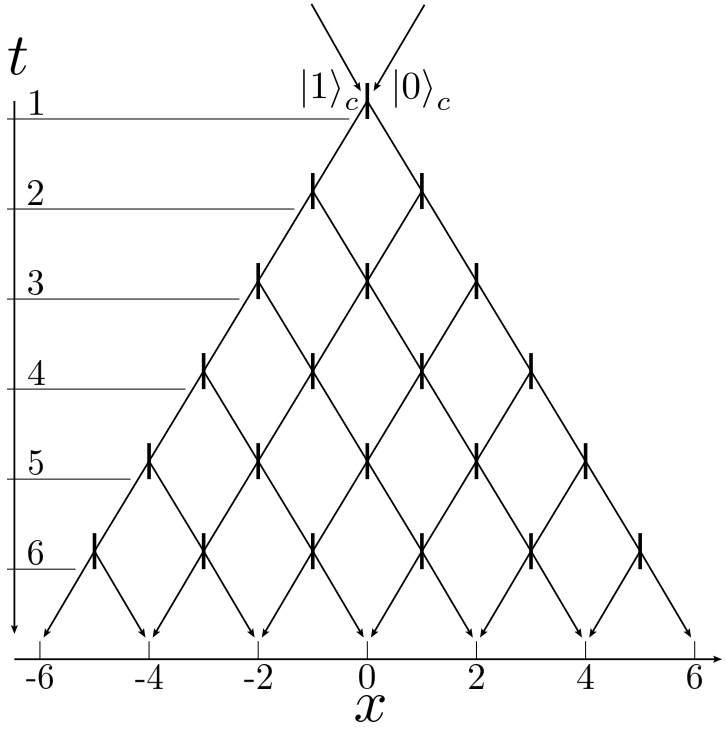

Figure 2.3. Typical representation of a QW up to the 6th step. Different rows correspond to different steps of the evolution, different black vertical lines on a row correspond to different sites. The two lines arriving at the same site represent the two different coin states. The vertical lines encode the effect of the coin and shift operators $\hat{C}$ and $\hat{S}$.

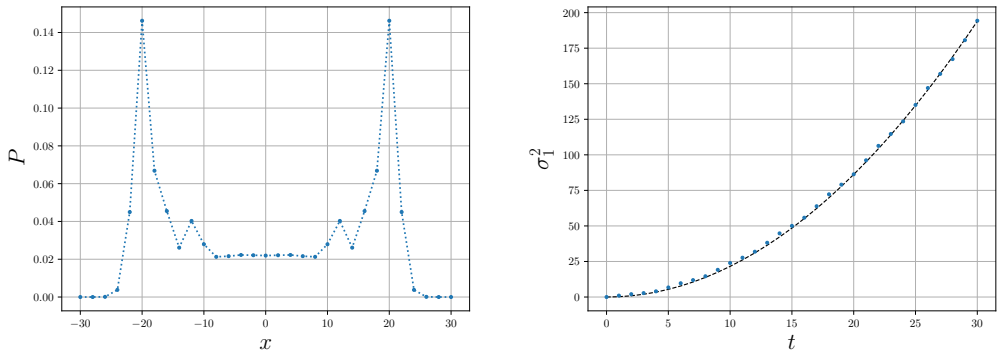

Figure 2.4. Left: walker probability distribution at step 30 for an ordered QW. **Right**: variance behaviour as a function of the step (dots) superimposed to a behavior proportional to x^2 (black dashed line). The actual quadratic behavior is only reached for a very large number of steps.

Regardless of the particular degree of freedom employed in the realization of the QW, each global state $|x\rangle \otimes |0\rangle_c$ (or $|x\rangle \otimes |1\rangle_c$) of the global Hilbert space $\mathcal{H}_p \otimes \mathcal{H}_c$ can be written in a second quantization formalism as $|x\rangle \otimes |0\rangle_c \equiv \hat{a}_i^\dagger |0\rangle_F = |1_i\rangle_F$, where the subscript i indicates the set of values of the degrees of freedom of the particle in which the site and the coin are encoded. Let us clarify this point by considering a single photon as the quantum walker. If the sites of the line correspond

to the arrival spatial points of the photon, while the coin states correspond to the arrival direction of the photon to the same spatial point, then $i \equiv \{x, \vec{k}\}$ (this is the case of the all-optical quantum walk described in section 2.5.1). This is exactly the situation depicted in Fig. 2.3. Other choices of coin and sites encoding can be made. For instance, one can choose the polarization $\vec{\pi}$ as the coin degree of freedom and the arrival time τ of the photon to the detector as the sites of the line. In this case, $i \equiv \{\vec{\pi}, \tau\}$ (this is the case of the split-time QW described in section 2.5.2).
Despite the second quantization formalism is the best one to describe evolution of photons, when dealing with only a single walker it is convenient to work with the proper formalism of QW, in which it is better enlightened the role of the coin during the evolution. When dealing with two particles, it is much better to work in the second quantization picture, such that typical effects such as Hong-Ou-Mandel interference are naturally retrieved.
Let's return to the evolution of the quantum walker. The evolution for T steps is obtained by applying T times the unitary operator $\hat{U}$ to the input state

$$|\psi\rangle_T = \hat{U}^T |\psi\rangle_{t=0} .$$

This framework is useful to describe the *ordered* QW, in which the evolution operator $\hat{U}$, and then the coin operator $\hat{C}$, is exactly the same at each step of the QW.
The resulting behaviour for this kind of QW is called *ballistic*, which is characterized by a variance which grows quadratically with the number of the steps, namely

$$\sigma_1^2(t) \propto t^2$$

in contrast with the CRW in which the spread is linear in time (see Fig. 2.4). The spatial probability distribution is very different from the Gaussian one obtained in the CRW case. In the QW scenario, the probability distribution depends on the initial state of the walker. For instance, the double picked distribution shown in Fig. 2.4 has been obtained by furnishing the walker with an initial coin state corresponding to $|\psi\rangle_c = \frac{1}{\sqrt{2}}(|0\rangle_c + i\,|1\rangle_c)$. When the walker is initially furnished with a coin state $|\psi\rangle_c = |0\rangle_c$ ($|\psi\rangle_c = |1\rangle_c$) the resulting probability distribution present a maximum in site -20 ($+20$), with the maximum in site $+20$ (-20) strongly suppressed. This happens due to the interferences effects which are sensible to the initial coin state. Nevertheless, in every case the variance grows quadratically with the step number.

2.4 Disordered Quantum Walks

A more general description of the quantum walker evolution implies the possibility to insert some kind of disorder along the QW. Quantum walks are subjected to localization phenomena just like condensed matter systems [63] and a lot of efforts have been made in the study of connection between localization and various type of disorder in quantum walks. Many theoretical and experimental studies, performed on various kinds of platforms and with different definitions of disorder, have been performed (see for example [64, 65, 18, 66, 30, 67, 68]). In particular, the localization effects hinder the spreading of the walk and the quantum walk seems to get more and more similar to a classical random walk, as the quantity of disorder increases. Several ways have been used to introduce disorder in the walk, for instance by means of decoherence (which is an explicit destruction of coherence, thus an explicit transiton to classicality); decoherence is a physical phenomenon that

typically arises from the interaction between quantum systems and their surrounding environment. Decoherence has been usually seen as an annoyance as it has been linked to loss of quantum information. Recent studies showed that can be useful for quantum algorithm building [38]. Decoherence occurring through measurement or free interaction with a classical environment is a typical framework for studying transitions of quantum walks into classical random walks [67, 17]. Other kinds of disorder, not implying destruction of coherence, can be adopted. The disorder we focus on in the following is coherent disorder. It doesn't destroy coherence, since it only consists of changing the shape of the coin operator, preserving coherence and then interference effects. This can be done by allowing a time and space dependence of the coin operator, such that the jumping probability amplitude from a site to the adiacent one, or the phases acquired by the walker during the step, are no more constant in time or space. In the following, we will examine three different disorder situations, which provide three distinct spreading behaviours.

2.4.1 Static disorder

Anderson localization

In 1958 P. W. Anderson theoretically showed that the wavefunction of a quantum particle can suffer an exponential localization in the presence of a statically disordered potential, namely a potential fixed in time but varying over space [63]. As a consequence, it is expected that particle and energy transport, governed by quantum mechanical laws, through a disordered medium should be strongly suppressed and that an initially localized wave packet should not spread out with time. Before Anderson's discovery, a Brownian motion model was used to describe the movement of electrons in such media (and in general transport phenomena), because of the fact that they were treated as point-like objects. However, in his paper, Anderson changed point of view revisiting the effect of disorder on the evolution of an electron's wavefunction in an otherwise periodic crystal. Anderson analysed the problem in the quantum regime and, by accounting for the wavefunction of the electron, he found that the classical diffusive motion of the electron breaks down and the electronic wavefunction becomes exponentially localized, under a broad range of conditions. Consequently, when the electron is initially localized on one atom, its wavefunction will no longer expand to cover the whole crystal with time, according to Bloch theory, but it will rather remain localized around its initial position. The material will cease to conduct charge, and eventually become an insulator. The interference between different paths, arising from multiple scattering of the electron by lattice defects, is responsible for this localization effect. The basic assumptions at the heart of Anderson's model is that the potential is time-invariant. In general, localization effects are lowered by the presence of temporal variations in the potential, which can arise from both lattice itself and external disorder. Moreover, the reduction of the coherence of the scattering, happening due to the presence of temporal fluctuations (such as phonons), destroys the interference effects and eventually leads to the recovery of Ohm's law. Even more importantly, Anderson's model describes a single particle, or an ensemble of non-interacting particles. For this reason, this model was hardly appliable to electrons, which are fundamentally interacting fermionic particles (they interact, for instance, through Coulomb's law or spin exchange). When interactions are included, the scenario changes dramatically and localization generally does not occur. These two preconditions underlying Anderson's model — time-invariance of the potential and the absence of interactions — made experimental observation of Anderson localization in crystals very hard to

perform. These conditions are, indeed, easily achievable in photonic systems.

Localization in photonic systems

Localization is essentially a wave mechanics phenomenon, thus it can be extended to every wave-like system [69, 70]. Optics is a suitable framework to study localization: in optics, coherence is easily preserved and photons are non-interacting bosons. The adaptation of the localization model to optical systems consists of the "transverse localization scheme", proposed separately by Abdullaev [71] and De Raedt and al. [72]. In this scheme, the evolution of a light beam is treated like the wave packet of a quantum particle, replacing time with the propagation direction z. So, the description passes through the Schrödinger-like paraxial equation:

$$i\frac{\partial\psi}{\partial t} = \left[-\frac{1}{2k}\left(\frac{\partial^2}{\partial x^2} + \frac{\partial^2}{\partial y^2} - \frac{k}{n_0}\Delta n(x,y,z)\right)\psi\right] \equiv \hat{H}\psi$$

where z is the propagation direction, which acts like time, x and y are transverse dimensions. ψ is the slow-varying envelope (we assume paraxial approximation) of the field $E(r,t) = Re\left[\psi(x,y,z)e^{i(kz-\omega t)}\right]$ of frequency ω and wavenumber $k = \frac{\omega n_0}{c}$, where n_0 is the average refraction index. Δn is the local change in refraction index, such that $|\Delta n| << n0$; it replaces the potential V of the Schrödinger equation, so, to have proper Anderson localization, it has to be independent of time, $n(x,y,z) = n(x,y)$. The first experimental evidence of this phenomenon was given by Schwartz and al. [73], highlighting the importance of ensemble-averaging in this scheme because of the shortness of the typical propagation distance, which does not allow self-averaging, making it necessary to average on multiple realizations of disorder. In this scheme, the most important observable is the intensity of the beam after a certain propagation length and averaged over many experiment with different spatial realizations of fixed-in-time disorder. This particular observable allows a quite direct appreciation of the localization of the wave packet: indeed, it is possible to "see" the wave packet expanding for a short time and then halting. The direct observation of the wave packet makes the transverse localization scheme one of the most convenient and direct ones for observing localization phenomenon. The main drawback is that it can be only applied to transport phenomena in one or two dimensions, making it impossible to observe the phase transition associated with Anderson localization in three dimensions. Schwartz et al. observed Anderson localization in disordered 2D photonic lattices; they studied the framework of increasing disorder, observing three different regimes:

- in absence of disorder the beam diffracts in the periodic structure, showing ballistic transport;
- the introduction of weak disorder generates a loss of symmetry and the light intensity tunnels randomly between sites, raising diffusive transport (like a classical random walk);
- by increasing the disorder level, the intensity pattern narrows and the beam localizes (after a short diffusive propagation).

A similar experiment was carried out by Lahini et al. [74], showing that in a 1D photonic lattice, transport changes from ballistic to localized without the intermediate diffusive regime.

Anderson localization in a Quantum Walk

A photon wandering in a QW, by definition, propagates. Therefore, many reasons make QWs a suitable framework for studying localization in optical systems, for instance:

- the propagation process is determined by unitary operations (except when decoherence is introduced) and it can be easily generalized (it is a good framework for simulations [75]);
- it is theoretically simple to introduce disorder and to control it;
- it is usually possible to extract information at any step, except for integrated quantum walks, which, on the other hand, provide extremly high phase-stability and minimum losses.

A very good example is provided by Schreiber et al. [67], who were able to implement many regimes of disorder on their QW, by means of a simple EOM, suitably tuned with respect to the laser's pulses repetition rate (see section 2.5.2 for an insight of such an implementation). An integrated quantum walk was used by Crespi et al. [66] to experimentally study Anderson localization for two particles (see next paragraph).

Colocalization

The experiments mentioned in the previous section used classical light, i.e. lasers, to explore the propagation in the presence of disorder. The behaviour of a single photon does not show any deviations from classical wave propagation, because only first order interference plays a role in the propagation dynamics. Something more arises when two or more indistinguishable particles propagate at the same time in the system. In fact, even without direct interaction, second order interference and quantum correlations affect the outcome. Correlations of two indistinguishable particles travelling in a periodic lattice were first described by Bromberg et al.[76]; his studies focused on true single-photon systems and in particular in the context of QWs [77, 31, 32], showing that the results for bosons and fermions were different (as expected, due to the respective bunching and anti-bunching properties) and that they could be simulated by suitable entangled photons states [31]. In a theoretical study, it has been shown by Lahini et al. [78] that the localization of one particle should influence the other one's localization, while, for long time scales, when both the particles have localized, the correlations between the two particles show some kind of oscillatory behaviour: the separation between localized bosons tends to an even number of sites, while the one between fermions favours an odd number of sites between the localization positions [79]. This phenomenon has been experimentally implemented in an integrated Quantum Walk by Crespi et al.[66].

2.4.2 Dynamic disorder

Anderson localization requires the potential to be stationary in time. If the disorder evolves dynamically, transport is resumed. There are many ways to introduce dynamical disorder, and different disordering approaches generate different outcomes. If the disorder is homogeneous in space, but not in time (like a refraction index

homogeneous in the medium, but varying during the propagation) the propagation of light comes back to diffusive regime [65]. Schreiber et al. [67] used a QW to show this phenomenon: they inserted disorder in the process by applying a random phase (spatially uniform) at each step. As a result, the photon undergoes a classical random walk, revealing a binomial probability distribution. The maximum phase applicable to the walker is stepwisely increased, showing a transition from ballistic to diffusive behaviour. In a system with dynamic disorder, decoherence reduces the expansion of the wave packet to the level of a diffusive classical particle. In contrast, static disorder leads to a stagnation of the spread and hence an even smaller variance. On the other hand, a spatially random potential which also fluctuates in time can give rise to hyper-transport, namely a super-ballistic behaviour [73]. Some earlier theoretical works [80, 81, 82, 83] showed that hyper-transport was possible, in presence of such a potential; the first experimental proof was provided by Levi et al. [84]. The fluctuating potential causes stochastic acceleration, which makes the original wave packets expand at a faster rate than ballistic, while its momentum spectrum expands, too. The latter does not happen in ballistic regime, namely ordered paths.

2.4.3 The p-diluted disordering model

In the present work we will focus on a particular kind of disorder, so called p-diluted, introduced for the first time in [18].
The basic idea of the model is to introduce a disorder parameter p which characterizes a particular class of evolutions. Suppose that the coin operator is no more constant over time and space. Thus, in principle, at each site and step of the evolution, the coin operator can be different from the Hadamard one, for example in the amplitudes of the mixing coefficients or in the phases introduced between the basis states. If this is the case, one can explicitly write the space and time dependence of the coin as $\hat{C}(x,t)$, where x is the site index and t the step number. The evolution (2.4) can then be modified as

$$|\psi\rangle_{t+1} = \hat{S} \cdot \sum_{x=-t}^{t} \hat{C}(x,t)\, |\psi\rangle_t \,.$$

In the p-diluted model, an initial setting of the coin operators $\hat{C}(x,t)$, which defines the action of the coin at each step and site of the evolution, is given. For instance, the initial setting could be the one typical of an ordered QW, with $\hat{C}(x,t) = \hat{C}$, namely the same coin for each site and step, or the one typical of the static disorder, in which $\hat{C}(x,t) = \hat{C}(x)$, i.e. the coin is time independent. Subsequently, the initial setting is modified with a given probability p in the following way:

$$\hat{C}(x,t) = \begin{cases} \hat{C}'(x,t) & \text{with probability } p \\ \hat{C}(x,t) & \text{with probability } 1-p \end{cases}$$

namely, the coin operator at site x and at step t remains unchanged with a probability $1-p$ or changes with a probability p.
The p-diluted model can be seen as a perturbation of an initial coin setting. This leads to a very broad applicability of the model, because it can be used to study in a controlled way the transition from a particular QW configuration, obtained when $p = 0$, to the completely disordered one, corresponding to the case $p = 1$. For instance, in the present work, the model has been experimentally implemented to

study the transition between the ordered and disordered QW, and the one between the Anderson localization and the diffusive spread. We show that this transitions are featured by (transient) superdiffusive and subdiffusive spread of the walker, respectively. Within this framework, the parameter p corresponds to the degree of disorder, namely the percentage of randomly changed coin operators with respect to the starting condition.
It is important to note that, for a given value of p, many different QW configurations can be obtained. Indeed, changes in the coin operators can happen in random sites at random steps according to the probability p, generating many different configurations. In the following we will call them phase maps or coin maps.

2.5 Experimental implementation

In this section, we will describe the experimental setups used to perform the experiments lying at the heart of this thesis work.
Firstly, we focus on the all-optical QW, a novel setup built in the Quantum Optics labs of the University of Rome "La Sapienza". The setup has been used to demonstrate the superdiffusive spread of a quantum walker subjected to a p-diluted model applied to an initially ordered QW [29, 18].
We will then focus on the time-split QW, a well established apparatus based to the Integrated Quantum Optics labs of the University of Paderborn. This setup has been used to reproduce the subdiffusive spread of the walker when the p-diluted technique is applied to a initially statically disordered QW [19].

2.5.1 All optical quantum walk

The movement of a quantum particle among the discretized sites of a one dimensional line can be realized by means of a beam splitters (BSs) network, each of them representing a particular site of the line, as depicted in Fig. 2.5. In this representation, each BS acts both as $\hat{C}$ and $\hat{S}$ operators.

Several implementations of such optical QWs have been realized, based on bulk optics schemes or femtosecond laser written photonic circuits [85, 86, 87, 31]. The bulk optics setup used in the present work is a completely free space realization of a BSs network, based on two displaced multi-pass Sagnac Interferometers (SIs) linked by a single central common BS, as depicted in Fig. 2.6 [88, 29].

To explain the functioning of the setup, let's focus on the *input 1* beam. The input radiation, which can be a continuous wave (CW) laser as well as single photons, is injected in the setup through a single mode fiber followed by a 10X objective. It is directed to the BS by means of a small square mirror of 5mm long side. The action of the BS can be described as follows. The BS is a glass cube formed by two halves, kept together with a cement glue. When an electromagnetic wave arrives at the separation surface between the two halves, part of it is reflected, the remaining part is transmitted. Then, the BS can be described by considering it as a 2-input 2-output modes device, as depicted in Fig. 2.7.

In a second quantization formalism, we can associate a creation operator to each of the four modes, considering $\hat{a}^\dagger, \hat{b}^\dagger$ as the operators of the input modes and $\hat{c}^\dagger, \hat{d}^\dagger$ as the operators of the output modes. The BS transformation can then be written as

$$\hat{a}^\dagger \longrightarrow t\hat{c}^\dagger + ir\hat{d}^\dagger$$
$$\hat{b}^\dagger \longrightarrow t\hat{d}^\dagger + ir\hat{c}^\dagger$$

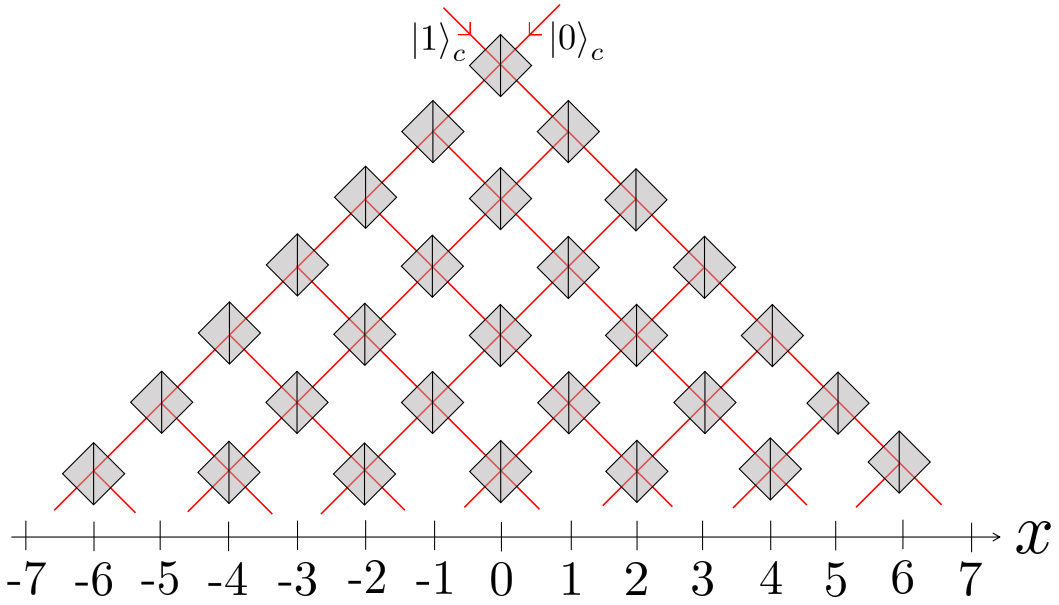

Figure 2.5. Typical representation of a QW using a BSs network. Each square represents a BS, with two input and two output modes. The two different arriving directions on the BS correspond to the two different coin states.

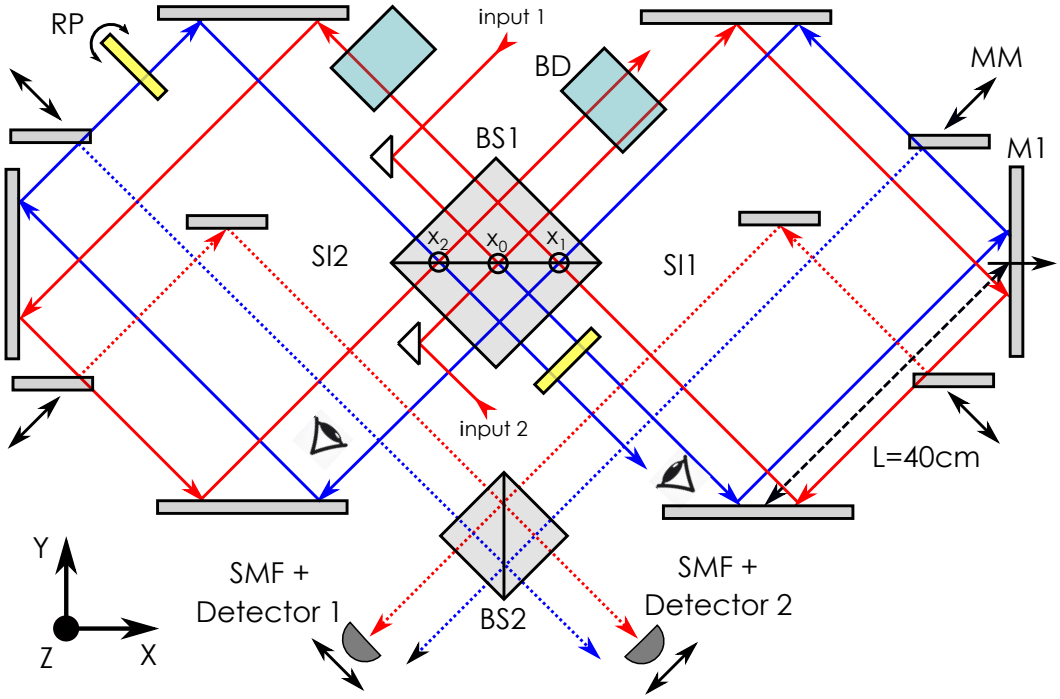

Figure 2.6. Sketch of free space QW scheme. BS: beam splitter, BD: beam displacer, RP: rotating glass plates, MM: moving mirror, SMF: single mode fiber. Blue and red beams circulate in opposite directions and impinge on the BS_1 in the same horizontal point but at different heights along the z direction, due to the effect of BD.

where t and r are the transmission and reflection coefficients, linked by the condition $t^2 + r^2 = 1$. By means of the identification

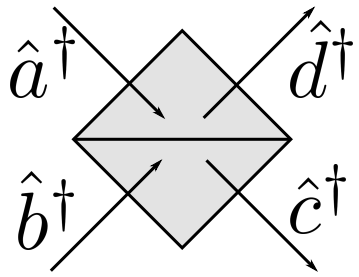

Figure 2.7. Sketch of a BS. Each mode is described by the respective creation operator.

$$\hat{a}^\dagger |0\rangle_F \equiv \begin{pmatrix} 1 \\ 0 \end{pmatrix}$$
$$\hat{b}^\dagger |0\rangle_F \equiv \begin{pmatrix} 0 \\ 1 \end{pmatrix}$$

we can write the BS transformation in a matrix form as

$$\hat{BS} = \begin{pmatrix} t & ir \\ ir & t \end{pmatrix}.$$

In the case $t = r = \frac{1}{\sqrt{2}}$ we obtain a transformation equivalent to the Hadamard gate between the input and the output states, apart for a phase factor on the reflection coefficients. The BS is then able to implement the coin operator needed to perform a QW.
At the first interaction with the BS, which happens in the horizontal point x_0, the radiation is split into two different paths, the reflected (clockwise, red path) and the transmitted one (counterclockwise, blue path), travelling in the first squared Sagnac interferometer SI_1. If all mirrors of SI_1 are placed at the angles of a rectangle (ideally a square), then the radiation will propagate along the same paths but in opposite directions, closing the loop in the same point of the BS where they started. By translating the farthest mirror M_1 of the SI_1 along the x axis of a quantity $\Delta x_M \sim 3.54$mm, the clockwise and counterclockwise directions will propagate along different paths, displaced of a quantity $\delta = \sqrt{2}\Delta x_M \sim 5.00$mm, and will recombine on the BS in the point x_1, shifted along the x axis of a quantity $\delta_{BS} = 2\Delta x_M \sim 7.07$mm with respect to x_0. This new point acts as a starting one for the second Sagnac interferometer. Here, all the mirrors are placed at the angles of the rectangle. Eventually, the paths recombine again on the BS in a third point, x_2, different from the previous ones, shifted along the x axis of a quantity $-\delta_{BS}$ with respect to x_0. At each interaction with the BS, a new point on the x axis is involved.
This geometric configuration generates in the $x - y$ horizontal plane of Fig. 2.6 a (quasi) infinite loop, equivalent to a chain of phase-stable and independently tunable Mach-Zehnder interferometers [88], as shown in Fig. 2.8. Despite the actual geometry gives birth to Mach-Zehnder interferometers, we will refer to them as SI instead, to resemble the starting geometry of the setup.

The maximum number T of passages, or steps, that can be performed is limited by the size of the optical elements, namely the mirrors and the BS, and in particular by the smallest of them. In our case this corresponds to the BS, then $T = \frac{\sqrt{2}L}{2\Delta x_M} = \frac{L}{\sqrt{2}\Delta x_M} \sim \frac{5.00\text{cm}}{5.00\text{mm}} \sim 10$ where $L \sim 5.00$cm is the length of the BS side.

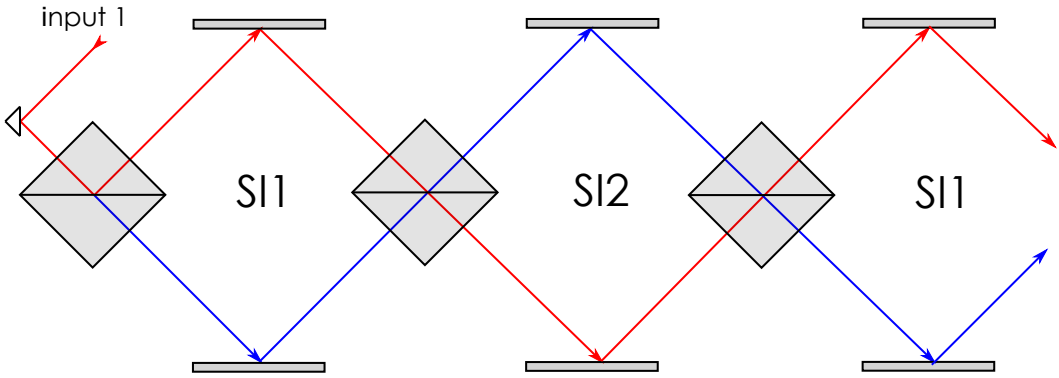

Figure 2.8. (Quasi) infinte chain of Mach-Zehnder interferometers which arises from the (quasi) infinite loop.

A QW network can be reproduced by exploiting the z axis of the BS as well as the x one. This can be done by means of a vertical beam displacer (BD), whose aim is to increase the height of the beam passing through it of a fixed quantity δh.
In the setup, BDs consist of a thick inclined glass prism. Its operation is represented in Fig. 2.9.

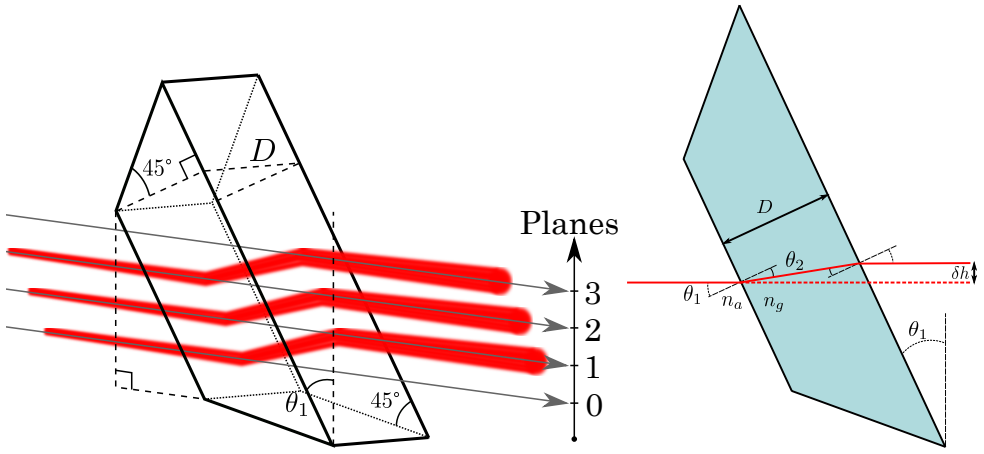

Figure 2.9. Sketch of the functioning of the BD used in the actual setup.

When a beam passes through it, it is vertically shifted by an amount δh, depending on the inclination, the thickness and the refractive index of the BD glass, following the relation

$$\delta h = D \frac{\sin(\theta_1 - \text{asin}(\frac{n_a}{n_g}\sin(\theta_1)))}{\cos(\text{asin}(\frac{n_a}{n_g}\sin(\theta_1)))}$$

in which θ_1 is the incidence angle of the beam with respect to the normal to the surface of the BD, $n_a = 1$ is the refractive index of the air, $n_g = 1.55$ is the refractive index of the glass and $D = 30$mm is the thickness of the prism. In order to have an increase of ~ 5.00mm (such that the vertical and horizontal separation of the beams result to be equal), the BD has to be inclined of an angle $\theta_1 \sim 25°$ with respect to the beam.
The parallelism between the BD's faces is a critical parameter. Indeed, if they are not

sufficiently parallel, the geometry of the setup could be compromised. A parallelism better than 1μrad is requested, which guarantees an interference visibility $V > 95\%$ up to the seventh step, mostly limited by unavoidable experimental errors in the setup alignment.
Two BDs are used in the setup, one of them intercepting only the clockwise paths in SI_1, the other one intercepting the counterclockwise paths in SI_2 (see Fig. 2.6). BDs actually act as the shift operator $\hat{S}$. Indeed, the path not passing through them are considered to be shifted to site $x-1$, while the ones passing through them are shifted to the site $x+1$.
After the action of the BD, the two paths in SI_1 will impinge on the BS in the same horizontal point x_1 but at different heights, the transmitted path travelling on the plane at height 0, the reflected one at height δ_h. This reproduces the second step of the QW network because two different interaction points of the BS can be seen as two different BSs, one in site -1 acting on the transmitted path and one in site $+1$ acting on the reflected path. As a result, four paths are generated. The ones travelling counterclockwise in the second SI pass through the second BD, such that their height is increased, while the clockwise paths travel at the same height as before impinging on the BS. When the loop closes again on the BS (third step of the evolution), the beams that increased once their height will impinge on it at the same x and z coordinates but from opposite faces of the BS, interfering. They actually represent the two coin states of site 0, which undergo interference due to the action of the coin operator. The other beams increased their height 0 or 2 times, corresponding respectively to sites -2 and 2 of the network. By extending such tracing to higher step, it is easy to prove that the setup geometry is capable to reproduce the whole network needed for a QW evolution.
Because of the fact that the same optical elements are involved in all the steps, and because of the Sagnac geometry, the setup is intrinsically stable in phase. A small phase instability is present only due to convective air modes, easily mitigated by means of a shielding box surrounding the whole setup.
A scheme of the beams pattern arising from the setup geometry is sketched in Fig. 2.10, as they appear when looking at the BS with blue modes travelling towards the observer (see Fig. 2.6, the eye symbols denote the points where one observes the represented patterns).

Beams corresponding to odd (even) steps circulate in SI_1 (SI_2); for each image in Fig. 2.10, the number of steps increases along the horizontal axis, going from inside to outside with respect to the central dashed line. Different sites of a given step are found to travel at different heights. The cyan-shaded region represents the active area of the BD while yellow circles represent different rotating glass plates (see later). Dots correspond to beams travelling towards the observer, then exiting from the plane of the figure, crosses to beams entering the plane of the figure. For a given step t of the evolution, the walker can be found on $t+1$ possible sites, corresponding to $2t$ output optical modes, half of them representing the state $|0\rangle_c$ of the coin (the ones circulating in the counterclockwise direction in SI_1 and in the clockwise one in SI_2, corresponding to dots in Fig. 2.10) while the remaining ones correspond to the $|1\rangle_c$ state of the coin (the ones circulating in the clockwise direction in SI_1 and in the counterclockwise one in SI_2, represented as crosses).
In this setup, the presence of a single fixed BS does not allow to change the transmission and reflection coefficients from site to site or from step to step. For this reason, the mixing coefficients of coin operator can not be tuned during the evolution. In order to act on the evolution of the walker we can instead change the phases introduced by the coin operator between the coin states. This can be done

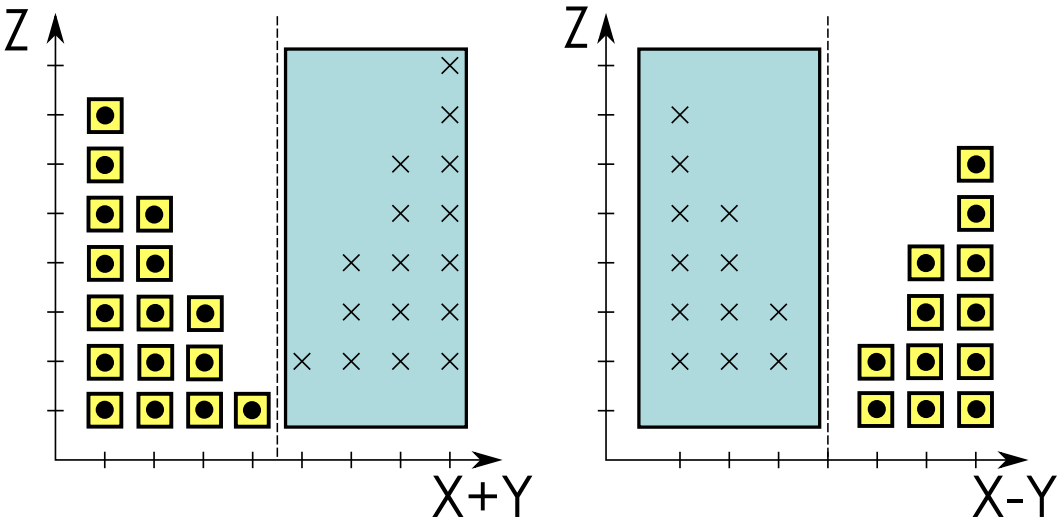

Figure 2.10. Beams pattern arising from the setup geometry. The cyan region denotes the BD while the yellow squares correspond to the rotating glass plates. **Left**: pattern of beams travelling in SI_1, corresponding to odd steps. **Right**: pattern of beams circulating in SI_2, corresponding to even steps. Dots correspond to beams that are exiting from the plane of the figure, crosses denotes beams that are entering in the plane of the figure.

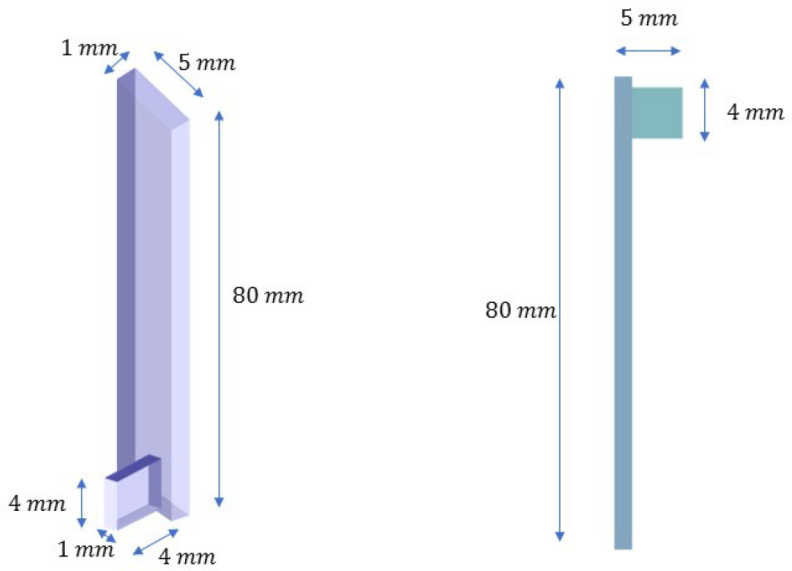

Figure 2.11. Sketch of the rotating glass plates used in the actual setup. Values of relevant geometrical parameters are reported.

independently in each site and step of the evolution by means of phase shifters, realized through rotating glass plates (RP). Because in an interferometric setup it is only accessible the phase difference between modes suffering interfercence, it is sufficient to insert the phase shifters such that they intercept modes corresponding to $|0\rangle_c$ states (yellow squares in Fig. 2.10). By varying their inclination with respect to the direction of propagation of the beam, the optical path is changed and a phase difference with respect to the other beam is generated. A sketch of a RP is shown in

Fig. 2.11, along with its dimensions. The particular shape of the RPs is necessary to intercept only a single beam without disturb the propagation of the other ones. A set of moving mirrors (MMs) is used to extract radiation at a given step for measurement. MMs consist of square mirrors on top of a micrometric stage, placed in such a way that they can intercept modes corresponding to step t^* leaving untouched the beams belonging to steps $t < t^*$. The extracted radiation is then coupled to a single mode fiber which is engineered to shift from a beam to the other ones by means of a horizontal and vertical stages system. The setup then can reproduce a tunable, phase stable, QW network allowing to measure every step and mode of the evolution.
A slight modification allows to inject two photons through the two different input ports of BS_1 (*input 1* and *input 2* in Fig. 2.6). The functioning of the setup is exactly the same as in the single input case but, after the extraction of the modes, a further BS (BS_2) is placed to intercept the modes, in order to split photons travelling along the same mode, allowing us to measure them in two different detectors. By adding a further coupler intercepting the extracted modes, coincidences between all possible modes at a given step can be measured and the whole two photon probability distribution can be experimentally reconstructed.
The setup allows to start the QW with any two-photon input state by injecting photons in a linear superposition of the two coin states, corresponding to the input ports of BS_1.
The closed loop geometry of the system allows in principle a very large number of steps which, as said, are limited by the dimension of the optical elements. However, another limitation is present in the system, consisting in the beam divergence. By reducing both the total length of the optical setup and the transverse distance of the travelling beams, we expect to double the maximum achievable number of steps. At the time of writing, each arm of the SIs is $\sim$ 40cm long. Thus, after each step, the walker propagates for $\sim$ 160cm.
The measured reflectivity value of both BS_1 and BS_2 used in the experiment was $|r|^2 = R = 0.45$. This asymmetry determines, together with other effects, mainly caused by the transmission losses of the optical elements of the setup, a behaviour of the actual QW which is sligthly discordant from the ideal one. This has been taken into account in simulations and experimental data analysis described in the following.

Two photon source

The whole potentiality of the all-optical bulk optics QW setup described in sec. 2.5.1 is exploited when it is paired with a two photon source. Indeed, the capability of the setup to accept as input any kind of two photon states, makes it a suitable platform to study multiparticle QWs, which can exhibit completely different phenomena with respect to the single photon case.
The source used in the present work consists of a phase-stable bulk optics triangular Sagnac interferometer, realized with two broadband dielectric mirrors on its vertices and a dual wavelength polarizing beam splitter (PBS) as the input/output vertex (see Fig. 2.12) [89].

A single-mode continuous wave laser at a wavelength of 405nm, coherence time $\sim 0.33\mu$s, enters the Sagnac after being reflected by an external dichroic mirror (DM). The DM reflects light at wavelength lower than a treshold value, transmitting higher wavelengths than it. The pump is then reflected and redirected toward the dual wavelength PBS. The polarization of the laser can be tuned by means of the quarter wave plate QWP_{λ_p} and the half wave plate HWP_{λ_p} encountered by the pump laser

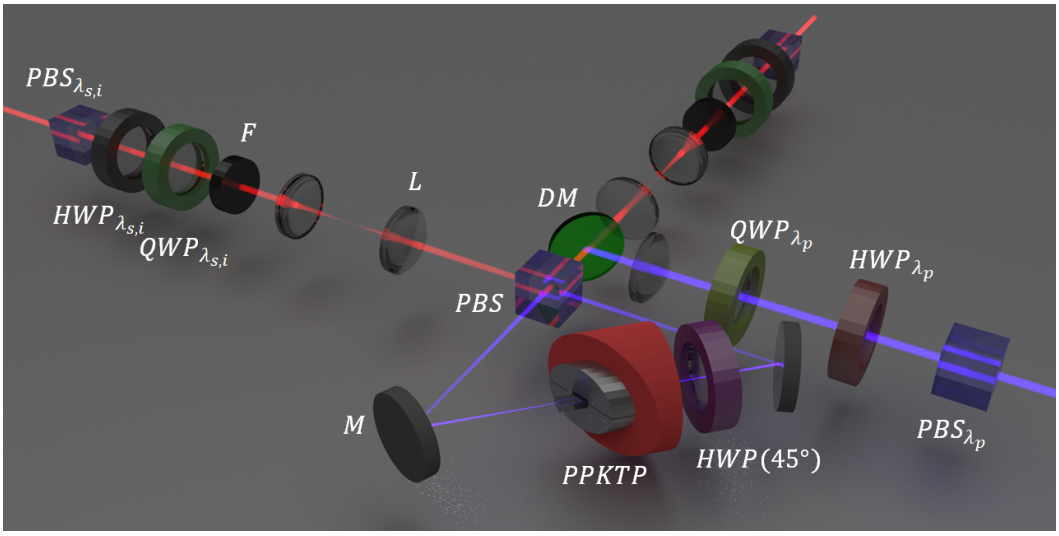

Figure 2.12. 3D drawing of the two photon source. Attached to each optical element is the name of the element itself.

before entering the Sagnac interferometer. For instance, the pump can be initialized in a diagonal polarization state $|\psi\rangle = \frac{1}{\sqrt{2}}(|H\rangle + |V\rangle)$. When impinging on the dual wavelength PBS, the projection $|H\rangle$ is transmitted along the counter-clockwise trajectory, while the $|V\rangle$ one is reflected along the clockwise one.
At the center of the Sagnac interferometer a non-linear, uniaxial negative, periodically poled potassium titanyl phosphate (PPKTP) crystal is placed. When the pump laser interacts with the PPKTP, the type II quasi-phase matching (QPM) condition has to be fulfilled in order to generate photon pairs from the spontaneous parametric down conversion (SPDC) process

$$n_e(\omega_p)\omega_p = (n_e(\frac{\omega_p}{2}) + n_o(\frac{\omega_p}{2}))\frac{\omega_p}{2}$$

where $n_e(\omega_p)$ is the extraordinary refractive index and $n_o(\omega_p)$ is the ordinary one, both depending on the pump laser frequency ω_p.
The crystal is placed inside an oven, which keeps it at the right constant temperature in order to avoid thermal dilations due to temperature changes and, consequently, changes in the QPM condition.
Due to the linear superposition of the polarization state of the pump, two SPDC processes take place in superposition. The H polarized part of the pump can generate two photons both at 810nm in a $|H, V\rangle$ state. The V polarized part of the pump, circulating clockwise, has to be rotated into $|H\rangle$ in order to fulfill the QPM relation and to produce photon pairs. This is accomplished by means of a broadband HWP placed just before the crystal. Also in this case, the photons generated are in a state $|H, V\rangle$. Note that the photons generated from the interaction of the H part of pump also travel through the HWP, such that their polarization is rotated. This does not influences the state generation.
The photons are then separated and spatially distributed by the central PBS to the two output modes, which we will call signal and idler modes. The photons travelling along the DM are transmitted because their wavelength is higher than the treshold wavelength of the DM. An interferential filter cenetered around 810nm is placed along both signal and idler modes, such that the residual pump laser exiting from

the Sagnac interferometer is completely absorbed by it The resulting state is then $\frac{1}{\sqrt{2}}(|H_i, V_s\rangle + e^{i\phi}|V_i, H_s\rangle)$, the first part of the state deriving from the clockwise interaction and the second part from the counter-clockwise interaction. The phase factor ϕ can be tuned by means of a QWP placed along the pump path before it enters the interferometer and also by using a liquid crystal (LC) placed along the idler (or signal) mode. The LC provides a refraction index different for horizontal and vertical polarization, tunable by the application of a electric field [90].
The balance between the first and the second part of the state, thus between the populations of the two states, can be achieved by rotating an external HWP intercepting the pump beam before it enters in the Sagnac.
The state generated by this setup is an entangled one, where the two photons are always found to be in opposite polarization states (for a insight over entanglement, see sec. 5.2). The source is also able to produce pairs of completely indistinguishable photons. On this purpose, the pump polarization is rotated such that it has only H (or V) component, so that a single possible generation event is produced. The resulting state then reads $|H_s, V_i\rangle$. After that, a polarization rotation can be imposed on one of the photons to have both of them identically polarized.

Indistinguishable photon pairs generation and HOM effect

In order to study the evolution of two indistinguishable photons travelling along the same QW network, one has to prepare them such that, when impinging on the interaction surface of the BS, the two particles are completely identical under every possible degree of freedom (DOF). If this is the case, the HOM effect takes place and the particles act as indistinguishable bosonic particles. Before entering in the experimental details, it is convenient to recall here the derivation and explanation of the HOM effect.
The HOM effect consists of the coalescence of two indistinguishable photons entering a BS from its two different input ports. If the photons are completely indistinguishable in all their degrees of freedom, for instance polarization, angular momentum, frequency, propagation mode, arrival time on the BS, etc..., then the probability for them to separately travel along the two output modes of the BS drops to zero, meaning that they are always found to travel coupled along the same mode, which one being completely random.
Of course, experimental imperfections can affect this ideal behaviour; for instance, non perfect indistinguishability of the two photons, as well as non ideal optical elements, generally decreases the intensity of the HOM effect, resulting in a probability different from 0 for the photons to travel along different modes. Experimentally, a direct way to characterize the degree of indistinguishability between a pair of photons consists of creating many copies of the pair and make interfere the two photons of each pair in a BS with a varying relative time delay between the particles: the higher the relative time delay, the higher the distinguishability of the particles, the lower the intensity of the HOM effect.

When the wavefunctions of the two photons completely overlap at the BS interaction surface, a minimum (ideally 0) in the probability for them to travel along different modes is reached. Thus, the behaviour of the coincidences between two detectors placed along the two output modes as a function of the time delay is represented by a dip-shaped function (for a qualitative representation of the HOM dip see Fig. 2.13; for a sketch of the experimental setup see Fig. 2.14). The particular shape of the dip depends on the shape of the wavefunction of the photons, on their indistinguishability, and in general on the process lying at the base of their generation. Nevertheless, the gaussian shape is typically adopted as a representation

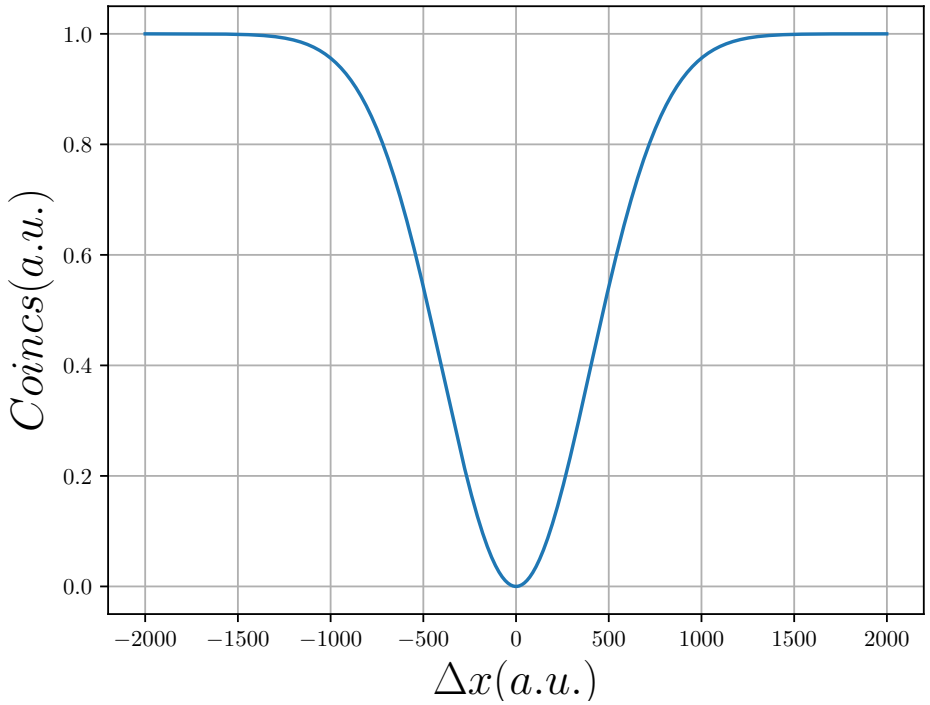

Figure 2.13. Theoretical behaviour of the coincidences as a function of the delay between two indistinguishable photons.

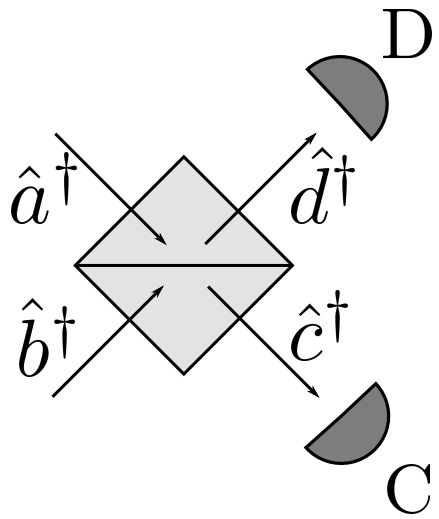

Figure 2.14. Sketch of the BS and the output detectors for the measurement of the HOM dip.

of the HOM dip.
One of the most important parameters which can be derived by the HOM dip is its visibility, defined as

$$V = \frac{MAX - min}{MAX} \tag{2.5}$$

with MAX corresponding to the number of photon pairs travelling along two different modes when no HOM effect occurs (i.e. when photons are distinguishable, for instance when the time delay is sufficiently large) and min corresponding to the same quantity obtained in the presence of HOM effect. The visibility quantifies the degree of indistinguishability of the photon pairs.
Let's formalize the above phenomenon in terms of second quantization formalism. Consider two photon travelling along modes a and b, corresponding to the input modes of the BS, associated with creation operators $\hat{a}^\dagger$ and $\hat{b}^\dagger$. We add the symbol "'" to the creation operator $\hat{b}^\dagger$ to denote the fact that the two photons differ in the properties of some degree of freedom, for instance the arrival time on the BS. The input state then reads

$$|\psi\rangle_{\text{in}} = \hat{a}^\dagger \hat{b}'^\dagger |0\rangle_F .$$

We can write the BS transformation as

$$\begin{aligned} \hat{a}^\dagger &\longrightarrow t\hat{c}^\dagger + ir\hat{d}^\dagger \\ \hat{b}'^\dagger &\longrightarrow t\hat{d}'^\dagger + ir\hat{c}'^\dagger . \end{aligned} \tag{2.6}$$

The coefficient r $(t) \in \mathbb{R}$ is the coefficient of reflectivity (transmissivity) of the BS, for which it holds $r^2 + t^2 = 1$. If the photons are indistinguishable in each degree of freedom, we can eliminate the symbol "'" such that the creation operators simply reduces to their expressions without the superscript.
After the BS, the input state modifies as

$$|\psi\rangle_{\text{out}} = (t^2 \hat{c}^\dagger \hat{d}'^\dagger + irt\hat{c}^\dagger \hat{c}'^\dagger + irt\hat{d}^\dagger \hat{d}'^\dagger - r^2 \hat{d}^\dagger \hat{c}'^\dagger) |0\rangle_F .$$

By tracing over all the degrees of freedom except the propagation mode, the probability for a pair of distinguishable photons to travel one along mode c and the other one along d is

$$P_{cd,\text{dist}} = T^2 + R^2 \tag{2.7}$$

where $R \equiv r^2$ $(T \equiv t^2)$ is the reflectivity (transmissivity) of the BS.
The probability for the photons to travel both along mode c or d is

$$P_{cc,\text{dist}} = P_{dd,\text{dist}} = RT.$$

The number of photons travelling along modes c and d is given by

$$M_{\text{theo}} = NP_{cd,\text{dist}} = N(T^2 + R^2) \tag{2.8}$$

N being the total number of photon pairs impinging on the BS. M_{theo} corresponds to the MAX value which should be inserted in expression (2.5). Experimentally, the corresponding number of photon pairs measured by the detectors is given by

$$M = M_{\text{theo}} \eta_C \eta_D = Coinc(C, D)_{\Delta t > \tau}$$

where η_I is the overall detection efficiency of the detector I placed along mode $i = c, d$. The quantity $Coinc(I, J)_{\Delta t > \tau}$ indicates the number of coincidence measured

by two detectors I and J placed respectively along modes i and j when photons impinge on the BS with a given temporal delay Δt greater than their coherence time τ, such that they behave as distinguishable particles.
When the photons share exactly the same features and reach the BS interaction surface at the same time, a number of coincidences equal to 0 is expected due to the HOM effect. Eventually, a larger value is measured, denoting the presence of non ideal experimental conditions. We can think about two different reasons at the base of such a behaviour: a) the non ideality of the BS, namely $R \neq T$, affecting the interference between indistinguishable photons, and b) the presence of a percentage of distinguishable photon pairs among the copies of the system impinging on the (non ideal) BS. Let's face the two problems independently.
In the case a) we deal with indistinguishable photons impinging on a non ideal BS; the evolution of an input state (note the absence of the symbol "'" because of the indistinguishability)

$$|\psi_{\text{in}}\rangle = \hat{a}^\dagger \hat{b}^\dagger |0\rangle_F$$

after having interacted with the BS reads (relations (2.6) without "'")

$$|\psi\rangle_{\text{out}} = ((t^2 - r^2)\hat{c}^\dagger \hat{d}^\dagger + irt(\hat{c}^\dagger \hat{c}^\dagger + \hat{d}^\dagger \hat{d}^\dagger))\,|0\rangle \tag{2.9}$$

and the probability for two indistinguishable photons to travel along modes c and d is

$$P_{cd,\text{ind}} = |T - R|^2.$$

In the ideal case $T = R$, which implies $P_{cd,\text{ind}} = 0$, corresponding to the HOM effect. The probability for two photons to travel both along c or d is

$$P_{cc,\text{ind}} = P_{dd,\text{ind}} = 2RT.$$

The number of indistinguishable photon pairs travelling along two different modes then reads

$$N_{cd,\text{ind}} = N\mathcal{G}P_{cd,\text{ind}} = N\mathcal{G}|T - R|^2$$

where we introduced the quantity $\mathcal{G}$ which is the percentage of photons pairs composed by indistinguishable particles. If $\mathcal{G} = 0$, all photons are distinguishable. On the contrary, if $\mathcal{G} = 1$ all photons are indistinguishable.
In case b) we have to deal with the presence of distinguishable photons impinging on the BS. We can use the very same relations already derived in (2.6), such that the probability for two distinguishable photons to travel along two different modes corresponds to (2.7). As a consequence, the number of distinguishable photon pairs travelling along modes c and d reads

$$N_{cd,\text{dist}} = N(1 - \mathcal{G})P_{cd,\text{dist}} = N(1 - \mathcal{G})(T^2 + R^2).$$

The total number of photon pairs travelling along mode c and d in the 0 time delay condition then can be written as

$$\begin{aligned} m_{\text{theo}} = N_{cd,\text{ind}} + N_{cd,\text{dist}} &= N\mathcal{G}P_{cd,\text{ind}} + N(1 - \mathcal{G})P_{cd,\text{dist}} \\ &= N\mathcal{G}|T - R|^2 + N(1 - \mathcal{G})(T^2 + R^2). \end{aligned} \tag{2.10}$$

Experimentally, the total number of coincidences measured by the detectors is

$$m = m_{\text{theo}}\eta_C\eta_D = Coinc(C,D)_{\Delta t=0}$$

corresponding to the number of coincidences measured when photons impinge on the BS with 0 temporal delay.
By computing the visibility V we obtain

$$V = \frac{M_{\text{theo}} - m_{\text{theo}}}{M_{\text{theo}}} = \frac{2\mathcal{G}RT}{R^2+T^2}. \tag{2.11}$$

Because of the fact that

$$\frac{M_{\text{theo}} - m_{\text{theo}}}{M_{\text{theo}}} = \frac{M-m}{M}$$

the value of the visibility can be experimentally obtained by computing

$$V = \frac{Coinc(C,D)_{\Delta t>\tau} - Coinc(C,D)_{\Delta t=0}}{Coinc(C,D)_{\Delta t>\tau}}. \tag{2.12}$$

In the limit case in which $\mathcal{G} = 1$ (i.e. completely indistinguishable photons) and $R = T = \frac{1}{2}$ a value of $V = 1$ is obtained, as expected in the completely ideal case.
By inverting relation (2.11) we can derive the expression for the percentage of indistinguishable photons $\mathcal{G}$ as

$$\mathcal{G} = \frac{V(R^2+T^2)}{2RT}.$$

The value of $\mathcal{G}$ is the relevant quantity because it quantifies the real amount of indistinguishability of the photons. Nonetheless, the multiplicative factor $\frac{(R^2+T^2)}{2RT}$ can be considered ~ 1. Indeed, also in the case $R = 0.45$ and $T = 0.55$, its value is ~ 1.02. For this reason, the value of V can be considered a good indistinguishability quantifier.

We want now demonstrate that it is also possible to measure the visibility of the HOM dip without performing measurements with different time delays. This is convenient since that the change in the time delay implies different experimental conditions, such as coupling to the fibers, divergence of the photon beam, etc... This aim can be accomplished by inserting a BS along each of the two output modes c and d of the interaction BS and by using 4 detectors instead of 2.
Suppose to insert BS_c and BS_d respectively along modes c and d, such that we end up with 4 different modes, say c_1, c_2, d_1 and d_2, and along each of them we place a detector, respectively detectors C_1, C_2, D_1 and D_2. The situation is sketched in Fig. 2.15.

The detectors are linked in such a way that each of them is able to measure coincidences with all the others (i.e. are registered coincidence between C_1 and C_2, C_1 and D_1, C_1 and D_2, and so on).
If photons arrive synchronized on the BS, there will be a number m_{theo} of photon pairs which will not undergo HOM effect for the very same reasons explained above. They will travel along mode c and d up to BS_c and BS_d where they are split into the last 4 output modes. The total number of photon pairs, one travelling along mode c and the other one along d, is given by relation (2.10). This quantity is linked to the experimental measurements through the following relation

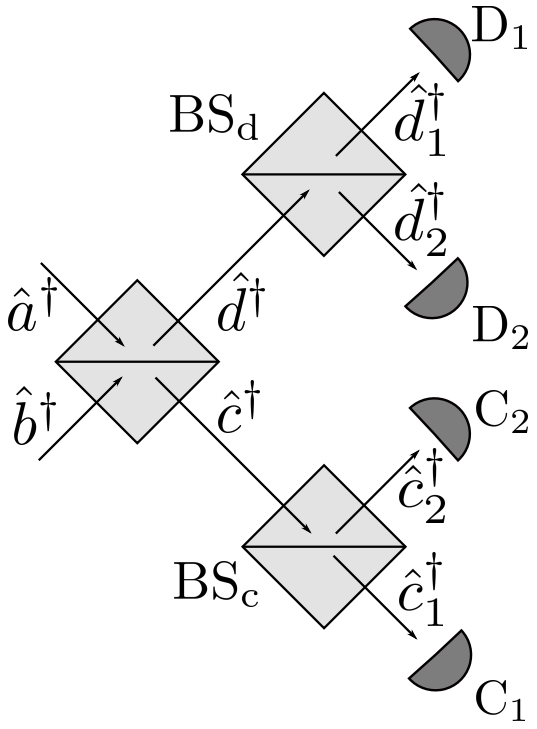

Figure 2.15. Sketch of the BSs sequence needed to measure the visibility of the HOM dip without changing the optical delay between the photons.

$$\begin{aligned} m &= m_{\text{theo}} T_c T_d \eta_{C_1} \eta_{D_1} + m_{\text{theo}} T_c R_d \eta_{C_1} \eta_{D_2} + m_{\text{theo}} R_c T_d \eta_{C_2} \eta_{D_1} + m_{\text{theo}} R_c R_d \eta_{C_2} \eta_{D_2} \\ &= Coinc(C_1, D_1) + Coinc(C_1, D_2) + Coinc(C_2, D_1) + Coinc(C_2, D_2) \end{aligned} \quad (2.13)$$

where $T_c(T_d), R_c(R_d)$ are the transmissivity and reflectivity of BS_c (BS_d) and η_I with $I = C_1, C_2, C_3, C_4$ is the overall efficiency of the detector I. By inverting this relation we can obtain the value of m_{theo} starting from experimental values of the coincidences.
To compute M_{theo}, needed to determine the visibility, we recall that it corresponds to the total number N of photon pairs impinging on the BS multiplied by a factor $P_{cd,\text{dist}} = R^2 + T^2$. This value can be computed by summing the number of photon pairs travelling along different modes, i.e. m_{theo}, and the ones travelling along the same mode (i.e. both along c or d). By considering the same experimental imperfections as above and relation (2.9) we can compute the number of indistinguishable photon pairs travelling along c or d

$$N_{cc,\text{ind}} = N_{dd,\text{ind}} = N\mathcal{G}P_{cc,\text{ind}} = N\mathcal{G}2RT.$$

On the other hand, the number of distinguishable photon pairs which travel along the same mode c or d reads

$$N_{cc,\text{dist}} = N_{dd,\text{dist}} = N(1-\mathcal{G})P_{cc,\text{dist}} = N(1-\mathcal{G})RT.$$

The number of photon pairs travelling along the same mode can then be written as

$$N_{cc} = N_{cc,\text{ind}} + N_{cc,\text{dist}} = N\mathcal{G}2RT + N(1-\mathcal{G})RT$$

and the same for mode d.
The total number of photon pairs can then be written as

$$N = N_{cc} + N_{dd} + m_{\text{theo}}. \tag{2.14}$$

Experimentally, we can reconstruct N_{cc} and N_{dd} with the following relations

$$\begin{aligned} N_{cc} &= \frac{Coinc(C_1, C_2)}{2R_cT_c\eta_{C_1}\eta_{C_2}} \\ N_{dd} &= \frac{Coinc(D_1, D_2)}{2R_dT_d\eta_{D_1}\eta_{D_2}}. \end{aligned} \tag{2.15}$$

By considering relation (2.8), (2.14) and (2.10) we obtain

$$V = \frac{M_{\text{theo}} - m_{\text{theo}}}{M_{\text{theo}}} = \frac{(N_{cc} + N_{dd} + m_{\text{theo}})(R^2 + T^2) - m_{\text{theo}}}{(N_{cc} + N_{dd} + m_{\text{theo}})(R^2 + T^2)} = \frac{2\mathcal{G}RT}{R^2 + T^2}$$

which is identical to relation (2.11).
This demonstrates that the two different approaches bring to exactly the same expression of the visibility.
By inverting relation (2.13) and using (2.15) to compute N_{cc}, N_{dd} and m_{theo} from experimental coincidences, we obtain

$$\begin{aligned} m_{\text{theo}} &= \frac{Coinc(C_1, D_1) + Coinc(C_1, D_2) + Coinc(C_2, D_1) + Coinc(C_2, D_2)}{T_cT_d\eta_{C_1}\eta_{D_1} + T_cR_d\eta_{C_1}\eta_{D_2} + R_cT_d\eta_{C_2}\eta_{D_1} + R_cR_d\eta_{C_2}\eta_{D_2}} \\ N_{cc} &= \frac{Coinc(C_1, C_2)}{2R_cT_c\eta_{C_1}\eta_{C_2}} \\ N_{dd} &= \frac{Coinc(D_1, D_2)}{2R_dT_d\eta_{D_1}\eta_{D_2}} \end{aligned} \tag{2.16}$$

from which it is possible to write the expression for the visibility as a function of experimental determined values of reflectivities, efficiencies and coincidences measured in the condition of temporal delay of photons equal to 0.
The efficiencies η_I can be written as

$$\eta_I = Q_I F_I$$

where Q_I is the quantum efficiency of detector I and F_I the coupling factor linked to the detector I, which takes into account coupling efficiencies to the fibers as well as losses.
If BS_c and BS_d consist of bulk optical elements, four different fibers are needed to couple the output modes. In this case, the factors F_I can be independently measured for each of them by measuring the power of a laser radiation, following the same path of the photons and coupling to the fiber, just after the fiber and dividing it by the value measured just before it. If, instead, the photons are coupled to a fiber and then split by a fiber BS (one placed along c and one along d), F_I can be measured by dividing the sum of the laser power at the two outputs of the fiber BS by its

input power. In this case, $F_{C_1} = F_{C_2}$ and $F_{D_1} = F_{D_2}$.
Because of the fact that it is much easier to measure relative quantum efficiencies instead of absolute ones, it is convenient to rewrite the above expressions in terms of relative efficiencies with respect to a given chosen efficiency (say η_{C_1}) as

$$\eta'_I = \frac{Q_I F_I}{Q_{C_1} F_{C_1}} = Q'_I \frac{F_I}{F_{C_1}}$$

where we defined $Q'_I = \frac{Q_I}{Q_{C_1}}$ as the relative quantum efficiencies of detector I. Expressions (2.16) can then be rewritten as

$$m_{\text{theo}} = \frac{F_{C_1}}{\eta_{C_1}^2} \cdot \frac{Coinc(C_1, D_1) + Coinc(C_1, D_2) + Coinc(C_2, D_1) + Coinc(C_2, D_2)}{T_c T_d Q'_{D_1} F_{D_1} + T_c R_d Q'_{D_2} F_{D_2} + R_c T_d Q'_{C_2} F_{C_2} Q'_{D_1} \frac{F_{D_1}}{F_{C_1}} + R_c R_d Q'_{C_2} F_{C_2} Q'_{D_2} \frac{F_{D_2}}{F_{C_1}}}$$

$$N_{cc} = \frac{F_{C_1}}{\eta_{C_1}^2} \cdot \frac{Coinc(C_1, C_2)}{2 R_c T_c Q'_{C_2} F_{C_2}}$$

$$N_{dd} = \frac{F_{C_1}}{\eta_{C_1}^2} \cdot \frac{Coinc(D_1, D_2)}{2 R_d T_d Q'_{D_1} F_{D_1} Q'_{D_2} \frac{F_{D_2}}{F_{C_1}}}$$

The common prefactor $\frac{F_{C_1}}{\eta_{C_1}^2}$ simplifies in the computation of the visibility, making it necessary to measure only relatives quantum efficiencies and coupling factors.
Despite the much more complicated expressions needed to compute the visibility with respect to expression (2.12), the above quantities have the important property that can be estimated simultaneously, i.e. in the very same experimental conditions.

As already said, in order to observe the HOM effect, pairs of photons indistinguishable in every possible degree of freedom have to be generated. In Fig. 2.16 we report a scheme of the optical setup used to find the HOM dip.

We briefly explain here how all possible DOFs can be made identical for both photons.
The easiest DOF to face is the polarization. When the photons travel inside the single mode fibers (SMFs) placed along both idler and signal modes, their polarization undergoes a unitary transformation due to a Berry phase collected by the particles. In order to obtain the desired polarization state at the output of the fibers, a polarization controller (PC) can be used. A PC allows to change the path travelled by the light inside the fibers such that it is possible to modify the Berry phase and obtain every kind of polarization state at their output. By placing a PBS in front of the detector which measures the photons exiting from the fiber under consideration and using the PC, one can rotate the polarization state of the photons, for instance, on the V polarization. Such condition is reached when the number of photons measured by the detector is minimum, ideally 0. By doing this for both photons, the same polarization can be reached.
The orbital angular momentum of the photons is assured to be the same because of the fact that they exit from two identical SMF. This implies that the electric fields is described by the fundamental transverse electromagnetic mode, i.e. TEM_{00}. The direction of propagation is a critical parameter. Indeed, a slight angular misalignement between the propagation direction of the photons can rapidly decrease

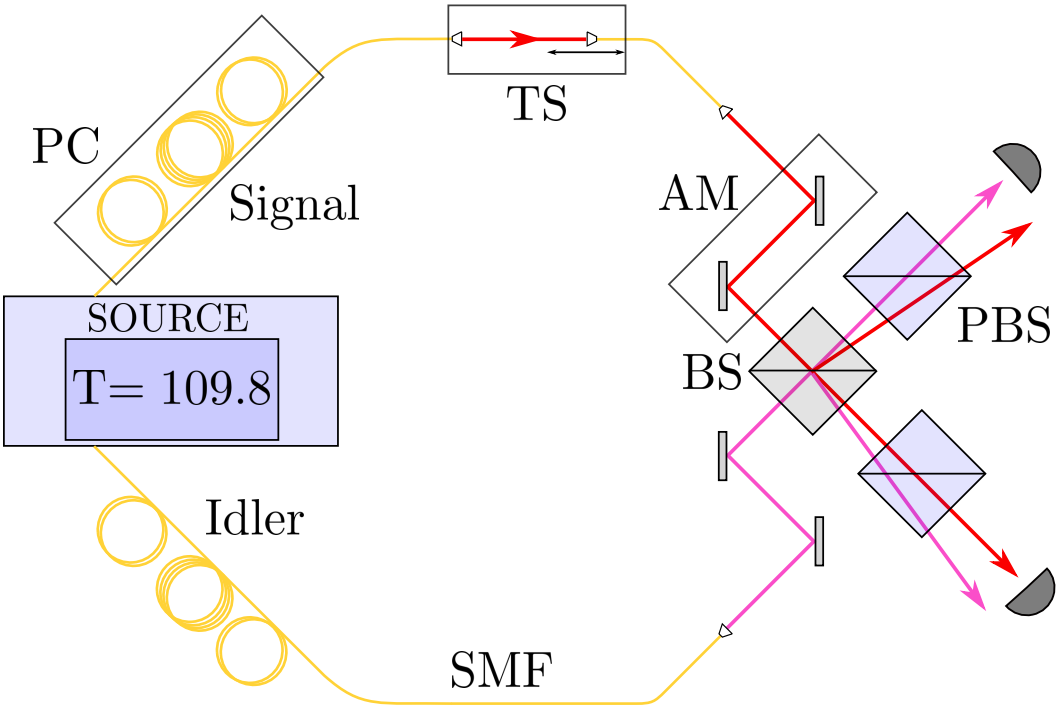

Figure 2.16. Sketch of the setup used to reproduce the HOM effect. The source is the one reported in Fig. 2.12. PC: polarization controller; TS: translational stage; AM: adjusting mirrors; PBS: polarizing beam splitter. Note that, after having generated the same polarization state for both the idler and signal photons, the PBS is removed from the setup.

the visibility of the HOM effect. To perfectly match the direction of propagation, the beam paths are modified such that, when they reach the BS, the transmitted part of the idler beam travels exactly along the same direction of the reflected part of the signal beam, and viceversa.
A crucial parameter in the HOM effect is the time synchronization of the photons at the interaction surface of the BS. Because of the finite coherence time τ_C and length L_c of the photons, if they impinge on the BS with a relative time delay $\tau > \tau_c$ (or, equivalently, a relative spatial delay $\Delta x > L_c$) they will behave as two distinguishable photons, not undergoing the HOM effect. For this reason, an automated translation stage has been inserted along one of the beam path (in our case the signal). By changing the optical path travelled by the signal, it is possible to synchronize the arrival time of both photons. The typical experimental signature indicating the right time synchronization is showed in the left image of Fig. 2.17, in which the number of coincidences is shown as a function of the spatial delay Δx between the two photons.

When the photons are not synchronized, a plateau in the coincidences count is measured. When their wavefunctions begin to overlap on the BS, the HOM effect appears and the number of coincidences decreases, reaching a minimum when $\Delta x = 0$. After that, when the spatial delay increases again, the distinguishable case is retrieved. In order to work with indistinguishable photons, one has to impose the time difference between the two particle to be 0, keeping it fixed for all the duration of the experiment. In the left image of Fig. 2.17 an experimental artifact can be observed. When $\Delta x \sim 1000\mu$m the coincidence counts start to drop, despite

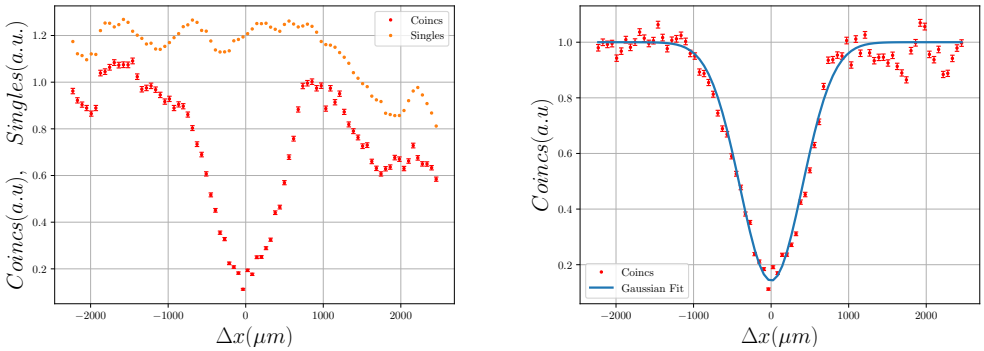

Figure 2.17. Left: Typical shape of the experimental trend of the coincidence of an HOM dip (red) and corresponding singles (orange). **Right**: same experimental data after correction (red) fitted with a gaussian curve (blue line).

the photons are completely distinguishable. This is due to the losses along one of the two paths, in particular the one with the translation stage. The translation stage is composed by two SMF: the light exits from one of them, travels a part of free space, and couples into the second fiber. By changing the path travelled in free space, which can be done by moving the first fiber with respect to the second one, the delay can be modified. During the movement some misalignement can arise, diminishing the coupling between the fibers. For this reason, the number of single photons measured by the detectors decreases and consequently the number of coincidences. One can mitigate this effect by normalizing the coincidences with respect to the single photon counts. The red dots in both left and right images of Fig. 2.17 show the same experimental data before (left) and after (right) the normalization. It is evident that the effect is strongly suppressed revealing a neat nearly gaussian shape (blue line corresponds to a gaussian function fitted to the data).
An other crucial degree of freedom consists of the wavelength of the photon pairs. The SPDC process at the base of the photons generation is based on two conservation laws: energy and momentum. The first one only implies that the sum of the energies of the generated photons must equal the energy of the pump photon. The second one is more restrictive and allows to generate only photons with a particular pair of wavelengths among the ones allowed by the energy conservation. The momentum conservation depends on the characteristics of the non linear crystal, such as the cutting edge, the period of the poling, and the temperature. The last one can be tuned by changing the temperature of the oven inside which the crystal is placed. In order to find the right temperature, namely the one at which two photons with identical wavelengths are generated, we performed a visibility study as a function of the temperature. Starting from $T = 109.0$deg, we increased the temperature by $\Delta T = 0.1$deg, the minimum possible for the oven used in the experiment, up to $T = 110.4$deg. For each value of the temperature a scan has been performed and the visibility measured. In Fig. 2.18 we report the scans for all the temperature under investigation in a heatmap plot. We can see three main effects as the temperature changes: the shape of the HOM dip changes, the visibility decreases out of the optimal temperature and the position of the minimum shifts.

All this effects can be explained by considering that the HOM effects is linked to the spatial and temporal shapes of the wavefunction of the two photons, which changes according to the phase matching condition. The exact description of the

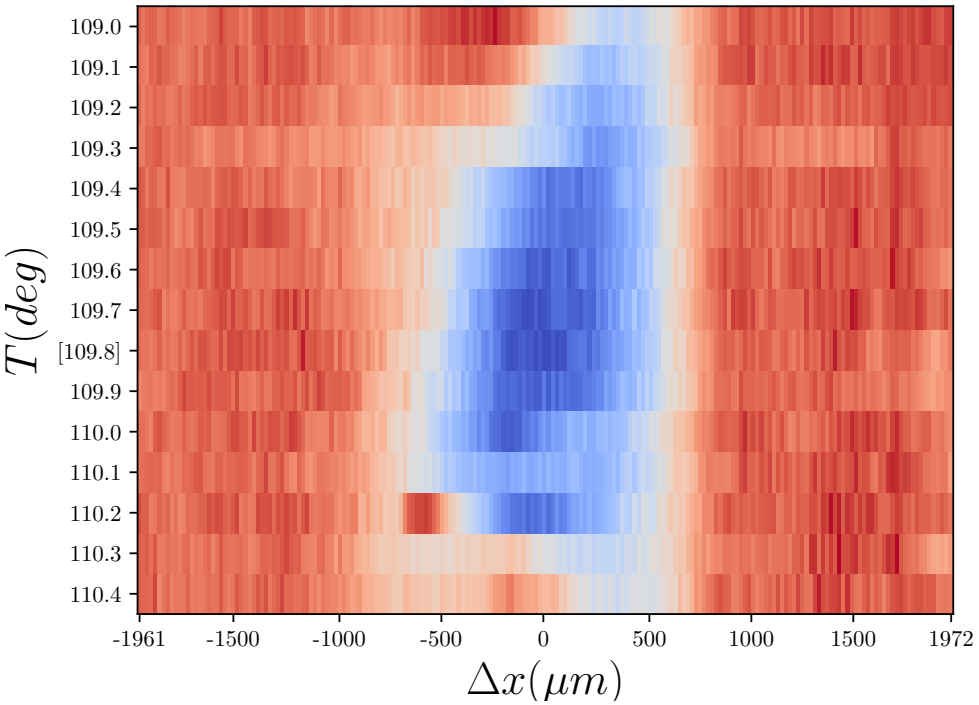

Figure 2.18. Experimental heatmap of the HOM dip for different values of the oven temperature. The best shape and visibility is obtained for $T = 109.8deg$.

shape of the HOM dip as a function of the temperature is behind the scope of this thesis, for more information see [89].
In order to choose the best temperature, each scan has been fitted with a gaussian relation from which we can derive the minimum and its exact position. In the right image of Fig. 2.17 we report the experimental data with a gaussian shaped function fitted to them. The best temperature resulted to be $T_{opt} = 109.8$deg, corresponding to a visibility of $V \sim 85\%$. Note that this is not the visibility of the HOM dip which will be used in the experiment. Indeed, a much accurate alignment has been performed before the experiment, in order to reach the higher possible value of V.

2.5.2 Split time quantum walk

A QW network can be realized relying on other degrees of freedom than the spatial one. Indeed, time and polarization can be used to reproduce the movement of a quantum particle [30, 67, 91].

The time-multiplexing scheme furnishes high resource efficiency, long-lasting stability, and homogeneity, which we exploit for the realization of QWs for a large number of steps. As we will see, this is mandatory for clearly distinguishing the signatures of the subdiffusive behaviour.
In the present scheme, the position degree of freedom is encoded in the arrival time bin of a coherent laser pulse that acts as the walker while the coin information is embedded in the polarization, $|H\rangle = |0\rangle_c$ and $|V\rangle = |1\rangle_c$. The walker pulse is derived from a laser with central wavelength of 1550 nm, pulse width of 1 ps, and repetition

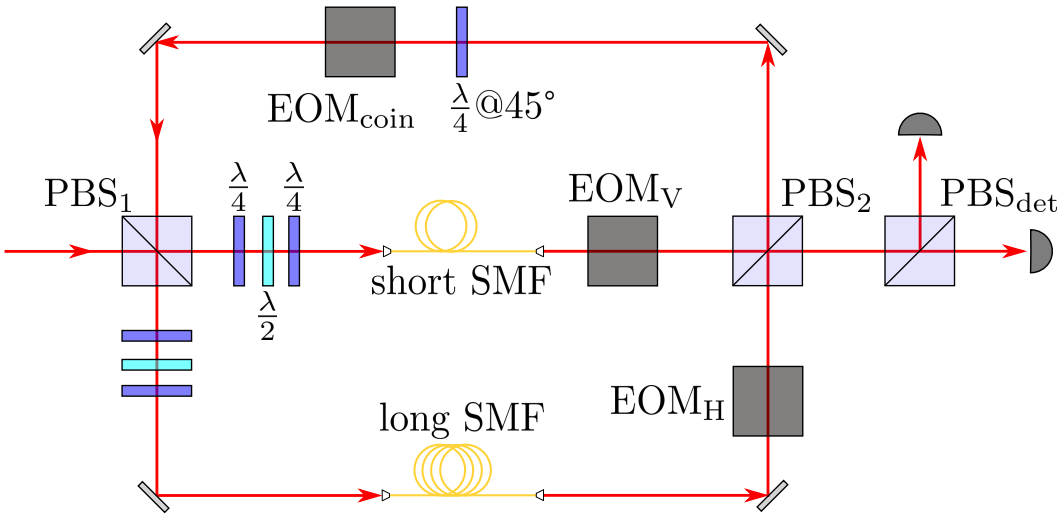

Figure 2.19. Schematics of the experimental layout, using the following elements: polarizing beam splitter (PBS), electro-optical modulator (EOM), quarter wave plates ($\lambda/4$) and half wave plates ($\lambda/2$). The sequence $\lambda/4 - \lambda/2 - \lambda/4$ allows to precisely compensate the polarization rotation caused by the propagation through the fibers. Note that the detection is, in fact, polarization resolving. This is achieved by splitting the output of the loop with PBS$_{\text{det}}$ followed by one detector for each polarization.

rate of $\sim$ 4 kHz. The walk starts when the pulse impinges from the top port of PBS$_1$ (see Fig. 2.19) for the first time. The walk is then initialized at position $x = 0$ with horizontally polarized light, $|\psi\rangle_{t=0} = |0\rangle \otimes |0\rangle_c$. The unbalanced Mach-Zehnder interferometer implements the step operation $\hat{S}$, which includes polarization dependent splitting at PBS$_1$, propagation of horizontal and vertical polarization through long ($\sim$ 473 m) and short ($\sim$ 453 m) fibers, respectively, to introduce a well-defined delay between the two polarizations, and finally coherent recombination of the two paths at PBS$_2$. By convention, we consider that the polarization travelling the longer (shorter) arm of the interferometer performs a unit step towards negative (positive) sites. The interferometer is closed with a free-space feedback loop, which redirects the light back to PBS$_1$ for the next step. The coin operator acts along the feedback path, modifying the polarization of the walker. In totality, this leads to the encoding of walker's position degree of freedom in the pulse arrival time to the detectors. The sets of waveplates placed along the two arms allow to compensate the polarization rotation caused by the passage of the pulses through the SMFs.
The capability of dynamical polarization rotation by the two fast-switching electro optical modulators (EOMs), EOM$_{\text{H}}$ and EOM$_{\text{V}}$, enables routing the pulses either back to the feedback loop or to the detection unit. This high-quality active polarization control facilitates deterministic in- and out-coupling, rendering it possible to implement sufficiently large number of steps by enhancing the roundtrip efficiency. The current setup is designed to have a step separation of $\sim$ 2.3 μs and position separation of $\sim$ 105 ns and has been utilized to demonstrate walks up to 36 steps by allowing time-bin interlacing for successive steps [91]. However, we restrict ourselves here to 20 steps which, as we will see, is sufficient to reach our goals, avoiding the problems deriving from interlacing. The detection unit allows for polarization-resolved photon counting at individual time bins, using PBS$_{\text{det}}$ and high-efficiency ($> 90\%$) superconducting nanowire single-photon detectors with a dead time of $\sim$ 100 ns, from which we deduce the evolution of walker's probability distributions.

Our investigation of particular spread behaviours mainly relies on the implementation of position and step dependent coin operation, $\hat{C}(x,t)$. This is achieved by extending the capability of the just explained setup via the introduction of another fast-switching EOM ($\mathrm{EOM_{coin}}$) followed by a QWP in the feedback path. The action of a QWP aligned at an angle 45° with respect to the polarization basis $\{|H\rangle, |V\rangle\}$ reads

$$\hat{C}_{\mathrm{QWP}} = \frac{1}{\sqrt{2}} \begin{pmatrix} 1 & -i \\ -i & 1 \end{pmatrix}.$$

The EOM operation can be written as

$$\hat{C}_{\mathrm{EOM}}(\phi) = \begin{pmatrix} \cos\phi & -i\,\sin\phi \\ -i\,\sin\phi & \cos\phi \end{pmatrix},$$

where the phase ϕ can be tuned by varying the voltage applied to the EOM. The presence of the $\lambda/4$ with the fast axis at $45deg$ with respect to the horizontal axis right before the EOM, generates the following operator

$$\hat{C}_{\mathrm{EOM}}(\phi) \cdot \hat{C}_{\mathrm{QWP}} = \begin{pmatrix} \cos(\phi) & -i\cdot\sin(\phi) \\ -i\cdot\sin(\phi) & \cos(\phi) \end{pmatrix} \mathrm{e}^{-i\cdot\frac{\pi}{4}} \frac{1+i}{2} \begin{pmatrix} 1 & -i \\ -i & 1 \end{pmatrix} = \frac{1}{\sqrt{2}} \begin{pmatrix} \cos(\phi)-\sin(\phi) & -i\cdot\cos(\phi) - i\cdot\sin(\phi) \\ -i\cdot\cos(\phi) - i\cdot\sin(\phi) & \cos(\phi)-\sin(\phi) \end{pmatrix}.$$

It is possible to write the expression of the latter matrix in terms of an "effective" EOM matrix. By operating the change of variable $\theta = \phi + \pi/4$ and considering that

$$\frac{1}{\sqrt{2}}(\cos(\phi) - \sin\phi) = \cos(\phi + \pi/4) = \cos(\theta)$$
$$\frac{1}{\sqrt{2}}(\cos(\phi) + \sin\phi) = \sin(\phi + \pi/4) = \sin(\theta)$$

it is possible to write

$$\hat{C}_{\mathrm{EOM}}(\phi) \cdot \hat{C}_{\mathrm{QWP}} = \begin{pmatrix} \cos(\theta) & -i\cdot\sin(\theta) \\ -i\cdot\sin(\theta) & \cos(\theta) \end{pmatrix} = E\hat{O}M(\theta) \tag{2.17}$$

with $\theta \in [0, \pi/2]$. The constraint over the values of θ arises because ϕ ranges in $[-\pi/4, \pi/4]$.
With these elements we can write the general expression of the coin operator as

$$\begin{aligned}\hat{C}(x,t) = |x\rangle_p \langle x|_p \otimes (\cos(\theta(x,t))\,|0\rangle_c \langle 0|_c - i\cdot\sin(\theta(x,t))\,|0\rangle_c \langle 1|_c \\ - i\cdot\sin(\theta(x,t))\,|1\rangle_c \langle 0|_c + \cos(\theta(x,t))\,|1\rangle_c \langle 1|_c).\end{aligned}$$

It is worth emphasizing that the present scheme utilizes free-space EOMs, which introduce very low losses (< 1%). The combination of active in- and out-coupling and free-space EOMs leads to a significantly improved roundtrip efficiency (> 80%) in comparison to the previous disordered time-multiplexing QW setup that used integrated EOM [67]. However, relatively high-voltage requirements for free-space EOMs comes with the hardware limitations that allow only three different voltage settings, $v \in \{-v_1, 0, +v_1\}$, during a single experimental run. In particular, $v = 0$

corresponds to $\phi = 0$, leading to a coin operation that equally mixes $|H\rangle$ and $|V\rangle$. We chose $v = \pm v_1$ such that $\phi = \mp\pi/4$. This yields to an identity coin that leaves the polarization states unchanged and a reflection coin that switches the polarizations. Notably, we find that these three accessible coin operations are sufficient for the exploration of the complete subdiffusive QW regime, thanks to the p-diluted disorder scheme.

Chapter 3

Anomalous diffusion in a QW framework

The present chapter deals with the main topic of this thesis, namely the anomalous diffusion in a QW framework.
In section 3.1 we describe the superdiffusion arising when applying the p-diluted disordering technique to an initially ordered QW. This section is based on [18].
In section 3.2 we study the subdiffusive regime, obtained when an initially statically disordered QW is perturbed by means of the p-diluted technique. This part will be based on [19]. The basic idea of the experiment came in my mind during the study of the superdiffusive behaviour, in an attempt to find a way to reproduce any kind of anomalous diffusion, without limiting to the superdiffusive case. The experiment has been performed during a 4-months period spent by me in the Integrated Quantum Optics of university of Paderborn, Germany, lead by Prof. Christine Silberhorn. During that time, I also orally presented my previous research work and my relevant scientific results.
In section 3.3 we report on our last findings in the field of quantum metrology by linking it to the disordered QW dynamics [92].

3.1 Superdiffusion

Quantum coherence is a fundamental feature in several energy transport phenomena in heterogeneous systems, like synthethic or biological media, ranging from tissues to computation nodes [12, 13]. The rate of these processes is believed to be enhanced by this kind of quantumness, enabling higher efficiencies [14, 93]. As a consequence of such conditions, it is not rare that a superdiffusive dynamic settles in the transport or propagation processes. This is the case, for instance, of heat excitation transport in peculiar condensed matter systems such as one dimensional (1D) metal lattices, described by the Luttinger liquids theory [16]. Several studies about this kind of transport phenomena, have shown a violation in the dichotomy between the ballistic transport, typically arising from quantum effects, and the diffusive one, typical of classical energy spread. There are several cases in which superdiffusion occurs, for instance in classical one-dimensional systems [94], when both disorder and non linear effects are present [95], and even in quantum systems experiencing many-body localization phase transitions [96].
Since QWs have long been found to efficiently describe coherent energy transport [14, 15], we asked ourself if, by suitably introducing disorder in a QW, would it be possible to modify the spreading behaviour of a quantum walker. In this sense, a

paradigmatic example is given by Anderson localization [63], originally formulated for condensed matter systems, and extensively demonstrated in the case of all-optical systems [97, 73, 86]. Many theoretical and experimental studies have been carried out on this topic, covering a wide range of phenomena, including hyper-transport of light [84, 98], and disordered QWs preserving the time dependence of spreading [23], as well as decoherence effects determining the transition from QWs to CRWs [98, 17]. In these studies the role of disorder source was played by decoherence or various types of unitary evolutions.
In our study, we dealt with the description of the transition between quantum and classical regimes, while the coherence of the evolution is preserved. By properly implementing disorder configurations through the p-diluted technique, we show that a different spread regime, as the superdiffusive one, intermediate between ballistic and diffusive spreads, establishes during the evolution. The capability to explore such a behaviour, by means of a coherent disordered QW dynamics, is of fundamental relevance in order to investigate the role of coherence in propagation processes.

3.1.1 p-diluted model for superdiffusion investigation

The disorder model used in this experiment is the p-diluted one, presented in sec. 2.4.3, which we report here from a slight different point of view.
In this particular realization, we realize a disordered QW by modifying the phases superimposed on the coin state of the walker by the coin operator, leaving untouched the jumping probability amplitudes. If the phases acquired by the states $|0\rangle_c$ and $|1\rangle_c$ are the same for each step and site, then the ordered QW is retrieved. By randomly shifting them, a controlled and quantifiable amount of disorder can be inserted during the evolution.
The starting point for the study is the ordered QW. At each step and site of the evolution we modified the phases acquired by the two basis states of the coin such that their value is independently and randomly changed with a given probability r. The parameter r, corresponding to the degree of disorder, also represents the ratio, or percentage, of randomly shifted phases with respect to the ordered case. In the case $r = 0$ the ordered QW is reproduced while for $r = 1$ a completely disordered QW is realized. Intermediate values are plenty of interest because of their capability to reproduce different behaviours than the ballistic or diffusive ones, as we show later in the text. It is important to note that, for a given value of r, many different configurations of phases, usually called phase maps, arise. Indeed, each mode connecting a site to its adjacent can undergo a phase shifts operation and, because of the randomness of the process, several different phase maps can be generated.
When focusing on the walker evolution for a given phase map, the evolution (2.4) changes to

$$|\psi\rangle_{t+1} = \hat{S} \cdot \hat{C} \cdot \sum_{x=-t}^{t} \hat{P}(x,t) \, |\psi\rangle_t$$

where $\hat{P}(x,t)$ corresponds to the phase shift operator, which depends on the site and on the step of the evolution and can be written as

$$\hat{P}(x,t) = |x\rangle \langle x| \otimes (e^{i\phi_{|0\rangle}(x,t)} \, |0\rangle_c \langle 0|_c + e^{i\phi_{|1\rangle}(x,t)} \, |1\rangle_c \langle 1|_c)$$

where $\phi_{|0\rangle}(x,t)$ ($\phi_{|1\rangle}(x,t)$) is the phase applied on the coin state $|0\rangle_c$ ($|1\rangle_c$) in site x at step t. It is worth noting that, in a ordered QW it holds $\phi_{|0\rangle}(x,t) = 0$

$(\phi_{|1\rangle}(x,t) = 0)\ \forall x, t$. In practice, the phase shift operator adds a phase independently to both the basis states of the coin, depending on the site and on the step.
The operator $\hat{C} \cdot \sum_{x=-t}^{t} \hat{P}(x,t)$ can be interpreted as an effective coin operator $\hat{C}(x,t)$ which now depends on the site and on the step of the evolution.
Because of the superposition principle, the effect of the interference, and ultimately of the phases, on the evolution of the walker is of fundamental relevance. By shifting the phases, the final probability distribution can be heavily modified, preserving the most important feature which distinguishes the QW from the CRW, namely the coherence. In this sense, the current model differs from the ones in which some kind of decoherence is applied during the evolution of the walker [99]. This allows to retain the main difference of the QW from the CRW while studying the transition between the two limit cases of random walk.
The insertion of disorder is a Bernoulli process, consisting of changing each phase acquired by the walker with a given probability r. The probabilistic nature of the process makes it possible that two different values of r bring to the same number of random phases or even to identical phase maps configuration. This can be understood by looking at the image in Fig. 3.1, in which we report the probability distribution of the number of random phases at step 30 for different values of the parameter r.

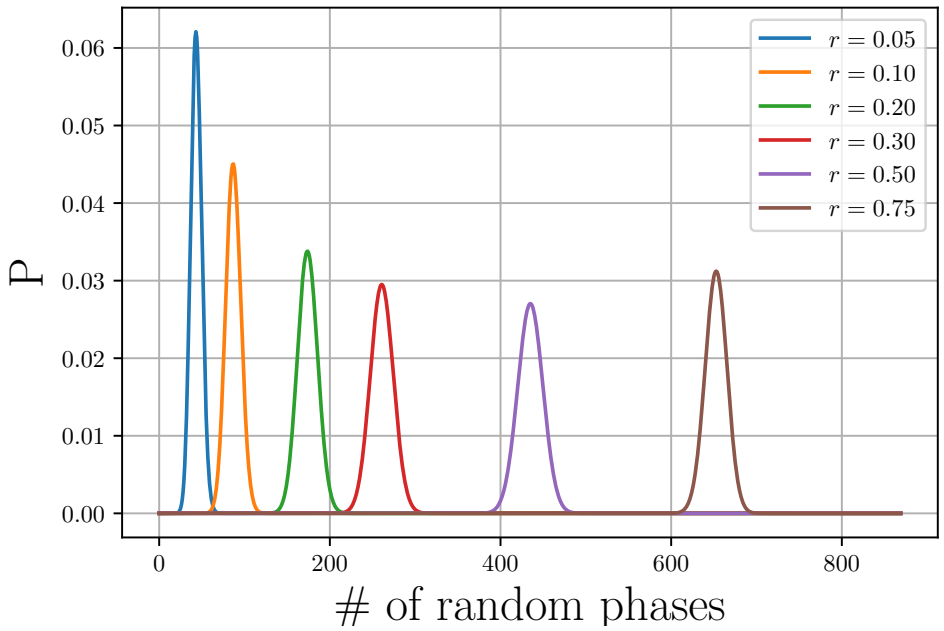

Figure 3.1. Probability distributions of the number of random phases for different values of the disorder r.

The peaks of the gaussian-shaped distributions are very far from each other, nevertheless some region with non-zero overlap still exists (see for instance the intersection between distributions for $r = 0.05$ and $r = 0.10$). Because of this, to study the transition from ordered to disordered spread behaviours, we chose values of the disorder for which the overlapping between the probability distributions is minimum, having always in mind that, as reported later, a clear superdiffusive regime can be observed for disorder values r between 0 and ~ 0.20. The selected values then resulted to be $r = 0.00, 0.05, 0.10, 0.20, 1.00$.

The presented realization of the p-diluted model can be easily mapped to the original one presented in 2.4.3. This can be done by noting that, at each step and site of the evolution, the probability for the ordered QW coin to be applied is $(1-r)^2$, corresponding to the probability for both phases not to be changed, i.e. to be both equal to 0; on the contrary, the probability to apply a different coin is $r^2+2r(1-r)$, corresponding to the cases in which one or both phases are different from 0. Thus, considering that

$$\begin{aligned} p &= r^2 + 2r(1-r) \\ q &= 1-p = (1-r)^2 \end{aligned}$$

the p-diluted model is retrieved. The coin operator can then be written as

$$\hat{C}(x,t) = \begin{cases} |x\rangle\langle x| \otimes (e^{i\phi_{|0\rangle}(x,t)} |0\rangle_c \langle 0|_c + e^{i\phi_{|1\rangle}(x,t)} |1\rangle_c \langle 1|_c) & \text{with probability } p \\ |x\rangle\langle x| \otimes (|0\rangle_c \langle 0|_c + |1\rangle_c \langle 1|_c) & \text{with probability } 1-p \end{cases}$$

where, in the first case, the phases are independently and randomly extracted. In this particular case, we are more interested in the parameter r than p. Indeed, the very first idea of the p-diluted model has come from the intuition that a completely random choice of the phases, parametrized by the parameter r, could bring to the superdiffusive behaviour. Obviously, in order to go from the parameter r to p, only a simple transformation on the values of r has to be done, which leaves completely unchanged all the results.

3.1.2 Simulations - Single walker

Several simplifications can be superimposed to the p-diluted model, depending on the quantities one is interested in. In the present work, we limit our analysis to the case in which the phases $\phi_{|0\rangle}(x,t)$ and $\phi_{|1\rangle}(x,t)$ can only be 0 or π, despite different choices of disorder in the p-diluted model can be done. For instance, one could consider a uniform phase distribution in some finite range of values.
The choice to restrict ourself to only two values finds its reason in two motivations. The first is that we are interested in studying how the quantum to classical transition, i.e. the transition between the ballistic QW to the diffusive one depends on the parameter r, without considering possible effects deriving from more complicated choices of the phases. The second one is experimental. In fact, as already said, despite the all optical QW described in sec 2.5.1 allows in principle to set every possible value of the phases, it is much easier to impose the 0 and π values.
We recall here that, for a given value of r, a very high number of different phase maps can be realized, due to the randomness in the choice of the phases for each state of the coin at every step and site. Different phase configurations, in principle, correspond to different evolutions of the probability distribution. Thus, the values of the relevant parameters belonging to evolution for a given value of disorder r have been computed by averaging over the ones obtained for many different phase map configurations, characterized by the same degree of disorder.

Variance analysis

The first quantity we focus on to study the single particle evolution behaviour is the variance of the position probability distribution (2.3), which we recall here

$$\sigma_1^2(t) = \sum_{x=-t}^{t} x^2 \cdot P(x,t) - \left(\sum_{x=-t}^{t} x \cdot P(x,t)\right)^2$$

where $P(x,t)$ is the probability to find the walker on site x at step t, regardless of the coin state.
It is well known that an ordered QW has a quadratic spread while a CRW has a linear spread. In general, we can write the dependence of σ_1^2 from t by means of a power law, expressed in our case by

$$\sigma_1^2(t) = \alpha t^{\beta} \tag{3.1}$$

with t corresponding to the number of steps. Values of $1 < \beta < 2$ unambiguously determine a superdiffusive spread [100], while the case $\beta = 2$ ($\beta = 1$) is typical of a ballistic QW (diffusive CRW).
We simulated the behaviour of the variance for different values of r up to 30 steps, in the range from $p = 0.00$ to 1.00, with a progressive increment of 0.01. For each of them, we reproduced the evolution of 1000 different phase maps, then we computed the mean value of the variance as a function of the step number t. For the sake of clarity, in the following we will report only the simulated data for the selected values $r = 0.00, 0.05, 0.10, 0.20, 1.00$. Results of the simulations are reported in Fig. 3.2.

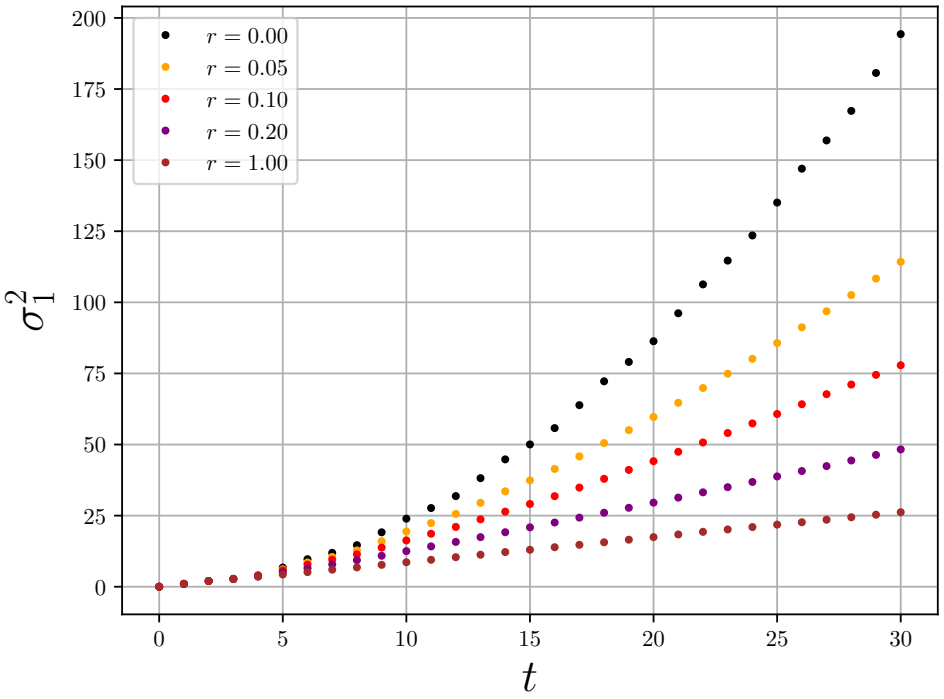

Figure 3.2. Simulated variance for different values of disorder up to 30 steps of evolution. Each point is obtained by averaging over 1000 different evolutions.

We found that, in the presence of disorder, the walker is characterized by a superdiffusive behaviour. This is clearly shown in Fig. 3.2, where the bending of the variance curves are less then quadratic (yellow, red and violet dotted curves). As

the disorder increases, the evolution became ever and ever more diffusive (brown dots, linear behavior).
It is worth noting that, if one simulates the behaviour for an higher number of steps, the superdiffusive behaviour became diffusive instead. This means that the superlinear dependence of the variance from the time is a transient behaviour and that the findings of the present work only apply to the initial part of the walk. Because of the experimental nature of this thesis, and because of the limited step number experimentally reproducible, we focused on such transient behaviour instead of the infinite time one. Nevertheless, one should note that the study of such a behaviour which, as shown in the simulations, holds for at least 30 steps, is still relevant for the comprehension of the QW evolution. Indeed, nowadays, 30 steps represent an high percentage of the walk itself as the maximum step number reproducible so far is $O(50-60)$ steps. For simplicity, from now on we will omit the adjective transient when talking about the transient superdiffusive behaviour.
In order to quantify the superdiffusivity, we need to estimate the diffusion coefficient β. Hence, it is better to work with a modified version of (3.1). By computing the logarithm on both sides of the equation we get (the base of the logarithm is not relevant)

$$\ln(\sigma_1^2) = \alpha' + \beta \cdot \ln(n) \tag{3.2}$$

where $\alpha = \mathrm{e}^{\alpha'}$.
We can than fit this relation to the simulated data in order to obtain the theoretical values for the parameters α' (and eventually α) and β. In a log-log scale we expect to obtain linear behaviours with different angular coefficients as the disorder value varies. It is worth noting that the disorder doesn't act before the third step. Indeed, a change in the phase value affects the evolution of the walker only when at least one interference effect occurs. For this reason, a real difference between the behaviours for different disorder values can be appreciated by looking and fitting the variance behaviour from step 4.

In Fig. 3.3 we report the logarithm of the simulated data along with the linear curves fitted to them. Data are nearly perfectly linear, confirming the superdiffusive spread of the walker during the evolution.

r	α'	α	β
0.00	-1.211	0.298	1.898
0.05	-0.855	0.425	1.650
0.10	-0.610	0.543	1.467
0.20	-0.388	0.679	1.259
1.00	-0.168	0.845	1.010

Table 3.1. Values of the parameters α', α and β obtained by fitting relation (3.2) to the simulated data

In Tab. 3.1 we report the numerical values of the parameters obtained through the fit. We can see that the β values lie in the range $1 \leq \beta \leq 2$, decreasing as the disorder strength increases. This trend unambiguously denotes the presence of superdiffusion when $0 < r < 1$. In the case of $r = 1$ a value ~ 1 is obtained for β, indicating that the diffusive regime can be reproduced by completely disordering the QW network. For $r = 0$ a value of 2 is expected. The obtained values is less than 2, but this is can be explained considering that the quadratic behaviour is only a limit case, valid for an infinite number of steps.
Of course, the obtained values are only indicative of the general behaviour and are

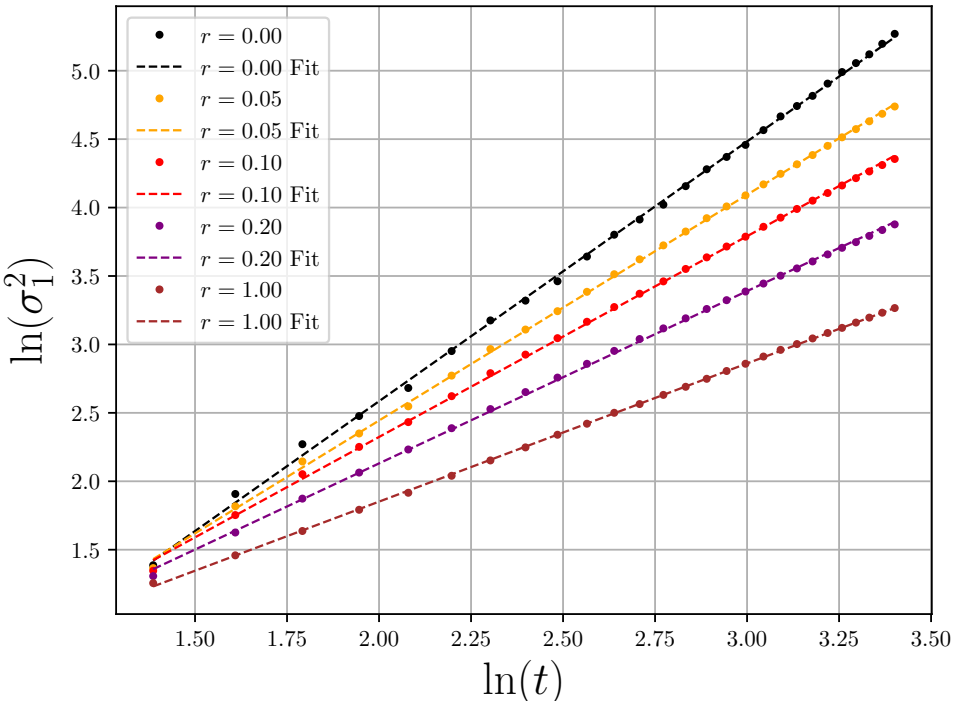

Figure 3.3. Logarithm of the simulated variance for different values of disorder up to 30 steps of the evolution as a function of the logarithm of the step number. Dashed lines corresponds to relation (3.2) fitted to the data. Each point is obtained by averaging over 1000 different evolutions.

susceptible to the number of the step under consideration, especially for a low t. In order to show how good this model of disorder is to study the superdiffusive regime, we computed the standard deviation of the variance distribution for each value of r.

This gives us an insight on the limits and capabilities of such a model. Results of simulation for 7 and 20 steps are shown in Fig. 3.4. In both cases the mean value of variance decreases when r increases, since a constant value around $p \sim 0.40$ is approached for both 7 and 20 steps. This indicates that the output distribution rapidly merges into a classical one for $r > 0.40$, while a genuine superdiffusive behaviour occurs between $0 < r \leq 0.20$. Focusing on this region we observe that, for a given value of $\sigma_1^2(r)$, the uncertainty on the corresponding value of r decreases with increasing of t. The analysis indicates that the model is much more accurate when the number of steps increases. This is directly linked to Fig. 3.1. Indeed, the overlap region between distributions of different disorder values increases when the number of step decreases, making it more and more difficult to distinguish between different values of disorder.

Distribution analysis

The superdiffusive behaviour of the walker can be analysed also by looking at the averaged probability distribution.

For a given value of disorder r, the mean probability distribution can be recon-

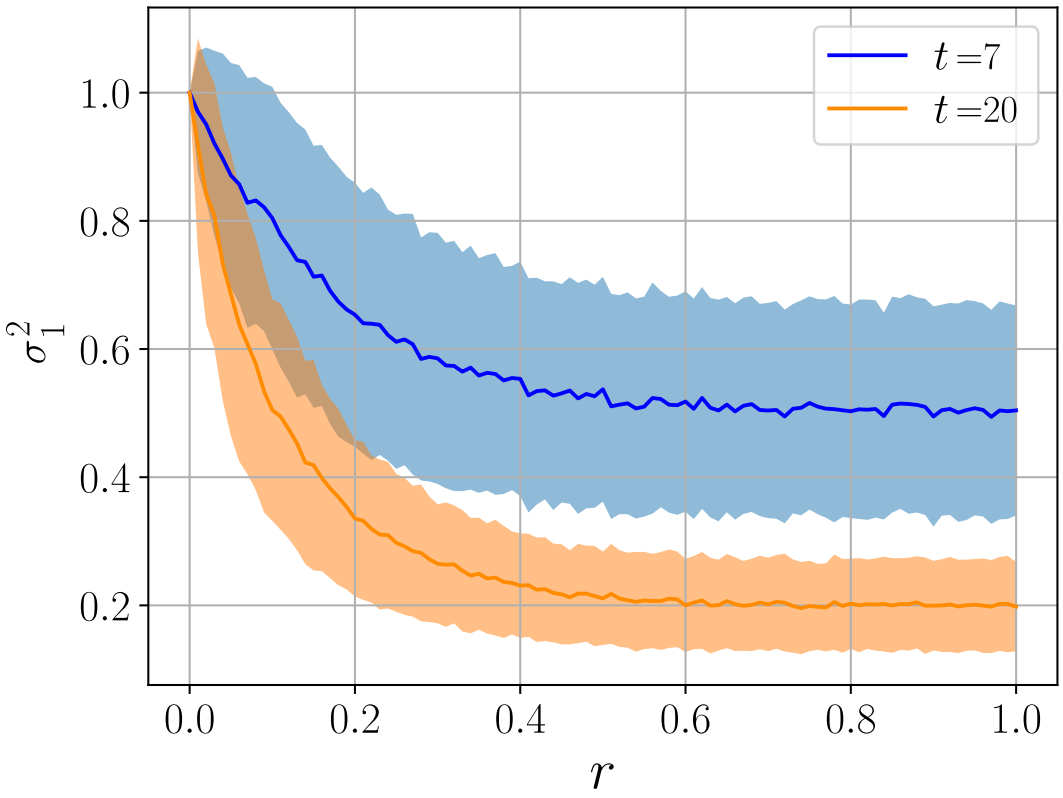

Figure 3.4. Simulation of the variance behaviour for 7 and 20 steps as a function of r. The average values of the variance have been calculated on a sample of 1000 different phase maps for each value of r. In the vertical axes σ_1^2 for 7 and 20 steps have been normalized to their maximum values. Error bands correspond to the standard deviation of the variance distributions.

structed by averaging it over a high number of phase maps configurations. In Fig. 3.5 we report the mean probability distribution for different values of the disorder r at step $T = 30$. In the case $r = 0$, the distribution is the typical one of an ordered QW, characterized by a symmetric shape with two specular peaks centered in sites $\sim \pm\frac{30}{\sqrt{2}}$. If the initial coin state is $|0\rangle_c$ ($|1\rangle_c$), only a single maximum in site $-\frac{T}{\sqrt{2}}$ ($+\frac{T}{\sqrt{2}}$) will be present, the other one being highly suppressed. When increasing the disorder level, the probability distribution became more and more localized around the starting site 0, the lateral peaks vanish and a central peak arises. Even with a very low value of disorder, i.e. $r = 0.05$, the typical shape of the ordered QW is completely suppressed, and a nearly constant behaviour is obtained in the range $-\frac{T}{\sqrt{2}}, +\frac{T}{\sqrt{2}}$. When the disorder reaches values around 0.20, the distribution is already similar to the gaussian shaped one, typical of CRW, and for $r \sim 0.40$ it is no more distinguishable from it. In order to quantify these considerations and to deeply analyse the behaviour of the probability distribution, we rely on the similarity, which is a measure of how much two distributions G and G' are similar

$$S(G, G') = \frac{(\sum_i \sqrt{G_i G'_i})^2}{\sum_i G_i \sum_j G_j}.$$

In the graph of Fig. 3.6, for several step number, we show the behaviour of the

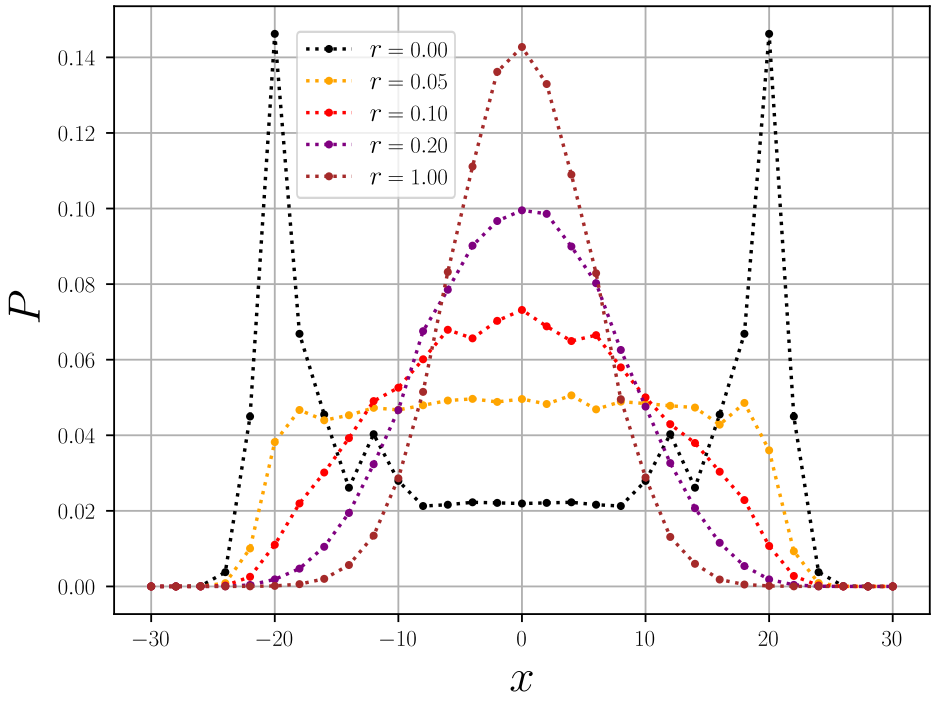

Figure 3.5. Probability distribution at step 30 for a initial coin state $|+\rangle$ for different values of the disorder r. Different colors stand for different values of the disorder r.

similarity between the average distribution for a given value of disorder r and the ordered or disordered distribution at varying of r (respectively, solid and dashed lines). The similarity with the disordered (ordered) distribution increases (decreases) with r since, the higher the disorder, the more destructive interference tends to reproduce the diffusive evolution. In the inset, the crossing points between the two quantities are highlighted. We identify these points as the one defining the transition value of r between quantum and classical regimes, identified in the ballistic and diffusive probability distribution, for a given number of step t. It is worth noting that the transition point decreases with t. This continuous transition occurs without loosing completely the quantum features of the evolution and can be interpreted as an evidence of the fact that the QW modifies its behaviour because of the total amount of disorder experienced along its spreading.

3.1.3 Experimental results - Single walker

In order to study the effect of the disorder on the walker evolution, we experimentally implemented five different values of r, namely $0.00, 0.05, 0.10, 0.20$ and 1.00. As already said, a clear superdiffusive behaviour characterizes the evolution for values of disorder ≤ 0.20. For higher disorder values, a rapid merging of the evolution in a CRW like one occurs. For each value of $r > 0$ we selected three different phase maps and experimentally reconstructed the output probability distribution for each step of the evolution.

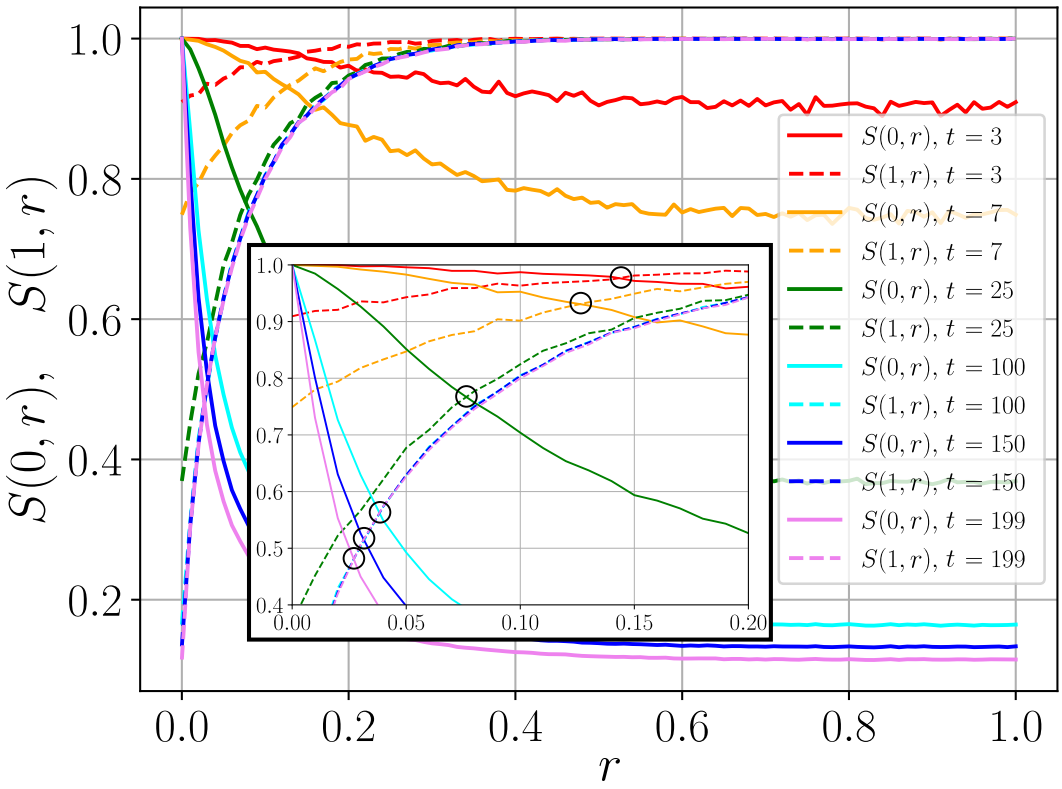

Figure 3.6. Computational simulations for similarity between disordered (dashed line) and ordered (solid line) distributions (respectively $G(r=1) \equiv G(1)$ and $G(r=0) \equiv G(0)$) and the average distribution for a given value r as a function of r and step number t. Here $S(0,r)$ ($S(1,r)$) stands for $S(G(0),G(r))$ ($S(G(1),G(r))$). In the inset, a zoom on the intersection region is reported. The crossing point shifts towards lower values of r when the step number increases.

The setup used in the experiment is the one reported in 2.5.1 and the evolution has been obtained up to the 7th step. The experimental setup allows to start the QW from the central position of the 1D-lattice and to use any of the two coin modes (input ports of BS_1). Accordingly, we studied the evolution for the input state $|\psi\rangle = |0\rangle \otimes |0\rangle_c$.

Variance

In Fig. 3.7 the average variance of the walker is reported as a function of the step number t. Experimental data (dots) are in excellent agreement with the theoretical prediction for the three chosen phase maps (dashed lines). The whole superdiffusive region, namely the one between the diffusive (red lines) and the ballistic (blue lines) behaviours, can be exploited by varying the values of r. A small amount of phase instability was present due to the large size of the apparatus. This effect has been included in the computation of errors bars. We also show in Fig. 3.7 the expected behaviours simulated by considering ideal optical elements for the two limit cases of ordered and completely disordered QW (respectively blue and red dotted lines). Ideal trends differ from the experimental data and, in particular, for each step they take lower values. The reason of this can be found in the non perfectly symmetric BS_1 used in the experiment, which presents a measured reflectivity $R = 0.45 \pm 0.01$

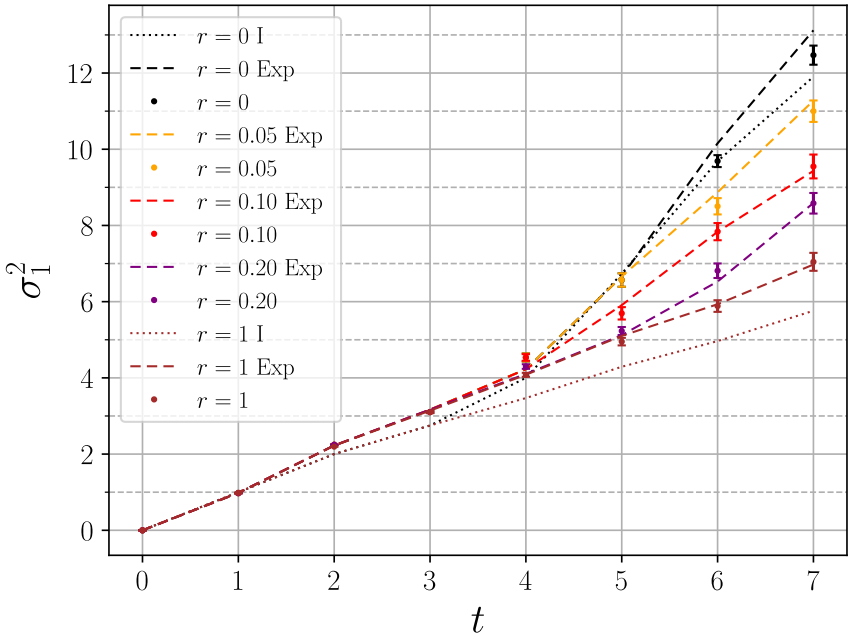

Figure 3.7. Average experimental values of the variance as a function of the step number t for disorder values $0.00, 0.05, 0.10, 0.20, 1.00$. Dots correspond to experimental data. For a given value of r, dashed line shows the expected average behaviour (Exp) of variance for the three selected phase maps. The expected trends were computed by taking into account the actual optical parameters of the setup, such as non ideality of BS_1 and lossy optical elements. Dotted lines show the ideal behaviour (I) of a perfectly symmetric BS_1 in the two limit cases, namely the ordered and disordered QWs. Note that, up to the third step, the variance is not affected by the phase, thus the red and blue dotted lines are coincident; the same effect occurs for all the dashed lines.

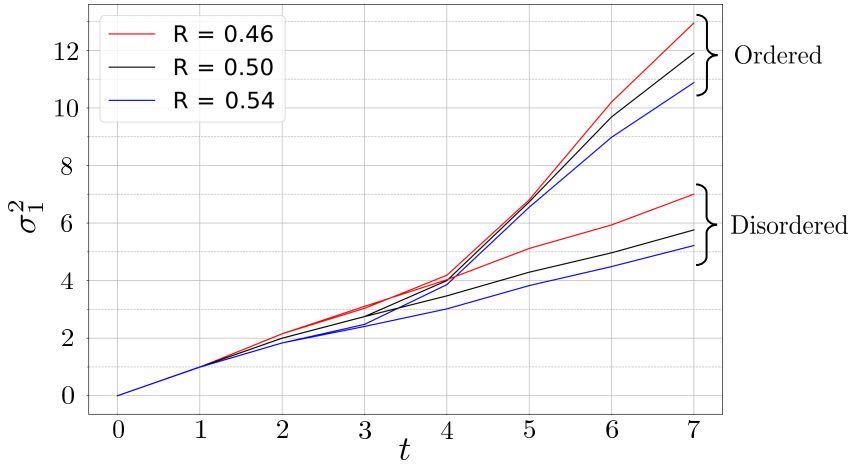

Figure 3.8. Expected variance behaviours corresponding to different values of R: the considered values are $0.46, 0.5$ (ideal case) and 0.54. The theoretical simulations for disordered QW are computed by averaging over 1000 different phase settings.

[29]. The larger probability of photons to be transmitted at each passage through the BS introduces preferential paths travelled by the walker. Such trajectories are those characterized by a lower number of reflections, while the path with the largest

probability is the one transmitted at each passage through the BS. As one can see from Fig. 3.8, the disordered QW is more sensitive to this effect than the ordered one. Indeed, in the first case the disorder tends to localize the walker around a single position, namely the starting one, while the non ideal BS brings the walker into a wide range of positions due to the preferential directions, thus increasing the variance. On the contrary, in the ordered case preferential directions concur to the ballistic behaviour of the walker resulting in a smaller discrepancy between experimental data and ideal theoretical predictions. By taking into account the real parameter of the BS in the simulation of the evolution, the difference between simulated behaviors and experimental data are strongly reduced. An opposite effect is expected in the case of R$\geq$ 0.5. Indeed, in this case the preferential directions are those characterized by an high number of reflections, such that the walker tends to be confined around a small range of positions This results in a smaller variance with respect to the ideal case for both ordered and disordered QW. Such effects are shown in Fig. 3.8, where we compare the different variance behaviours expected for $R = 0.46, 0.5, 0.54$. As said, when $R < 0.5$ the variance is larger than the one calculated for the ideal case ($R = 0.5$) and the disordered QW is more affected if compared with the ordered one; when $R > 0.5$ the variance is smaller with respect to the ideal case for both ordered and disordered QW, however in this case the disordered QW is less affected by this effect when compared with the ordered one. The actual superdiffusive behaviour of the experimental evolutions is confirmed by the values of the parameter β obtained by fitting relation (3.2) to the experimental data.

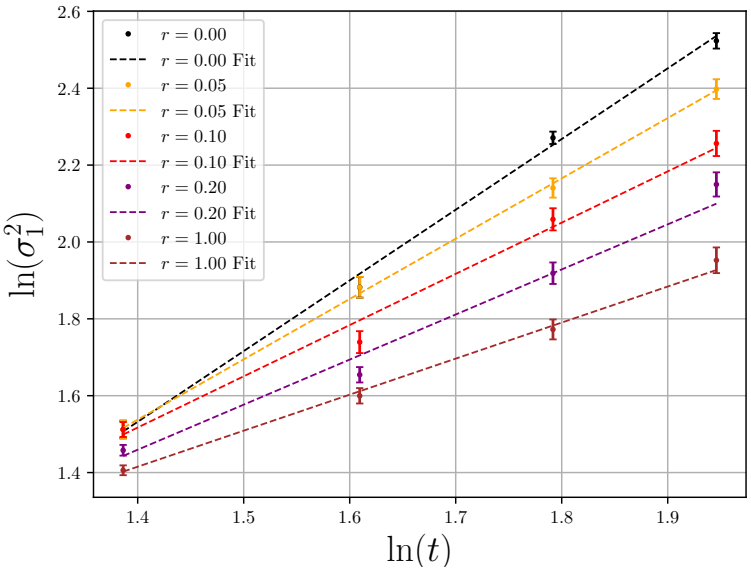

Figure 3.9. Data and relation (3.2) fitted to them in a log-log scale. The nearly perfectly linear behaviours confirm the actual superdiffusive spread of the quantum walker.

In Fig. 3.9 we report the data and relation (3.2) fitted to them. We recall here that the disorder doesn't act before the third step of the evolution and a real

r	β_{Theo}	β_{Fit}
0.00	1.898	1.839 ± 0.052
0.05	1.650	1.569 ± 0.058
0.10	1.467	1.333 ± 0.060
0.20	1.259	1.173 ± 0.051
1.00	1.010	0.938 ± 0.050

Table 3.2. Expected (β_{Theo}) and experimental (β_{Fit}) values of the diffusion parameter β for different values of r. The values between 1 and 2 for $r > 0$ clearly demonstrate the superdiffusive feature of the evolution.

difference between the behaviours for different disorder values can be appreciated by looking at the evolution starting from step 4. For this reason, only data from step 4 to 7 have been considered for fitting. Results are shown in Tab. 3.2, where we report both theoretical and experimental values of β. The observed discrepancies can be explained as follows:

- The β_{Theo} values have been obtained without considering the experimental components imperfections, e. g., BS asymmetry and losses.
- Numerical simulations for $r > 0$ have been obtained, as said, by averaging over 1000 disorder configurations, while three phase maps were used in the experiment. Thus, we expect the simulation results to be far more accurate, while the experimental ones are more sensitive to stochastic deviations.

It is worth noting that, for the ordered case, the values of β_{Theo} and β_{Fit} are lower than the expected value of 2. Indeed the quadratic growth is an asymptotic behaviour, expected to be achieved for long evolution times.
We can conclude that a superdiffusive behaviour, uniquely identified by the condition $1 < \beta < 2$, can be simulated using p-diluted QWs, making them a useful tool for further investigations on diffusion processes.
As a final remark, it is worth noting that the values of the parameters reported in Tab 3.2 are slightly different from the ones reported in [18]. Indeed, here we based our analysis on the linearized version of (3.1) (i.e. relation (3.2)), which has been fitted to data starting from step 4. In contrast, in [18], relation (3.1) has been fitted to simulated data from step 0, thus explaining the slightly different values of the anomalous exponent. Despite this, the values of β reported in [18] and the ones reported in Tab 3.2 are compatible, thus showing the robustness of the results to different analysis approaches.

Probability distribution

In Fig. 3.10 we report on the average density plots of the evolutions of the single photon QW in the cases $r = 0.00, 0.05, 0.10, 0.20$ and 1.00. On the horizontal axis the sites of the discretized line that the walker can reach up to the 7th step of the evolution are reported, while the vertical one represents the step number, increasing from top to bottom. For a better visual representation, data for each step are normalized to the maximum measured value. For each disorder strength $r > 0$, the probability distributions of three experimental realizations with different phase maps have been averaged. Both experimental data and theoretical predictions are reported by taking into account the real parameters of the optical setup. In Tab. 3.3 we report the values of the similarity between the theoretical prediction and the experimental distributions. The very high values show the capability of the setup to

reproduce QW evolution with high precision.
By looking at the distribution for $r = 0.00$, one can note that the maximum of the probability distribution is localized around site -5, which is typical for a walker propagating in an ordered QW [11]. When the disorder increases, ($r = 0.05, 0.10$) the maximum shifts towards higher site numbers (-3). For $r = 0.20$ the mean position of the distribution approaches the starting position 0 and, in the limit case of complete disorder, the walker tends to reproduce the CRW distribution. The bar plots allow to better appreciate this behavior. The probability distribution corresponding to the 7th step is reported. Black-contoured bars represent theoretical predictions by taking into account real parameters of the optical setup while gray bars correspond to the experimental data.

r	*Similarity*
0.00	0.999 ± 0.001
0.05	0.999 ± 0.001
0.10	0.998 ± 0.002
0.20	0.998 ± 0.002
1.00	0.993 ± 0.001

Table 3.3. Similarities between expected probability distributions and experimental ones for the single photon QW for different values of r. Errors computation takes into account a small amount of phase instability due to large dimensions of the optical setup.

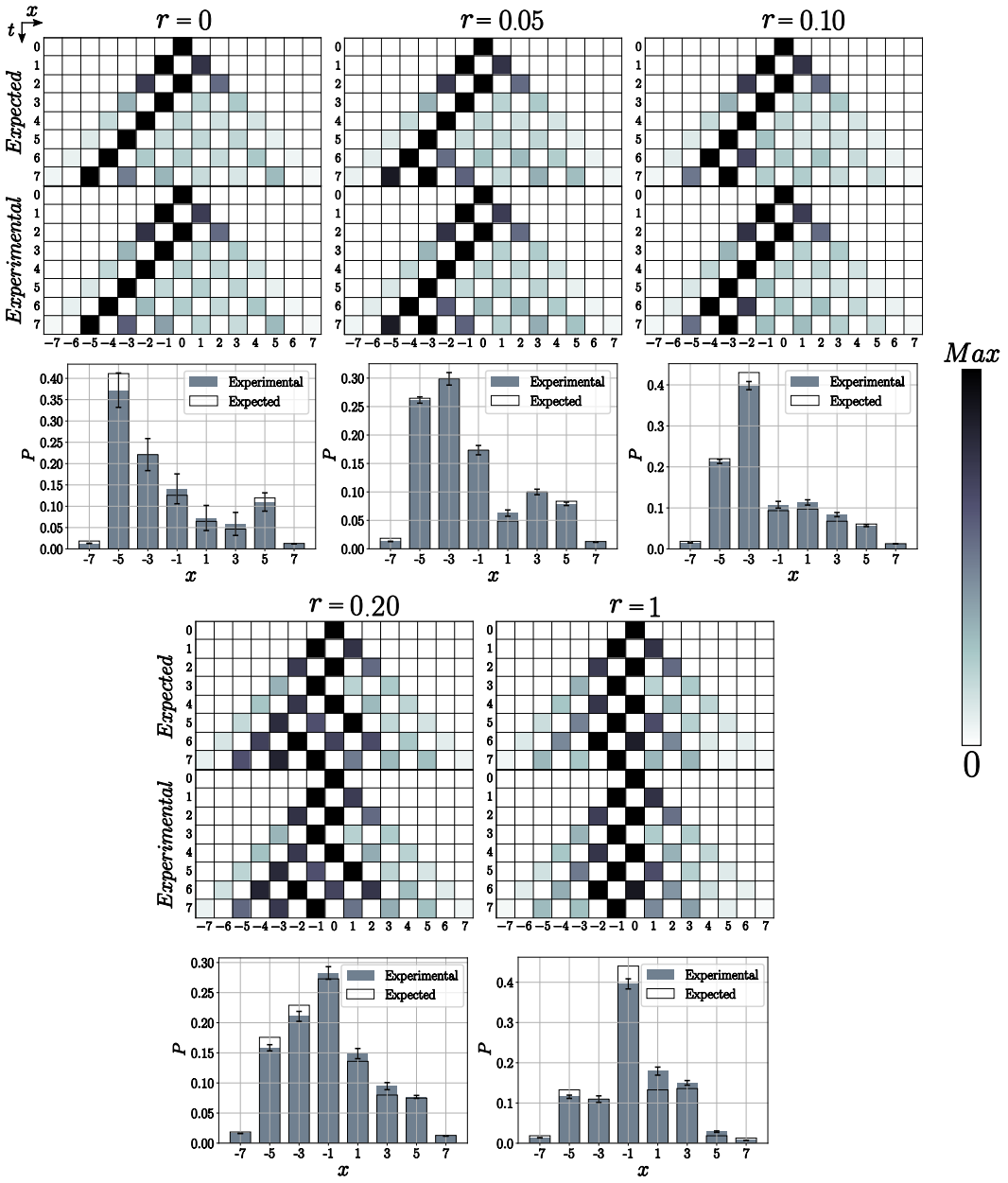

Figure 3.10. Density plots: time evolution of the probability distributions for $r = 0.00, 0.05, 0.10, 0.20, 1.00$ in the single photon case. Experimental data and simulations taking into account real parameters of the optical setup are reported, respectively referred to as Experimental and Expected. **Bar plots**: 7th step probability distributions for the implemented values of r. Black-contoured bars represent expected values taking into account real parameters of the setup, gray bars represent experimental data. Data for $r > 0$ are the result of the average over three different phase maps.

3.1.4 Simulations - Two walkers

A natural question arises, namely whether the superdiffusive regime also holds in the multiple photon case or if it is only present in the single photon evolution. In order to answer the question, we studied both cases of two indistinguishable and

distinguishable photons entering the QW in two opposite coin states. In the first case, the evolution will be the result of the combined effect of classical interferences and pure quantum ones, namely HOM effects. In the second case, only classical interferences will play a role.
We mainly focused our attention on the dependence of the variance from the step number, which in this case can be written as

$$\sigma_2^2(t) = \sum_{x,y=-t}^{t} (\frac{x+y}{2})^2 \cdot P(x,y,t) - (\sum_{x,y=-t}^{t} \frac{x+y}{2} \cdot P(x,y,t))^2$$

which represents the variance of the mean position of the two walkers. Here, $P(x,y,t)$ is the probability to find a photon in the site x and the other one in the site y at step t, regardless of whom is where.
In Fig. 3.11 we report the simulated variance behaviours for different values of the disorder r up to step 30.

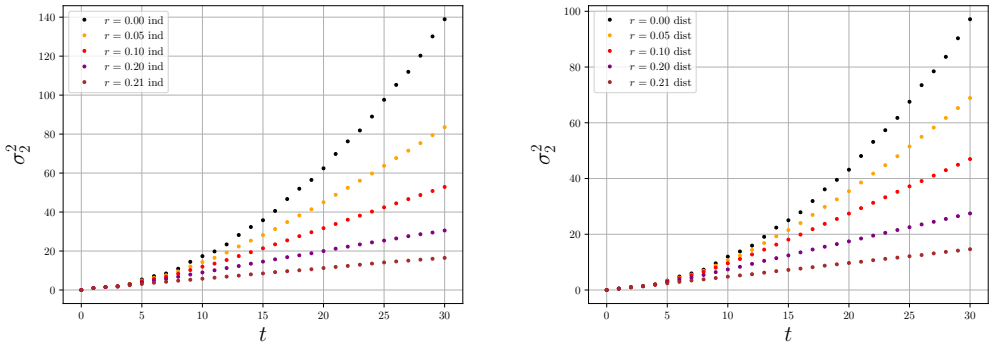

Figure 3.11. Left: variance behaviour for indistinghuishable photons. **Right**: same for distinguishable ones.

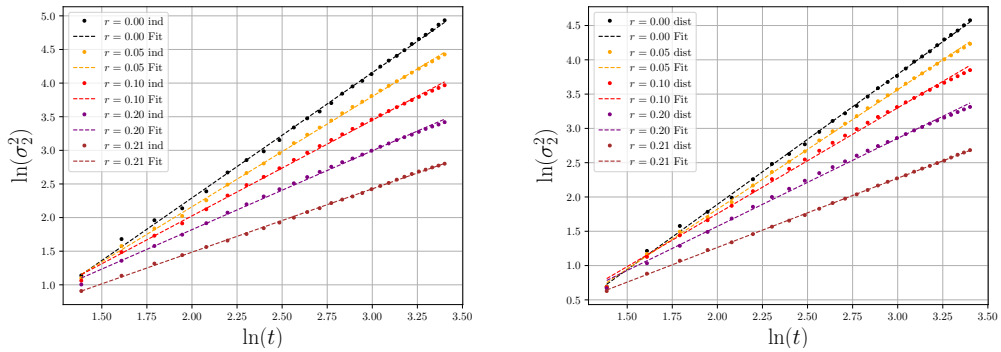

Figure 3.12. Left: variance behaviour for indistinghuishable photons in the log-log scale. **Right**: same for distinguishable ones.

Because of the much higher amount of time needed to simulate the evolution of two photons, data have been extracted from 400 phase maps for each value of disorder r instead of 1000 as in the single photon case up to step 30. Nevertheless, relevant properties of the evolution, as the superdiffusive behaviour, are still clearly

observable. In both cases of indistinguishable and distinguishable photons, the superdiffusive regime is achievable as showed in Fig. 3.12. This is indeed confirmed by the values of the parameter β, which is between 1 and 2, as shown in Tab. 3.4.

r	α'_{ind}	α_{ind}	β_{ind}	α'_{dist}	α_{dist}	β_{dist}
0.00	-1.43335	0.23851	1.86303	-1.90410	0.14896	1.89797
0.05	-1.11813	0.32689	1.63963	-1.66455	0.18928	1.74303
0.10	-0.82150	0.43977	1.42316	-1.32876	0.26481	1.54274
0.20	-0.52498	0.59156	1.17274	-0.99749	0.36880	1.28421
1.00	-0.39828	0.67147	0.94184	-0.75639	0.46936	1.01011

Table 3.4. Expected values of the diffusion parameter β and proportionality parameter α for different values of r for both indistinguishable and distinguishable photons cases. The values between 1 and 2 for $r > 0$ clearly demonstrate the superdiffusive feature of the evolution.

A main difference between the two cases can be observed: indistinguishable photons spread more than the distinguishable ones. Indeed, the values of σ_2^2 is greater in the first case than in the second one for all disorder strength r under study. This can be explained by considering the HOM effects having place during the evolution.

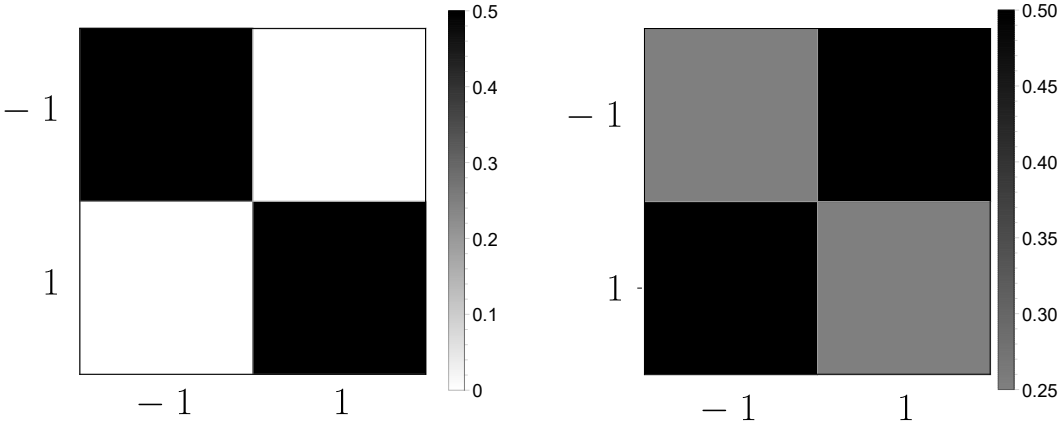

Figure 3.13. Left: probability distribution in the indistinguishable photons case. **Right**: same for distinguishable ones. When the photons are indistinguishable, the low probability to find them travelling separated along two different modes increases the value of the variance, which is indeed lowered in the distinguishable photon case.

Two indistinguishable photons tend to travel along the same mode with a higher probability with respect to distinguishable ones, leading to lower values of probability to find them in opposite sites, which gives 0 contribution to the computation of σ_2^2. In the distinguishable case, HOM effect doesn't take place and a higher probability to find the particles in opposite sites lowers the values of σ_2^2.
This effect can be appreciated in the Fig. 3.13, in which we report the position probability distribution for two indistinguishable and distinguishable photons after one step of the QW. Each square corresponds to the probability to find a photon travelling along the mode identified by the row and the other one along the mode identified by the column, regardless of which photon is found on which mode. As

a consequence we end up with a symmetric matrix whose superior triangular part (including the diagonal) sums up to 1 for normalization condition. It is clear from the image that the probability to find two photons travelling along the modes $x, y = -x$ in the first case is strongly suppressed with respect to the same probability in the second case. This is a consequence of the pure quantum two-photon coalescence, which has not classical counterpart. It is also worth noting that the higher spread in the indistinguishable photons case is not due to an higher value of β, which is smaller than in the distinguishable case, but due to the higher values of α.

3.1.5 Experimental results - Two walkers

We experimentally investigated the case of indistinguishable photons entering the QW through the two BS_1's input ports (see Fig. 2.6). In order to do that, synchronization of their arrival time on the BS_1 was necessary. To this aim, a Hong-Ou-Mandel dip has been measured (see Fig. 3.14).

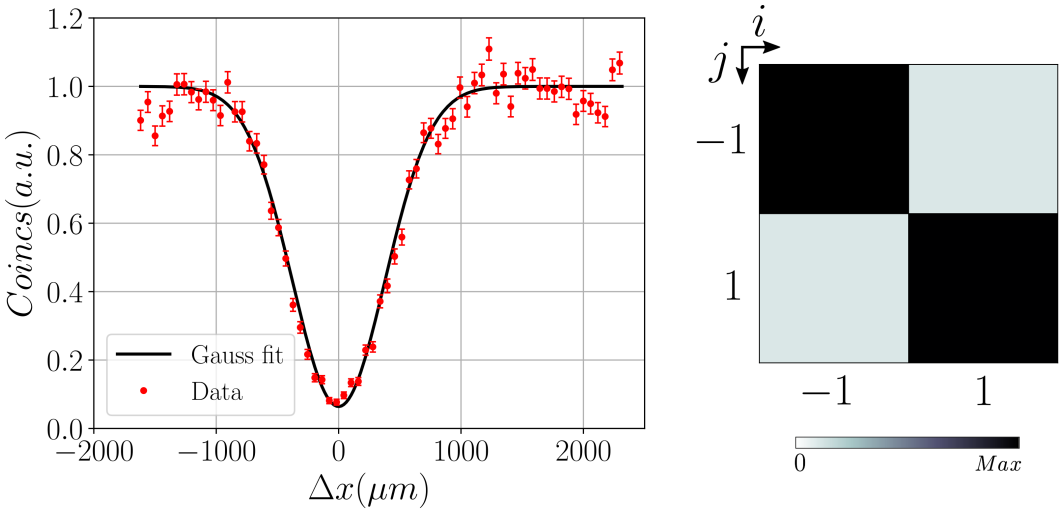

Figure 3.14. Left: normalized coincidences vs photons optical delay. Red dots represent experimental data with error bars computed considering poissonian distributed coincidences. Black line corresponds to a gaussian function fitted to the experimental data. Photon indistinguishability is confirmed by the high dip visibility $V \sim 93\%$. **Right**: normalized experimental coincidences matrix for the first step of the QW. Index i (j) represents sites of the first (second) detector.

After correction for accidental coincidence, the measured visibility was $V \sim 93\%$. The non perfect indistinguishability of the photons can be due to finite precision in the experimental alignement procedure as well as to imperfections in setting polarization and frequencies of the photons. Nevertheless, the above 90% value is still very good to perform the experiment. The value of the visibility has been taken into account in the simulated data, in order to predict with the highest possible accuracy the expected value of the variance.
The condition of equal arrival time on the interaction surface of BS_1 corresponds to the first step of the QW with indistinguishable photons, whose coincidences matrix is reported in the right image of Fig. 3.14. In order to measure the probability to find two photons travelling along the same output mode, a further BS (BS_2) was used to split them with a given probability, as shown in Fig. 2.6. By means of the BS_2 it has been possible to collect coincidences between all possible pairs of modes. In Fig. 3.15 we report the simulated and experimental behavior of σ_2^2 as a function

of the step number t. Green dots represent the measured evolution for $r = 0.10$, the blue and red dotted lines correspond respectively to the simulated behaviour for $r = 0.00$ and $r = 1.00$. In this case the number of steps is limited to $T = 5$ mostly for two reasons: the losses present in the apparatus and the growth of the number of modes on which the photons can travel, both of them limiting the number of detectable coincidences. Experimental data are in very good agreement with theoretical simulation taking into account the real setup parameters. Error bars are larger than the ones in the single photon case due to the fact that here a little variation of the phase must be considered twice, because it is experienced by both photons. Moreover, a Poissonian error on the coincidences count has been taken into account.
By fitting relation (3.2) to the experimental data starting from step 3 we obtained $\beta = 1.41 \pm 0.2$. The result indicates that a superdiffusive spread characterizes the evolution of the two photons, despite an high uncertainty over the value of the diffusion coefficient.

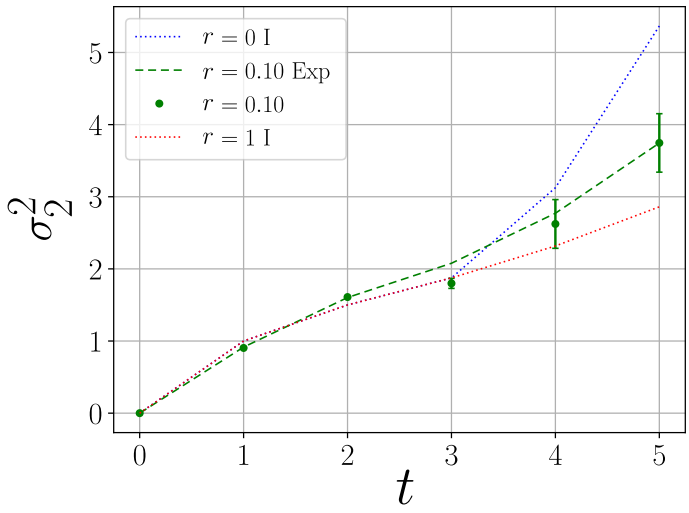

Figure 3.15. Experimental values of σ_2^2 for the two indistinguishable photon QW. Green dots represent experimental data, dashed line corresponds to the expected behaviour obtained by taking into account the real parameters of the setup (Exp). Blue and red dotted lines correspond respectively to the limit cases of ideal ordered and disordered two photon QW (I). Note that, up to the third step, the variance is not affected by the phases, thus the red and blue dotted lines are coincident.

t	*Similarity*
1	0.999 ± 0.001
2	0.999 ± 0.001
3	0.99 ± 0.02
4	0.99 ± 0.05
5	0.97 ± 0.05

Table 3.5. Similarities between expected coincidence matrices and experimental ones for the two photons QW up to the fifth step. Error values take into account a small amount of phase instability due to large dimensions of the optical setup.

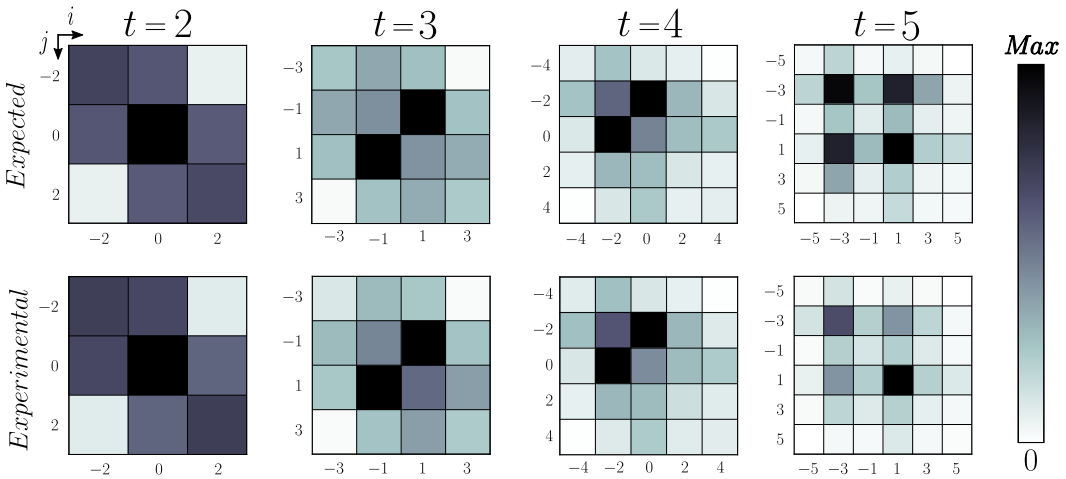

Figure 3.16. Experimental (top) and simulated (bottom) probability distributions up to the fifth step when two indistinguishable photons enter the QW. For the sake of clarity, each matrix is normalized to its own maximum value. Similarities between expected and experimental matrices are reported in Tab.3.5.

We reconstructed the coincidence matrices up to the step 5 in the case of $r = 0.10$. Experimental data, together with the respective theoretical predictions taking into account the real parameter of the setup are shown in Fig. 3.16. Similarities between experimental and expected results are quite high, demonstrating the feasibility of the apparatus even for two photon measurements (see Tab. 3.5).

3.1.6 Conclusions

In the last paragraphs, we have reported on the experimental investigation of the superdiffusion process, intermediate between the quantum and classical transport regimes, performed by introducing tunable disorder, through suitable phase map configurations, in a discrete time QW. The intrinsically stable bulk optic system used in the experiment allows to operate with any kind of phase map.
In the single photon case, the results, both simulated and experimental, have shown that a clear superdiffusive regime arises when a completely random disorder over space and time is introduced along the evolution of the quantum particle. For all the disorder values under investigation, superdiffusion has been experimentally obtained, despite the relatively low number of steps, i.e. 7, experimentally reproducible. This is confirmed by the values of the diffusion coefficient β, resulted to be between 1 and 2 for all values of disorder strength.
The two photon case has also been computationally and experimentally investigated. In the first case, both dynamics of indistinguishable and distinguishable photons have been studied. Results show that, in both cases, the superdiffusive regime can be achieved, with the indistinguishable particle spreading more than the distinguishable ones. From an experimental point of view, we reported the case of the evolution for $r = 0.10$ up to 5th step of the evolution for identical particles. The value of the parameter β confirms the superdiffusive regime, despite the relative high uncertainty. In order to increase the accuracy on the estimation of β, two main improvements can be done: the first one consists of increasing the number of coincidences revealed by the detector, in order to decrease the relative error on the measured coincidences; the second one, of course, is to follow the evolution of the photons for more than

5 steps. Both this improvements are not straightforward to realize: the first one implies having at disposal a source with higher photon flux as well as decreasing the losses of the setup; the second one implies an alignement such that the two photons remain indistinguishable during the whole evolution. This means that their direction of propagation have to be identical for more than $O(10)$m (considering the actual setup dimensions). Both problems could be partially solved by diminishing the dimension of the setup. In this way, losses due to beam divergence would be suppressed and the requirements of alignement would be less demanding. This is actually an improvement measure which we adopted during the realization of the experiment reported in section 4.

3.2 Subdiffusion

As previously said, transport phenomena are extremely common in the description of physical processes. It is quite common that the dynamics of a natural processes does not spread linearly with time. Indeed, rather, the system is characterized by a distribution which broadens according to a nonlinear power law [9, 101]. In particular, the case of a sublinear relation between variance and time, i.e., subdiffusion, can be frequently observed in nature, for instance in biological processes [102, 103, 104, 105], wave propagation and scattering [106, 107], the movement of charge carriers in amorphous semiconductors [108], disordered media [100], and many-body localization transitions [109]. Subdiffusion even applies to certain economic models [110]. Because of this vast range of applications and its fundamental relevance, many attempts have been made in the last years to uncover the underlying physical mechanisms which can lead to anomalous diffusion. Such theoretical models rely on a variety of physically motivated or more abstract approaches, such as fractal theory [111, 112], fractional Brownian motion [113], and continuous-time random walks. [114, 115]. As a consequence, the possibility to simulate all kinds of anomalous diffusive spreading in a tunable manner, can not only lead to significant understandings about complex mathematical models but also allows us to study a plethora of processes in nature. In this section, we continue such a simulation task, exceeding the results presented in the previous ones, which focused on the superdiffusive regime. As we showed in section 3.1, by actively influencing the evolution of the walker, the functional dependency of the broadening can be altered, e.g., for reproducing the classical normal diffusion of incoherent processes, after exploring an intermediate spread regime, featured by superdiffusive behaviour. This approach fundamentally proves that superdiffusion is accessible by introducing inhomogeneities in the QW's evolution, being based on the so-called p-diluted model. If, from one hand, the superlinear regime has been studied because of the natural superdiffusive nature of the QW, on the other hand, the less accessible entirety of the subdiffusive domain remains largely unexplored. Among other reasons, a lack of a fitting experimental platform hindered such a realization to date. The need of a scalable, dynamically reconfigurable, and compatible platform, supporting the introduction of controlled disorder in spatial and temporal domain in order to realize advanced disorder models is unavoidable.
In the present section, we experimentally demonstrate that the conceptual idea of p-diluted disorder can be extended to subdiffusive regime as well as to the superdiffusive one. The need of an higher number of steps with respect to the previous investigation, obliged us to use the highly flexible time-multiplexing scheme presented in section 2.5.2. By controlling disorder in the spatial degree of freedom (here, time bins) and in time (here, number of steps), we demonstrate that it is possible to realize any sublinear propagation regime—starting from statically disordered QWs, giving birth to Anderson localization, up to completely disordered QWs, corresponding to normal diffusion—which is achieved by implementing different disorder levels.

3.2.1 p-diluted model for subdiffusion investigation

To investigate the evolution of a quantum walker along a disordered QW, the p-diluted model described in 2.4.3 was implemented. By properly inserting random dynamic disorder in an already statically disordered QW, we show that a subdiffusive evolution can be reproduced.
The starting point for the study of the subdiffusive regime, is the the static disorder. It is characterized by a space-dependent disorder, which can be represented as a space varying coin, i.e. $\hat{C}(x,t) = \hat{C}(x)$. This kind of disorder leads to the Anderson

localization, which is a purely quantum and static effect, consisting in the exponential localization of the walker around the starting position $x = 0$ [63]. In Fig. 3.17 we show a QW network characterized by a static disorder.

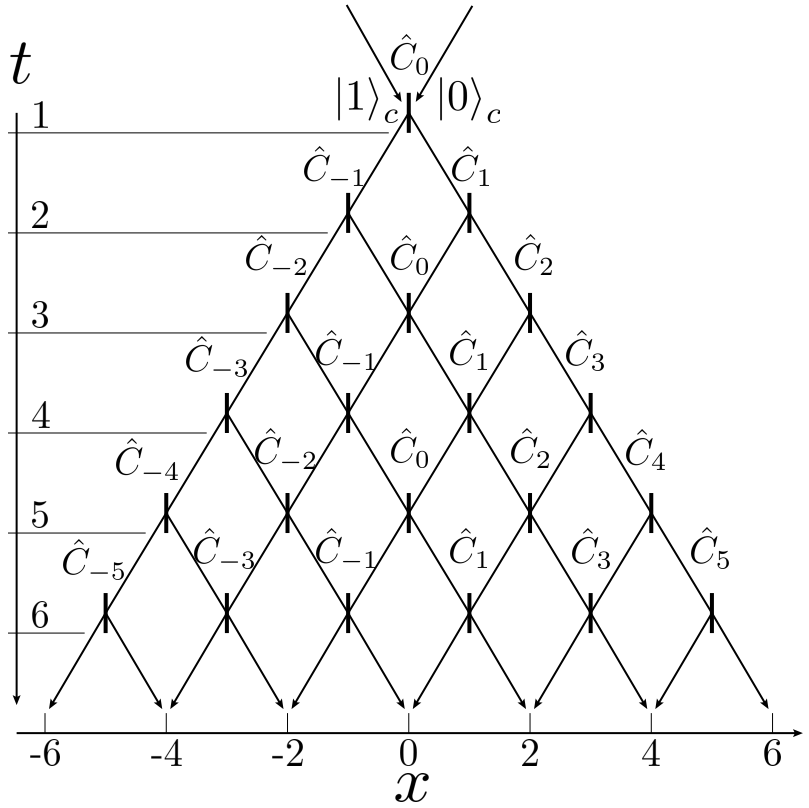

Figure 3.17. Example of a statically disordered QW. The coin at a given site x is the same at each time of the evolution.

As one can see, the coin in a given site x is constant over time, despite it changes from site to site.
The basic idea which allows to reproduce the subdiffusive spread consists of perturbing the staticity of the disorder by means of a random, time-dependent one. This can be done by using the p-diluted model, allowing to independently and randomly change the coin operator at each site and step of the QW network according to a probability p

$$\hat{C}(x,t) = \begin{cases} \hat{C}'(x,t) & \text{with probability } p, \\ \hat{C}(x,t) & \text{with probability } 1-p. \end{cases}$$

i.e., the coin operator at site x and at step t remains unchanged with a probability $1 - p$ or changes with a probability p. Specifically, $p = 0$ corresponds to the case of static disorder, yielding to the Anderson localization, while $p = 1$ results in a completely disordered QW, for which a diffusive spread is expected. As in the previous case of superdiffusion, also in this realization of the p-diluted model, a high number of different configurations, which we will refer to as coin maps, can be obtained due to the randomness in the choice of the site and time of coin modification. The present implementation of the p-diluted model is exactly the one described in

2.4.3, as the probability p to randomly pick a new coin operator directly corresponds to the ratio of coins different from the initial static disorder configuration.
The disorder interval $0 < p < 1$ should theoretically enable us to control our QW in such a way that it explores the full intermediate range of exponential spatial decays between the diffusive spread and Anderson localization.

3.2.2 Theoretical description of subdiffusion

It is useful to recap and reformulate the theory of diffusion in randomized media to have a coherent treatment of the subdiffussive spread. The model will be based on the description given in Ref. [116]. There, the approach was based on the Laplace transform in the temporal domain, but it is more convenient to discuss that method in terms of the Fourier transform in the spatial domain. Eventually, we relate this approach to p-diluted models.
It is worth noting that we used this model in a heuristic way, in order to give an insight on the possible physical mechanism at the base of the subdiffusive spread of the walker.
We start the description from the equation

$$0 = \frac{\partial P(x,t)}{\partial t} + \mathcal{L}(-\frac{\partial^2}{\partial x^2}, t)P(x,t), \tag{3.3}$$

where $P(x,t)$ represents a space-time dependent probability distribution and $\mathcal{L}$ is a potentially time-dependent differential operator in the spatial degree of freedom x. For example, $\mathcal{L} \propto -\frac{\partial^2}{\partial x^2}$ describes the heat equation that results normal diffusion. More generally, the operator $\mathcal{L}$ is a potentially time-dependent differential operator. Eq. (3.3) describes a general model of diffusion in a one-dimensional system. In the continuous limit, this equation also models the asymptotic behavior of a discrete system, such as our QW. Furthermore, the differential operator depends on $\frac{\partial^2}{\partial x^2}$ for a positive (i.e., dispersive) behavior because of $-\frac{\partial^2 e^{ixk}}{\partial x^2} = k^2 e^{ixk}$ and $k^2 \geq 0$. It is much more convenient to work in the Fourier space by computing the Fourier transform, defined as

$$\Phi(k,t) = \int_{-\infty}^{+\infty} dx\, e^{-ikx} P(x,t)$$

We can then rewrite Eq. (3.3) as

$$0 = \frac{\partial \Phi(k,t)}{\partial t} + \mathcal{L}(k^2, t)\Phi(k,t). \tag{3.4}$$

whose solution can be formally expressed in form of the Green's function as

$$\tilde{G}(k,t) = \exp\left(-\int_0^t dt'\, \mathcal{L}(k^2, t')\right). \tag{3.5}$$

This solves Eq. (3.4) as $\Phi(k,t) = \tilde{G}(k,t)\Phi(k,0)$, where $\Phi(k,0)$ represents the initial distribution. In our case, this is modeled by a singular input at the center position, thus $\Phi(k,0) = 1$ in the Fourier domain. Ref. [116] shows that, for large times ($t \gg 1$), solutions follow the functional form

$$P(x,t) = \frac{ab}{2\sigma(t)\Gamma(1/b)} \exp\left(-\left|\frac{ax}{\sigma(t)}\right|^b\right), \tag{3.6}$$

with Γ being the Gamma function and $\sigma(t)$ denoting a time-dependent standard deviation. In addition, we define $a = \sqrt{\Gamma(3/b)/\Gamma(1/b)}$ while b relates to the type of exponential decay; e.g., $b = 1$ and $b = 2$ define a linear and quadratic (i.e. Gaussian) spatial shape, respectively.
The moments of this distribution can be evaluated as well; odd moments vanish and even moments read

$$E(x^{2n}) = \frac{\Gamma\left(\frac{2n+1}{b}\right)}{\Gamma\left(\frac{1}{b}\right)} \left[\frac{\sigma(t)}{a}\right]^{2n}.$$

These expression enables us to expand the characteristic function in a Taylor series as

$$\begin{aligned} \Phi(k,t) &= \sum_{n=0}^{\infty} E(x^n) \frac{[ik]^n}{n!} \\ &= 1 + \sigma(t)^2 \frac{-k^2}{2} + \frac{\Gamma\left(\frac{5}{b}\right)\Gamma\left(\frac{1}{b}\right)}{\Gamma\left(\frac{3}{b}\right)^2} \sigma(t)^4 \frac{k^4}{24} + \cdots . \end{aligned} \tag{3.7}$$

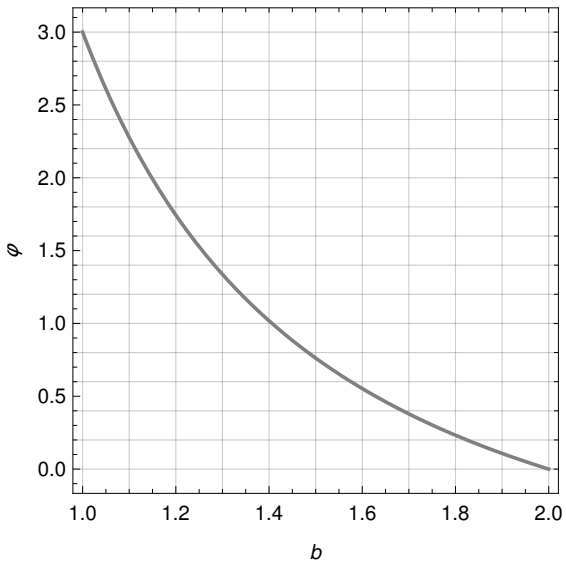

Figure 3.18. Function $\varphi = f(b) = \Gamma\left(\frac{5}{b}\right)\Gamma\left(\frac{1}{b}\right)/\Gamma\left(\frac{3}{b}\right)^2 - 3$ is shown in the relevant interval $1 \leq b \leq 2$. In this region, f is strictly monotonously decreasing, allowing for defining its inverse for determining b from φ.

Similarly, we can expand the generator of the evolution, $\mathcal{L}(k^2,t) = \sum_{n=0}^{\infty} \lambda_{2n}(t) \frac{k^{2n}}{(2n)!}$. This further allows us to expand the Green's function from Eq. (3.5)

$$\begin{aligned}&\tilde{G}(k,t)\\ =&\tilde{G}(0,t)+\left[-\int_0^t dt'\,\lambda_2(t')\right]\tilde{G}(0,t)\frac{k^2}{2}\\ &+\left[-\int_0^t dt'\,\lambda_4(t')+3\left[\int_0^t dt'\,\lambda_2(t')\right]^2\right]\tilde{G}(0,t)\frac{k^4}{24}\\ &+\cdots,\end{aligned} \tag{3.8}$$

where $\tilde{G}(0,t)=\exp\left(\int_0^t dt'\,\lambda_0(t')\right)$.

Because of our initial conditions, resulting in $\Phi(k,t)=\tilde{G}(k,t)$, we can now equate the coefficients for $\tilde{G}$ in Eq. (3.8) and Φ in Eq. (3.7). Since this identification has to be satisfied for all times $t>0$, we find

$$\lambda_0(t)=0,\quad \int_0^t dt'\,\lambda_2(t')=\sigma(t)^2,\quad \text{and}$$
$$-\int_0^t dt'\,\lambda_4(t')=\underbrace{\left[\frac{\Gamma\left(\frac{5}{b}\right)\Gamma\left(\frac{1}{b}\right)}{\Gamma\left(\frac{3}{b}\right)^2}-3\right]}_{\overset{\text{def.}}{=}\varphi=f(b)}\sigma(t)^4.$$

Importantly, $b=f^{-1}(\varphi)$ determines the exponent in Eq. (3.6). See Fig. 3.18 for the graph of f.

A first consequence of the aforementioned relations is that the spread $\sigma(t)$ is given by the time dependency of the first nonzero Taylor coefficient $\lambda_2(t)$, resulting in the corresponding power law, such as

$$\sigma(t)=ct^d$$

with constants $c,d>0$ [116]. The quantity $2d$, which corresponds to the parameter β in (3.1), determines the spread of the variance over time and c is another scaling factor. In the following, we will use equally $2d$ or β to refer to the spread coefficient. For example, for $b=2$ and $2d=1$, we get a Gaussian distribution in space with a linear increase of the variance. In addition, the parameters $b=1$ and $2d=0$ result in Anderson localization as a result of static disorder. Thus, the introduction of dynamic disorder, changing the time-dependence of the generator $\mathcal{L}$, generally results in an increment of the power coefficient d.

As a second observation, we have a look at the relation that includes $\lambda_4(t)$. This coefficient is typically negative which allows one to substitute it by $-\lambda_4(t)=\rho(t)\lambda_2(t)^2$. With this, we can rewrite the above relation as

$$\begin{aligned}\varphi=&\frac{\int_0^t dt'\,\rho(t')\lambda_2(t')^2-\left(\int_0^t dt'\,\rho(t')\lambda_2(t')\right)^2}{\left(\int_0^t dt'\,\lambda_2(t')\right)^2}\\ &+\left(\frac{\int_0^t dt'\,\rho(t')\lambda_2(t')}{\int_0^t dt'\,\lambda_2(t')}\right)^2.\end{aligned}$$

Herein, the numerator of the first term plays a role a variance, quantifying the fluctuation in $\lambda_2(t)$, that influences $b=f^{-1}(\varphi)$.

With these considerations, we can conclude that our p-diluted model dynamically

changes the generator $\mathcal{L}$ by altering the coin operations. As discussed above, this broadens the spread in time (increasing d via λ_2). Secondly, it changes the spatial exponential decay. That is, if only a few coins are changed per time step (low p), those are unlikely the same coins, leading to a high fluctuation in λ_4, thus high φ, thus low b (Fig. 3.18). The other way around, a high p results in low φ and a high b. In the present study, we aim at exploring the theoretically predicted intermediate regime, $1 < b < 2$, with a subdiffusive behavior, $0 < d < 1/2$. As established in section 3.1, discrete QWs have been shown their ability to simulate certain diffusion regimes, such as superdiffusive power laws [18].

3.2.3 Simulations - Single walker

In analogy with the superdiffusive investigation, also in this case it is convenient to work with a limited range of possible coins. In this case, the limitation is more demanding than in the superdiffusive investigation. Indeed, in the previous study the starting point for the investigation was the ordered QW, which presents only a single configuration, i.e. the one with all the phases equal to each others. On the contrary, in this case, we start from a static disordered QW which can be realized by several different coin configurations. Besides this, we introduce a random dynamic disorder, which then increases the number of possible coin maps. It is worth noting that, for a given value of the disorder p, for each coin map we decided to start from a different initial statically disordered QW, to avoid the final results to depend from a particular choice of the starting disorder configuration. Because of the large size of the configurations space, we decided to limit the possible choices of the coin operators to three possible values. By considering the expression of the coin operator (2.17), the three chosen expression of the coin are

$$\hat{C} = \begin{pmatrix} 1 & 0 \\ 0 & 1 \end{pmatrix},$$

which leaves untouched the state of the coin

$$\hat{C} = \begin{pmatrix} 0 & -i \\ -i & 0 \end{pmatrix},$$

which exchanges each other the amplitudes of the two basis states of the coin and multiply them for a factor $-i$, and

$$\hat{C} = \frac{1}{\sqrt{2}} \begin{pmatrix} 1 & -i \\ -i & 1 \end{pmatrix},$$

which mixes the amplitudes of the two basis states of the coin.
We recall that, in this realization of the p-diluted model, $p = 0.00$ corresponds to the case in which only static disorder is present in the network.

Variance analysis

As in the superdiffusive case, to observe the spread of the walker during its evolution, the variance of the probability distribution as a function of the step has to be computed. As usual, for a given value of p, many coin maps can be generated. Because of this, average values of the interesting quantities should be computed in order to gain information about the evolution. Two different approaches can be used for the variance computation:

- in the first one, for a given value of p, the whole spatial probability distribution for each step and for each coin map is independently retrieved. From them, the variance for each coin map as a function of the step number is obtained. Finally, the average value of the variance at each step is computed;

- in the second one, for a given value of p, the average probability distribution over different coin maps is obtained and variance is computed over it.

The two approaches differ in the fact that, in the first one, the average of different values of the variance is computed while in the second one we compute the variance over the average probability distribution. Due to the non linear dependence of σ_1^2 from the probability distribution (see relation (2.3)), the two quantities are generally different. Despite this, simulations show that a clear subdiffusive behaviour is obtained in both cases. In the following, we will report only the simulations for the second case, which is the one we implemented experimentally.
It is worth noting that, in the superdiffusive case, the first approach was used. For subdiffusion study, although the same approach is theoretically implementable, it is no more suitable from an experimental point of view. Indeed, the setup used in the experiment, i.e. the split time QW described in section 2.5.2, allows to implement a high number of different coin maps ($O(400)$) for each value of the disorder p. The implementation of the first approach within the split time QW is very demanding from a time and resource point of view. For this reason, the second one has bee used, which is much more efficient than the first one. Indeed, for a given value of disorder p and for each step of the evolution, instead of measuring a very high number of probability distributions we only measured the average one resulting from all the implemented coin maps.

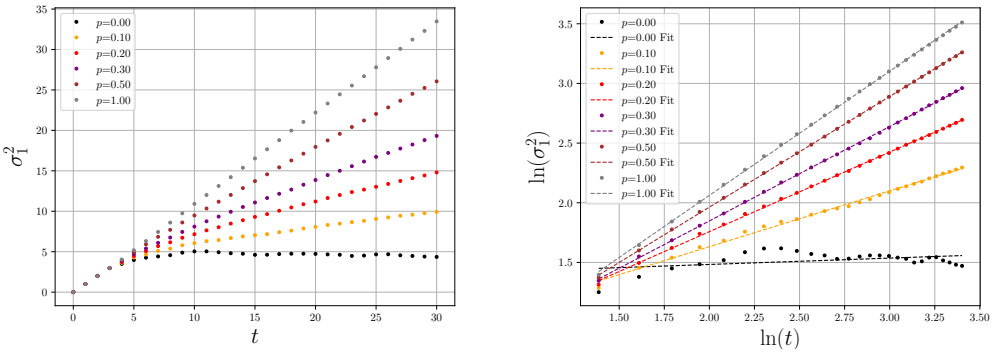

Figure 3.19. Simulated data for a $|0\rangle_c$ input state of the coin. **Left**: variance of the average probability distribution vs the number of step for different values of the parameter p. For each value of the disorder, 10000 phase maps have been simulated and the value of the variance over the average probability distribution has been calculated (dots). **Right**: linearized data (dots) and relation (3.2) fitted to them (dashed curve).

Simulated data for an input state $|0\rangle \otimes |0\rangle_c$ are reported in Fig. 3.19. In the left image, data on a linear scale are reported. For all the values of p under study it is clear that the spread is less then diffusive, condition which is reached only in the case of $p = 1.00$. Black dots correspond to the case $p = 0.00$, which reproduces the Anderson localization effect. As said, the expected behaviour of the variance is

p	α	β
0.00	3.562	0.097
0.10	1.879	0.504
0.20	1.440	0.686
0.30	1.376	0.776
0.50	1.232	0.894
1.00	0.967	1.043

Table 3.6. *α and β values obtained by fitting relation* (3.2) *to the simulated data when the initial coin state is* $|0\rangle_c$.

$$\sigma_1^2(t) = \alpha t^\beta \tag{3.9}$$

with $\beta < 1$ which can be linearized as

$$\ln(\sigma_1^2(t)) = \alpha' + \beta \ln(t). \tag{3.10}$$

In the right image of Fig. 3.19, the same simulated data in a log-log scale are reported. The image clearly shows that, for each value of p, data are very well described by a linear dependence of $\ln(\sigma_1^2)$ from $\ln(t)$. Dashed lines correspond to relation (3.10) fitted to simulated data starting from step 4. This choice finds its motivation in the fact that the walker needs some step of the evolution before starting to behave subdiffusively. This is in fact confirmed by the case $p = 0.00$, in which the walker reaches a constant trend in the variance, as expected when Anderson localization holds, only from step $\sim 4, 5$. For this reason, relation (3.10) has been fitted to data starting from step 4. Fit parameters are reported in Tab. 3.6.

Distribution analysis

As described in the previous section, one can analyse the subdiffusive evolution of the walker also by looking at the spatial probability distribution, which should follow Eq. (3.6). In Fig. 3.20 we report the probability distribution at step 20 for different values of the disorder p. For the sake of clarity we report the behaviours in multiple images. In the top-left image of Fig. 3.20 we report the simulated data for step 20 for values of the disorder $p = 0.00, 0.20, 0.50$, while in the top-right image we report data for $p = 0.10, 0.30, 1.00$.

The exponential localization is extremely clear in the case of $p = 0.00$, while the spread increases when the disorder increases. In the limit case $p = 1.00$, a gaussian shaped function is obtained. As in the case of the variance, it is convenient to work with a modified version of (3.6). As first thing, we rewrite it in more suitable form for analysis such that it depends on two parameters

$$P(x) = \frac{\sqrt{\Gamma(3/b)\Gamma(1/b)} \cdot b}{\sigma \Gamma(1/b)} e^{-\left| \frac{\sqrt{\Gamma(3/b)\Gamma(1/b)} \cdot x}{\sigma} \right|^b}$$

where two parameters have to be found, namely b, and σ. By computing the logarithm of both sides of the equation we get

$$\ln(P(x)) = \ln\left(\frac{\sqrt{\Gamma(3/b)\Gamma(1/b)} \cdot b}{\sigma \Gamma(1/b)} \right) - \left| \frac{\sqrt{\Gamma(3/b)\Gamma(1/b)} \cdot x}{\sigma} \right|^b \tag{3.11}$$

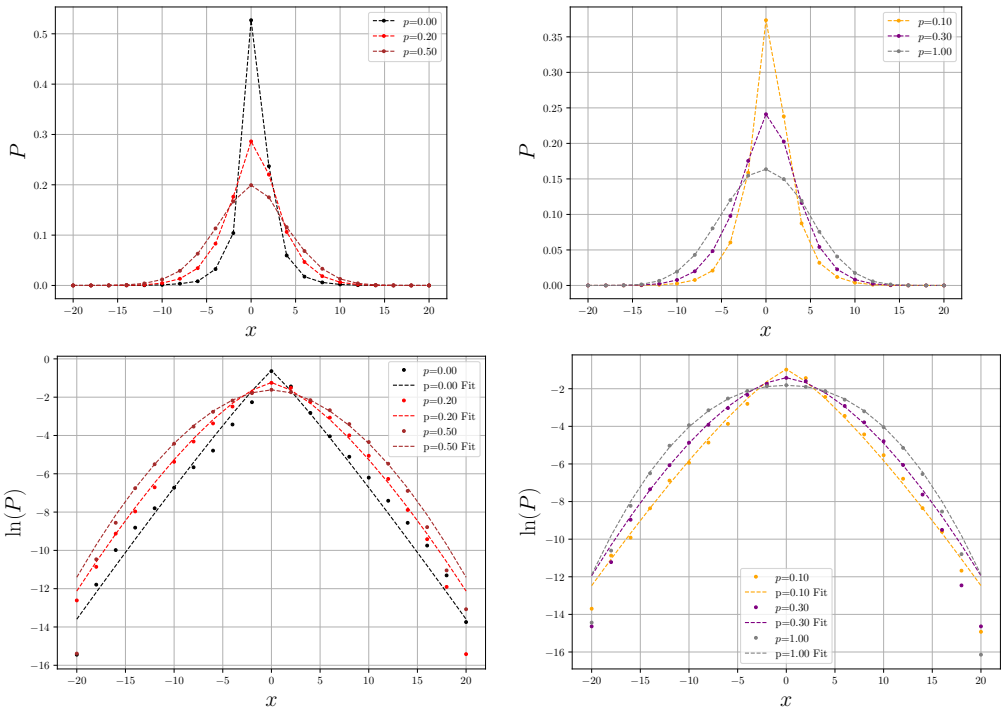

Figure 3.20. Top: simulated probability distributions in a linear scale. **Bottom**: same quantities in a log scale. **Left**: simulated data corresponding to $p = 0.00, 0.20, 0.50$. **Right**: same for $p = 0.10, 0.30, 1.00$.

We are interested in the value of parameter b, which gives the functional form of the distribution. From expression (3.11) we can see that, in the case of $b = 2$, a quadratic dependence from the space variable x is expected, which corresponds to a gaussian shape typical of diffusive phenomena. On the contrary, when $b = 1$, a linear dependence of P from x is expected, which characterizes an exponentially localized distribution. From the images we can follow the transition of the spatial probability distribution from an exponentially localized one to a diffusive one, passing through an intermediate regime.

p	b
0.00	0.800
0.10	1.126
0.20	1.378
0.30	1.568
0.50	1.863
1.00	2.138

Table 3.7. Values of the exponent b obtained by fitting relation (3.11) to the simulated data.

Bottom left and right images of Fig. 3.20 show the same simulated data in a x-log scale. From them one can appreciate the change in the bending of the probability distribution. Fit parameters are reported in Tab. 3.7. The values of $1 < b < 2$ for disorder values $p \neq 0.00, 1.00$ univoquely witnesses a subdiffusive spread of the

walker.

A comment about the long time evolution

As already stated in the superdiffusion section 3.1, the non linear dependence of the variance vs time only holds for a finite evolution time. Indeed, if one performs simulations for an higher number of steps, it is easy to see that the sublinear behaviour eventually ceases to hold and a linear regime is retrieved. This is clearly shown in Fig. 3.21, in which simulations up to 100 step for 10000 different coin maps for the values of p under investigation are reported.

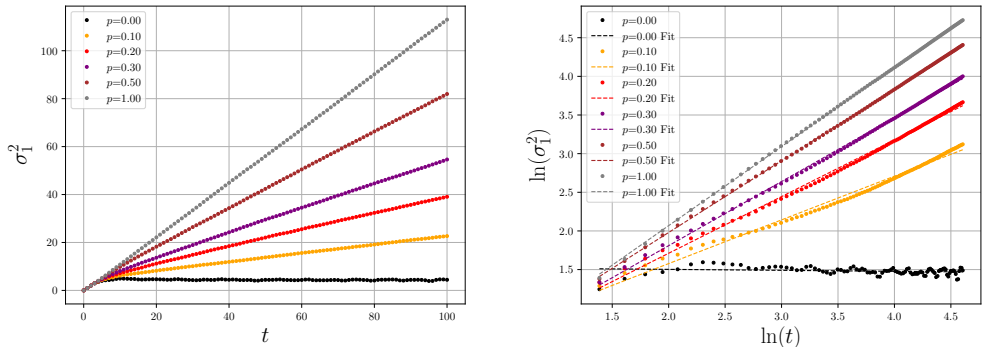

Figure 3.21. Left: linear scale behaviour of the variance up to 100 steps. **Right**: same data in a double logarithmic scale.

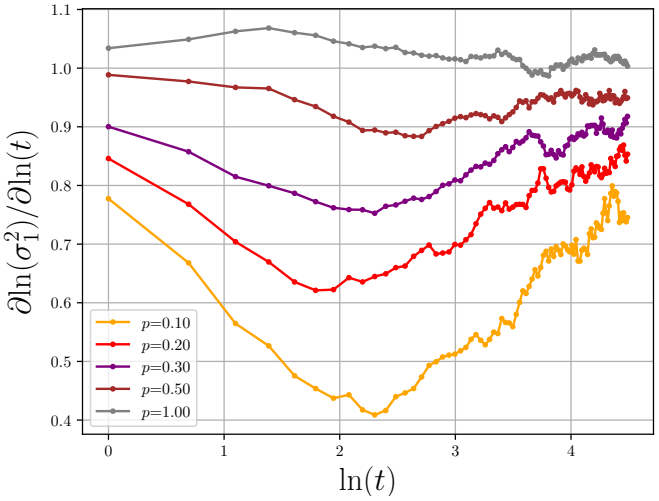

Figure 3.22. Time behaviour of the exponent β for different values of the disorder.

It is clear that the higher the step the more diffusive (i.e. linear) the evolution is. Indeed, in the log-log scale graph, the simulated data do not perfectly follow a linear behaviour. Nevertheless, a more accurate analysis, relying on the numeric derivative $\frac{\partial log(\sigma_1^2)}{\partial log(t)}$, allows us to study further details of the dynamics. We compute the numeric derivative by considering intervals of 10 time steps to mitigate the step

to step statistical oscillations due to the finite number of coin maps; in particular, the quantity $\frac{log(\sigma_1^2(t+10))-log(\sigma^2(t))}{log(t+10)-log(t)}$ has been computed and plotted as function of the logarithm of the evolution step t (see Fig. 3.22,) The temporal behaviour of the anomalous exponent β, for each value p of the disorder, decreases up to step ~ 10, then increases. On one hand, from the graph it is clear that, for an infinite evolution time, a unit value is reached; on the other hand, for a given finite evolution time T it is possible to find a value of p for which the walker never spreads diffusively, i.e. with $\beta = 1$. This means that, even a very small amount of disorder is actually relevant when considering the long term evolution of a quantum walker. In this perspective, our results, despite confined in a finite time evolution, could be useful for a deeper comprehension of the dynamic of a particle subjected to a disordered QW dynamics also for a longer evolution time.

3.2.4 Experimental results - Single walker

As showed in the simulations section, a clear subdiffusive regime can be achieved by varying the level of the dynamic disorder in the QW network. The theoretical approach described in section 3.2.2 holds when the continuous limit applies to the probability distribution. For this reason, in theory, for a sufficiently large number of steps, our measured data for a discrete time QW should approach the continuous model of subdiffusion.
We experimentally implemented 400 coin maps for each disorder scenario under study,

$$p \in \{0.00, 0.10, 0.20, 0.30, 0.50, 1.00\}, \tag{3.12}$$

and the average probability distribution has been measured for step numbers

$$t \in \{5, 8, 11, 14, 17, 20\}.$$

For each of the resulting 2 400 coin maps, a different statically disordered coin configuration was created, which was then perturbed according to the chosen level p of disorder. The random choice of the starting static disorder assures that the final results are not biased by a particular static configuration but only depend on the disorder level p.
Our measured data allows us to analyse both the temporal evolution of σ_1^2, for which it is expected to obtain $0 < \beta < 1$, and the spatial probability distribution P, characterized by an exponential behavior with $1 < b < 2$. Let us begin with the former and then proceed with the latter.

Variance analysis

To clearly show the subdiffusive spread with our data, we fitted relation (3.10) to experimental values of the variance of the probability distribution.

Results are reported in Fig. 3.23 in both linear and double logarithmic scales. Dashed lines correspond to the curve in Eq. (3.10) which is fitted to the experimental data (dots) for different values of the disorder p. The nearly perfect linear behaviour with slopes $0 \lesssim \beta \lesssim 1$ (see Table 3.8 for numerical values) confirms the actual subdiffusive spread of the QW evolution. A discrepancy between the data and the fit can be observed for $p = 0.00$ because of the extreme sensitivity of Anderson localization with respect to unavoidable experimental imperfections. Here, one would also expect a constant variance, which, however, is only approached in the limit $t \to \infty$, even in theory. Error bars on the experimental data have been computed

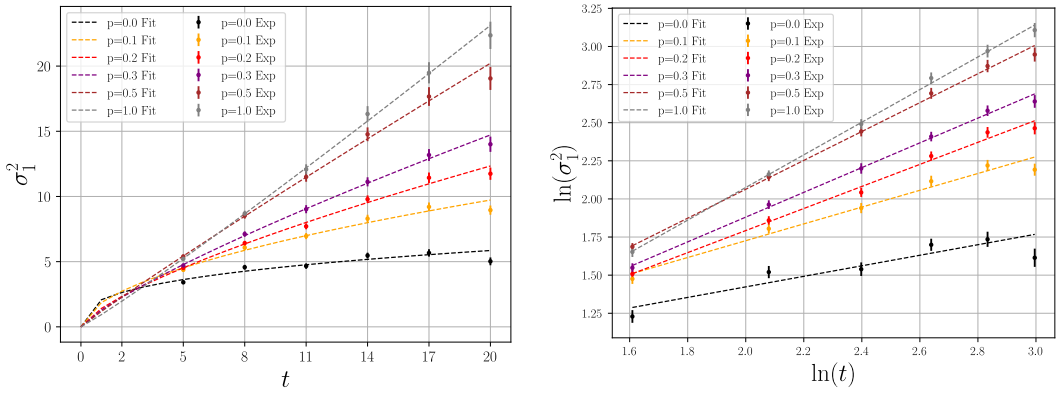

Figure 3.23. Right: Experimental data (dots) of the variance as a function of the step number t in a double logarithmic scale for disorder values p in Eq. (3.12). Dashed lines correspond to relation (3.10). The linear behaviour with slopes between zero and one in this doubly logarithmic graph for each value of p demonstrates an excellent agreement with the predicted subdiffusive nature of the evolution. **Left**: same experimental data on a linear scale. Dots correspond to experimental data; dashed lines show the behaviour according to Eq. (3.9) with parameters computed from the fit on a double logarithmic scale.

p	β_{num}	β_{exp}
0.00	0.097	0.346 ± 0.040
0.10	0.504	0.551 ± 0.030
0.20	0.686	0.723 ± 0.032
0.30	0.776	0.812 ± 0.028
0.50	0.894	0.947 ± 0.027
1.00	1.043	1.070 ± 0.032

Table 3.8. Values of the temporal exponent $\beta = 2d$ for the implemented values of disorder. The values have been estimated by means of a least square fit to theoretical predictions. Quantities with the subscript "*num*" have been extracted from our numerical model, considering 10 000 coin maps. The subscript "*exp*" indicates quantities obtained from our data, realizing 400 coin maps.

considering a Poissonian statistic of counting as well as experimental imperfections of the setup.

Distribution analysis

For a fixed step number t, and for $p = 0.00$, an exponentially localized distribution is expected, corresponding to Anderson localization. With increasing disorder level p, we expect a broadening of the distribution. Eventually, for $p = 1.00$, a Gaussian shape should be obtained, typical for the diffusive behaviour.

Experimental probability distributions as a function of x and t are reported in Fig. 3.24 for all selected p values. Because of the fact that the greater part of the probability distributions is localized around the central position, for the sake of clarity, images show only positions $-11 < x < 11$ for all selected time steps t. For a enhanced data visualization, each row is normalized to the maximum of the corresponding probability distribution. From the image it is clear that the spread of the distribution increases with p, starting from a condition in which the walker remains strongly localized for all the steps of the evolution ($p = 0.00$) up to the

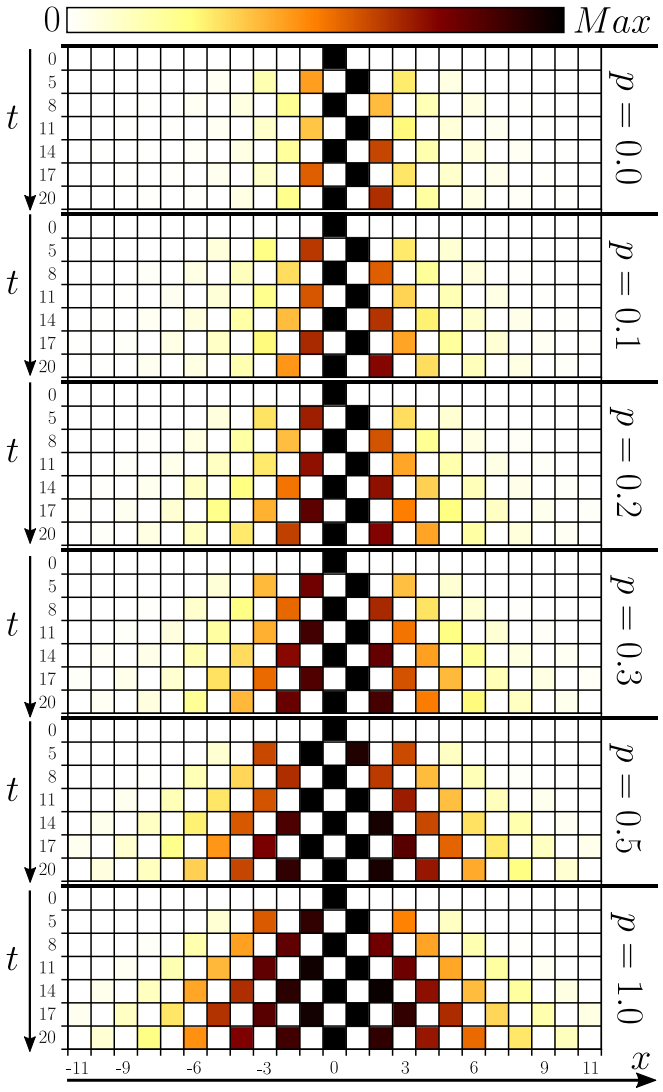

Figure 3.24. Experimentally measured normalized intensity distributions $P(x,t)$. Each panel corresponds to one parameter p, increasing from top to bottom. Data are reported for $x \in [-11, 11]$ (horizontal axis) and for several selected times $t \in [5, 20]$ (vertical axis).

behaviour typical of a completely disordered QW ($p = 1.00$).

In order to witness the subdiffusive spread of the walker, the parameters that best describe the measured probability distribution have to be found. To this aim we fit relation (3.11) to experimental data, focusing on the last step of the evolution, i.e. $t = 20$. Experimental data for different amounts of disorder are reported in Fig. 3.25. In the left plot, dots correspond to experimentally obtained probability distributions. Dotted lines represent values of the theoretical probability distribution expected considering the 400 coin maps experimentally implemented, obtained from a numerical simulations. Similarities between experimental and theoretical probability distributions for each step and p values are above 99%, indicating a very good agreement even without considering many unavoidable experimental imperfections in our simulations. The right panel of Fig. 3.25 is more conclusive when it comes to determining the characteristic exponent b. The plot shows the same experimental

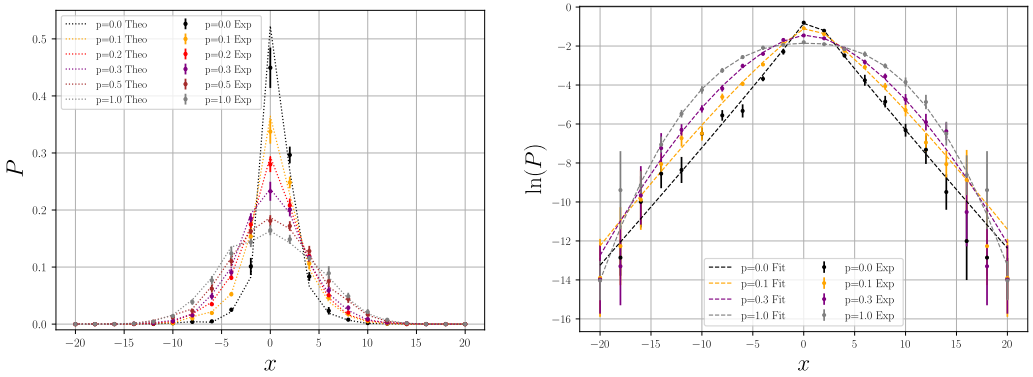

Figure 3.25. **Left**: Probability distribution P for various values p of the disorder, Eq. (3.12). Experimental data (dots) agree within the uncertainties with the theoretical simulated results (dotted lines). Error bars take into account Poissonian statistics and experimental imperfections of the setup. **Right**: Logarithm of the experimental probability distribution (dots) together with Eq. (3.11) fitted to them (dashed lines) according to . For the sake of clarity, only selected p values are depicted.

p	b_{num}	b_{exp}
0.0	0.800	0.953 ± 0.044
0.1	1.126	1.199 ± 0.048
0.2	1.378	1.489 ± 0.046
0.3	1.568	1.639 ± 0.066
0.5	1.863	2.071 ± 0.077
1.0	2.138	2.422 ± 0.083

Table 3.9. Values of the spatial exponent b for the implemented values of disorder. The values have been estimated by means of a least square fit to theoretical predictions. Quantities with the subscript "*num*" have been extracted from our numerical model, considering 10 000 coin maps. The subscript "*exp*" indicates quantities obtained from our data, realizing 400 coin maps.

data as the left image in a log scale. Experimental data (dots) along with the fitted curves (dashed lines) according to Eq. (3.11) are shown, covering the range from a linear ($b \approx 1$) to a parabolic ($b \approx 2$) decay in this logarithmic depiction. It is clear from the graph that, by increasing the value of disorder p, the probability to find the walker in the starting site 0 decrease. Consequently, the probability to find it in more distant positions increases, resulting in a broadened distribution. This effect arises due to the breaking of the staticity of the disorder. The subdiffusivity of the evolution of the walker is confirmed by the values of the parameter b, reported in Table 3.9.

Full space-time-coin analysis

Our actual setup allows one to study the polarization-resolved evolution of the walker, without limiting to the analysis of the site-resolved distribution. Such a potentiality allows one to follow the average behaviour of the particle by decoupling the two coin states. In Fig. 3.26 measurements corresponding to the evolution of the $|0\rangle = |H\rangle$ (center) and $|1\rangle = |V\rangle$ (right) coin states are reported . The left plot shows the total space-time-dependent characterization of the QW after tracing over the coin degree of freedom, as already reported in Fig. 3.24. Each column

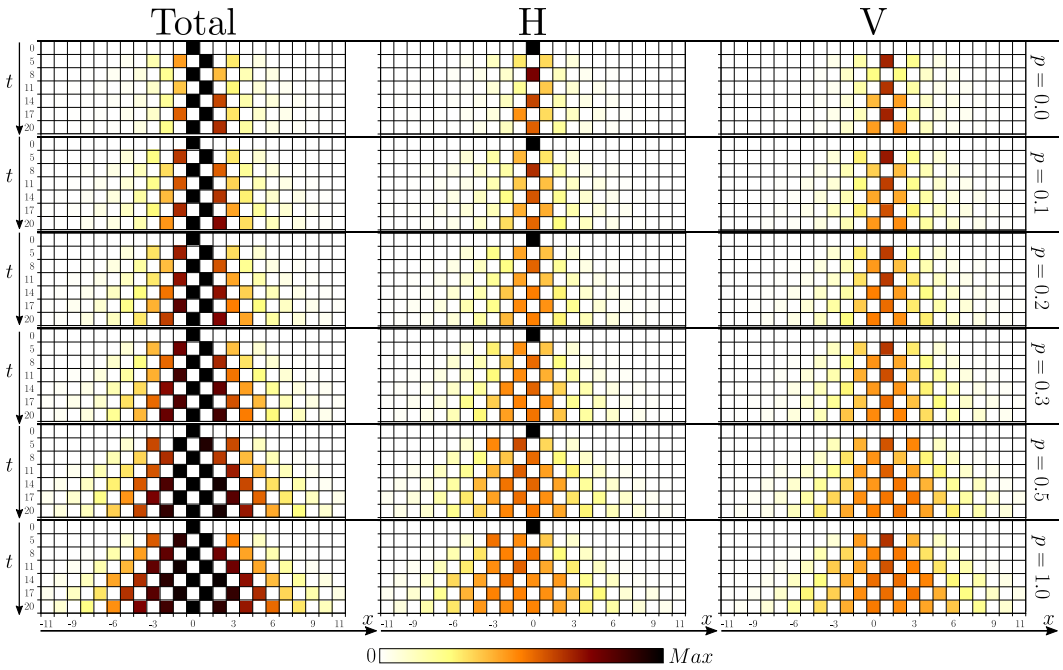

Figure 3.26. Time evolution of the walkers position-dependent distribution by independently considering the two coin states, for all disorder values p under investigation [see eq.(3.12)). **Left**: overall space-time behavior after tracing over the coin degree of freedom. **Center**: time evolution corresponding to the coin state $|0\rangle$. **Right**: same for $|1\rangle$ state. For an enhanced visualization, each row of the total distribution is normalized to its maximum while each row of the H and V plots are normalized to the maximum of the corresponding row of the left plot.

represents the time behaviour of the probability distribution as a function of the site (from site -11 to $+11$) for different values p of the disorder. At step $t = 0$, the coin state has 0 probability to be found in the $|1\rangle_c$ state. Indeed, the walker is initially furnished with $|0\rangle_c$ coin state. It is worth noting that the distribution for $|0\rangle$ is centered in site -1. On the contrary, the one for $|1\rangle$ is centered in site $+1$. This is due to the effect of the step operator $\hat{S}$, which shifts the walker with coin $|0\rangle$ and $|1\rangle$ to the left and right, respectively, thus steering the coin distribution towards different sites of the line. A compensation of the effect is obtained when tracing over the polarization degree of freedom. A under diffusive spread for both coin states is observed, with very similar characteristics with respect to the one obtained when tracing over the coin degree of freedom. Indeed, Anderson-like localization is retrieved in the case of $p = 0.0$, while a diffusive (i.e. a Gaussian distribution) spread is obtained in the case of complete disorder. For all values of $p < 1.0$, a more confined spread with respect to $p = 1.0$ is obtained. Thus, in addition to the usual and relevant characterization of spatial and temporal features of various QWs, we can also investigate the coin-dependent transient behavior with our setup. In this particular case, such a fine-grained analysis resembles the overall properties of the system but, however, in other scenarios, this additional degree of resolution can be a helpful asset to separate the distinct caracteristics of the system when conditioned to a given coin state.

Comments over experimental results

As presented in sec. 3.2.3, we performed simulations of the evolutions aimed to compare our experimental results with expected ones. We implemented a numerical simulation that produces 10 000 different coin maps for a given level p of disorder. Recall, a coin map is a set of coin configurations which are obtained by starting from static disorder $\hat{C}(x)$ and randomly changing a percentage p of coins. Thus, the distribution that is obtained by averaging over all numerically implemented coin maps, models our experiment. However, theoretical values have been computed in the completely ideal case, i.e., without considering unavoidable setup imperfections. Despite this, this approach was already sufficient to match the results of the experiment sufficiently well.
In addition to the space-time dependent depiction of our data in Fig. 3.24, the comparison between relevant values obtained experimentally and numerically are given in Tabs. 3.9 and 3.8. These values follow the expected trend: the higher the disorder, the higher the exponential decay in space and temporal dispersion, quantified by b and β, respectively. In particular, the reported values confirm that we mostly operate in the subdiffusive regime of the QW, $1 \leq b \leq 2$ and $0 \leq \beta \leq 1$. Small discrepancies can be observed between theoretical predictions and experimental values. These can be caused by imperfect randomization since the former parameters have been extracted by averaging the probability distributions over 10 000 coin maps while only 400 have been implemented in the latter case. Nevertheless, estimates for parameters from numerics and data mostly agree with each other within the confidence interval.
One can see that experimental values of both β and b are higher than the respective simulated values. This can be generally explained by considering experimental imperfections, such as a nonideal operation of the EOMs as well as the QWP, less than 100% visibility of interference, and slight setup misalignment, all of which contribute to increase the spread of the walker. The highest discrepancies to the theory can be observed for the extremal cases of disorder, $p = 0.00$ and $p = 1.00$, affecting both numerics and experiment. On one hand, for $p = 0.00$, the discrepancy can be understood by considering that Anderson localization arises from a strict periodicity in the disorder pattern. Because of this, it is much more sensitive to small imperfections compared to other disorder values, resulting in an higher deviation from the theory. Moreover, a nonspreading regime is only feasible for $t \to \infty$. Secondly, the discrepancy for $p \to 1.00$ amplifies some of the effects previously mentioned even further. For instance, p-diluted models describe a convolution of the initial (Anderson-like) behavior with another distribution for dynamic disorder, causing imperfections of all initial realizations to add up. Also, imperfections propagate along with the spreading of the walker over time.
Within this work, we analyzed both the spatial and temporal impact of the amount of disorder p, which is beyond earlier experimental studies on this fields. With our results, we can confirm that our approach enables us to simulate almost any subdiffusive behavior. Thus, the sublinear spread of the walker over time and the characteristic shapes of the measured spatial distributions indicates that the interplay between a static disorder and completely random disorder, freely controlled and interpolated via p, is a viable way to reproduce complex subdiffusion phenomena through discrete QWs.

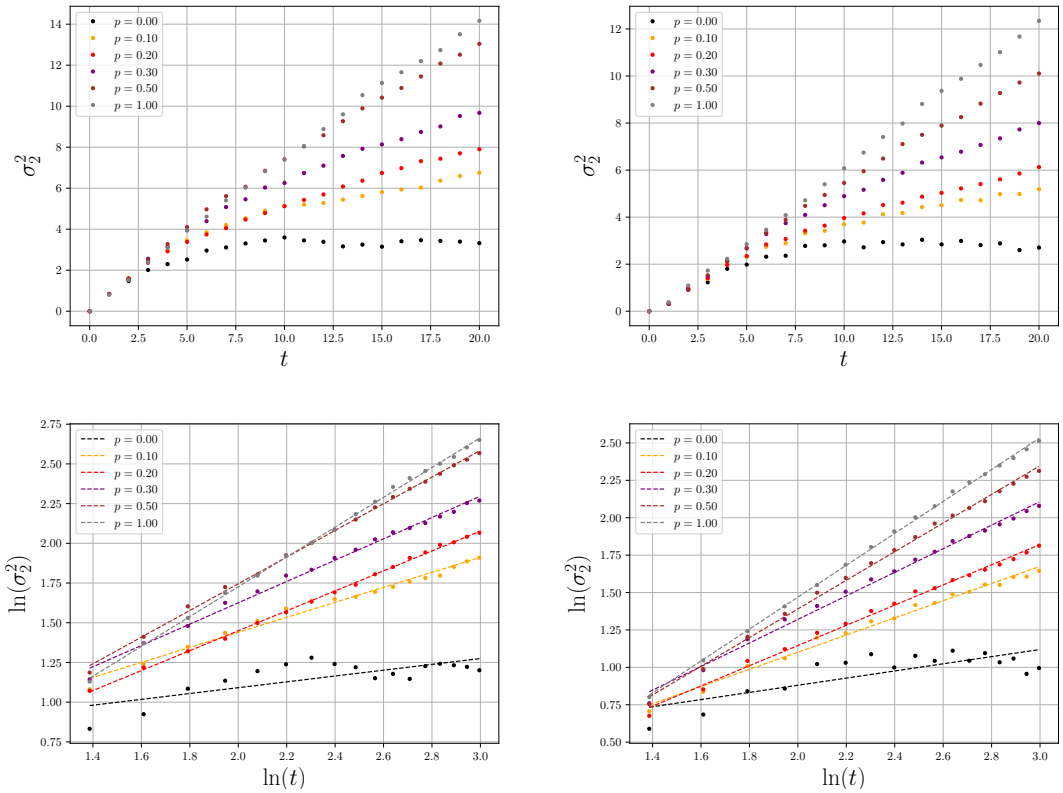

Figure 3.27. Variance behaviour in the two walker case. **Top**: simulated data represented on a linear scale. **Bottom**: same data in a log-log scale. **Left**: data corresponding to indistiguishable photons. **Right**: data corresponding to distininguishable photons.

3.2.5 Simulations - Two walkers

As in the superdiffusive case, which was investigated from point of views of both one- and two-walker, one can ask whether also subdiffusion still holds in the two photon case. To this aim, we applied the same p-diluted model to the evolution of two photon, for both distinguishable and indistinguishable cases. Due to the fact that the time needed for simulations increases exponentially with the number of the photons inside the QW, for each value of disorder we numerically implemented 400 coin maps instead of 10000 as in the single walker case. By computing the average probability distribution and then its variance as a function of the step, we obtained a clear subdiffusive behaviour. Results are shown in the top images of Fig. 3.27, in which we report the variance behaviour of the mean position as a function of the step number t for $p = 0.00, 0.10, 0.20, 0.30, 0.50, 1.00$.

From linear scale plots it is clear that the spread of the walkers for all p values is less with respect to the limit case $p = 1.00$, which is a clear sign of a less then diffusive spread. In the bottom figures, same data in a double logarithmic scale are reported. A nearly perfect linear behaviour for all values of p under investigation witnessess the presence of subdiffusivity during the evolution. To analyse the subdiffusive spread, we fitted relation (3.10) to the data. Results are reported in Tab. 3.10. As one can see from the numerical values of β, a subdiffusive spread can be reproduced in both cases of distinguishable and indistinguishable photons. To obtain an higher precision

p	β_{ind}	β_{dist}
0.00	0.18359	0.23908
0.10	0.47227	0.57356
0.20	0.62744	0.67503
0.30	0.67102	0.78768
0.50	0.83995	0.95710
1.00	0.93850	1.06609

Table 3.10. β values obtained by fitting relation (3.2) to the simulated data when the initial coin state in both cases of indistinguishable and distinguishable photon cases.

on the values of the diffusion coefficient we are currently running simulations with a higher number of steps and coin maps. We are also currently working on the experimental realization of the two photon evolution to reproduce such a behaviours in a real QW network.

3.2.6 Conclusions

In this chapter we have demonstrated the ability to experimentally simulate subdiffusive transport phenomena, having a wide range of applications, via disordered QWs. By analyzing our data regarding the spatial and temporal features of the evolution, we have been able to map the landscape of characteristic properties of subdiffusion. Firstly, we controlled our system such that it leads to position distributions of the walker ranging from Anderson localization to a normal Gaussian distribution, passing through an intermediate regime. Secondly, anomalous diffusion in the sublinear regime was explored to characterize the spread of the walker over time. This complements earlier findings that have been restricted to superdiffusion, in which a starting starting ordered QW was perturbed by means of the p-diluted model. Because of our unique control over the coin operator at each position (time bin) and for each step of the QW, the demanding goal of realizing subdiffusion was achieved with our setup. By starting from an initial statically disorderd QW, which is at the base of the realization of the Anderson localizaion effect, we perturbed it by realizing a p-diluted QW. We added dynamic noise in a controlled manner to steer our system towards the subdiffusive regime. Specifically, this method introduces additional fluctuations, with probabilities p and $1-p$ for the static and the dynamic disorder contributions, respectively. The very good agreement between the measured data and the theoretical predictions for both the quantities under study, namely the shape of the position distribution and the change of the variance in time, clearly demonstrates that the evolution of the coherent walker is featured by a subdiffusive spread.
Pursuing the ultimate goal of implementing a universal quantum simulator and exceeding our proof-of-concept realization reported here, our results provide a promising starting point for future studies as well. Furthermore, we are currently working on the implementation of two photon QW, in both cases of distinguishable and indistinguishable photon cases, which is an achievable task with the present split time QW [117]. This could further foster other simulations of sophisticated correlated diffusion phenomena. For instance, it is known that Anderson localization holds in the case of entangled photons [66], but more extended study on exotic states can be performed. However, the general impact of correlated (p_1, p_2)-diluted dynamical noise for the walkers 1 and 2 is entirely unknown but could potentially be studied in our system.

3.3 Quantum metrology approach to anomalous diffusion

The high number of studies about transport features in a QW, as far as we know, is not properly balanced by the same amount of investigations in a quantum metrology fashion. The idea behind the following part of the thesis is to infer how much information about the features of the QW network can be extracted from the characteristics of the quantum walker evolution. In order to do that, tools from quantum metrology will be used, first of all the quantum Fisher information (QFI), which quantifies the extractable information about an unknown parameter, such as a phase ϕ. As it will be explained in the following section, QFI is also linked to the measurement accuracy of the estimation strategy. We will exploit quantum Fisher information to describe the different transport regimes of information due to the properties of the quantum network. We found that the disorder pattern plays a significant role in the spreading behaviour of quantum information. The growth trend of QFI allows one to characterize the anomalous and normal spreading pattern, as well as Anderson localization of the walker.

3.3.1 Fundamentals of quantum metrology

In this section we will provide some basic notions about Quantum Metrology (QM), without the aim of completeness. For a complete review of the field and the description of the state of the art from both a theoretical and experimental point of view see [118].
Metrology is one of the most important task in physical science. The ability to precisely measure a physical quantity is of fundamental relevance, for instance in order to precisely test predictions of a theory. Along with the measurement of a quantity, an uncertainty has to be provided, summarizing both the technical and fundamental errors. The first type of error mostly consists in accidental errors, due to imperfect control in the measurement process. The second type of error is of a different nature: they are imposed by physical laws. Quantum mechanics is useful in this sense, as nowadays it provides a limit over the maximum achievable precision in the estimation of a physical quantity.
Aim of metrology is to measure an unknown physical parameter ϕ, characterizing a physical system, by means of an interaction between a probe and the system itself, after which the information is encoded in the probe state. The general scheme of a measurement process can then be outlined as

- preparation of a probe $\hat{\rho}_0$ sensitive to variations of the parameter ϕ;
- interaction between the probe and the system through the evolution $\hat{U}_\phi$ as $\hat{\rho}_\phi = \hat{U}_\phi \hat{\rho}_0 \hat{U}_\phi^\dagger$;
- extraction of the information by means of suitable operators acting on the probe;
- application of a suitable estimator which provides an estimation $\Phi(x)$ of the unknown parameter ϕ based on the measurement result x.

Such a protocol has to be repeated ν times in order to obtain a more and more precise estimation of the value of ϕ. An estimator Φ can have different properties. It is called consistent when it asymptotically converges to the real value of the parameter. It is called unbiased if its mean value corresponds to the unknown parameter, i.e.

$$\bar{\Phi} = \sum_x P(x|\phi)\Phi(x) = \phi$$

where $P(x|\phi)$ is the output probability of obtaining a certain measurement result x, conditioned to a certain value of the parameter ϕ.
The quantification of the accuracy of the measurement is usually given in terms of the mean square error (MSE), defined as

$$\mathrm{MSE}(\phi) = \sum_x (\Phi(x) - \phi)^2 P(x|\phi)$$

which, for an unbiased estimator, gives us an estimate of the variance of the parameter

$$\Delta\phi^2 = \sum_x (\Phi(x) - \bar{\Phi})^2 P(x|\phi).$$

The measurement protocol can be optimized by different points of view, in order to increase the precision in the parameter estimation: one can optimize the choice of the estimator, the measurements performed over the probe and the probe state itself. Suppose the probe state and the measurement performed over it are fixed and that an optimization over the estimator is performed. We can define a quantity called Fisher information (FI) as

$$F(\phi) = \sum_x P(x|\phi) \left(\frac{\partial \log(P(x|\phi))}{\partial \phi} \right)^2 = \sum_x \frac{1}{P(x|\phi)} \left(\frac{\partial P(x|\phi)}{\partial \phi} \right)^2$$

which quantifies the amount of information encoded in the output probabilities of the estimation protocol. By introducing the symmetric logarithm derivative (SLD) $\hat{L}_\phi$ defined by the relation

$$F(\phi) = \frac{\partial \hat{\rho}_\phi}{\partial \phi} = \frac{\hat{\rho}_\phi \hat{L}_\phi + \hat{L}_\phi \hat{\rho}_\phi}{2}$$

we can rewrite the FI as

$$F(\phi) = \sum_x \frac{\mathrm{Re}[\mathrm{Tr}[\hat{\rho}_\phi \hat{E}_x \hat{L}_\phi]]}{\mathrm{Tr}[\hat{\rho}_\phi \hat{E}_x]}$$

where $\hat{E}_x$ are the chosen measurements.
The sensitiveness of $F(\phi)$ to variations of the parameter ϕ is based on the dependence of $F(\phi)$ on the derivative with respect to ϕ. To formalize such dependence, the Cramer Rao bound (CRB) is introduced, which links F to the ultimate bound on precision achievable by the variance of any estimator, with fixed probes and measurements

$$\Delta\Phi^2 = \sum_x (\Phi(x) - \bar{\Phi})^2 P(x|\phi) \geq \frac{\partial \bar{\Phi}/\partial \phi}{\nu F(\phi)}$$

which, in the case of local unbiased estimator ($\partial\bar{\Phi}/\partial\phi = 1$) becomes

$$\Delta\phi^2 \geq \frac{1}{\nu F(\phi)}.$$

Such limit, which we recall has been found after an optimization over the estimator, can be overcame by maximizing the Fisher information over the possible measurements performed on the probe after the interaction with the system. In fact, the quantum Fisher information (QFI) is defined as the maximum value of the Fisher information over the possible measurements $\hat{E}_x$ which can be performed on the probe

$$F_Q(\phi) = max_{\{\hat{E}_x\}} F(\phi).$$

By definition it holds $F_Q(\hat{\rho}_\phi) \geq F(\phi)$ and the CRB can be extended to the quantum CRB. The bound over the maximum achievable precision then becomes

$$\Delta\phi^2 \geq \frac{1}{\nu F(\phi)} \geq \frac{1}{\nu F_Q(\phi)}.$$

The right hand side of this equation represents the ultimate limit on the achievable precision value regardless of the measurement, while it still depends on the particular choice of the probe state $\hat{\rho}_\phi$.
It can be shown that the QFI is related to the symmetric logarithmic derivative $\hat{L}_\phi$ by the following relation

$$F_Q(\phi) = Tr[\hat{\rho}_\phi \hat{L}_\phi^2].$$

The ultimate fundamental bound of the maximum achievable precision can be obtained by maximizing the QFI over all the possible input states which, up to now, have been kept fixed. By considering m independent and at most classically correlated states, we obtain the so called standard quantum limit:

$$\Delta\phi \geq \frac{1}{\sqrt{\nu m F_Q^{\max}}}$$

where $F_Q^{\max}$ is the maximum F_Q over the m states. By inserting quantum correlations in the input states, such as entanglement, this limit can be overcame and the Heisenberg limit can be reached, which corresponds to a linear inverse dependence of $\Delta\phi$ on m, i.e. $\Delta\phi \propto \frac{1}{m}$.

3.3.2 Theoretical proposal

We aim at designing a quantum probing protocol to investigate the spreading behavior of the information in a QW framework, by studying the extractable information that the quantum walker can assess, examining the problem by quantum estimation strategy.
The main aim of quantum estimation strategy is to furnish an estimate on the maximum extractable information about an unknown parameter, which we call ϕ, from repeated measurements on a probe state which interacts with a system. Typically, the unknown parameter ϕ is encoded in a unitary operator. Here, we consider the case in which the parameter ϕ is encoded in the QW process through the unitary operator $\hat{U}(\phi) = \hat{S}(\hat{I} \otimes \hat{C})\hat{P}$, where $\hat{P}(t)$ is a phase-shift operator given by:

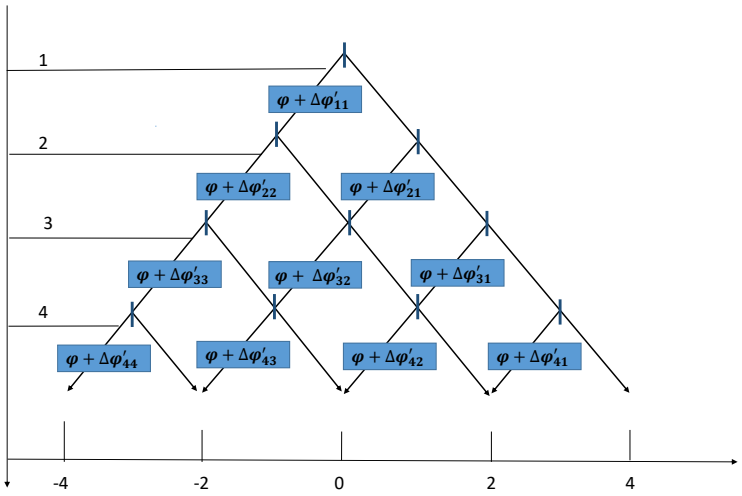

Figure 3.28. Representation of a quantum probing protocol using disordered quantum walk representation.

$$\hat{P}(t) = \sum_x |x\rangle\langle x| \otimes \left(|1\rangle_c \langle 1|_c + e^{i(\phi + \Delta\phi'(t,x))} |0\rangle_c \langle 0|_c \right).$$

As shown in Fig. 3.28, the phase-shift operator $\hat{P}$ is responsible for the presence of a phase difference ϕ between the two coin states $|1\rangle_c$ and $|0\rangle_c$ after each position. However, here we analyse the condition in which the application of ϕ might come with unwanted time-position-dependent fluctuations $\Delta\phi'(t,x)$ that coherently affect the coding process. In this way, the static and dynamic disorder can affect the QW process.
In a quantum metrology scenario, the measurement sensitivity of the parameter is given by the Cramér-Rao inequality $\Delta\phi \geq \Delta\phi_{min} = 1/\sqrt{\nu F_Q(\phi)}$ where $\Delta\phi$ is the mean square error in the measure of parameter ϕ and ν is the number of the measurements [119, 120, 121, 122, 123]. The QFI is given by $F_Q(\phi) = Tr[\hat{L}^2\hat{\rho}]$, where $\hat{\rho}$ is the density operator and $\hat{L}$ is the Symmetric Logarithmic Derivative (SLD) operator satisfying the equation $d\hat{\rho}/d\phi = \{\hat{L}, \hat{\rho}\}/2$ where $\{.,.\}$ denotes the anticommutator. For a pure state it holds $\hat{\rho}^2 = \hat{\rho}$ and the SLD operator reduces to $\hat{L} = 2d\hat{\rho}/d\phi$. One can numerically obtain the QFI using the walker state at step t $|\Psi_t\rangle = \hat{U}(\phi)|\Psi_{t-1}\rangle$, and its derivative with respect to parameter ϕ given by:

$$|\frac{\partial\psi_t}{\partial\phi}\rangle_t = \frac{\partial\hat{U}(\phi)}{\partial\phi}|\psi\rangle_{t-1} + \hat{U}(\phi)|\frac{\partial\psi_{t-1}}{\partial\phi}\rangle.$$

We limit our analysis to the case in which the random fluctuations $\Delta\phi'(t,x)$ can only be 0 or π. Thus, the degree of disorder p is defined as the percentage of random phases that the walker experiences during the evolution. This simply means that a p percentage of the random fluctuation $\Delta\phi'(t,x)$ are selected to have π or 0 value and to be randomly distributed in time and position.
For this particular study, it is useful to slightly modify the way the static disorder is inserted with respect to its original implementation, adopted for instance in the subdiffusion study (see 3.2). Here, instead of starting from a statically disordered QW and perturbing it with the typical p-diluted technique, as done in the previous

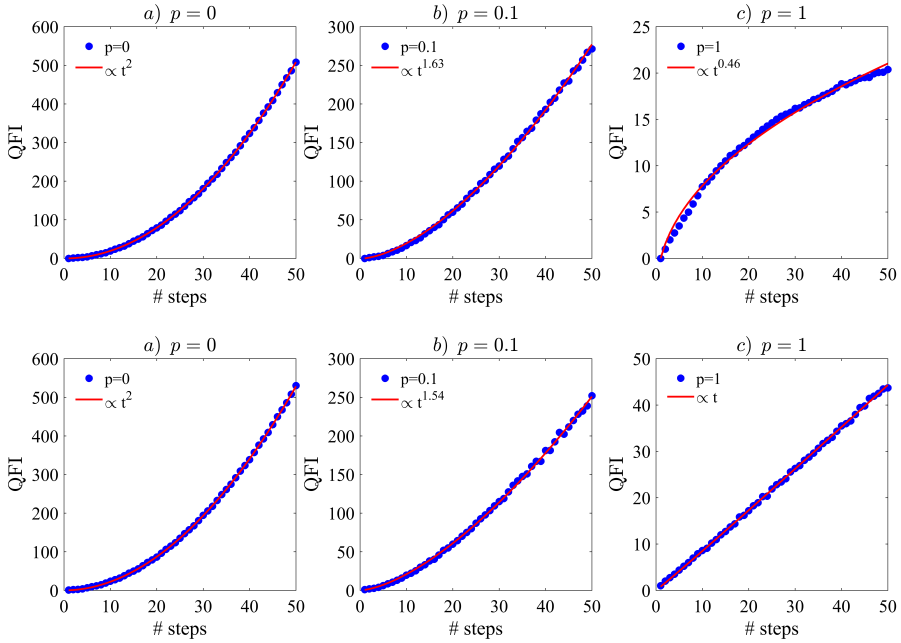

Figure 3.29. Quantum Fisher information: average QFI F_Q of a quantum walker (blue dots) as a function of the number of steps t for different values of disorder. **a)** $p = 0$, **b)** $p = 0.1$ and **c)** $p = 1$ for both static (**top**) and dynamic disorder (**bottom**). For each graph the initial input is $|\psi_0\rangle = |0\rangle_p \otimes |0\rangle$. Red lines correspond to the fitted curve $F \propto t^{\alpha}$

sections, we start from an ordered QW and we perturb it in a static way, according to the given percentage p of disorder. This means that, if the phase acquired by the walker when it travels, for instance, for the first time from site x to $x-1$ is modified by the random fluctuation $\Delta\phi'$, it stays so for each subsequent step. In such a way, when $p = 0$ an ordered QW is obtained while when $p = 1$ a completely statically disordered QW is retrieved. Despite the two different approaches to the the p-diluted technique, also in this case a clear subdiffusive regime is obtained. The main difference between the two approaches consists in the fact that, while in the first one we observe a transition from the Anderson localization to a diffusive regime when increasing the values of p, passing through the subdiffusive spread, in the present case we start from a ballistic behaviour ($p = 0$), we explore the superdiffusive case, the diffusive and the subdiffusive ones up to the Anderson localization ($p = 1$). It is worth noting that, in the case of dynamic disorder, the usual p-diluted technique is implemented.
By iterating over enough random phase samples, it is possible to numerically calculate the QFI in the presence of a given percentage of randomness p.

3.3.3 Results

Let us first focus on the simplest case in which a particle starts the QW in site $x = 0$ with the $|0\rangle_c$ coin state, given by the state $|\psi_0\rangle = |0\rangle \otimes |0\rangle_c$. For both static and dynamic disorder, we simulated the behavior of the average QFI for different values of disorder p. For each of them, the simulation has been performed by averaging over 10000 different phase maps. The average QFI is reported in Fig. 3.29 as a

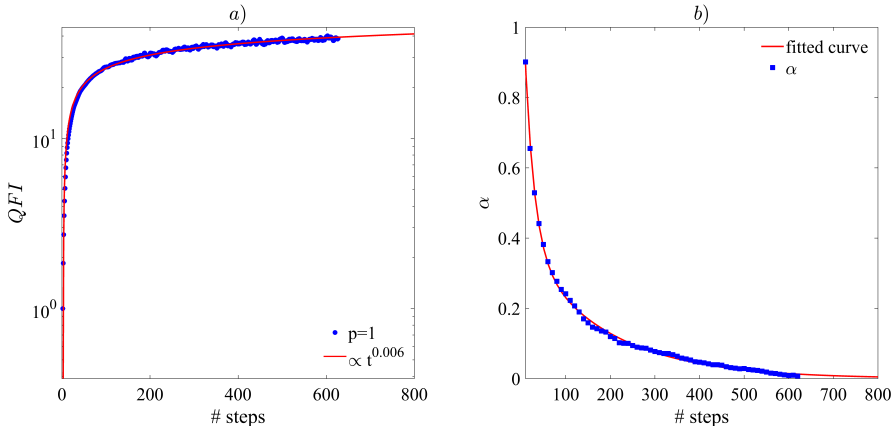

Figure 3.30. **a)** Logarithmic scale of average QFI F_Q of a quantum walker (blue dots) and fitted curve $F \propto t^{\alpha}$ (red line) in terms of number of steps t for complete static disordered, corresponding to $p = 1$. **b)** Step-dependent coefficient $\alpha(t)$ (blue dots) and its fitted curve (red line) in terms of number of steps.

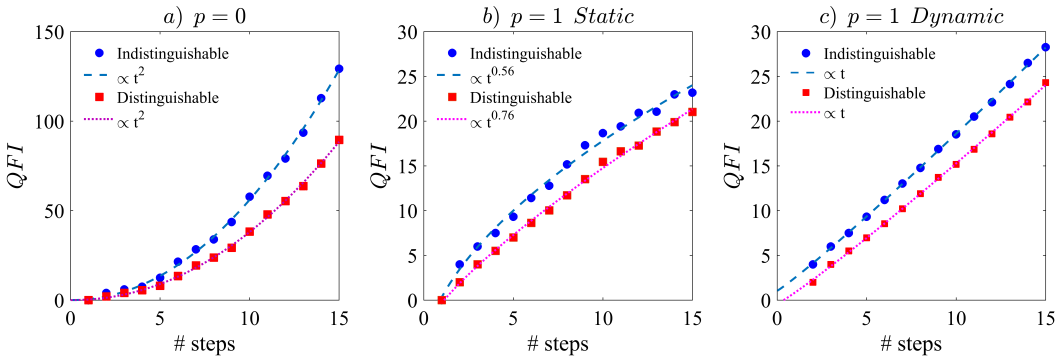

Figure 3.31. Quantum fisher information: average QFI F_Q of a quantum walker as a function of the number of steps t for **a)** the ordered case $p = 0$, **b)** complete static disordered case $p = 1$, and **c)** $p = 1$ complete dynamic disordered case. In all plot, the blue circles and red squares correspond to indistinguishable and distinguishable two-particle inputs respectively.

function of the step number t. By fitting a power law function to the numerical data, we found that the average QFI is $F_Q \propto t^{\alpha}$ where the range of α is $0 \leq \alpha \leq 2$ for the static disorder and $1 \leq \alpha \leq 2$ for the dynamic disorder. Without any disorder ($p = 0$), the QFI of the QW grows quadratically in time $F \propto t^2$, analogously with a ballistic transport pattern, as displayed in Fig. 3.29 a). Also, this means that the phase variance upper-bound is proportional to the inverse of the number of steps, i.e $\Delta\phi \propto t^{-1}$.

In the static disorder case (Fig. 3.29 top), the super-diffusive $\alpha > 1$ to sub-diffusive $\alpha < 1$ transition is achieved by increasing the value of disorder p out of 50 steps. These result show how the information spread along the quantum network can be determined as a result of the disorder strength: the higher the disorder, the lower the extractable information about the unknown parameter ϕ.

In the case of dynamic disorder, we plot the average QFI (Fig. 3.29 bottom). Here, we use the QFI to probe the transition from the ballistic regime with $p = 0$ (Fig. 3.29 a)), through the super-diffusive one with $p = 0.1$ (Fig. 3.29 b)) down to the diffusive

spread with maximum degree of disorder $p = 1$ (Fig. 3.29 c)), analogous to the case of a classical probe. The presented results indicate that the output information, which is inferred trough measurements performed exclusively on the probe, show a super-diffusive to classical transition in transport pattern. The observed fluctuations in the QFI values are due to the unavoidably limited number of iterations which have been realized for each step number. Similarly to the variance of the position operator of the quantum walker [67, 18, 19], QFI provides a simple measure to quantify the transport pattern of the walker.
It is worth mentioning that the probing pattern depends on the number of steps that a walker takes. In the static disorder case, we found out that the QFI decreases with respect to the step number. This is a clear signature of Anderson localization given by average upper-bound of QFI. In Fig. 3.30 a), the logarithmic scale of the average QFI is reported versus the number of steps. Fig. 3.30 a) shows that the growth trend declines until it reaches a maximum value. As an additional clarification, the QFI is fitted with the power function $F \propto t^{\alpha(t)}$, where $\alpha(t)$ is the step-dependent coefficient in a nonlinear fitting process. In Fig. 3.30 b), the $\alpha(t)$ is obtained by increasing the step number of the QW process. It is clear that the growth trend depends on the step number t, and that significantly declines by considering an higher t. This testifies that information stops spreading in the quantum network as an indicator of particle localization.
Besides the single walker analysis, to enrich the physics of phenomenon, one might consider two quantum walkers either distinguishable or indistinguishable with initial opposite coin states. In the first case, the state can be written in a separable form in the first quantization formalism as $|\psi_0^s\rangle = |0\rangle_{1p}|\uparrow\rangle_{1c} \otimes |0\rangle_{2p}|\downarrow\rangle_{2c}$, while in the latter case, the state is entangled in coin state $|\psi_0^{\pm}\rangle = |0\rangle_{1p}|0\rangle_{2p} \otimes \left(\frac{1}{\sqrt{2}}(|\uparrow\rangle_{\mathbf{1c}}|\downarrow\rangle_{2c} \pm |\downarrow\rangle_{1c}|\uparrow\rangle_{2c})\right)$. The evolution can be studied by applying the two-particle unitary operator $\hat{U}(\phi) \otimes \hat{U}(\phi)$ to the states above. We plot the average QFI in terms of the step number t in Fig. 3.31 for the ordered case $p = 0$ and the completely disordered one $p = 1$, for both the cases of b) static and c) dynamic disorder. In general, the state of two indistinguishable particles would exhibits a higher value of QFI compared to the distinguishable one. This property is explained by the fact that particle indistinguishability is an enriching resource for quantum information distribution within a composite system of identical particles. It is also interesting to note that both input states follow the same spreading pattern. In the case of ordered case $p = 0$, the growth pattern is ballistic, while for the completely disordered one $p = 1$, the QFI follows a sub-diffusive pattern (Fig. 3.31 b)) and a classical one (Fig. 3.31 c)), due to static and dynamic disorder, respectively.

3.3.4 Conclusions

In this study, we have proposed and analysed a quantum probing protocol using the quantum walk process to infer information about a parameter ϕ encoded in the QW evolution, subjected to defects and perturbations. This goal can be achieved by applying quantum metrology techniques to the QW process. The QFI has been used to derive the amount of extractable information concerning the unknown phase acquired by a quantum walker at each step plus random fluctuations in the QW itself. Even though the framework is general, we focused on coherent static and dynamic disorder in the QW to describe the transport pattern of information about the unknown parameter ϕ. We found that different disorder regimes, corresponding to a disorder percentage p in the QW process, lead to different spreading patterns, including ballistic, super-diffusive, classical, sub-diffusive regimes, and Anderson

localization. Quantum Fisher information, as a spreading pattern indicator, is independent of the number of quantum walkers, while the variance dimension grows accordingly to the number of particles.
Such a study intimately links QW dynamics with quantum metrology theory, exploiting the usefulness of quantities as QFI in the analysis of QW dynamics. The presented results could pave the way for the integration between two main branches of quantum information theory which, as far as we know, up to now basically remain independent from each other. Moreover, due to the increasing interest in studying the spread of information in complex networks, the present work represents a basis to deepen such investigations, for instance by enlarging the space over which the walker can moves, as well as the number of walkers.

Chapter 4

Two photon correlations in a Quantum Walk

In this chapter, which is based on [124], we present our latest result about the topic of quantum correlations in a QW. We show that, on the one hand, an ordered QW dynamics tends to decrease the quantum correlations initially present between two indistinguishable photons. On the other hand, the insertion of disorder can be useful in this sense, as it allows to retrieve the initial value of non classical correlation. We experimentally prove the theoretically predicted results by allowing two indistinguishable photons to propagate through a p-diluted disordered QW network.

4.1 Introduction

The effect of quantumness in a QW's evolution as well as the effective quantumness of QWs have been questioned on many sides [125, 126]; a genuine quantum behaviour in a QW evolution is observed only if authentic quantum correlations in the QW input are present. [127, 128]. Among the most important non-classical features, entanglement has been quantified in a quantum information theory framework [129, 130], both from a thermodynamical perspective [131, 132] and a geometrical one [133], revealing unique features, useful for many applications. Entanglement is not the only resource that can be exploited to reproduce pure genuine quantum walker evolution. Indeed, particle statistics also highlights the presence of non-classicality: the bosonic-fermionic dualism has no classical analog and it relies on the quantum feature of indistinguishability. The treatment of indistinguishability as a quantum resource has been mainly developed in the framework of quantum metrology and quantum information, through the connection with other non-classical features [134, 135, 136, 137, 138]; besides, the high complexity exploited by Boson Sampling algorithms relies on particles indistinguishability, too [139, 140, 141]. In this sense, Hong-Ou-Mandel (HOM) is a paradigmatic effect, just because of the fact that it has no classical analogue. For this reason, its presence certifies the pure quantumness of photons [6].
In this context, it is interesting to understand how non-classicality quantifiers based on indistinguishability behave in a dynamical framework, specifically in the case of bosons propagating through a non-homogeneous system. From this perspective, the presence of noise and disorder has been largely demonstrated to provide speed-ups and beneficial effects in various quantum processes, such as in biological systems [14], and quantum algorithms [38]. These effects commonly appear due to the interaction

with an external environment, either quantum or not [142, 143]. A suitable framework to perform such a study is represented by QWs. The way quantum correlated photon pairs evolve in an optical lattice, or a QW, has been studied from both theoretical and experimental point of views [76, 32, 144, 31, 145] and the effect of static disorder in a QW network has been observed for photon pairs, too [78, 86]. In particular, photons in a separable state show a different behaviour whether they are distinguishable or indistinguishable [145]. As we will see in a greater detail later, this difference can be quantified by the violation of the disequation:

$$V_{i,j} = \frac{2}{3}\sqrt{P_{i,i}P_{j,j}} - P_{i,j} < 0 \tag{4.1}$$

where $P_{i,j}$ is the probability of finding a photon travelling along mode i and the other one along j, thus corresponding to the probability of measuring a coincidence between modes i and j.
Our aim is to find out whether the presence of disorder (referring in particular to the so-called p-diluted model) might have a significant role in how the correlations existing between the output modes of a photonic QW change. We experimentally show that non-classical correlations based on indistinguishability are sensitive to the presence of disorder, as a consequence of the propagation through a one dimensional inhomogeneous QW. We also demonstrate that, by merely imposing some specific disorder configurations while keeping the system isolated, it is possible to significantly retrieve the initial non-classicality of the system, after a certain number of evolutions steps. Our findings unambiguously show that the presence of disorder can be helpful in the dynamical enhancement of quantum correlations, paving the way for its possible employment in quantum information scenarios.

4.2 Theoretical model

Eq. (4.1) links three experimentally measurable quantities, i.e. $P_{i,i}, P_{j,j}$, and $P_{i,j}$ to the quantumness of the correlations between modes i and j or, more precisely, to the degree of indistinguishability of the photons travelling along those modes. This disequation, in fact, stands for classically correlated light and its violation is assumed at the same time as a witness and as a quantifier[145] of quantum correlations [76, 32].
To clarify the meaning of Eq. (4.1) lets focus on the HOM effect. As showed in section 2.5.1, when two indistinguishable photons (i. e. photons with exactly the same features and with same arrival time on the BS) impinge on a BS from the two input ports, in the completely ideal case the output state reads

$$|\psi\rangle_{ind} = \frac{i}{2}(\hat{a}^{\dagger^2} + \hat{b}^{\dagger^2})\,|0\rangle_F = \frac{i}{\sqrt{2}}(|2,0\rangle_F + |0,2\rangle_F)$$

where the ket states are written as $|\hat{a}^\dagger, \hat{b}^\dagger\rangle_F$. It comes out that the probability to find the particles travelling along two different modes, i.e. $P_{a,b}$ drops to 0, while the probability to find them travelling along the same mode, namely $P_{a,a}$ and $P_{b,b}$ is 0.5. From these values we obtain $V_{a,b} = \frac{1}{3} > 0$.
In the case of distinguishable photons, the output state after the interaction with the BS reads

$$|\psi\rangle_{dist} = \frac{1}{2}(i\cdot\hat{a}^\dagger\hat{a'}^\dagger + \hat{a}^\dagger\hat{b'}^\dagger - \hat{b}^\dagger\hat{a'}^\dagger + i\cdot\hat{b}^\dagger\hat{b'}^\dagger)\,|0\rangle = \frac{1}{2}(i\cdot|1,1,0,0\rangle_F + |1,0,0,1\rangle_F - |0,1,1,0\rangle_F + i\cdot|0,0,1,1\rangle_F)$$

where the ket states are written as $|\hat{a}^\dagger, \hat{a'}^\dagger, \hat{b}^\dagger, \hat{b'}^\dagger\rangle$. When computing the probabilities by tracing over the different degrees of freedom of the photons, the probability $P_{a,b} = P_{a,b'} + P_{b,a'}$ results to be $\frac{1}{2}$ while, for $P_{a,a'}$ and $P_{b,b'}$ we get $\frac{1}{4}$. Thus, the resulting value of $V_{a,b}$ is $-\frac{1}{3} < 0$. In the indistinguishable photons case, a positive value witnesses the presence of non classical correlation between the two modes under study, namely they are correlated in a way that can not be justified with any type of classical input state. On the contrary, in the distinguishible case, we obtain a value < 0 which implies that the very same correlations can be obtained with a classical input.
Being interested in studying if and how the quantumness in the modes correlation depends on the phase disorder, introduced through the p-diluted model, we can perform some easy calculation to have an insight on how V changes with phase noise. To simplify the calculation, consider the Mach-Zehnder interferometer in Fig. 4.1.

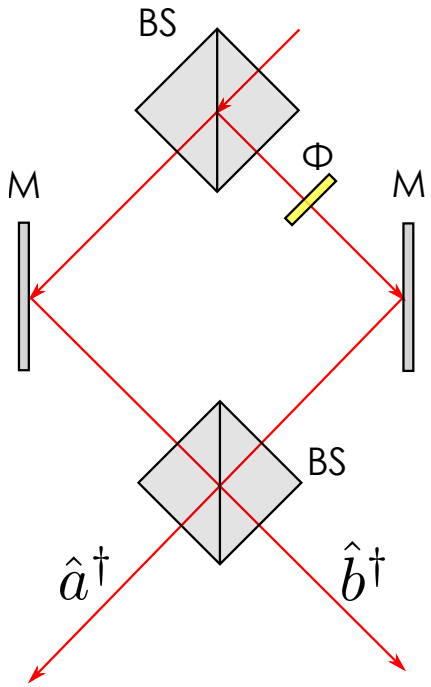

Figure 4.1. Sketch of a Mach-Zehnder interferometer. The yellow rectangle denotes the insertion of a phase along one of the two arm.

Its output is related to the one of the central modes of the QW at the third step. When inserting a phase shift along one of the two modes, for instance the b mode, in the case of indistinguishable photons we obtain the following analytic expression for the value of $V_{a,b}$ as a function of the phase ϕ

$$V_{a,b} = -\frac{1}{3} - \frac{2}{3}\cos(2\phi)$$

whose plot is reported in Fig. 4.2.
In the distinguishable photons case, we obtain the following relation

$$V_{a,b} = -\frac{2}{3} - \frac{1}{3}\cos(2\phi)$$

whose plot is also reported in Fig. 4.2

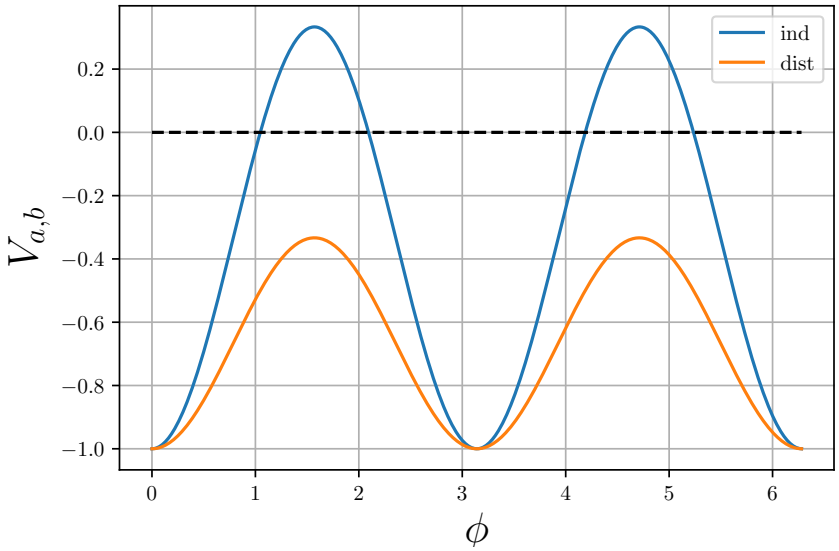

Figure 4.2. Values of V as a function of the phase ϕ for indistinguishable (blue) and distinguishable photons (orange). Dashed black line indicates the 0 value, separating the quantum and classical regions.

It is clear that, while in the distinguishable photon case the curve never overcame the 0 value, in the indistinguishable case it is possible to obtain values larger than 0 that univoquely witness the presence of a quantum input travelling the network.
At this point, we can try to establish a link between the value of the violation and the state corresponding to it, by investigating the case in which two partially indistinguishable photons enter the QW. The initial state can be written as:

$$\hat{\rho}_0 = (1-q)\hat{a}^\dagger\hat{b}^\dagger\left|0\right\rangle\left\langle 0\right|\hat{a}\hat{b} + q\hat{a}^\dagger\hat{b'}^\dagger\left|0\right\rangle\left\langle 0\right|\hat{a}\hat{b'} = \\ (1-q)\left|1,1\right\rangle_{ind}\left\langle 1,1\right|_{ind} + q\left|1,1\right\rangle_{dist}\left\langle 1,1\right|_{dist}$$

where q can represent the probability of "bad" generation of the input state or rather the actual overlap of the two photons wave functions, such that the photons are distinguishable with classical probability q. The resulting state after the action of a supposedly balanced BS shall be:

$$\hat{\rho}_1 = (1-q)\left(i\cdot\frac{|2,0\rangle + |0,2\rangle}{\sqrt{2}}\right)\left(...\right)^T + \\ + q\left(\frac{i\cdot|1,1,0,0\rangle + |1,0,0,1\rangle - |0,1,1,0\rangle + i\cdot|0,0,1,1\rangle}{2}\right)\left(...\right)^T.$$

The inequality (4.1) can be evaluated with the output probabilities of the process, so that $P_{a,a} = P_{b,b} = \frac{1-q}{2} + \frac{q}{4}$ and $P_{a,b} = \frac{q}{2}$. The inequality then has the form:

$$\frac{2}{3}(\frac{1}{2} - \frac{q}{4}) - \frac{q}{2} < 0$$

which, in order to be violated, requires a value $q > \frac{1}{2}$, corresponding to photons which are more likely to be indistinguishable than distinguishable. Hence, the inequality (4.1) provides a straightforward quantifier of the effective indistinguishability of photons, in the operative context of boson bunching occurrence.
In the general case of a BSs network, a value of $V_{ij} > 0$ can be subject to multiple interpretations. For a pure initial state, after t steps of propagation, the system will be in a superposition state which can be written highlighting the modes of interest, denoted with the subscript $1, 2$:

$$\begin{aligned}|\Phi\rangle &= \sqrt{1-\Pi}(...)+ \\ &+ \sqrt{\Pi}(\alpha_{11}\,|2\rangle_1\,|0\rangle_2 + \alpha_{12}\,|1\rangle_1\,|1\rangle_2 + \alpha_{22}\,|0\rangle_1\,|2\rangle_2)\end{aligned}$$

where Π is the overall probability of having both photons in the selected modes, which normalizes the α_{ij} coefficients. It is possible, obviously, also to have single photon states of the two modes, but they would be invisible to coincidence-like measurements. In this case, the violation between modes 1 and 2 can be computed as:

$$V_{12} = \Pi * (\frac{2}{3}\sqrt{|\alpha_{11}|^2|\alpha_{22}|^2} - |\alpha_{12}|^2). \tag{4.2}$$

Therefore, the violation value depends on two factors:

- the actual non-classicality of the correlation determining a positive or negative value;
- the global probability of the selected output modes (given by Π).

The first factor is the one pointing out the form of a hypothetically post-selected state of the two photons emerging from the considered modes. The higher this factor, the cleaner is the distillation of NOON states by post-selection, since it necessarily corresponds to a low $|\alpha_{12}|^2$. The second factor is an amplification parameter, which gives the probability of actually finding two photons in the two-modes selected subsystem, hence it gives the efficiency of the NOON states distillation. In conclusion, the violation value gives an indication over the composite effect of the two parameters, hence its maximization can be related to either one or the other. Thus, in a hypothetical application of this protocols, that needs to be taken into account. For instance, the most external output modes of the QW will provide the most pure NOON states, since they are the mere propagation of the first HOM resulting state, but with a very low probability. On the other hand, by means of disorder, it is possible to manipulate the probability for central modes, in order to get an higher efficiency, at the cost of a non-zero chance of extracting a useless state. The question underlying the investigation reported in the following sections then is: how this violations can be tuned and controlled by means of the p-diluted QW? Or, in other words, is there a particular condition in which the p-diluted disorder on phases allows to maximize the value of $V_{i,j}$? These questions are ultimately linked to the possible applications: because of the fact that the value of V is linked to the

amount of the indistinguishability of the photons and that this has been shown to be a full quantum resource, the ability to control its values along a QW evolution could be a starting point for a new class of algorithms based on the manipulation of the information through QW and indistinguishability of the photons.

4.3 Simulation results: violation properties for average distributions

The first analysis we carried on was the study of the average behaviour of violation of the system by considering the probability distribution obtained by the average over many different evolution realizations, characterized by the same amount of disorder p.

4.3.1 Distributions

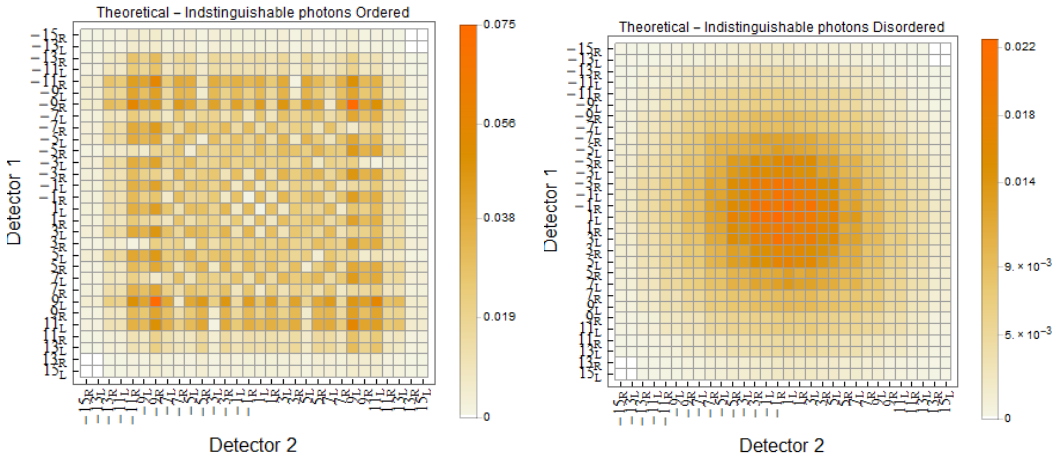

Figure 4.3. Step 15 output distributions of indistinguishable photons in the ordered and completely disordered case.

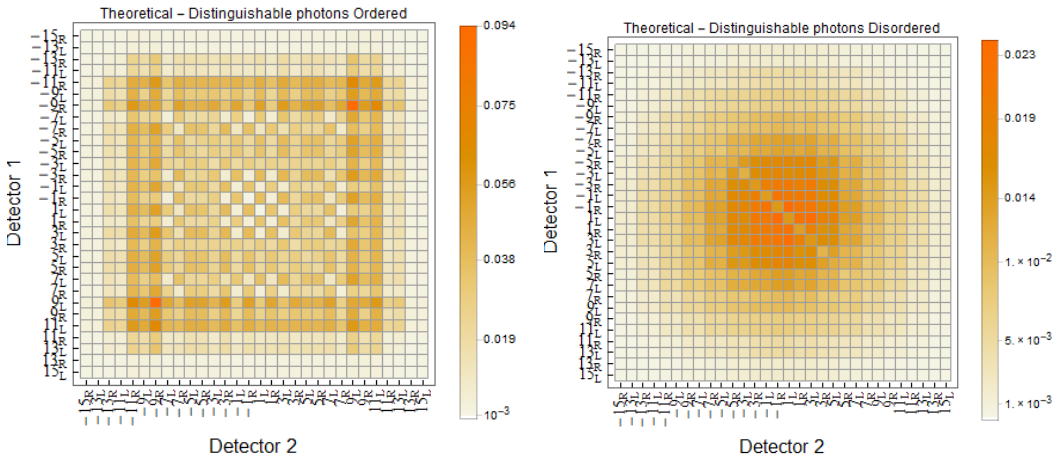

Figure 4.4. Step 15 output distributions of distinguishable photons in the ordered and completely disordered case.

The first aspect we focus on is the probability distribution in both cases of distinguishable and indistinguishable photons, at varying of the disorder value p. The average output probability distributions of coincidences for indistinguishable and distinguishable photons (Fig. 4.3 and 4.4) appear more similar when the disorder level is high. According to the variance results shown in section 3.1 this is expected: indeed, for increasing values of disorder, the spread of the walkers is more and more diffusive for both cases and increasingly similar probability distribution are expected. This is also highlighted by the trend of the similarity between the output distributions of distinguishable and indistinguishable distributions as the value of p grows (Fig. 4.5). We point out that, in the present notation, the QW modes are denoted by the position basis states combined with the coin basis states (Left (L) and Right (R)).

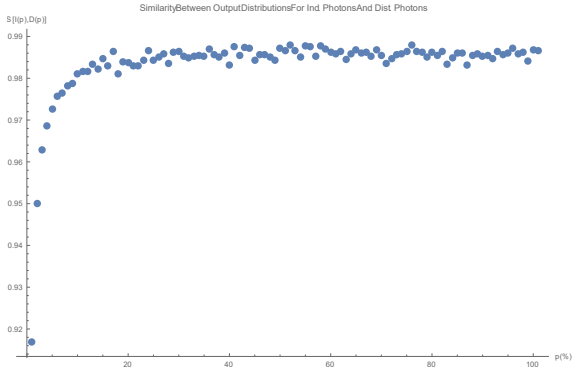

Figure 4.5. Similarity between average output distributions at step 15 of indistinguishable and distinguishable photons as a function of the disorder value p.

It is quite clear that the observation of the output distributions of coincidences can not provide information about the nature of correlations between the photons, while it could be deduced by the violation of Eq. (4.1).

4.3.2 V-matrices

When dealing with the values of $V_{i,j}$ between each pair of modes, for each probability distribution a corresponding V-matrix can be derived, showing the correlations between the modes. The distributions of the values of $V_{i,j}$ for indistinguishable photons are shown in Fig. 4.6. The violations are present either in the ordered and in the disordered case, though there is an evident migration of the violating values towards the distribution tails.

It is worth comparing the distribution of violation with the coincidences one (Fig. 4.3). By a qualitative analysis, non-classical correlations tend to appear between modes which have low coincidences (and less population); in some way, it can be a witness of the fact that correlations generated specifically by the QW evolution are classical and, in an intuitive way, smother the underlying non-classical correlations, which are free to show up where the evolution tends to provide low populations.
As expected, in the case of distinguishable photons, violations are not present at any disorder rate (see Fig. 4.7).

The dynamical average behavior of non-classicality has been studied through Total Violation, defined as the sum of all the $V_{i,j}$ of the violating coincidences. It has been considered as a measure of the total non-classicality present in the system. In Fig. 4.8 the normalized trend as a function of the disorder increase is reported,

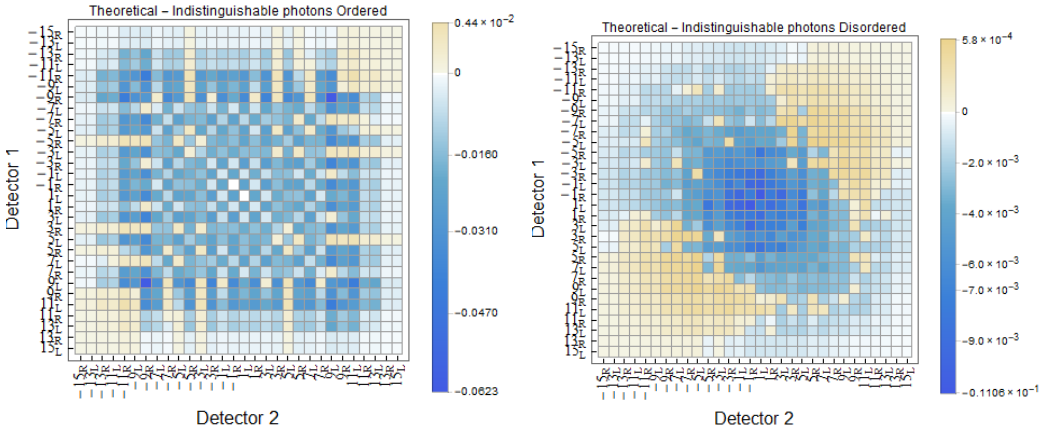

Figure 4.6. Step 15 distribution of the value of relation (4.1) for indistinguishable photons in the ordered and completely disordered case.

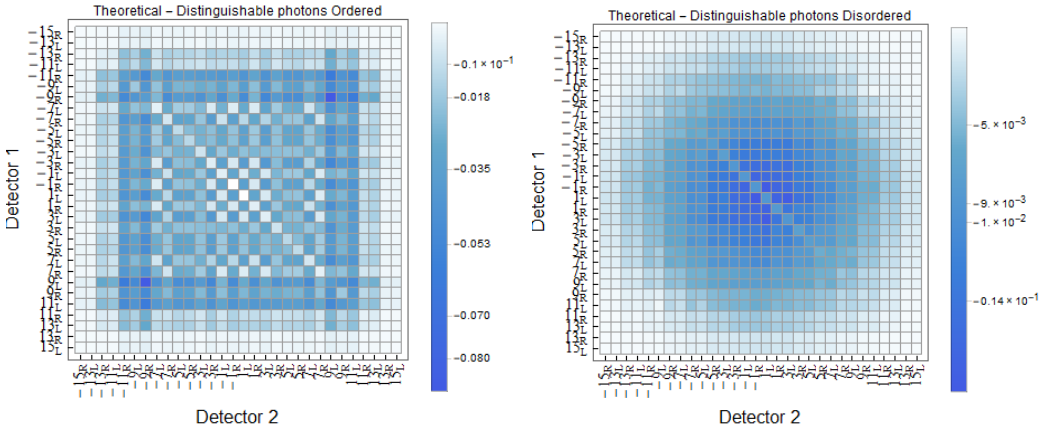

Figure 4.7. Step 15 distribution of the value of relation (4.1) for distinguishable photons in the ordered and completely disordered case.

for different evolution time lengths. Total Violation has a decreasing trend as p increases, which can be seen as a consequence of the migration picture described above. Since violations are bound to appear only between scarcely populated modes, the global non-classicality in correlations diminishes. Nevertheless, this non-classicality degradation can be challenged by specific single realizations of disorder.

4.4 Simulation results: violation properties for single phase map

When dealing with single disorder realizations, the disorder level p looses its meaning. Indeed, despite it is possible to compute the exact value of p from a single disorder realization, the very same phase map can be obtained from different values of p, because of the randomness in generation method of the map itself. For this reason, in the following we will focus on the time evolution of the relevant quantities, disregarding their behaviour as a function of the disorder value.

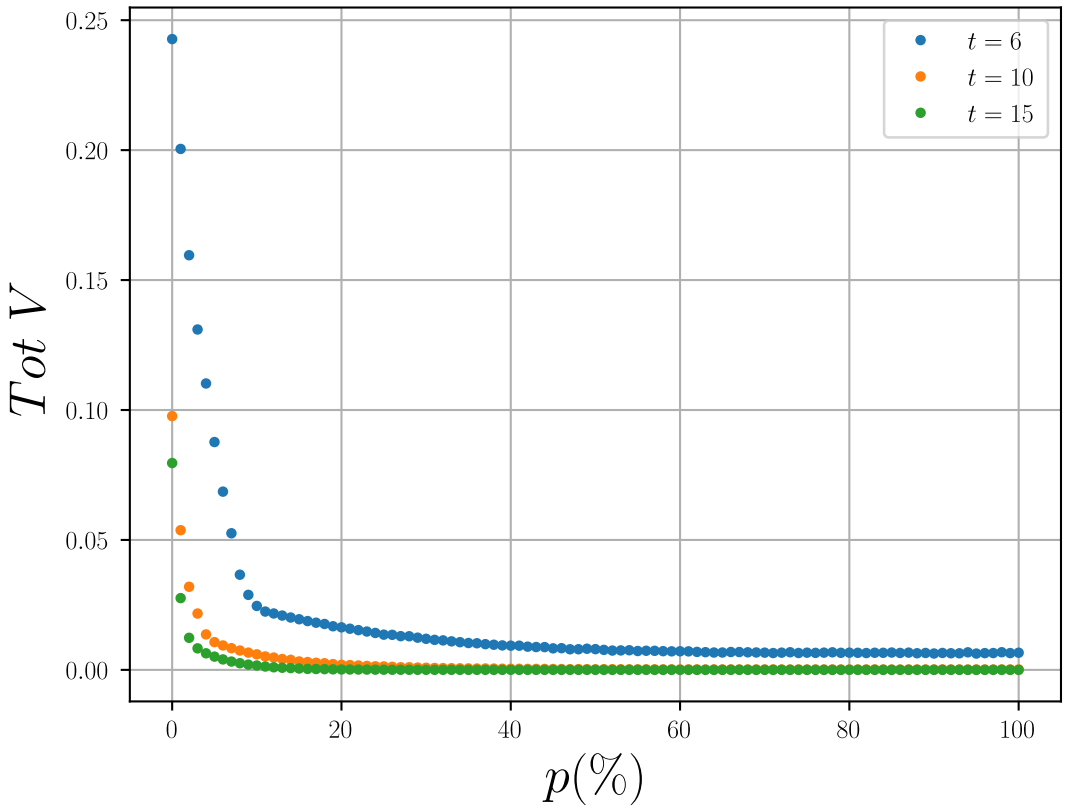

Figure 4.8. Step 15, step 10 and step 6 plot of the average Total Violation, computed over 10000 disorder configurations, as a function of the disorder level p. The average detrimental effect of disorder has a lower bound, independent of the time step. Besides, the evolution appears naturally featured by a decrease of global non-classicality in time.

4.4.1 Maximum achievable violation (MAV)

As already stated, the bosonic correlation quantifier holds only in the case of indistinguishable photons. For this reason, simulations were carried on in a specific experimentally-oriented framework: two indistinguishable photons travelling a bulk-optics 1D DTQW, provided with space-time disorder.
The analysis pursued a well defined direction: the search for single disorder configurations able to increase the violation values between a generic pair of mode. As we will show, the analysis demonstrates that disorder may not only modify the distribution of non-classicality in the output correlations of the system, but also that specific phase maps can produce non-classicality enhancements in the output state. We simulated the evolution with 10^4 different phase maps for each step number t up to 30 steps, for a total amount of explored configurations equal to $3 \cdot 10^5$. We computed the V_{ij} between each pair of output modes for each simulated probability distribution, obtaining the corresponding violation matrices, in which the entire set of V_{ij} elements corresponding to any combination of i and j modes are reported. We then compared the values for any pair (i, j) and each phase map at a given step, in order to find the Maximum Achievable Violation (MAV), i.e. the maximum positive value of V_{ij} which could be achieved at that given step.
Simulation results are shown in Fig. 4.9, in which we report the MAV as a function of the step number and the step-wise trend of the maximum achievable Total Violation, defined as the sum of all the positive V_{ij} values of the considered violation matrix.

The analysis over the MAV highlights that disorder may help retrieving non-classicality after a specific step of QW; hence, the MAV starts growing with respect to the standard ordered case, reaching a peak at the 9th step in our framework. Similar, but not identical, results were obtained for the system's maximum Total Violation, suggesting that the two quantities are related, but not bound to be maximized together. Indeed, both reach a minimum at step 5, but present maxima for different steps. Moreover, in the ordered case, a relevant maximum is obtained for the total violation at sixth step, not corresponding to a maximum in the MAV plot. This can be explained by considering that, in the ordered case, many different pairs of modes at step 6 present a positive value of $V_{i,j}$, but none of them overcomes the maximum achievable value at step 7, which corresponds to a local maximum for the MAV. From the numerical results, we can conclude that disorder, acting through mere interference, shall heavily modify the evolution of the walker, not only reshaping the probability distribution, but also affecting the amount of quantum correlations. As a consequence, disorder may allow to enhance non-classicality in the correlations of a multipartite system.

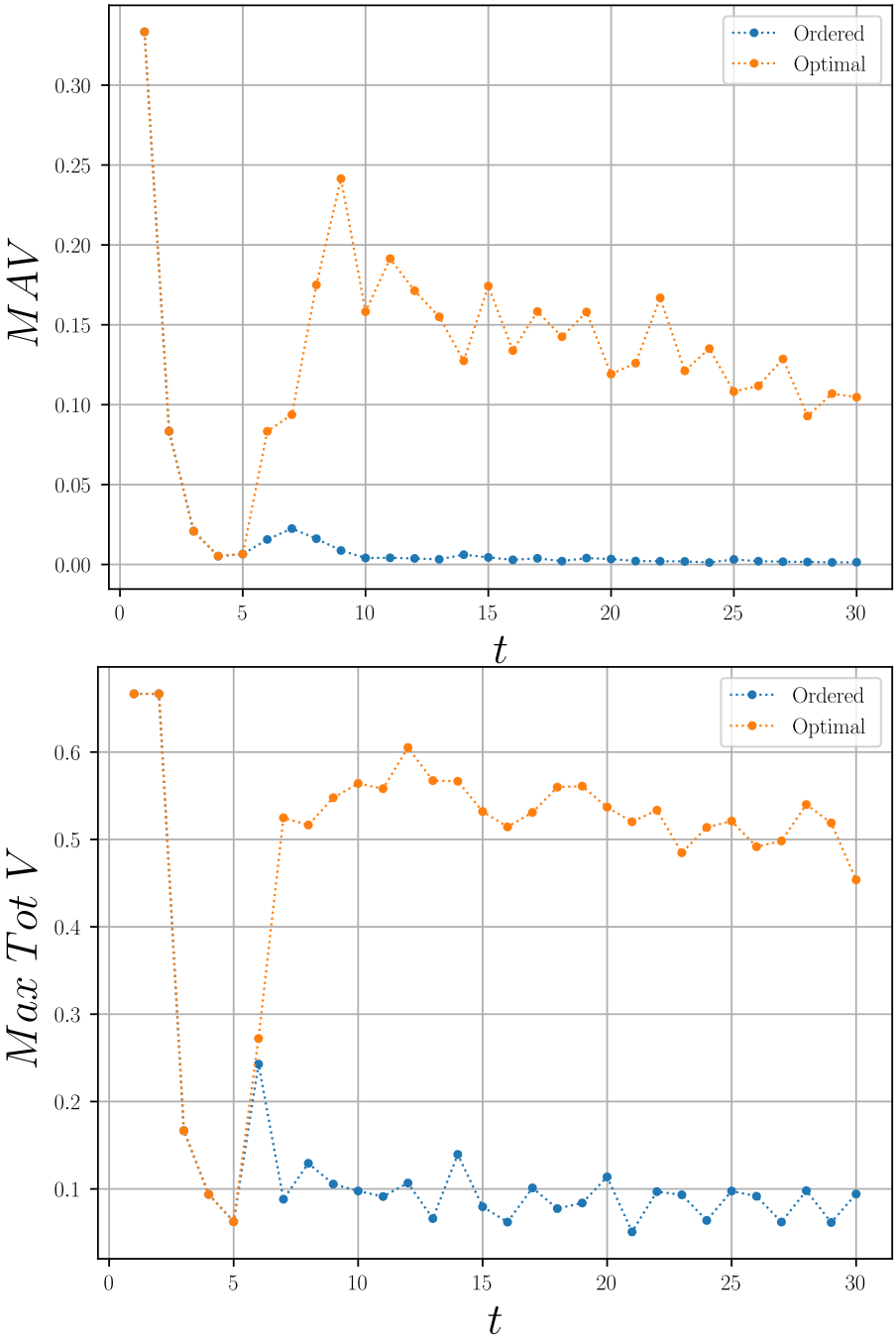

Figure 4.9. Comparison between the theoretical step-wise trend in the ordered case and in the disordered optimal one for MAV (**top**) and global violation (**bottom**). In the present framework, a clear enhancement due to disorder is achievable after the 5th evolution step, while in the standard homogeneous evolution non-classicality would reach a plateau for both quantities: this corresponds to a dispersion of non-classicality in the distribution.

4.4.2 Analysis of local maxima for optimal step number

Since our main interest is currently devoted to the interpretation of the violation (4.2) as a resource for certain tasks, the most interesting quantity is $V_{i,j}$ value itself, since that is closely related to the shape of the output state which is extractable from the corresponding modes.

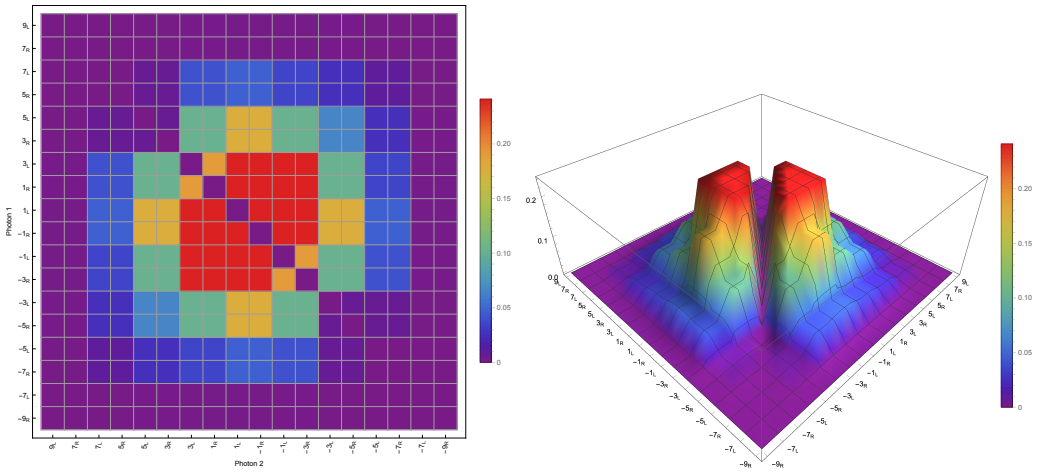

Figure 4.10. Maximum achievable values of $V_{i,j}$ for each mode pair i, j at step 9, planar representation (**left**) and 3D landscape (**right**). The values have been obtained by comparing 1.2 million disorder realizations. The maximum can be achieved in the central region, since the photons detected in those modes have interfered the most.

The step for which the MAV of local violation is maximum appears to be the 9th. Therefore, we accurately analyzed the output violation distribution, seeking the MAV of $V_{i,j}$ for each fixed pair of modes (i, j); the values reported in Fig. 4.10 have been calculated from a total of 1.2 million disorder realizations.

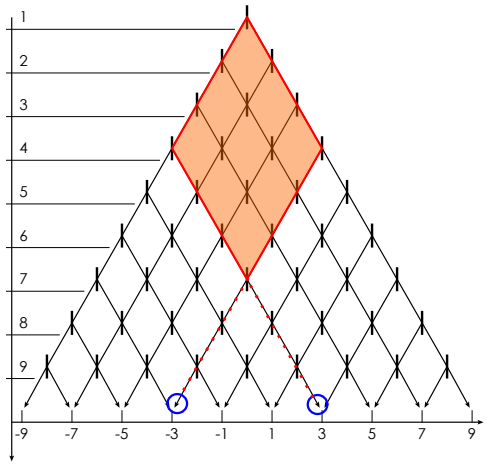

Figure 4.11. Schematic representation of a Quantum Walk at step 9: for instance, if we take into account the two blue circled output modes, the corresponding common MZIs will be the ones highlighted in red.

By the resulting picture of the aforementioned analysis we can conclude that the MAVs can be obtained in several ways: considering many different mode pairs

and many different disorder configurations. Nevertheless, it is possible to outline some constraint: there is a minimum of mutual interference that the photons have to experience in order to achieve the maximum; this can be represented by the number of common Mach Zender Interferometers (MZIs) they travel along their evolution, as highlighted in Fig. 4.11. This constraint is not sufficient to reach the maximum, since, as mentioned before, there are leaks along the propagation; furthermore, other effects arise from the limited range of phase values which can be set according to the model. We can conclude that the step-wise maximum of local violation (not considering the first step, corresponding to a perfect HOM effect) is achieved at the 9th step, with a value $V_{i,j} \approx 0.24$. We are currently studying how the various optimal phase maps are related between them.

4.5 Experimental results

The experimental setup used to test and verify theoretical and simulated results is the all-optical QW described in sec. 2.5.1, in the two photon input configuration. We reproduced the evolution of the two walkers up to the sixth step of the evolution, which is sufficient to prove the violation enhancement due to disorder. Indeed, in the present case of study, the first clear appearence of non-classicality enhancement due to disorder shall occur in the output of the QW 6th step; in order to demonstrate this effect, the output violation matrices for optimal phase maps were measured up to the 6th step.

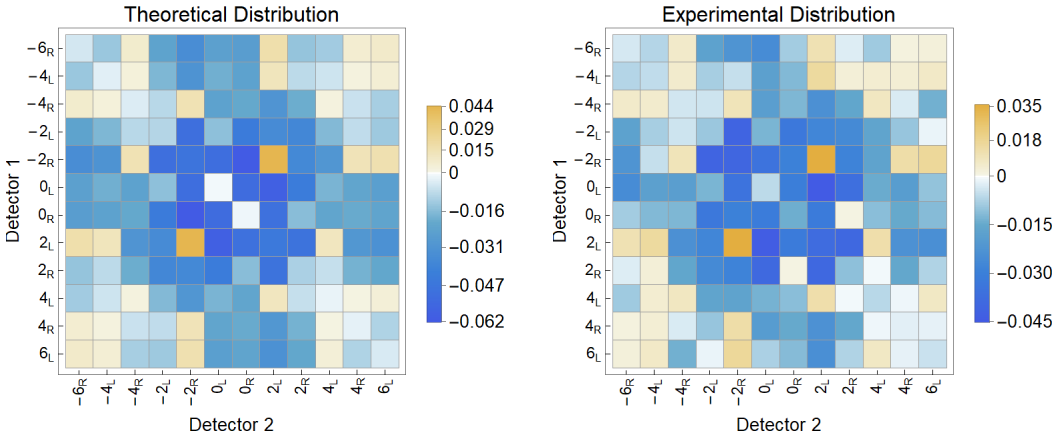

Figure 4.12. Comparison between the theoretical (**left**) and experimental (**right**) violation matrices at the 6th step for an enhancing disorder configuration. Theoretical results are obtained by numerical simulations performed accounting for experimental parameters. The expected peak in the value of V is experimentally found, while the measured output coincidence distributions reach globally a similarity value of 97.5(±0.2)%. Deviations with respect to the expected matrix are due to the relative significance of experimental errors for close-to-zero values, which can produce non-classical signatures where they are not expected and vice versa.

Since there is no enhancement until the 5th step, the corresponding optimal phase maps can be considered equivalent to the ordered one, while for the 6th step it is possible to find a specific disorder configuration enhancing the non-classicality in the correlation between two chosen output modes. In our case of study, the same configuration also features an enhancement in the total amount of non-classicality of the system.

The ordered QW output distributions were measured up to the 5th step; in particular, the 5th step distribution was also measured for a random disordered configuration, in order to experimentally confirm disorder-induced changes in the violation matrix, despite the absence of any unambiguous increase in the amount of violation. Experimental violation matrices for the fifth step of the evolution, along with the expected matrices, are reported in Fig. 4.13, from which it is clear that the introduction of disorder alters the distribution of the violations.

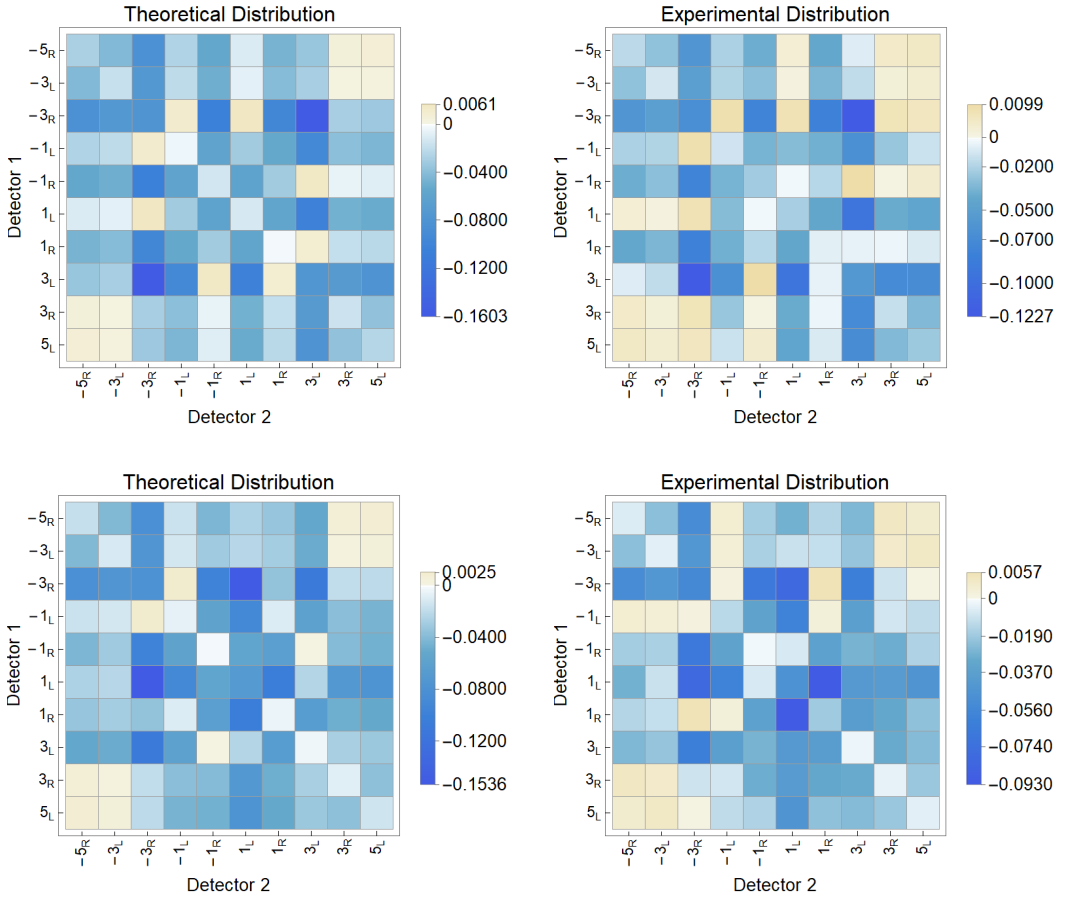

Figure 4.13. Comparison between theoretical (**left**) and experimental (**right**) violation matrices at the 5th step for ordered evolution (**top**) and disordered evolution (**bottom**). The disorder configuration has been chosen randomly, in order to demonstrate how inhomogeneities along the evolution can modify the non-classicality pattern in correlations. The experimental results appears to be not in perfect agreement with the expected ones, since, in this case, the error on $V_{i,j}$ values is big with respect to the measured absolute values of violation.

For the 6th step, a phase map which could realize the MAV was chosen and experimentally implemented; the corresponding experimental output violation matrix is shown in Fig. 4.12, compared with the expected one. A strong non-classicality peak appears, confirming the expectations and the non-classicality enhancement effect. Besides, it suggests that non-classicality maxima can be induced by disorder only in correlations between "central" output mode pairs: in fact, photons emerging from these modes will have the most interfering paths, getting to be more affected by

inhomogeneities along the evolution. This phenomenon is quite understandable by considering the underlying network structure of the evolution. Indeed, central modes are subjected to more complex interference phenomena with respect to the ones close to the boundaries, even more complex when their correlations are considered. This can be directly linked to the amount of MZIs jointly travelled by photons emerging from the two selected modes, i.e. the amount of phase shiftings which are imposed over both photons. In these cases, the manipulation of non-classicality results more powerful and effective.

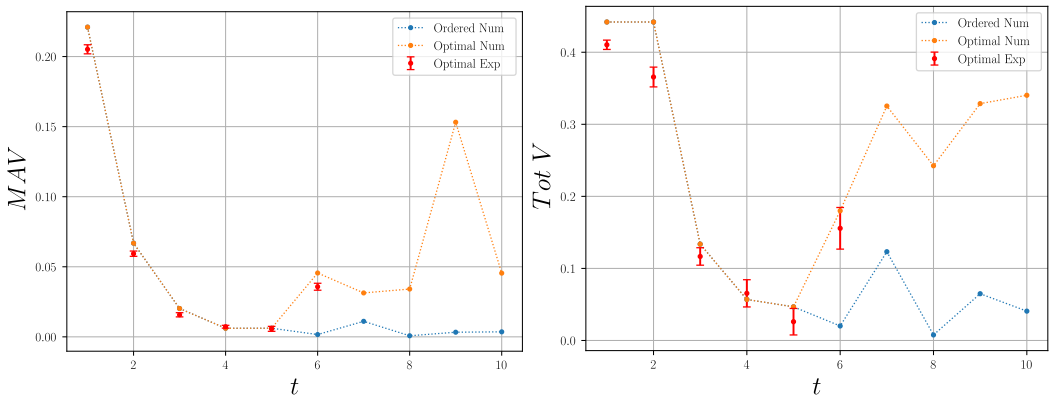

Figure 4.14. Experimental step number trends up to the 6th step of local MAV (**left**) and global violation (**right**) computed over the same output distributions aimed to maximize the local violation. The trends are compared with the simulated ones and the ones expected for ordered evolution: an enhancement of MAV due to the presence of non-homogenities is unambiguously achieved, in comparison with the ordered expected results. The expected results are obtained by numerical simulations performed accounting for experimental parameters, so that the theoretical trends show some discrepancies with respect to the ones in Fig. 4.9. Experimental errors are derived from the Poissonian statistics of the measured coincidences. Deviations from the expected results are mainly due to small drops in photons indistinguishability along the evolution, which slightly affect the exact violation values, while not changing the overall trend.

As a further relevant result, the experimental step-wise trend for MAV is exhibited in comparison with the expected optimal one, also computed accounting for experimental parameters (Fig. 4.14 left). They are plotted together with the ordered case trend, in order to provide a clear display of the beneficial effect of the non-homogeneous evolution. Theoretical patterns are shown up to the 10th step, as a reference. The corresponding trends for the Total Violation computed over the same output distributions are also reported in Fig. 4.14 right. Simulations of the MAV values in the ordered case show that non-classicality delocalizes travelling a homogeneous network, so that the values of V_{ij} are going to vanish as the propagation proceeds. On the other hand, also the Total Violation shall not experience in the ordered case a revival comparable to the disordered one, as the evolution carries on. Asymmetries in the experimental setup, specifically the exploitation of an unbalanced BS ($R = 45/T = 55$), are responsible for discrepancies between theoretical trends shown in Fig. 4.9 and the ones in Fig. 4.14. While the Total Violation trend for the ordered case is strongly modified by such asymmetries, the MAV mantains its rapidly flattening pattern, which can be clearly challenged by specific disorder configurations, as shown by our experimental results. In this case, the very same configuration is also helpful in the enhancement of global non-classicality of the system.
The insertion of inhomogeneities enriches the interference patterns imposed on the particles, leading to the possibility of manipulating and focusing non-classicality

over a range of opportunities which broadens as the network broadens.

4.6 Conclusions

The presented numerical and experimental analysis demonstrates that non-classicality based on indistinguishability, which disperds through the lattice and rapidly decays in an ordered evolution, can actually be retrieved by inserting suitable inhomogeneity patterns in the system, after a minimum evolution time. This local (and global) enhancement of non-classicality can be tuned in position and intensity by changing the disorder configuration; this corresponds to having an adaptive network whose parameters evaluation determines the focusing of non-classical resources in a selected position, or rather the homogeneous distribution of them. In particular, since the violation of Eq. (4.1) is connected to the presence of a NOON state, this method could be useful in Quantum Metrology issues, accounting for the caveats we reported along the text on the state shape linked to the violation value.
It is yet to understand whether this enhancement procedure can be generalized to systems with $N > 2$ photons or not; that could result in a benchmarking outcome in the context of Quantum Resource Theories.

Chapter 5

Open Quantum System dynamics

In this chapter, which is based on [88], we will describe an experimental implementation of a collisional model for the study of Markovian and non Markovian dynamics. This field has been widely studied in recent years since the study of the interaction between a system and an environment lies at the heart of the capability to precisely control the evolution of a system. One of the aims of such research activity consists in exploiting in our favour such kind of interaction, for instance trying to preserve information encoded in a quantum state subjected to external actions.
The experimental realization presented in this chapter is built on a quasi-infinite chain of Mach Zehnder interferometers, each of them stable and independently tunable in phase. This experimental investigation has been performed earlier than the study of the QW dynamics presented in the previous chapters. Indeed, the experimental scheme reproducing the QW (presented in 2.5.1) has been obtained by the one used in this study, slightly modified by means of the introduction of the vertical beam displacers. Thus, the main point of contact between this investigation and the other studies reported in this thesis is the sharing of nearly the same experimental setup. Nonetheless, a stronger connection could be found between QWs and open quantum system dynamics. Indeed, it could be interesting to interpret the evolution of a quantum walker from the point of view of the theory of open quantum systems, despite it is not the aim of the following chapter.

5.1 Introduction

Future quantum technologies require precise control of quantum states [146, 147]. The processing protocols of quantum information should be aimed to preserve and distribute microscopic quantum correlations in macroscopic scenarios, where quantum systems are subjected to the unavoidable environmental noise. To this scope, it is essential to understand the robustness of quantum dynamical process in order to implement the best way to control the information transport between the systems and the surrounding environment [148, 149, 150, 151, 152, 153]. Because of the interplay between the system under study and the environment with which the system is in contact, a quantum dynamical process usually acts on a Hilbert space which is larger than the one in which the system and the environment belong [154, 155]. Let's consider a non-isolated sample system s, which we will refer to as open quantum system (OQS), characterized by a state $\hat{\rho}_s \in \mathcal{H}_s$ as well as the

environment e, which is described by a state $\hat{\rho}_e \in \mathcal{H}_e$. By considering both the system and the environment, we can assume that the extended system $s - e$, living in $\mathcal{H} = \mathcal{H}_s \otimes \mathcal{H}_e$, is closed and then no information can be lost; it can only flow inside $\mathcal{H}$ [156, 157]. By considering the temporal evolution of an OQS, its dynamics is called Markovian if each continuous or discrete section of the total evolution does not depend on the previous ones. In the opposite case, it is called non Markovian [158]. CRW is an example of classical Markovian process, while a QW can be seen as a combination of a Markov process and interference effects [159].

5.2 Theoretical background notions

In this section we will briefly give a description of the basic elements of quantum information (QI) theory, in the measure of which they will be used in the following. We have no claim to be exhaustive in the description of the theory of QI, we only aim at giving the useful elements to understand the work presented later in the text. For a complete description of QI, please refer to [2, 3, 4].

5.2.1 Qubit, pure and mixed states

A quantum bit, usually called qubit, is the basis resource of QI, which is used to store quantum information consisting of a two dimensional quantum system. As a classical bit, it can be found in two mutually exclusive logical states, namely 0 and 1, which we will refer to as $|0\rangle$ and $|1\rangle$, represented by

$$|0\rangle \equiv \begin{pmatrix} 1 \\ 0 \end{pmatrix}, \quad |1\rangle \equiv \begin{pmatrix} 0 \\ 1 \end{pmatrix}$$

and which are usually called computational basis states. At a variance with a classical bit, a qubit can be also found in a linear superposition of both basis states. This peculiar feature is highlighted by the fact that, in writing the qubit state, it is possible to change representation from one basis to another one. Two relevant basis are the diagonal one,

$$|+\rangle \equiv \frac{|0\rangle + |1\rangle}{\sqrt{2}} = \frac{1}{\sqrt{2}} \begin{pmatrix} 1 \\ 1 \end{pmatrix}, \quad |-\rangle \equiv \frac{|0\rangle - |1\rangle}{\sqrt{2}} = \frac{1}{\sqrt{2}} \begin{pmatrix} 1 \\ -1 \end{pmatrix}$$

and the circular one

$$|R\rangle \equiv \frac{|0\rangle + i\,|1\rangle}{\sqrt{2}} = \frac{1}{\sqrt{2}} \begin{pmatrix} 1 \\ i \end{pmatrix}, \quad |L\rangle \equiv \frac{|0\rangle - i\,|1\rangle}{\sqrt{2}} = \frac{1}{\sqrt{2}} \begin{pmatrix} 1 \\ -i \end{pmatrix}.$$

The generic state of a qubit in the computational basis can be written as

$$|\psi\rangle = \alpha\,|0\rangle + \beta\,|1\rangle$$

where α and β are complex numbers subjected to the condition $|\alpha|^2 + |\beta|^2 = 1$, which is necessary to interpret $|\alpha|^2$ ($|\beta|^2$) as the probability to find the qubit in the state $|0\rangle$ ($|1\rangle$).
In order to extract information from a qubit, it has to be measured, namely we have to acquire information about the state of the system. Measurement process of an observable A can be represented by an operator $\hat{A}$ acting on the quantum state $|\psi\rangle$ of the qubit. The action of $\hat{A}$ is defined by means of the eigenvalues equation

$$\hat{A}\,|n\rangle = a_n\,|n\rangle$$

where $|n\rangle$ are the eigenvalues of the operator itself associated to the corresponding eigenvalue a_n. We consider the eigenstates to be orthonormal, namely $\langle n|m\rangle = \delta_{nm}$ where δ is the Kronecker delta. The operator can then be written as

$$\hat{A} = \sum_n a_n \left|n\right\rangle \left\langle n\right|$$

where we defined the bra of a generic state $|\psi\rangle$ as $\langle\psi| \equiv |\psi\rangle^*$, namely the conjugate transpose of a ket. When a measurement of the observable A is made on a generic state $|\psi\rangle$, the quantity $|\langle n|\psi\rangle|^2 \equiv p_n$ represents the probability to obtain the eigenvalue a_n. The state $|\psi\rangle$ can then be written as a linear superposition of the the $\hat{A}$'s eigenstates

$$|\psi\rangle = \sum_n c_n \left|n\right\rangle$$

where $|c_n|^2 = p_n$. The expectation value of the observable A over the state $|\psi\rangle$ is then given by

$$\langle\hat{A}\rangle = \langle\psi|\hat{A}|\psi\rangle = \sum_m c_m^* \langle m| \sum_n c_n a_n \left|n\right\rangle = \sum_n a_n \cdot p_n.$$

Such a description of a qubit is not sufficient to explore the whole potentiality of QI theory. The states described so far are called pure, but the introduction of a mixed states is required to describe the whole kinds of states that can be encountered. A mixed state differs from a pure one in the presence of classical probabilities p_i, which determine the probability of occurence of the corresponding pure state $|\psi_i\rangle$, deriving from the ensamble $\{|\psi_i\rangle\}$. A mixed state can be written by means of a density matrix, or density operator, $\hat{\rho}$ as

$$\hat{\rho} = \sum_i p_i \left|\psi_i\right\rangle \left\langle\psi_i\right| .$$

It is always true that $\sum_i p_i = 1$. If only a pure state is present in the ensamble, then the density matrix reduces to

$$\hat{\rho} = \left|\psi\right\rangle \left\langle\psi\right|$$

whose elements are computable as

$$\rho_{ij} = \langle i|\hat{\rho}|j\rangle$$

where $|i\rangle$ are the basis ket of a generic orthonormal basis of a n-dimensional HIlbert space (in the case of qubit $n = 2$). When dealing with mixed states, the expectation value of the operator $\hat{A}$ linked to the observable A can be written as

$$\langle\hat{A}\rangle = Tr(\hat{\rho}\hat{A})$$

where Tr is the trace operation which is given by

$$Tr(\hat{O}) = \sum_i \langle i|\hat{O}|i\rangle .$$

The elements ρ_{ij} of a density matrix, for $i = j$, can be interpreted as the population and represent the occupation of the basis states while for $i \neq j$ they represent the coherences and are the manifestation of quantum coherence, giving rise to interference effects. The density matrix must respect three fundamental properties:

- $\hat{\rho}$ is self-adjoin, namely $\rho_{ij} = \rho_{ij}^*$
- $Tr(\hat{\rho}) = 1$
- $\hat{\rho}$ is a positive operator, i.e. its set of eigenvalues consists of non-negative real numbers.

Moreover, the shape of the density matrix depends on the particular choice of the basis states used to represent it.
A useful quantity in the analysis of a quantum state is the purity

$$\gamma = Tr(\hat{\rho}^2)$$

which is a measure of how much a state is pure. For $\gamma = 1$ the state is completely pure, otherwise it is partially mixed, and for $\gamma = 0$ it is completely mixed.
An other relevant quantity is the fidelity, defined as

$$F(\hat{\rho}_1, \hat{\rho}_2) = \left(Tr\{\sqrt{\sqrt{\hat{\rho}_1}\hat{\rho}_2\sqrt{\hat{\rho}_1}}\} \right)^2$$

which measure how much two states are similar. It can take values from 0 to 1, respectively in the cases of orthogonal states and coincident ones.

5.2.2 Two qubit states, separability and entanglement

Up to now, we introduced a quantum system as composed by only a single qubit. In general, more than one qubit is present in the system. When dealing with N qubits, the generic wavefunction of a pure state can be written as

$$|\psi\rangle = \sum_{i=1}^{2^N} c_i |i\rangle = \sum_{i=1}^{2^N} c_i |i_1\rangle \otimes |i_2\rangle \otimes \cdots \otimes |i_N\rangle$$

in which $|i\rangle$ corresponds to the tensor product of the $|i_n\rangle$ state of the n-th qubit. The state $|i\rangle$ lives in a Hilbert space resulting from the tensor product of N 2-dimensional Hilbert spaces.
Lets consider the Hilbert space in the case $N = 2$, namely in the case of two qubits. In the computational basis, the most general pure state of is

$$|\psi\rangle = \alpha |00\rangle + \beta |01\rangle + \gamma |10\rangle + \delta |11\rangle$$

where the basis states of the four dimensional Hilbert space $\mathcal{H} = \mathcal{H}_A \otimes \mathcal{H}_B$, with $\mathcal{H}_A$ ($\mathcal{H}_B$) the Hilbert space of qubit A (B), are

$$|00\rangle \equiv \begin{pmatrix} 1 \\ 0 \\ 0 \\ 0 \end{pmatrix}, \quad |01\rangle \equiv \begin{pmatrix} 0 \\ 1 \\ 0 \\ 0 \end{pmatrix} |10\rangle \equiv \begin{pmatrix} 0 \\ 0 \\ 1 \\ 0 \end{pmatrix} |11\rangle \equiv \begin{pmatrix} 0 \\ 0 \\ 0 \\ 1 \end{pmatrix}$$

while it holds $|\alpha|^2 + |\beta|^2 + |\gamma|^2 + |\delta|^2 = 1$.
In the case in which the generic state of a two qubit system can be written as a tensor product of two states belonging to the two different Hilbert spaces, i.e. $|\psi\rangle = |i\rangle_A \otimes |j\rangle_B$, then the state is called separable. If this is not the case, i.e. if it is not possible to assign a individual state vectors to the two subsystems, then

the state is called entangled. The most famous entangled states are the Bell states, which also act as basis states of a two qubit system

$$|\phi^+\rangle \equiv \frac{|00\rangle + |11\rangle}{\sqrt{2}}, \quad |\phi^-\rangle \equiv \frac{|00\rangle - |11\rangle}{\sqrt{2}}$$
$$|\psi^+\rangle \equiv \frac{|01\rangle + |10\rangle}{\sqrt{2}}, \quad |\psi^-\rangle \equiv \frac{|01\rangle - |10\rangle}{\sqrt{2}}.$$

An entangled state presents quantum correlations, which do not depend on the basis states used to write the state: an entangled state stays so in the computational basis, the diagonal and the circular ones, as well as in every other basis representation. This corresponds to a pure quantum effect, which is not reproducible in the classical world.
When dealing with observables in two qubit case, the partial trace starts playing a role. To properly introduce it, suppose we want to compute the mean value of an observable O_A, namely an observable linked to the subsystem A

$$\langle O_A \rangle = \langle \psi | \hat{O}_A \otimes \hat{\mathbb{I}}_B | \psi \rangle = \sum_{mn} \sum_{ij} c^*_{mn} c_{ij} \langle mn | \hat{O}_A \otimes \hat{\mathbb{I}}_B | ij \rangle = \sum_{mij} c^*_{mj} c_{ij} \langle m | \hat{O}_A | i \rangle$$

where $\hat{\mathbb{I}}_B$ is the identity operator acting on the subsystem B and where we used the fact that $\langle n|j\rangle = \delta_{nj}$. This relation can also be written as

$$\langle O_A \rangle = Tr(\hat{O}_A \hat{\rho}_A)$$

where $\hat{\rho}_A$ is the reduced density matrix relative to the subsystem A

$$\hat{\rho}_A = Tr_B(\hat{\rho}) \equiv \sum_{mij} c^*_{mj} \langle i | m \rangle$$

were we defined the partial trace over the system B.
Various criteria have been developed to determine whether a state is entangled or not, such as the Schmidt decomposition method for pure states or the Peres-Horodeckis criterion, which applies to mixed states. However, these criteria can not be used as entanglement quantifiers, but only as entanglement witnesses. One of the most used entanglement quantifiers for pure states is the concurrence

$$C(|\psi\rangle) = |\langle \psi | \tilde{\psi} \rangle|$$

where

$$|\tilde{\psi}\rangle = (\hat{\sigma}_y \otimes \hat{\sigma}_y) |\psi\rangle .$$

The operator $\hat{\sigma_y}$ is the spin flip operator, whose expression is

$$\hat{\sigma}_y = \begin{pmatrix} 0 & -i \\ i & 0 \end{pmatrix}.$$

When the spin flip operator is applied to to a pure product state, it takes the state of each qubit and transforms it to the orthogonal one. Then, a projection on the initial state is performed. The concurrence of a product state is then 0. On the other hand, a completely entangled state is left invariant by the qubit flip, except for a possible phase factor difference, so that the value of C is 1. For mixed states

of two qubits, the average concurrence of the ensamble of pure state must be found by the minimization over all decompositions of the density matrix $\hat{\rho}$

$$C(\hat{\rho}) = inf \sum_i p_i C(|\psi_i\rangle).$$

It is possible to write an explicit formula of the concurrence

$$C(\hat{\rho}) = max\{0, \lambda_1 - \lambda_2 - \lambda_3 - \lambda_4\}$$

where $\lambda_{1,2,3,4}$ are the square roots of the eigenvalues, ordered from the highest to the lowest, of the operator $\hat{\tilde{\rho}} \cdot \hat{\rho}$, with

$$\hat{\tilde{\rho}} = (\hat{\sigma}_y \otimes \hat{\sigma}_y)\hat{\rho}^{\dagger}(\hat{\sigma}_y \otimes \hat{\sigma}_y).$$

5.2.3 Tomography

Tomography is the task of reconstructing the state of a quantum system by performing measurements on it. The basic idea is to "look" at the state from different points of views, i.e. to perform measurements in different basis states, in order to join the information and have a global view of the state under investigation.

Single qubit tomography

We will describe here the tomography technique for the single qubit case, and then we will extend it to multiple qubit case. The density matrix $\hat{\rho}$ of a qubit can be represented as a linear combination of the four Pauli matrices

$$\hat{\sigma}_0 \equiv \hat{\mathbb{I}} = \begin{pmatrix} 1 & 0 \\ 0 & 1 \end{pmatrix}, \quad \hat{\sigma}_1 \equiv \hat{\sigma}_x = \begin{pmatrix} 0 & 1 \\ 1 & 0 \end{pmatrix}$$
$$\hat{\sigma}_2 \equiv \hat{\sigma}_y = \begin{pmatrix} 0 & -i \\ i & 0 \end{pmatrix}, \quad \hat{\sigma}_3 \equiv \hat{\sigma}_z = \begin{pmatrix} 1 & 0 \\ 0 & -1 \end{pmatrix}$$

with coefficients $\{S_0, S_1, S_2, S_3\}$ as

$$\hat{\rho} = \frac{1}{2} \sum_{i=0}^{3} S_i \hat{\sigma}_i.$$

The parameters S_i correspond to the average value of the Pauli operators on the state to be examined, namely

$$S_0 = P_{|0\rangle} + P_{|1\rangle}, \quad S_1 = P_{|+\rangle} - P_{|-\rangle}$$
$$S_2 = P_{|R\rangle} - P_{|L\rangle}, \quad S_3 = P_{|0\rangle} - P_{|1\rangle}$$

where $P_{|\phi\rangle}$ is the probability to measure the state $|\phi\rangle$. The number of measurements needed to compute the four parameters is then 6. For pure states it holds that $\sum_{i=1}^{3} S_i^2 = 1$, for partially mixed states < 1 and for completely mixed states $= 0$. Parameter S_0 is 1 for the normalization condition. In the case of the polarization, the four parameters are called Stokes parameters.

Multiple qubit tomography

Given a n-qubit state, it can be written in terms of a tensor product of the Pauli matrices as

$$\hat{\rho} = \frac{1}{2^n} \sum_{i_1,i_2,\ldots,i_n=0}^{3} S_{i_1,i_2,\ldots,i_n} \hat{\sigma}_{i_1} \otimes \hat{\sigma}_{i_2} \otimes \cdots \hat{\sigma}_{i_n} = \frac{1}{2^n} \sum_{\nu=0}^{4^n-1} S_\nu \hat{\Gamma}_\nu$$

where the term $S_0 = 1$ for the normalization condition. The parameters S_ν correspond to the average values of the tensor product of the Pauli operators on the state to be examined. Their determination requires 6^n measurements.
In the two qubit case, 36 measurements are required to reconstruct the 16 needed parameters S_ν. From the measured concidences counts $n_\nu = \mathcal{N} \langle \psi_\nu | \hat{\rho} | \psi_\nu \rangle$ one can reconstruct the parameters S_ν and consequently the density matrix $\hat{\rho}$ representing the state.
In both cases of single and multiple qubit tomographies, the density matrix which is obtained by means of the above described technique usually doesn't represent the state of the system. Indeed, in general it will not respect the constraints of a matrix representing a physical system, such as unitary trace and hermitianicity. For this reason, a numerical approach is used in order to obtain the real physical matrix representing the state. It consists in looking for the density matrix which has the minimum distance with respect to the measured one, under the constraints of unitary trace and hermitianicity.

5.2.4 Dynamical maps

Consider a system state $\hat{\rho}_{AB}$ composed by two subsystems, living in the joint Hilbert space $\mathcal{H}_A \otimes \mathcal{H}_B$. The two subsystems are initially not entangled and their state can be written, without loss of generality, as

$$\hat{\rho}_{AB} = \hat{\rho}_A \otimes |0\rangle_B \, {}_B\langle 0|.$$

The subsystem B is in a pure state but, if this is not the case, it is always possible to enlarge the Hilbert space and purify it. The time evolution of the global system is given by

$$\hat{\rho}'_{AB} = \hat{U} \hat{\rho}_{AB} \hat{U}^\dagger = \hat{U} (\hat{\rho}_A \otimes |0\rangle_B \, {}_B\langle 0|) \hat{U}^\dagger$$

where the symbol $'$ denotes the density matrix at time t. In order to study only the evolution of the subsystem A, the partial trace over the subsystem B has to be performed:

$$\hat{\rho}'_A = Tr_B(\hat{\rho}'_{AB}) = Tr_B(\hat{U} \hat{\rho}_{AB} \hat{U}^\dagger) = \sum_k {}_B\langle k|\hat{U}|0\rangle_B \hat{\rho}_A \, {}_B\langle 0|\hat{U}^\dagger|k\rangle_B$$

from which we can define the Kraus operator $\hat{E}_k$

$$\hat{E}_k \equiv {}_B\langle k|\hat{U}|0\rangle_B$$

which is an operator acting on the Hilbert space $\mathcal{H}_A$. Since the operator $\hat{U}$ is unitary, the Kraus operator satisfies the following relation

$$\sum_k \hat{E}_k^\dagger \hat{E}_k = \sum_k {}_B\langle 0|\hat{U}^\dagger|k\rangle_B \, {}_B\langle k|\hat{U}|0\rangle_B = {}_B\langle 0|\hat{U}^\dagger \hat{U}|0\rangle_B = \hat{\mathbb{I}}_B$$

where the completeness relation $\sum_k |k\rangle_B \, {}_B\langle k| = \hat{\mathbb{I}}_B$ has been used. We can then write the Kraus representation of the evolution of $\hat{\rho}_A$ as

$$\hat{\rho}'_A = \sum_k \hat{E}_k \hat{\rho}_A \hat{E}_k^\dagger$$

which defines a linear map from linear operators to linear operators

$$\mathcal{E} : \hat{\rho}_A \to \hat{\rho}'_A.$$

$\mathcal{E}$ is known as quantum operator or superoperator and satisfies the following properties

- $\mathcal{E}$ is linear:
$$\mathcal{E}(\lambda\hat{\rho}_1 + (1-\lambda)\hat{\rho}_2) = \lambda\mathcal{E}(\hat{\rho}_1) + (1-\lambda)\mathcal{E}(\hat{\rho}_2)$$
- it preserves hermiticity
- it preserves trace
- it is completely positive.

A map $\mathcal{E}_P$ is said to be positive (P-map) if its action on a given Hilbert space $\mathcal{H}$ preserves the positivity of its eigenvalues. Thus, a positive map transforms physical states into physical states, and in the process the trace is preserved. If any extension $\mathcal{E}' = \mathcal{E}_{CP} \otimes \hat{\mathbb{I}}$ of the map $\mathcal{E}_{CP}$ is also positive, then it is called completely positive map (CP-map) [160, 161]. Unlike $\mathcal{E}_{CP}$, when $\mathcal{E}_P \otimes \hat{\mathbb{I}}$ acts on an entangled state, it looses the eigenstates positivity. This difference can be used to distinguish separable states from entangled ones. A map $\mathcal{E}$ is also known as quantum channel and corresponds to the mathematical representation of an open quantum system, characterized by a non isolated Hilbert space $\mathcal{H}$ which can exchange information, energy or matter with the surrounding environment.

5.3 Markovian and non-Markovian evolutions

5.3.1 The master equation

The derivation of the coherent evolution of a quantum system is performed by means of the associated Hamiltonian, describing the evolution of the system over an infinitesimal time interval. Likewise, it is possible to describe the evolution of a density operator (not necessarily coherent) by means of a differential equation which is called master equation (ME). The existence of a differential equation describing the decoherence of an open system is not obvious. Indeed, such a description exists only if the evolution of the system is Markovian, that is, local in time. For the evolution of the density operator $\hat{\rho}(t)$ to be governed by a differential equation in t, $\hat{\rho}(t+dt)$ must be completely determined by $\hat{\rho}(t)$.
Consider a system S interacting with a surrounding environment E. The evolution of an isolated closed system corresponding to the extended system $S \otimes E$ is governed by its Hamiltonian as

$$|\psi(t+dt)\rangle = e^{-i\hat{H}dt/\hbar}\,|\psi(t)\rangle$$

and in the density matrix form as

$$\hat{\rho}(t+dt) = \hat{\rho}(t) - \frac{i}{\hbar}[\hat{H}, \hat{\rho}(t)]$$

where dt is an infinitesimal time interval. This relation does not guarantee that the evolution of S is Markovian, since the information can flow from S to E and vice versa. In that case it is necessary to know the density matrix $\hat{\rho}_S$ at any time, because $\hat{\rho}_S(t+dt)$ is not completely determined by $\hat{\rho}_S(t)$.
The Markovian evolution for the infinitesimal time interval dt of an open quantum system can be represented by means of the Kraus operator

$$\hat{\rho}(t+dt) = \mathcal{E}_{dt}(\hat{\rho}(t)) = \sum_k \hat{E}_k(dt)\hat{\rho(t)}\hat{E}_k^\dagger(dt) \tag{5.1}$$

$\mathcal{E}_{dt}$ is a superoperator mapping $\hat{\rho}(t)$ into $\hat{\rho}(t+dt)$ while the operators $\hat{E}_k(dt)$ refer to infinitesimal transformation.
By adopting such a Markovian description, we consider that, after each infinitesimal transformation of the joint state of the system and the environment, the state of the environment is traced out and replaced by a new state, which is not entangled with the system. We can write the Kraus operator as

$$\hat{E}_0 = \hat{\mathbb{I}} + \frac{1}{\hbar}(-i\hat{H} + \hat{K})dt$$
$$\hat{E}_k = \hat{L}_k\sqrt{dt}$$

where $\hat{K}$ is an hermitian operator while $\hat{L}_k$ are known as Lindblad operators, which are related to each other by the Kraus normalization condition

$$\left[\hat{\mathbb{I}} + \frac{1}{\hbar}(i\hat{H} + \hat{K}dt)\right]\left[\hat{\mathbb{I}} + \frac{1}{\hbar}(-i\hat{H} + \hat{K})dt\right] + \sum_k \hat{L}_k^\dagger\hat{L}_k dt = \hat{\mathbb{I}}$$

which can be simplified as

$$\frac{2}{\hbar}\hat{K}dt + \sum_k \hat{L}^\dagger\hat{L}_k + O(dt^2) = 0$$

which, by neglecting the second order term in dt, implies

$$\hat{K} = -\frac{\hbar}{2}\sum_k \hat{L}_k^\dagger\hat{L}_k.$$

By substituting $\hat{K}$ in (5.1) we obtain

$$\frac{d\hat{\rho}}{dt} = \mathcal{L}(\hat{\rho}) = -\frac{i}{\hbar}\left[\hat{H}, \hat{\rho}(t)\right] + \sum_k \left(\hat{L}_k\hat{\rho}(t)\hat{L}_k^\dagger - \frac{1}{2}\hat{L}_k^\dagger\hat{L}_k\hat{\rho}(t) - \hat{\rho}(t)\hat{L}_k^\dagger\hat{L}_k\right)$$

where the operator $\hat{\mathcal{L}}$ is called Lindbladian of the evolution. The first term of the second part of the equation is the usual Schrodinger term which generates unitary evolutions while other terms describe the possible transitions which can happen after the interaction with the external environment. This equation is the general one for a Markovian evolution of quantum states.

5.3.2 Non-Markovian evolutions

When dealing with the dynamics of an open quantum system, it can happen that the flow of information, energy and mass can happen in both senses, from system to environment but also in the opposite direction. This can result in a non-Markovian evolution of the system. For any open quantum system, non-Markovian fluctuation are unavoidable and an exact Markovian description of the system is impossible. The definition of non-Markovianity requires the introduction of the concept of P and C divisible maps [162]. Let's consider the evolution of an open quantum system $\hat{\rho}$ through the map $\mathcal{E}(t, t_0)$

$$\hat{\rho}(t) = \mathcal{E}(t, t_0)[\hat{\rho}(t_0)] = \sum_k (t, t_0)\hat{E}_k(t, t_0)\hat{\rho}(t_0)\hat{E}_k^\dagger(t, t_0)$$

where the Kraus operators create a family of dynamical maps $\{\mathcal{E}(t, t_0)|t_0 \leq t\}$. The dynamical map $\mathcal{E}(t, t_0)$ must satisfy the properties of trace preservation, linearity and complete positivity (CP map) and the semi-group property of the family can be written as

$$\mathcal{E}(t_2, t_0) = \mathcal{E}(t_2, t_1) \cdot \mathcal{E}(t_1, t_0) \quad \text{for} \quad t \geq t_2 \geq t_1 \geq t_0. \tag{5.2}$$

A family of dynamical maps $\mathcal{E}(t_2, t_0)$ is called P-divisible if, for all $t_2 \geq t_1 \geq t_0$ there exist a P-map $\mathcal{E}(t_2, t_1)$ such that (5.2) holds. Moreover, if $\mathcal{E}(t_2, t_1)$ is a CP-map then it is named CP-divisible. If a dynamical map $\mathcal{E}(t_2, t_0)$ describing the evolution of an open quantum system is not CP-divisible it is defined as non-Markovian, otherwise it is defined as Markovian [163]. The impossibility to separate the evolution in two or more parts, namely the fact that the dynamical map is not CP-divisible, can be interpreted in terms of memory effects: if the final state of the system only depends on its present state, then the map can be decomposed and the evolution is Markovian. On the contrary, if the final state depends on its history then the dynamical map can not be decomposed and the evolution is non-Markovian [164].

5.3.3 Measurements of non-Markovianity

In the quantum scenario, three different approaches are usually used to quantify the degree of non-Markovianity of a process [165, 166]. The first one consists of the measurement of information back-flow from the environment, acting in this case as a reservoir of information, towards the system [167, 168, 169]. Indeed, in the OQS framework, a communication link between $\mathcal{H}_s$ and $\mathcal{H}_e$, being them part of the total system-environment state $\hat{\rho}_{s,e} \in \mathcal{H}$, is established. In this condition, the strength of the information flow between the system and the environment as a consequence of their interaction can be used to evaluate the level of non-Markovianity of the process. The second approach focuses on the divisibility of the process in Completely Positive (CP) maps, defining the evolution as non-Markovian if the decomposition can not be performed, at some time of the evolution [165, 170]. In cases were such CP divisibility holds, a master equations can be defined [171]. In this work we used the third method, focused on the study of the behaviour of the entanglement between the system and an isolated ancilla. This method is strictly related to the two approaches mentioned above. In order to clarify it, we refer to the next section and to [165, 172].

5.4 Theoretical Model

The theoretical model used to study the evolution of an open quantum system is based on the fact that the environment can be represented by an ensemble of independent Hilbert spaces $\mathcal{H}_e = \mathcal{H}_{e_1} \otimes ... \otimes \mathcal{H}_{e_k}$, and that the system space $\mathcal{H}_s$ interacts sequentially with each of them at discrete times. Such kind of framework defines the so called collisional model (CM) [173, 174, 175, 176, 177], which is an extremely powerful tool in the approximation of continuous-time quantum dynamics through discrete sequential interactions and in the analysis of non-Markovian dynamics of OQSs [178, 179, 180, 181, 182, 183]. Linear optics platforms have been thoroughly exploited for the implementation of CMs [184, 185]. A simple and effective implementation has been proposed, for instance, in [186]. There, the spatial modes of an initial photon state $\hat{\rho}_s(t_0) \in \mathcal{H}_s$ collide sequentially with the modes of an environment ensemble. The environment can be considered as a double space one, i.e. $\mathcal{H}_e = \mathcal{H}_{e_1} \otimes \mathcal{H}_{e_2}$, with the subspace e_2 always prepared in a certain generic state $\hat{\rho}_{e_2} \in \mathcal{H}_{e_2}$ at any step of the process. The interaction between the Hilbert spaces $\mathcal{H}_s$ and $\mathcal{H}_{e_1}$ then controls the evolution of $\hat{\rho}_s(t_k)$. The memory effects are tuned by the inter-environment collisions between $\mathcal{H}_{e_1}$ and $\mathcal{H}_{e_2}$, which also produces an effective evolution in $\hat{\rho}_{e_1}(t_k) \in \mathcal{H}_{e_1}$.

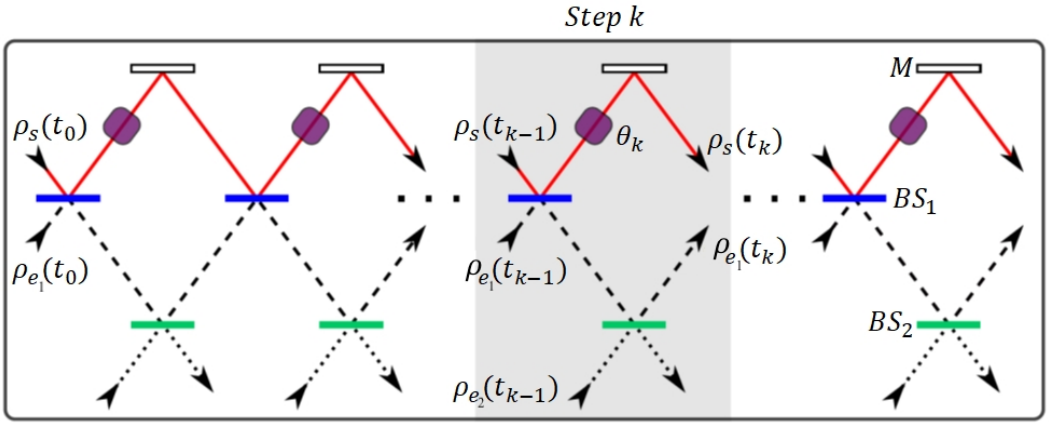

Figure 5.1. Linear optics scheme for the CM: each step k starts with the $s - e_1$ collision in BS_1 (in blue) and it ends with the $e_1 - e_2$ interaction in BS_2 (in green). The phase factor θ_k mediates the collision of the step $(k+1)$ by optical interference.

The optical implementation of the CM reported in [186] is realized by means of a sequence of Mach-Zehnder interferometers (MZIs), as shown in Fig. 5.1. There, the continuous trajectories are associated to $\hat{\rho}_s$, while the segmented ones to $\hat{\rho}_{e_1}$ and the the dotted ones to $\hat{\rho}_{e_2}$. At the k-th step of the evolution, $\hat{\rho}_s(t_{k-1})$ interferes with $\hat{\rho}_{e_1}(t_{k-1})$ in the BS_1, while the inter-environment collision between $\hat{\rho}_{e_1}$ and $\hat{\rho}_{e_2}$ occurs in BS_2, featured by a variable reflectivity $\mathrm{R}_2 \in [0, 1]$ to control the environment memory.
In our proposal (shown in Fig. 5.2 a), we consider that all BS_2 have reflectivity $\mathrm{R}_2 = 1$, such that they can be replaced with perfectly reflective mirrors M. In Fig. 5.2, the continuous red trajectories correspond to the system modes (s-modes), while the segmented black ones correspond to the first environment subspace (e_1-mode), as in Fig. 5.1. In this implementation, the interaction between the first environment subspace e_1 and the second one is performed by means of an absorption interaction and, consequently, it has not defined path (not present in Fig. 5.2). The absorption is realized through the action of a polarization independent neutral filter

F_k placed along the e_1-mode. The super-operator representing the process, which acts on both system and environment, $\mathcal{E}(t_k, t_{k-1})$ is composed by a quarter wave plate (QWP) acting on the s-mode and a half wave plate (HWP) on the e_1-mode, both at fixed rotation angle $\phi = 0$, as shown in Fig. 5.2 b). The actual degree of Markovianity is controlled by the environment memory, which is tuned by the transmissivity factor $T_k \in [0, 1]$ of F_k. The filter links the e_1 modes to the vacuum states stored by $\hat{\rho}_{e_2} = |0\rangle\langle 0|$, thus effectively mimicking the interaction with the dotted-lines of Fig. 5.1. The phase factor θ_k, tuned by means of rotating glass plates, mediates the collision mechanism by controlling the optical interference. By considering this implementation, a purely Markovian dynamics corresponds to the minimum information backflow from $\mathcal{H}_{e_1}$ to $\mathcal{H}_s$. This condition is achieved when the maximum loss of information from $\mathcal{H}_{e_1}$ to $\mathcal{H}_{e_2}$ is reached, corresponding to $T_k = 0$. Non-Markovian dynamics instead can arise whenever $T_k \neq 0$.

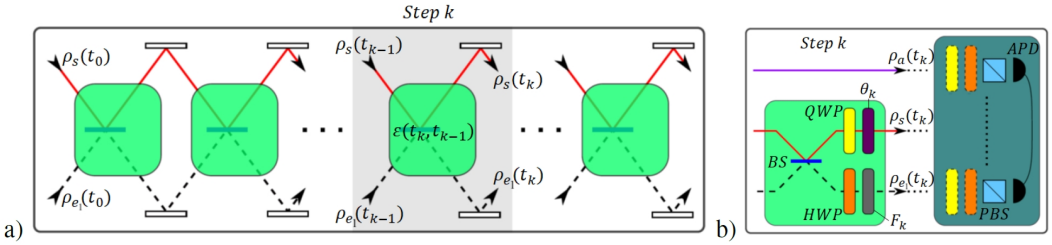

Figure 5.2. Proposed optical scheme, alternative to the one of Fig. 5.1: a) when $R_2 = 1$ each BS_2 can be replaced by a perfectly reflecting mirror M. The system-environment collision occurs whenever $\hat{\rho}_s(t_{k-1})$ interferes with $\hat{\rho}_{e_1}(t_{k-1})$. The interaction process is represented by the green box associated to $\mathcal{E}(t_k, t_{k-1})$. b) A zoom over the generic k-th step. The green boxes include a BS, a QWP and a rotating glass plate inserting a phase factor θ_k in the s-mode, a HWP and a filter F_k in the e_1-mode. The environment memory is controlled by the transmission coefficient T_k of F_k, while θ_k mediates the collision of the step $(k+1)$ as in the original CM. Two-qubit polarization tomographies can be performed between a-s modes or a-e_1-modes [187] by registering the photon coincidences between two avalanche photo-detectors (APDs) after a series of polarization projections through a polarizing beam splitter (PBS).

Suppose that the s-mode is initially maximally entangled with an external ancillary system (a-mode) such that the joint state can be written as $|\Psi^{\pm}_{a,s}\rangle = \frac{1}{\sqrt{2}}(|H\rangle_a |V\rangle_s \pm |V\rangle_a |H\rangle_s)$, where $|H\rangle$ ($|V\rangle$) represents the horizontal (vertical) polarization of the photon. Both the environmental modes are initialized in a vacuum Fock state $|0\rangle$, such that the complete initial state of both the system and the environment corresponds to $\hat{\rho}_{a,s,e_1,e_2}(t_0) = |\Psi^{\pm}\rangle\langle\Psi^{\pm}|$, with

$$
\begin{aligned}
|\Psi^{\pm}\rangle &= \frac{1}{\sqrt{2}}(\hat{a}^{\dagger}_{a,H}\hat{a}^{\dagger}_{s,V} \pm \hat{a}^{\dagger}_{a,V}\hat{a}^{\dagger}_{s,H})\,|0\rangle_{a,s,e_1,e_2} \\
&\equiv \frac{1}{\sqrt{2}}\,(|1_h\rangle_a |1_v\rangle_s \pm |1_v\rangle_a |1_h\rangle_s) \otimes |0\rangle_{e_1} \otimes |0\rangle_{e_2}
\end{aligned}
$$

where $\hat{a}^{\dagger}_x$ is the photon creation operator associated with the x-mode. Note that the probability to loose the s-photon during the propagation, for instance after its interaction with the e_2-mode, is in general $\neq 0$. For this reason, our scheme actually describes the evolution of a qutrit system, with canonical basis given by the states $|1_h\rangle_s$, $|1_v\rangle_s$ and $|0\rangle_s$, where the information is only stored in the bidimensional subspace associated with one-photon states. In our scenario the system-environment

interactions are controlled by a series of operations, such as the BS one, acting on both the system and the e_1 spaces as

$$\begin{aligned}
\hat{BS}_{s,e_1} \cdot \left[|1\rangle_s \otimes |0\rangle_{e_1} \right] &\longrightarrow ir\,|1\rangle_s \otimes |0\rangle_{e_1} + \sqrt{1-r^2}\,|0\rangle_s \otimes |1\rangle_{e_1}\,, \\
\hat{BS}_{s,e_1} \cdot \left[|0\rangle_s \otimes |1\rangle_{e_1} \right] &\longrightarrow ir\,|0\rangle_s \otimes |1\rangle_{e_1} + \sqrt{1-r^2}\,|1\rangle_s \otimes |0\rangle_{e_1}\,, \\
\hat{BS}_{s,e_1} \cdot \left[|0\rangle_s \otimes |0\rangle_{e_1} \right] &\longrightarrow |0\rangle_s \otimes |0\rangle_{e_1}\,,
\end{aligned}$$

where we defined $|1\rangle \equiv (\alpha\,|1_h\rangle + \beta\,|1_v\rangle)/\sqrt{|\alpha|^2+|\beta|^2}$ and $r = \sqrt{R}$ as the reflectivity factor of the BS.
The wave plates act according to

$$H\hat{W}P_{s,e_1} = \hat{\mathbb{I}}_s \otimes \hat{\sigma}^z_{e_1} \quad \text{and} \quad Q\hat{W}P_{s,e_1} = \hat{\sigma}^{z/2}_s \otimes \hat{\mathbb{I}}_{e_1},$$

with $\hat{\sigma}^z = |1_h\rangle\langle 1_h| - |1_v\rangle\langle 1_v| + |0\rangle\langle 0|$, $\hat{\sigma}^{z/2} = |1_h\rangle\langle 1_h| + i\,|1_v\rangle\langle 1_v| + |0\rangle\langle 0|$ and $\hat{\mathbb{I}} = |1_h\rangle\langle 1_h| + |1_v\rangle\langle 1_v| + |0\rangle\langle 0|$.

The absorption operation applied by the filter F links the environment space of the remaining light ($\mathcal{H}_{e_1}$) with the space of the absorbed light ($\mathcal{H}_{e_2}$) according to

$$\begin{aligned}
\hat{F}_{e_1,e_2} \cdot \left[|1\rangle_{e_1} \otimes |0\rangle_{e_2} \right] &\longrightarrow \sqrt{T}\,|1\rangle_{e_1} \otimes |0\rangle_{e_2} + \sqrt{1-T}\,|0\rangle_{e_1} \otimes |1\rangle_{e_2}\,, \\
\hat{F}_{e_1,e_2} \cdot \left[|0\rangle_{e_1} \otimes |1\rangle_{e_2} \right] &\longrightarrow |0\rangle_{e_1} \otimes |1\rangle_{e_2}\,, \\
\hat{F}_{e_1,e_2} \cdot \left[|0\rangle_{e_1} \otimes |0\rangle_{e_2} \right] &\longrightarrow |0\rangle_{e_1} \otimes |0\rangle_{e_2}\,.
\end{aligned}$$

The action of F_k generates the effective inter-environment collisions that reset the e_1-mode to the vacuum state depending on the absorption factor $1-T$. Finally, the phase control acts as

$$\hat{\theta}_{s,e_1} = |0\rangle_s\langle 0|_s \otimes |0\rangle_{e_1}\langle 0|_{e_1} + |0\rangle_s\langle 0|_s \otimes |1\rangle_{e_1}\langle 1|_{e_1} + e^{i\theta}\,|1\rangle_s\langle 1|_s \otimes |0\rangle_{e_1}\langle 0|_{e_1}\,.$$

By considering all the previous relations, we can write the expression of the super-operator as

$$\mathcal{E}(t_k, t_{k-1}) = \hat{\mathbb{I}}_s \otimes \hat{F}_{e_1,e_2} \cdot \left(\left(\hat{\theta}_{s,e_1} \cdot H\hat{W}P_{s,e_1} \cdot Q\hat{W}P_{s,e_1} \cdot \hat{BS}_{s,e_1} \right) \otimes \hat{\mathbb{I}}_{e_2} \right).$$

Consequently, according to our CM, represented in Fig. 5.2, the input state $\hat{\rho}_{a,s,e_1,e_2}(t_0)$ evolves as

$$\hat{\rho}_{a,s,e_1,e_2}(t_1,t_0) = \left(\hat{\mathbb{I}}_a \otimes \mathcal{E}(t_1,t_0) \right) \cdot \hat{\rho}_{a,s,e_1,e_2}(t_0) \cdot \left(\hat{\mathbb{I}}_a \otimes \mathcal{E}(t_1,t_0) \right)^\dagger,$$

at the first step of the evolution. Subsequent steps can be performed by applying the same superoperator $\mathcal{E}(t_k, t_{k-1})$ or by changing it. At the end of the evolution, one can extract the system and measure the ancilla-system state by performing the trace over the environmental spaces $\hat{\rho}_{a,s}(t_k) = Tr_{e_1,e_2}[\hat{\rho}_{a,s,e_1,e_2}(t_k)]$ or the ancilla-environment state by tracing out the system degree of freedom $\hat{\rho}_{a,e_1}(t_k) = Tr_{s,e_2}[\hat{\rho}_{a,s,e_1,e_2}(t_k)]$. The measurements are performed by recording the coincidences needed to reconstruct the density matrix of the subsystems we are

focusing on after the action of the kth single step process.
A characterization of the non-Markovianity of the process can be obtained by studying the evolution of the concurrence $C_{a,s}$ between the ancilla a and the system s at varying of the steps of the evolution. From the results of [165, 188] we know that when the relation $C_{a,s}(t_k) > C_{a,s}(t_{k-1})$ holds for some $k > 1$, a back-flow of information from e_1 to s has occurred, resulting in a clear indication of a non-Markovian character of the system dynamics. On the contrary a null increase of $C_{a,s}(t_k)$ cannot be used as an indication of Markovianity. The magnitude of all information backflows between two steps of the evolution witnesses the degree of non-Markovianity, which can be estimated by considering the integral of the concurrence variation [189, 190], over the time intervals in which it increases, i.e. the quantity

$$\mathcal{N} = \int_{\dot{C}_{a,s}>0} \dot{C}_{a,s}(t)dt. \tag{5.3}$$

As already mentioned, our system s is intrinsically 3-dimensional. For this reason, the $C_{a,s}$ appearing in Eq. (5.3) should be the qutrits concurrence [190] instead of the standard qubit one [189]. However, for the sake of simplicity, in the experimental implementation which we present in the following sections, we shall restrict the analysis only to the entanglement between the single-photon sectors of s and a, by property post-selecting our data. Accordingly, our measurements do not complete capture the full non-Markovian character implicit in Eq. (5.3).

5.5 Experimental Implementation

The experimental implementation of the CM is based on two concatenated bulk optics squared Sagnac interferometers (SIs) as depicted in Fig. 5.3. The two SI are initially prepared in a collinear configuration. By displacing the mirror M in SI_1, the collinear scheme is transformed in a displaced multipass one that replicates the CM of Fig. 5.2. The displaced Sagnac geometry is exactly the same as the one presented in the previous chapters for the realization of the all optical QW. In fact, the QW scheme is based on the one of the CM, which has been realized before the QW, modified by the introduction of the two vertical BDs. In the present realization of the collisional model, we exploit a geometry endowed with high intrinsic phase stability, where different BSs (present in the scheme of Fig. 5.1) are realized by means of different transversal points on a single BS. In the setup, odd steps circulate in SI_1, while even ones circulate in SI_2. The Sagnac configuration is equivalent to the model presented in Fig. 5.2, since we can associate the s-modes and the e_1-modes respectively with the clockwise and counter-clockwise trajectories inside each SI. For the sake of simplicity, from now on we will use the label "e-environment" only for the non absorbed space of the environment, because its complementary part cannot be accessed in our configuration.

The relative phase factors θ_k are realized by inserting a fixed glass plate along all the e-modes inside each SI and different glass plates in every s-mode which are tilted independently (see Fig. 5.3). The presence of FG is mandatory to compensate for the difference in optical path due to the insertion of the TGs, which is greater than the coherence time of the photons. A slight tilt of TG changes the phase of the s-mode with respect to the e-mode through the insertion of a difference in optical paths which is much less than the coherence time of the photon.
The transmissivity factors $\mathrm{T}_k = \frac{\mathrm{T}^e_k}{\mathrm{T}^s_k}$ are implemented by means of a single neutral density filter F^e with transmissivity T^e for each Sagnac interferometer, intersecting

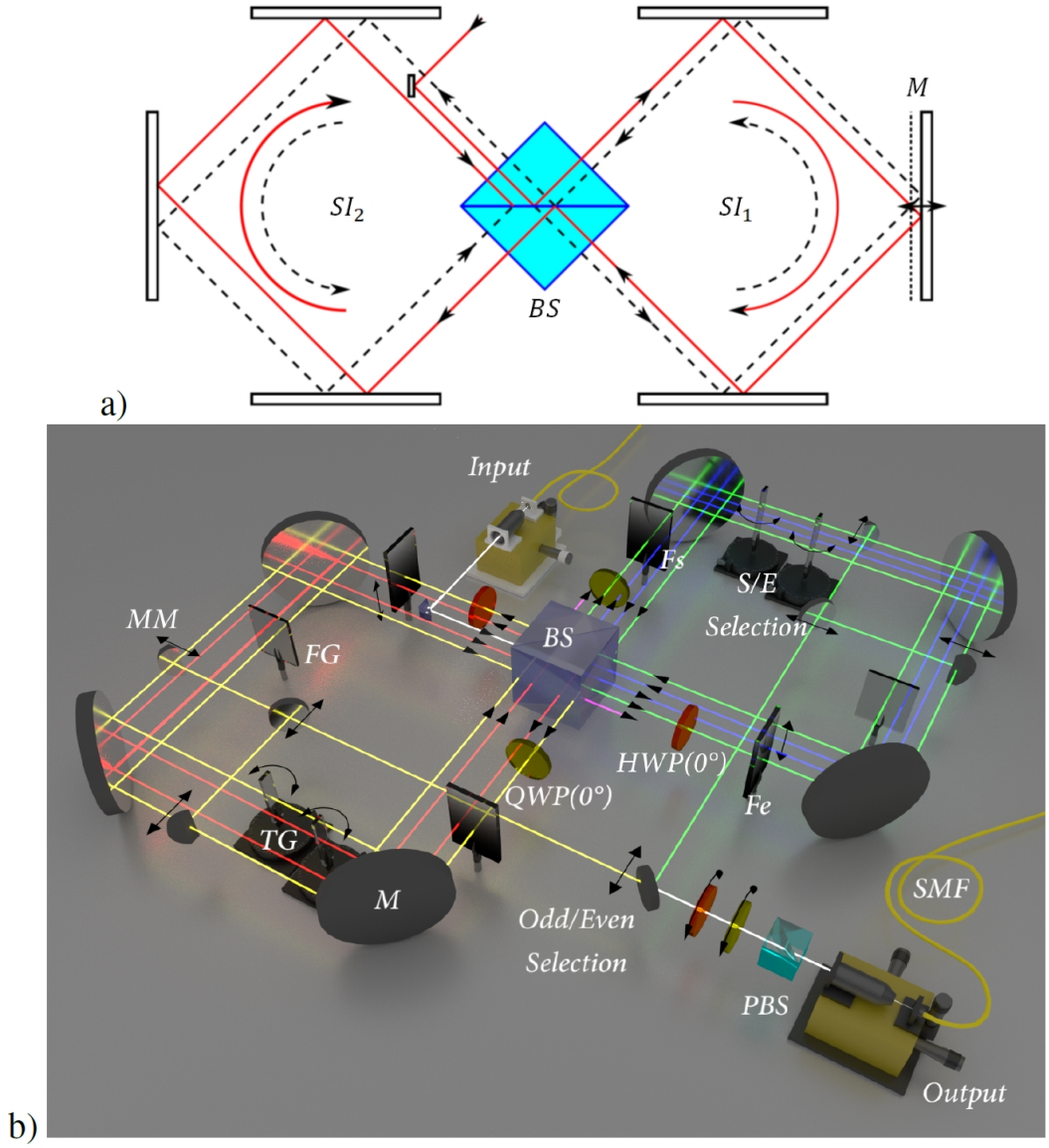

Figure 5.3. **a)** Scheme of the concatenated multipass SI configuration. The s-modes and e-modes circulate in the clockwise and counter-clockwise trajectories inside each SI, respectively. **b)** Complete setup for the collisional model in a 3D view. Different colors of the beams correspond to different steps of the evolution. Here, the blue beams correspond to the first step, red beams to second step, the green ones to the third step and yellow ones to the fourth step. One can extract $\hat{\rho}_{a,s}(t_k)$ or $\hat{\rho}_{a,e}(t_k)$ by selecting the trajectories direction, the odd or even steps by choosing the SI, and the step number by using the external moving mirrors (MM) with translational stages. A single filter F^s and a single filter F^e for all odd and even steps are used such that the evolution is the same at each step k. The phase factor θ_k is tuned by tilting glass plate (TG) with respect to the fixed glass (FG) placed along the environmental modes. Any output qubit can be measured in the tomography stage together with the external ancillary qubit.

all the e-modes, while another filter F^s with transmissivity T^s intersects all the s-modes for time-compensation between both optical paths, as in the glass plates case. Both filters introduce only a controlled absorption, that represents an intrinsic degree

of Markovianity. The s-e absorptions can be mapped by the relative absorption factor T_k. In the same fashion, a single QWP intersects all s-modes of each SI, while a single HWP intersects all the e-modes, such that the evolution is the same at each step of the evolution. Since s- and e-modes contain the same kind of optical elements, the trajectories are temporally compensated with an uncertainty of $< 30\mu m$ per step. The superposition of the 2^k trajectories at step k is collected by a single-mode optical fiber (SMF) after the tomography stage of s-e modes. Analogously, another SMF collects the external a-mode. In the present work, we focused our attention on the case in which all the steps are identical, meaning that a unique filtering factor T_k =F and phase factor $\theta_k = \theta$ are used. Such a regime can be described by

$$\mathcal{E}(t_k, t_0) = (\mathcal{E}(t_1, t_0))^k$$

which corresponds to the case of a stroboscopic evolution (SE) [186].

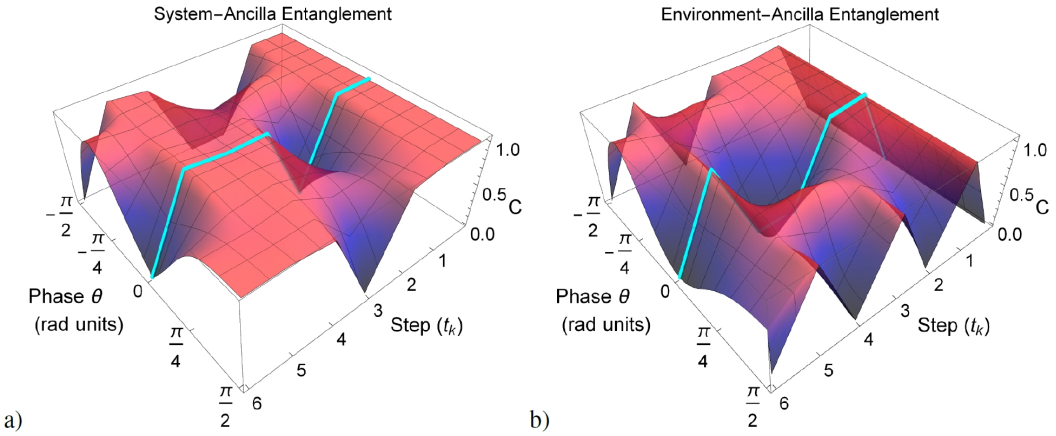

Figure 5.4. Simulated non-Markovian SE of an ideal Bell input state $|\Psi^{\pm}\rangle$ and ideal optical elements. In these simulations, all the steps are prepared with environment memory parameter T= 1 (full non-Markovian regime) and phase difference θ. **a)** Concurrence for system-ancilla state $\hat{\rho}_{a,s}(t_k)$. **b)** Concurrence for environment-ancilla state $\hat{\rho}_{a,e}(t_k)$.

The entangled state $\hat{\rho}_{a,s}(t_0) = |\Psi^{\pm}_{a,s}\rangle \langle\Psi^{\pm}_{a,s}|$ is prepared by means of the entangled photon source described in sec. 2.5.1. One of the two photons generated through the SPDC process is injected in the s-mode of the setup, while the other travels along the external a-mode. Finally, the post-selected state associated to the single-photon sectors of the density matrices $\hat{\rho}_{a,s}(t_k)$ or $\hat{\rho}_{a,e}(t_k)$ is recontructed by means of bipartite hyper-complete tomographies between their associated modes (see Fig. 5.2 b).

In Fig. 5.4 we report the simulated behaviour of the possible non-Markovian dynamics under the SE with maximum environment memory (T= 1) and variable phase factors θ. Simulations were performed by considering ideal Bell input state $|\Psi^{\pm}\rangle$ as well as ideal optical elements, e.g. symmetric BS and no-losses elements. They are useful in the understanding and identification of the flows and back-flows of information, which can be used to engineer s-e couplings and its permeability or temporally localized communications for noise avoidance. Besides the s-e collision, the e-mode also suffers inter-environment collisions with the absorption space of the environment, mediated by the absorptive filters. Thus, there is a complex information exchange where it is difficult to identify particular correlations exclusively between both a-s and a-e concurrence behaviours.
In Fig. 5.5 we report a comparison between three different SEs considering ideal

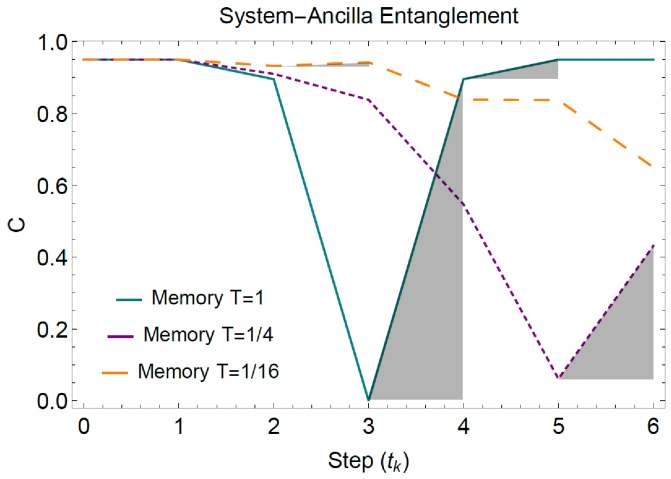

Figure 5.5. Simulated non-Markovian SE for the experimental input state $|\Psi^{\pm}\rangle_{exp}$ in the case of ideal optical elements and $\theta = \pi/4$. The area of the grey shaded regions correspond to the integral contributions in the quantifier $\mathcal{N}$. For finite number of steps, the entanglement revival is lower at lower values of T.

optical elements, the actual experimental input state $|\Psi\rangle_{exp}$, a phase factor $\theta = \pi/2$ and different degrees of memory T. In the case T= 1 it results a fast entanglement fluctuation with a clear non-Markovian degree, quantified by $\mathcal{N} = 0.475$ up to the sixth step. In the case T= 1/4 one obtains a slower entanglement revival, associated with $\mathcal{N} = 0.185$, while in the case T= 1/16, it emerges an even slower fluctuation and a value $\mathcal{N} = 0.005$ (all values of $\mathcal{N}$ reported here are computed on the post-selected single-photon sectors).

5.6 Experimental Results

The experimental test was restricted to the case of a SE with $\theta = 0$, corresponding to the light-blue lines of Fig. 5.4 a) and Fig. 5.4 b), but considering real optical elements. Before sending the system photon in the setup for the evolution, a two qubit tomography of the s-a state has been performed, whose results are reported in Fig. 5.6. The prepared entangled state $\Omega_{a,s}$ showed a purity of 0.956 ± 0.001 and a concurrence $C = 0.954 \pm 0.001$, denoting a very good but not perfect realization of a maximally entangled state. Indeed, the measured fidelity was $F = |\langle\Psi^{\pm}_{a,s}|\,\Omega_{a,s}\,|\Psi^{\pm}_{a,s}\rangle| = 0.9712 \pm 0.0004$.

We then simulated data considering the imperfect realization of the entangled state, described with a Werner input mixed state [191, 192, 193] $\Omega_{a,s} = \frac{4F-1}{3}|\Psi^{\pm}_{a,s}\rangle\langle\Psi^{\pm}_{a,s}| + \frac{1-F}{3}\hat{\mathbb{I}}_a \otimes \hat{\mathbb{I}}_s$.

In order to study the concurrence behavior, two qubit tomographies had to be performed between a and s modes at each step of the evolution. This has been done by selectively extracting the system modes at each step of the evolution and sending them to the tomography stage, measuring coincidences with the ancilla photons. In Fig. 5.7 we present the concurrence trend of the single-photon sectors expressed in the post-selected density matrices $\hat{\rho}_{a,s}(t_k)$ and $\hat{\rho}_{a,e}(t_k)$ during the SE. These states are reconstructed by normalizing the remaining non absorbed coincident photons, and by consequence the associated concurrence values become invariant under losses. Both dynamics behave according to the simulation for the Werner-like input state $\Omega_{a,s}$.

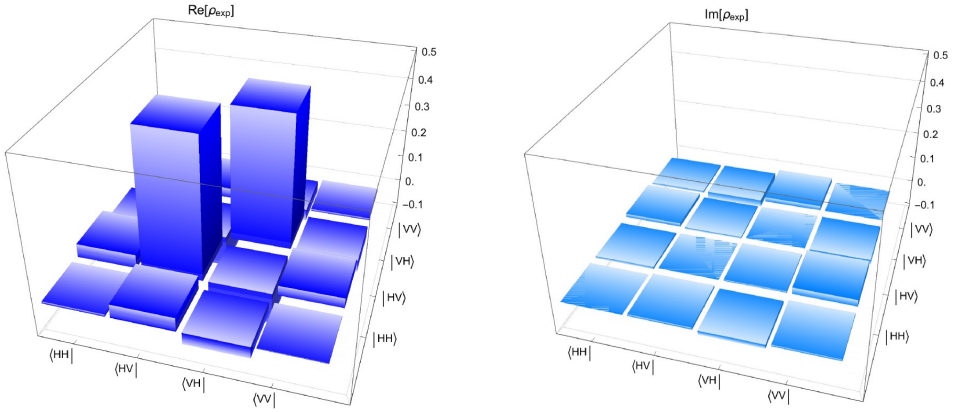

Figure 5.6. Left: real part of the density matrix of the state $\Omega_{a,s}$at the 0-th step. **Right**: imaginary part of the same density matrix.

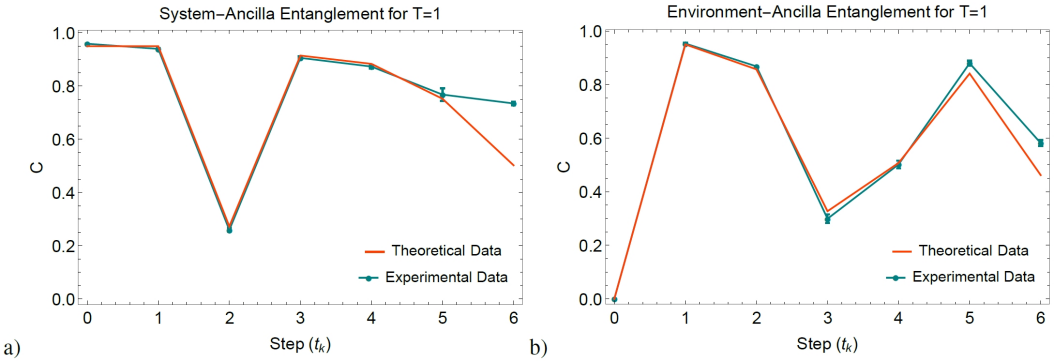

Figure 5.7. Non-Markovian dynamics with maximum memory (T= 1). **a)** Concurrence of $\hat{\rho}_{a,s}(t_k)$. **b)** Concurrence of $\hat{\rho}_{a,e}(t_k)$. All error bars were calculated from the propagation of 100 Monte-Carlo simulations with Poisson statistics, while theoretical data were simulated by considering the actual optical elements of the interferometric setup and the real measured state $\Omega_{a,s}$.

In the case of complete environment memory, i.e. T= 1 of Fig. 5.7 a) we obtained the highest possible non-Markovianity, where the large concurrence fluctuations give us $\mathcal{N} = 0.3232 \pm 0.0001$. As expected from Fig. 5.8, in a reduced memory condition, in this case T= 0.209, we obtained reduced concurrence revivals and a non-Markovianity value of $\mathcal{N} = 0.1442 \pm 0.0001$, while in the complete memoryless case T= 0 we confirmed the lowest possible non-Markovianity by obtaining a near to zero value on $\mathcal{N} = 0.0044 \pm 0.0001$. For our particular CM, these results confirm that entanglement revivals are strictly connected to the environment memory. Indeed, they show with high precision that decreasing values on T correspond to reduced information back-flows to the s-mode from the *e*-mode. The slight deviation from the expected theoretical simulations originates from the not perfect superposition of all possible photon trajectories. Even so, this error is strongly minimized by the use of SMFs as final spatial filters.

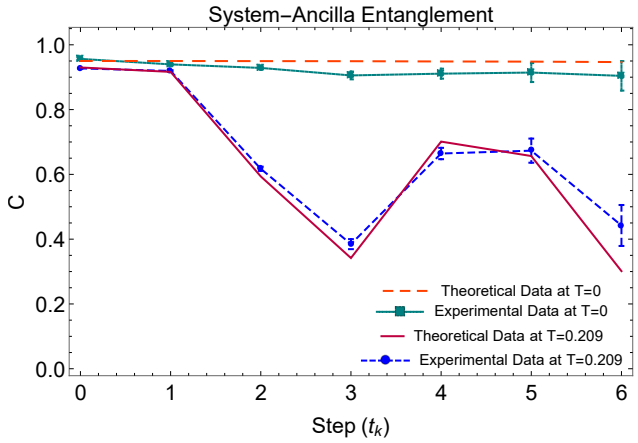

Figure 5.8. Evolution of Polarization Entanglement with reduced memory (T= 0 and T= 0.209). Concurrence of the single-photon sectors, post-select density matrix $\hat{\rho}_{a,s}(t_k)$. All error bars were calculated from the propagation of 100 Monte-Carlo simulations with Poisson statistics, while theoretical data were simulated by considering the actual optical elements of the interferometric setup.

5.7 Conclusions

In this chapter we presented a linear optics setup able to simulate several open quantum systems dynamics, based on a novel interferometric structure that guarantees high phase stability and a multipass evolution in a compact setup, making it possible to study the dynamics up to 6 steps at least. The dynamics studied here represents the very first implementation of the so-called collisional model for open quantum systems [186], and our results correspond to a particular case of it. The ability of the setup in simulating a wide variety of stroboscopic evolutions, from strictly Markovian all the way up to strongly non-Markovian dynamics, where quantum memory effects show their contribution, is extremely useful in the study of such dynamics. With the present setup, we can experimentally track the role of system-environment and intra-environment interactions in the arising of non-Markovian features and characterize the transition between the two regimes. Because of the fact that the field of quantum technologies spreads, more and more attention has being addressed to the study of non-Markovian dynamics. It can, in principle, be used for efficient information processing [194, 195, 196, 197, 198], as well as for engineering novel interesting quantum states [199, 200, 201]. In this perspective, the present setup can be of great interest, thanks to its stability, modular nature and direct access to both system and environmental degrees of freedom.

Chapter 6

Conclusions

This thesis work mainly dealt with the experimental study of the evolution of quantum particles subjected to a 1D QW dynamics. The approach that has been used throughout the study consisted of the introduction of a particular kind of disorder, named p-diluted, on top of a pre-existing one, characterizing the QW network. Aim of the study was to investigate the behaviour of (more than) one quantum walker subjected to move in a discretized space, subjected to random noise. The principal effects which have been theoretically predicted and experimentally confirmed, directly arising from the presence of disorder, were: superdiffusion, when an ordered quantum walk is perturbed with the p-diluted disorder; subdiffusion, when the same disordering technique is applied to a starting statically disordered QW; anomalous diffusion, in both meanings of super- and subdiffusion, of the information flow through the network; enhancement of quantum bosonic correlation due to the presence of some particular disorder configuration.
In the first case, we have reported on the experimental investigation of the superdiffusion process, intermediate between the quantum and classical transport regimes, arising from the introduction of space and time uncorrelated disorder. We studied both cases of single and two indistinguishable photon travelling the line. In the first case, simulated results have shown an unmistakable superdiffusive behaviour and, for all the disorder values under investigation, superdiffusion has been experimentally obtained, despite the relatively low number of steps, i.e. 7 for the single photon evolution and 5 for the two walker case, experimentally reproducible. This is confirmed by the values of the diffusion coefficient β, resulted to be between 1 and 2 for all values of disorder strength.
By means of the very same technique, used to perturb an initial statically disordered QW, the subdiffusive regime has been explored. By analyzing our data regarding the spatial and temporal features of the evolution, we have been able to map the landscape of characteristic properties of subdiffusion, complementing the findings regarding superdiffusion. The very good agreement between the measured data and the theoretical predictions for both the quantities under study, namely the shape of the position distribution and the change of the variance in time, clearly demonstrates that the evolution of the coherent walker is featured by a subdiffusive spread.
The presented experimental results are the first ones confirming the anomalous diffusion properties of the movement of a particle along a discretized line, when it is subjected to completely uncorrelated disorder. Moreover, these findings have been obtained in a completely different way with respect to other earlier studies, in which disorder usually presented some kind of correlation, being it present in time or space degree of freedom. Both studies about superdiffusion and subdiffusion pursued the ultimate goal of implementing a universal quantum simulator. Exceeding our

proof-of-concept realization reported here, our results provide a promising starting point for future studies as well. For instance, a relevant achievement could be the mapping between a simple model, as the QW is, with real systems undergoing the presence of noise.

As a natural prosecution of these studies, we focused on the two walker evolution, considering the correlation between them as the relevant point of interest. The presented numerical and experimental analysis demonstrates that non-classicality based on indistinguishability disperds through the lattice and rapidly decays in an ordered evolution. This behaviour can be challenged by inserting suitable inhomogeneity patterns in the system, which allow to partially retrieve the initial amount of quantum correlations, after a minimum evolution time. This local (and global) enhancement of non-classicality can be tuned in position and intensity by changing the disorder configuration; this corresponds to having an adaptive network whose parameters evaluation determines the focusing of non-classical resources in a selected position, or rather the homogeneous distribution of them. In particular, since the amount of violation is connected to the presence of a NOON state, this method could be useful in Quantum Metrology issues. A step forward in such study could be the possibility to apply similar enhancement procedure to systems with $N > 2$ photons or not; that could result in a benchmarking outcome in the context of Quantum Resource Theories.

Finally, in tight connection with this study, we established a link between the two branches of QW and QI, by analyzing the spread of the information about a parameter encoded in the QW dynamics, when some noise is present during the evolution of the walker. This goal can be achieved by applying quantum metrology techniques to the QW process; in particular, QFI has been used to derive the amount of extractable information concerning the unknown phase acquired by a quantum walker at each step plus random fluctuation in the QW itself. By following the very same path explored in the anomalous diffusion study, we focused on coherent static and dynamic disorder in the QW to describe the transport pattern of information about the unknown parameter ϕ. Surprisingly, we found that the very same disorder regimes leading to anomalous spread of the walker, also lead to the same behaviour for the QFI evolution. Such a study intimately links QW dynamics with quantum metrology theory, exploiting the usefulness of quantities as QFI in the analysis of QW dynamics. The presented results could pave the way for the integration between two main branches of quantum information theory which, as far as we know, up to now basically remain independent from each other. Moreover, due to the increasing interest in studying the spread of information in complex networks, this study represents a basis to deepen such investigations, for instance by enlarging the space over which the walker can move, as well as the number of walkers.

In conclusion, the results obtained during this thesis work can be useful in future investigations, as a starting point for a more deep study about anomalous diffusion and its control as well as about the connection between the QW and QI, which will be more and more relevant with the increasing fields of application of Quantum Mechanics.

Chapter 7

Publication and scientific contributes

Publications

- Laneve, A., Nosrati, F., **Geraldi, A.**, Mahdavipour, K., Pegoraro, F., Shadfar, M. K., Franco, R. L., Mataloni, P., "Experimental enhancement of non-classical bosonic correlations", arXiv preprint arXiv:2102.04755, Submitted, (2020)

- Nosrati, F., Laneve, A., Shadfar, M. K., **Geraldi, A.**, Mahdavipour, K., Pegoraro, F., Mataloni, P., Franco, R. L. "Quantum information spreading in a disordered quantum walk", arXiv preprint arXiv:2010.10592, Submitted, (2020)

- **Geraldi, A.**, De, S., Laneve, A., Barkhofen, S., Sperling, J., Mataloni, P., Silberhorn, C., "Subdiffusion via Disordered Quantum Walks", Accepted for publication on PRResearch, (2020)

- **Geraldi, A.**, Laneve, A., Bonavena, L. D., Sansoni, L., Ferraz, J., Fratalocchi, A., Sciarrino, F., Cuevas, A., Mataloni, P., "Experimental investigation of superdiffusion via coherent disordered Quantum Walks", Physical Review Letters, 123(14), 140501, (2019)

- **Geraldi, A.**, Bonavena, L. D., Liorni, C., Mataloni, P., Cuevas, A., "A Novel Bulk-Optics Scheme for Quantum Walk with High Phase Stability", Condensed Matter, 4(1), 14 (2019).

- Ciampini, M. A., **Geraldi, A.**, Cimini, V., Macchiavello, C., Sipe, J. E., Liscidini, M., and Mataloni, P., "Stimulated emission tomography: beyond polarization", Opt. Lett. 44, 41-44 (2019)

- Cuevas, A., **Geraldi, A.**, Liorni, C., Bonavena, L. D., De Pasquale, A., Sciarrino, F., Giovannetti, V., Mataloni, P. "All-optical implementation of collision-based evolutions of open quantum systems", Scientific reports, 9(1), 3205 (2019)

Oral communications

- "Experimental investigation of anomalous diffusion via coherent disordered

Quantum Walks", September 2020, Accepted at IMEKO TC-4 2020, Palermo, Italy.

- "Experimental Realization of an Innovative Phase-Stable Bulk-Optic Scheme for Quantum Walks", May 2019, Quantum 2019 - From Foundations of Quantum Mechanics to Quantum Information and Quantum Metrology Sensing, Turin, Italy.
- "Stimulated emission tomography of Hyperentangled states", May 2018, CLEO-laser science to photonic application in San Jose', California, USA.
- Stimulated emission tomography of Hyperentangled states, February 2018, 6th International Symposium on Optics and its Applications (Optics 2018) in Trento, Italy.

Poster presentations

- "Experimental study of superdiffusive behaviour in all-optical Quantum Walks", September 2019, Causality in the quantum world: harnessing quantum effects in causal inference problems, Anacapri, Italy.
- "Experimental realization of an innovative Phase-Stable Bulk-Optic scheme for Quantum Walks", June 2019, 26th Central European Workshop on Quantum Optics, Paderborn, Germany.
- "All-Optical Implementation of Collision Based Evolutions of Open Quantum Systems", May 2019, Quantum 2019 - From Foundations of Quantum Mechanics to Quantum Information and Quantum Metrology Sensing, Turin, Italy.
- "Experimental Realization of an Innovative Phase-Stable Bulk-Optic Scheme for Quantum Walks", April 2019, Quantum Information and Measurement (QIM) V: Quantum Technologies, OSA Technical Digest (Optical Society of America, 2019), Rome, Italy.

Bibliography

[1] David J Griffiths and Darrell F Schroeter. *Introduction to quantum mechanics*. Cambridge University Press, 2018.

[2] Giuliano Benenti, Giulio Casati, and Giuliano Strini. *Principles of Quantum Computation and Information-Volume I: Basic Concepts*. World scientific, 2004.

[3] Giuliano Benenti, Giulio Casati, and Giuliano Strini. *Principles of Quantum Computation and Information-Volume II: Basic Tools and Special Topics*. World Scientific Publishing Company, 2007.

[4] Michael A Nielsen and Isaac Chuang. Quantum computation and quantum information, 2002.

[5] Jun John Sakurai and Eugene D Commins. Modern quantum mechanics, revised edition, 1995.

[6] Chong-Ki Hong, Zhe-Yu Ou, and Leonard Mandel. Measurement of subpicosecond time intervals between two photons by interference. *Physical Review Letters*, 59(18):2044, 1987.

[7] Yakir Aharonov, Luiz Davidovich, and Nicim Zagury. Quantum random walks. *Physical Review A*, 48(2):1687, 1993.

[8] Albert Einstein. On the motion required by the molecular kinetic theory of heat of small particles suspended in a stationary liquid. *Annalen der Physik*, 17(8):549–560, 1905.

[9] Ralf Metzler and Joseph Klafter. The restaurant at the end of the random walk: recent developments in the description of anomalous transport by fractional dynamics. *Journal of Physics A: Mathematical and General*, 37(31):R161, 2004.

[10] Manuel O Cáceres and Marco Nizama. The quantum levy walk. *Journal of Physics A: Mathematical and Theoretical*, 43(45):455306, 2010.

[11] Salvador Elías Venegas-Andraca. Quantum walks: a comprehensive review. *Quantum Information Processing*, 11(5):1015–1106, 2012.

[12] Gregory S Engel, Tessa R Calhoun, Elizabeth L Read, Tae-Kyu Ahn, Tomáš Mančal, Yuan-Chung Cheng, Robert E Blankenship, and Graham R Fleming. Evidence for wavelike energy transfer through quantum coherence in photosynthetic systems. *Nature*, 446(7137):782, 2007.

[13] Neill Lambert, Yueh-Nan Chen, Yuan-Chung Cheng, Che-Ming Li, Guang-Yin Chen, and Franco Nori. Quantum biology. *Nature Physics*, 9(1):10, 2013.

[14] Masoud Mohseni, Patrick Rebentrost, Seth Lloyd, and Alan Aspuru-Guzik. Environment-assisted quantum walks in photosynthetic energy transfer. *The Journal of chemical physics*, 129(17):11B603, 2008.

[15] Stephan Hoyer, Mohan Sarovar, and K Birgitta Whaley. Limits of quantum speedup in photosynthetic light harvesting. *New Journal of Physics*, 12(6):065041, 2010.

[16] Vir B Bulchandani, Christoph Karrasch, and Joel E Moore. Superdiffusive transport of energy in generic luttinger liquids. *arXiv preprint arXiv:1904.09287*, 2019.

[17] Matthew A Broome, Alessandro Fedrizzi, Benjimain P Lanyon, Ivan Kassal, Alan Aspuru-Guzik, and Andrew G White. Discrete single-photon quantum walks with tunable decoherence. *Physical Review Letters*, 104(15):153602, 2010.

[18] Andrea Geraldi, Alessandro Laneve, Luis Diego Bonavena, Linda Sansoni, Jose Ferraz, Andrea Fratalocchi, Fabio Sciarrino, Álvaro Cuevas, and Paolo Mataloni. Experimental investigation of superdiffusion via coherent disordered quantum walks. *Physical Review Letters*, 123(14):140501, 2019.

[19] Andrea Geraldi, Syamsundar De, Alessandro Laneve, Sonja Barkhofen, Jan Sperling, Paolo Mataloni, and Christine Silberhorn. Transient subdiffusion via disordered quantum walks. *arXiv preprint arXiv:2007.12526, accepted for publication on PRResearch*, 2020.

[20] Edward Farhi and Sam Gutmann. Quantum computation and decision trees. *Physical Review A*, 58(2):915, 1998.

[21] Frederick W Strauch. Connecting the discrete-and continuous-time quantum walks. *Physical Review A*, 74(3):030301, 2006.

[22] Andrew M Childs, Edward Farhi, and Sam Gutmann. An example of the difference between quantum and classical random walks. *Quantum Information Processing*, 1(1-2):35–43, 2002.

[23] Todd A Brun, Hilary A Carteret, and Andris Ambainis. Quantum walks driven by many coins. *Physical Review A*, 67(5):052317, 2003.

[24] Pedro Ribeiro, Perola Milman, and Remy Mosseri. Aperiodic quantum random walks. *Physical Review Letters*, 93(19):190503, 2004.

[25] Norio Inui, Norio Konno, and Etsuo Segawa. One-dimensional three-state quantum walk. *Physical Review E*, 72(5):056112, 2005.

[26] Norio Inui and Norio Konno. Localization of multi-state quantum walk in one dimension. *Physica A: Statistical Mechanics and its Applications*, 353:133–144, 2005.

[27] Andris Ambainis, Eric Bach, Ashwin Nayak, Ashvin Vishwanath, and John Watrous. One-dimensional quantum walks. In *Proceedings of the thirty-third annual ACM symposium on Theory of computing*, pages 37–49, 2001.

[28] Troy D Mackay, Stephen D Bartlett, Leigh T Stephenson, and Barry C Sanders. Quantum walks in higher dimensions. *Journal of Physics A: Mathematical and General*, 35(12):2745, 2002.

[29] Andrea Geraldi, Luís Diego Bonavena, Carlo Liorni, Paolo Mataloni, and Álvaro Cuevas. A novel bulk-optics scheme for quantum walk with high phase stability. *Condensed Matter*, 4(1):14, 2019.

[30] Andreas Schreiber, Katiuscia N Cassemiro, V Potoček, Aurél Gábris, Peter James Mosley, Erika Andersson, Igor Jex, and Christine Silberhorn. Photons walking the line: A quantum walk with adjustable coin operations. *Physical Review Letters*, 104(5):050502, 2010.

[31] Linda Sansoni, Fabio Sciarrino, Giuseppe Vallone, Paolo Mataloni, Andrea Crespi, Roberta Ramponi, and Roberto Osellame. Two-particle bosonic-fermionic quantum walk via integrated photonics. *Physical Review Letters*, 108(1):010502, 2012.

[32] Alberto Peruzzo, Mirko Lobino, Jonathan CF Matthews, Nobuyuki Matsuda, Alberto Politi, Konstantinos Poulios, Xiao-Qi Zhou, Yoav Lahini, Nur Ismail, Kerstin Wörhoff, et al. Quantum walks of correlated photons. *Science*, 329(5998):1500–1503, 2010.

[33] Maximilian Genske, Wolfgang Alt, Andreas Steffen, Albert H Werner, Reinhard F Werner, Dieter Meschede, and Andrea Alberti. Electric quantum walks with individual atoms. *Physical Review Letters*, 110(19):190601, 2013.

[34] Ashwin Nayak and Ashvin Vishwanath. Quantum walk on the line. *arXiv preprint quant-ph/0010117*, 2000.

[35] Jozef Košík. Two models of quantum random walk. *Central European Journal of Physics*, 1(4):556–573, 2003.

[36] Hilary A Carteret, Mourad EH Ismail, and Bruce Richmond. Three routes to the exact asymptotics for the one-dimensional quantum walk. *Journal of Physics A: Mathematical and General*, 36(33):8775, 2003.

[37] Hilary A Carteret, Bruce Richmond, and Nico M Temme. Evanescence in coined quantum walks. *Journal of Physics A: Mathematical and General*, 38(40):8641, 2005.

[38] Viv Kendon and Ben Tregenna. Decoherence can be useful in quantum walks. *Physical Review A*, 67(4):042315, 2003.

[39] Frederick W Strauch. Reexamination of decoherence in quantum walks on the hypercube. *Physical Review A*, 79(3):032319, 2009.

[40] Hideaki Obuse and Norio Kawakami. Topological phases and delocalization of quantum walks in random environments. *Physical Review B*, 84(19):195139, 2011.

[41] Jozef Košík, Vladimír Bužek, and Mark Hillery. Quantum walks with random phase shifts. *Physical Review A*, 74(2):022310, 2006.

[42] Neil Shenvi, Julia Kempe, and K Birgitta Whaley. Quantum random-walk search algorithm. *Physical Review A*, 67(5):052307, 2003.

[43] Avatar Tulsi. Faster quantum-walk algorithm for the two-dimensional spatial search. *Physical Review A*, 78(1):012310, 2008.

[44] Andris Ambainis, Julia Kempe, and Alexander Rivosh. Coins make quantum walks faster. *arXiv preprint quant-ph/0402107*, 2004.

[45] Nicola Dalla Pozza and Filippo Caruso. Quantum state discrimination on reconfigurable noise-robust quantum networks. *Physical Review Research*, 2(4):043011, 2020.

[46] Andrew M Childs. Universal computation by quantum walk. *Physical Review Letters*, 102(18):180501, 2009.

[47] Neil B Lovett, Sally Cooper, Matthew Everitt, Matthew Trevers, and Viv Kendon. Universal quantum computation using the discrete-time quantum walk. *Physical Review A*, 81(4):042330, 2010.

[48] Philip Walther, Kevin J Resch, Terry Rudolph, Emmanuel Schenck, Harald Weinfurter, Vlatko Vedral, Markus Aspelmeyer, and Anton Zeilinger. Experimental one-way quantum computing. *Nature*, 434(7030):169–176, 2005.

[49] Andrea Crespi, Stefano Longhi, and Roberto Osellame. Photonic realization of the quantum rabi model. *Physical Review Letters*, 108(16):163601, 2012.

[50] Mikael C Rechtsman, Julia M Zeuner, Yonatan Plotnik, Yaakov Lumer, Daniel Podolsky, Felix Dreisow, Stefan Nolte, Mordechai Segev, and Alexander Szameit. Photonic floquet topological insulators. *Nature*, 496(7444):196–200, 2013.

[51] Robert Keil, Changsuk Noh, Amit Rai, Simon Stützer, Stefan Nolte, Dimitris G Angelakis, and Alexander Szameit. Optical simulation of charge conservation violation and majorana dynamics. *Optica*, 2(5):454–459, 2015.

[52] Andrea Crespi, Linda Sansoni, Giuseppe Della Valle, Alessio Ciamei, Roberta Ramponi, Fabio Sciarrino, Paolo Mataloni, Stefano Longhi, and Roberto Osellame. Particle statistics affects quantum decay and fano interference. *Physical Review Letters*, 114(9):090201, 2015.

[53] Maxime Lebugle, Markus Gräfe, René Heilmann, Armando Perez-Leija, Stefan Nolte, and Alexander Szameit. Experimental observation of n00n state bloch oscillations. *Nature communications*, 6(1):1–7, 2015.

[54] M B Plenio and S F Huelga. Dephasing-assisted transport: quantum networks and biomolecules. *New Journal of Physics*, 10:113019, 2008.

[55] M Christandl, N Datta, A Ekert, and A J Landahl. Perfect state transfer in quantum spin networks. *Physical Review Letters*, 92:187902, 2004.

[56] A Ahlbrecht, A Alberti, D Meschede, V B Scholz, A H Werner, and Werner R F. Molecular binding in interacting quantum walks. *New Journal of Physics*, 14:073050, 2012.

[57] Vinay V Ramasesh, Emmanuel Flurin, M Rudner, Irfan Siddiqi, and Norman Y Yao. Direct probe of topological invariants using bloch oscillating quantum walks. *Physical Review Letters*, 118(13):130501, 2017.

[58] Sonja Barkhofen, Thomas Nitsche, Fabian Elster, Lennart Lorz, Aurél Gábris, Igor Jex, and Christine Silberhorn. Measuring topological invariants in disordered discrete-time quantum walks. *Physical Review A*, 96(3):033846, 2017.

[59] L Xiao, X Zhan, ZH Bian, KK Wang, X Zhang, XP Wang, J Li, K Mochizuki, D Kim, N Kawakami, et al. Observation of topological edge states in parity–time-symmetric quantum walks. *Nature Physics*, 13(11):1117–1123, 2017.

[60] Thomas Nitsche, Tobias Geib, Christoph Stahl, Lennart Lorz, Christopher Cedzich, Sonja Barkhofen, Reinhard F Werner, and Christine Silberhorn. Eigenvalue measurement of topologically protected edge states in split-step quantum walks. *New Journal of Physics*, 21(4):043031, 2019.

[61] Gunter M Schütz and Steffen Trimper. Elephants can always remember: Exact long-range memory effects in a non-markovian random walk. *Physical Review E*, 70(4):045101, 2004.

[62] Julia Kempe. Quantum random walks: an introductory overview. *Contemporary Physics*, 44(4):307–327, 2003.

[63] Philip W Anderson. Absence of diffusion in certain random lattices. *Physical Review*, 109(5):1492, 1958.

[64] Alejandro Romanelli. Driving quantum-walk spreading with the coin operator. *Physical Review A*, 80(4):042332, 2009.

[65] Andre Ahlbrecht, Volkher B Scholz, and Albert H Werner. Disordered quantum walks in one lattice dimension. *Journal of Mathematical Physics*, 52(10):102201, 2011.

[66] Andrea Crespi, Roberto Osellame, Roberta Ramponi, Vittorio Giovannetti, Rosario Fazio, Linda Sansoni, Francesco De Nicola, Fabio Sciarrino, and Paolo Mataloni. Anderson localization of entangled photons in an integrated quantum walk. *Nature Photonics*, 7(4):322, 2013.

[67] A Schreiber, KN Cassemiro, V Potoček, A Gábris, I Jex, and Ch Silberhorn. Decoherence and disorder in quantum walks: From ballistic spread to localization. *Physical Review Letters*, 106(18):180403, 2011.

[68] Andre Ahlbrecht, Holger Vogts, Albert H Werner, and Reinhard F Werner. Asymptotic evolution of quantum walks with random coin. *Journal of Mathematical Physics*, 52(4):042201, 2011.

[69] Diederik S Wiersma, Paolo Bartolini, Ad Lagendijk, and Roberto Righini. Localization of light in a disordered medium. *Nature*, 390(6661):671–673, 1997.

[70] Hefei Hu, A Strybulevych, JH Page, Sergey E Skipetrov, and Bart A van Tiggelen. Localization of ultrasound in a three-dimensional elastic network. *Nature Physics*, 4(12):945–948, 2008.

[71] SS Abdullaev and F Kh Abdullaev. On propagation of light in fiber bundles with random parameters. *Radiofizika*, 23(6):766–767, 1980.

[72] Hans De Raedt, AD Lagendijk, and Pedro de Vries. Transverse localization of light. *Physical Review Letters*, 62(1):47, 1989.

[73] Tal Schwartz, Guy Bartal, Shmuel Fishman, and Mordechai Segev. Transport and anderson localization in disordered two-dimensional photonic lattices. *Nature*, 446(7131):52, 2007.

[74] Yoav Lahini, Assaf Avidan, Francesca Pozzi, Marc Sorel, Roberto Morandotti, Demetrios N Christodoulides, and Yaron Silberberg. Anderson localization and nonlinearity in one-dimensional disordered photonic lattices. *Physical Review Letters*, 100(1):013906, 2008.

[75] Alán Aspuru-Guzik and Philip Walther. Photonic quantum simulators. *Nature physics*, 8(4):285–291, 2012.

[76] Yaron Bromberg, Yoav Lahini, Roberto Morandotti, and Yaron Silberberg. Quantum and classical correlations in waveguide lattices. *Physical Review Letters*, 102(25):253904, 2009.

[77] Yoav Lahini, Rami Pugatch, Francesca Pozzi, Marc Sorel, Roberto Morandotti, Nir Davidson, and Yaron Silberberg. Observation of a localization transition in quasiperiodic photonic lattices. *Physical Review Letters*, 103(1):013901, 2009.

[78] Yoav Lahini, Yaron Bromberg, Demetrios N Christodoulides, and Yaron Silberberg. Quantum correlations in two-particle anderson localization. *Physical Review Letters*, 105(16):163905, 2010.

[79] Vadim Oganesyan and David A Huse. Localization of interacting fermions at high temperature. *Physical Review B*, 75(15):155111, 2007.

[80] AM Jayannavar and N Kumar. Nondiffusive quantum transport in a dynamically disordered medium. *Physical Review Letters*, 48(8):553, 1982.

[81] Leonardo Golubović, Shechao Feng, and Fan-An Zeng. Classical and quantum superdiffusion in a time-dependent random potential. *Physical Review Letters*, 67(16):2115, 1991.

[82] Marshall N Rosenbluth. Comment on "classical and quantum superdiffusion in a time-dependent random potential". *Physical Review Letters*, 69(12):1831, 1992.

[83] Yevgeny Krivolapov, Liad Levi, Shmuel Fishman, Mordechai Segev, and Michael Wilkinson. Super-diffusion in optical realizations of anderson localization. *New Journal of Physics*, 14(4):043047, 2012.

[84] Liad Levi, Yevgeny Krivolapov, Shmuel Fishman, and Mordechai Segev. Hyper-transport of light and stochastic acceleration by evolving disorder. *Nature Physics*, 8(12):912, 2012.

[85] Binh Do, Michael L Stohler, Sunder Balasubramanian, Daniel S Elliott, Christopher Eash, Ephraim Fischbach, Michael A Fischbach, Arthur Mills, and Benjamin Zwickl. Experimental realization of a quantum quincunx by use of linear optical elements. *JOSA B*, 22(2):499–504, 2005.

[86] Andrea Crespi, Roberto Osellame, Roberta Ramponi, Vittorio Giovannetti, Rosario Fazio, Linda Sansoni, Francesco De Nicola, Fabio Sciarrino, and Paolo Mataloni. Anderson localization of entangled photons in an integrated quantum walk. *Nature Photonics*, 7(4):322, 2013.

[87] Fulvio Flamini, Nicolò Spagnolo, and Fabio Sciarrino. Photonic quantum information processing: a review. *Reports on Progress in Physics*, 82(1):016001, 2018.

[88] Álvaro Cuevas, Andrea Geraldi, Carlo Liorni, Luís Diego Bonavena, Antonella De Pasquale, Fabio Sciarrino, Vittorio Giovannetti, and Paolo Mataloni. All-optical implementation of collision-based evolutions of open quantum systems. *Scientific reports*, 9(1):3205, 2019.

[89] Alessandro Fedrizzi, Thomas Herbst, Andreas Poppe, Thomas Jennewein, and Anton Zeilinger. A wavelength-tunable fiber-coupled source of narrowband entangled photons. *Optics Express*, 15(23):15377–15386, 2007.

[90] Shin-Tson Wu. Birefringence dispersions of liquid crystals. *Physical Review A*, 33(2):1270, 1986.

[91] T Nitsche, S Barkhofen, R Kruse, L Sansoni, M Štefaňák, A Gábris, V Potoček, T Kiss, I Jex, and C Silberhorn. Probing measurement-induced effects in quantum walks via recurrence. *Science Advances*, 4(6):eaar6444, 2018.

[92] Farzam Nosrati, Alessandro Laneve, Mahshid Khazaei Shadfar, Andrea Geraldi, Kobra Mahdavipour, Federico Pegoraro, Paolo Mataloni, and Rosario Lo Franco. Quantum information spreading in a disordered quantum walk. 2020.

[93] M B Plenio and Susana F Huelga. Dephasing-assisted transport: quantum networks and biomolecules. *New Journal of Physics*, 10(11):113019, 2008.

[94] Henk Van Beijeren. Exact results for anomalous transport in one-dimensional hamiltonian systems. *Physical Review Letters*, 108(18):180601, 2012.

[95] Eunho Kim, Alejandro J Martínez, Sean E Phenisee, PG Kevrekidis, Mason A Porter, and Jinkyu Yang. Direct measurement of superdiffusive energy transport in disordered granular chains. *Nature communications*, 9(1):640, 2018.

[96] Romain Vasseur and Joel E Moore. Nonequilibrium quantum dynamics and transport: from integrability to many-body localization. *Journal of Statistical Mechanics: Theory and Experiment*, 2016(6):064010, 2016.

[97] Mordechai Segev, Yaron Silberberg, and Demetrios N Christodoulides. Anderson localization of light. *Nature Photonics*, 7(3):197, 2013.

[98] A Schreiber, KN Cassemiro, V Potoček, A Gábris, I Jex, and Ch Silberhorn. Decoherence and disorder in quantum walks: from ballistic spread to localization. *Physical Review Letters*, 106(18):180403, 2011.

[99] Viv Kendon. Decoherence in quantum walks–a review. *Mathematical structures in computer science*, 17(6):1169–1220, 2007.

[100] Shlomo Havlin and Daniel Ben-Avraham. Diffusion in disordered media. *Advances in physics*, 51(1):187–292, 2002.

[101] Ralf Metzler, Jae-Hyung Jeon, Andrey G Cherstvy, and Eli Barkai. Anomalous diffusion models and their properties: non-stationarity, non-ergodicity, and ageing at the centenary of single particle tracking. *Physical Chemistry Chemical Physics*, 16(44):24128–24164, 2014.

[102] I Bronstein, Y Israel, E Kepten, S Mai, Yaron Shav-Tal, E Barkai, and Y Garini. Transient anomalous diffusion of telomeres in the nucleus of mammalian cells. *Physical Review Letters*, 103(1):018102, 2009.

[103] Helena LE Coker, Matthew R Cheetham, Daniel R Kattnig, Yong J Wang, Sergi Garcia-Manyes, and Mark I Wallace. Controlling anomalous diffusion in lipid membranes. *Biophysical Journal*, 116(6):1085–1094, 2019.

[104] Benjamin M Regner, Dejan Vučinić, Cristina Domnisoru, Thomas M Bartol, Martin W Hetzer, Daniel M Tartakovsky, and Terrence J Sejnowski. Anomalous diffusion of single particles in cytoplasm. *Biophysical Journal*, 104(8):1652–1660, 2013.

[105] Yonatan Golan and Eilon Sherman. Resolving mixed mechanisms of protein subdiffusion at the t cell plasma membrane. *Nature Communications*, 8(1):1–15, 2017.

[106] Stefano Marano and Massimo Franceschetti. Ray propagation in a random lattice: a maximum entropy, anomalous diffusion process. *IEEE Transactions on Antennas and Propagation*, 53(6):1888–1896, 2005.

[107] Matti S Toivonen, Olimpia D Onelli, Gianni Jacucci, Ville Lovikka, Orlando J Rojas, Olli Ikkala, and Silvia Vignolini. Anomalous-diffusion-assisted brightness in white cellulose nanofibril membranes. *Advanced Materials*, 30(16):1704050, 2018.

[108] Harvey Scher and Elliott W Montroll. Anomalous transit-time dispersion in amorphous solids. *Physical Review B*, 12(6):2455, 1975.

[109] Kartiek Agarwal, Sarang Gopalakrishnan, Michael Knap, Markus Müller, and Eugene Demler. Anomalous diffusion and griffiths effects near the many-body localization transition. *Physical Review Letters*, 114(16):160401, 2015.

[110] Jaume Masoliver, Miquel Montero, and George H Weiss. Continuous-time random-walk model for financial distributions. *Physical Review E*, 67(2):021112, 2003.

[111] Wen Chen, Hongguang Sun, Xiaodi Zhang, and Dean Korošak. Anomalous diffusion modeling by fractal and fractional derivatives. *Computers & Mathematics with Applications*, 59(5):1754–1758, 2010.

[112] Daniel Ben-Avraham and Shlomo Havlin. *Diffusion and reactions in fractals and disordered systems*. Cambridge University Press, 2000.

[113] Jae-Hyung Jeon and Ralf Metzler. Fractional brownian motion and motion governed by the fractional langevin equation in confined geometries. *Physical Review E*, 81(2):021103, 2010.

[114] Elliott W Montroll and George H Weiss. Random walks on lattices. ii. *Journal of Mathematical Physics*, 6(2):167–181, 1965.

[115] E Abad, SB Yuste, and Katja Lindenberg. Reaction-subdiffusion and reaction-superdiffusion equations for evanescent particles performing continuous-time random walks. *Physical Review E*, 81(3):031115, 2010.

[116] Massimiliano Giona and H Eduardo Roman. Fractional diffusion equation for transport phenomena in random media. *Physica A: Statistical Mechanics and its Applications*, 185(1-4):87–97, 1992.

[117] T Nitsche, S De, S Barkhofen, E Meyer-Scott, J Tiedau, J Sperling, Gábris A, I Jex, and C Silberhorn. Local versus global two-photon interference in quantum networks. *arXiv:2005.07219*.

[118] Emanuele Polino, Mauro Valeri, Nicolò Spagnolo, and Fabio Sciarrino. Photonic quantum metrology. *arXiv preprint arXiv:2003.05821*, 2020.

[119] Carl W Helstrom. Quantum detection and estimation theory. 1976.

[120] Alexander S Holevo. *Probabilistic and statistical aspects of quantum theory*, volume 1. Springer Science & Business Media, 2011.

[121] Dénes Petz and Csaba Sudár. Geometries of quantum states. *Journal of Mathematical Physics*, 37(6):2662–2673, 1996.

[122] Dénes Petz. Covariance and fisher information in quantum mechanics. *Journal of Physics A: Mathematical and General*, 35(4):929, 2002.

[123] Matteo GA Paris. Quantum estimation for quantum technology. *International Journal of Quantum Information*, 7(supp01):125–137, 2009.

[124] Alessandro Laneve, Farzam Nosrati, Andrea Geraldi, Kobra Mahdavipour, Federico Pegoraro, Mahshid Khazaei Shadfar, Rosario Lo Franco, and Paolo Mataloni. Enhancing nonclassical bosonic correlations in a quantum walk network through experimental control of disorder. *arXiv preprint arXiv:2102.04755*, 2021.

[125] Peter L Knight, Eugenio Roldán, and JE Sipe. Propagating quantum walks: the origin of interference structures. *journal of modern optics*, 51(12):1761–1777, 2004.

[126] Hyunseok Jeong, Mauro Paternostro, and Myungshik S Kim. Simulation of quantum random walks using the interference of a classical field. *Physical Review A*, 69(1):012310, 2004.

[127] Y Omar, N Paunković, L Sheridan, and S Bose. Quantum walk on a line with two entangled particles. *Physical Review A*, 74(4):042304, 2006.

[128] PK Pathak and GS Agarwal. Quantum random walk of two photons in separable and entangled states. *Physical Review A*, 75(3):032351, 2007.

[129] Charles H Bennett, David P DiVincenzo, John A Smolin, and William K Wootters. Mixed-state entanglement and quantum error correction. *Physical Review A*, 54(5):3824, 1996.

[130] Vlatko Vedral, Martin B Plenio, Michael A Rippin, and Peter L Knight. Quantifying entanglement. *Physical Review Letters*, 78(12):2275, 1997.

[131] Sandu Popescu and Daniel Rohrlich. Thermodynamics and the measure of entanglement. *Physical Review A*, 56(5):R3319, 1997.

[132] Fernando GSL Brandao and Martin B Plenio. Entanglement theory and the second law of thermodynamics. *Nature Physics*, 4(11):873–877, 2008.

[133] Abner Shimony. Degree of entanglement. *Annals of the New York Academy of Sciences*, 755(1):675–679, 1995.

[134] Rosario Lo Franco and Giuseppe Compagno. Quantum entanglement of identical particles by standard information-theoretic notions. *Scientific reports*, 6:20603, 2016.

[135] Jan Sperling, Armando Perez-Leija, Kurt Busch, and Ian A Walmsley. Quantum coherences of indistinguishable particles. *Physical Review A*, 96(3):032334, 2017.

[136] Armando Perez-Leija, Diego Guzmán-Silva, Roberto de J León-Montiel, Markus Gräfe, Matthias Heinrich, Hector Moya-Cessa, Kurt Busch, and Alexander Szameit. Endurance of quantum coherence due to particle indistinguishability in noisy quantum networks. *npj Quantum Information*, 4(1):1–12, 2018.

[137] Rosario Lo Franco and Giuseppe Compagno. Indistinguishability of elementary systems as a resource for quantum information processing. *Physical Review Letters*, 120(24):240403, 2018.

[138] Alessia Castellini, Rosario Lo Franco, Ludovico Lami, Andreas Winter, Gerardo Adesso, and Giuseppe Compagno. Indistinguishability-enabled coherence for quantum metrology. *Physical Review A*, 100(1):012308, 2019.

[139] Scott Aaronson and Alex Arkhipov. The computational complexity of linear optics. In *Proceedings of the forty-third annual ACM symposium on Theory of computing*, pages 333–342, 2011.

[140] Nicolo Spagnolo, Chiara Vitelli, Marco Bentivegna, Daniel J Brod, Andrea Crespi, Fulvio Flamini, Sandro Giacomini, Giorgio Milani, Roberta Ramponi, Paolo Mataloni, et al. Experimental validation of photonic boson sampling. *Nature Photonics*, 8(8):615–620, 2014.

[141] Han-Sen Zhong, Hui Wang, Yu-Hao Deng, Ming-Cheng Chen, Li-Chao Peng, Yi-Han Luo, Jian Qin, Dian Wu, Xing Ding, Yi Hu, Peng Hu, Xiao-Yan Yang, Wei-Jun Zhang, Hao Li, Yuxuan Li, Xiao Jiang, Lin Gan, Guangwen Yang, Lixing You, Zhen Wang, Li Li, Nai-Le Liu, Chao-Yang Lu, and Jian-Wei Pan. Quantum computational advantage using photons. *Science*, 2020.

[142] R Lo Franco, Bruno Bellomo, Erika Andersson, and Giuseppe Compagno. Revival of quantum correlations without system-environment back-action. *Physical Review A*, 85(3):032318, 2012.

[143] Jin-Shi Xu, Kai Sun, Chuan-Feng Li, Xiao-Ye Xu, Guang-Can Guo, Erika Andersson, Rosario Lo Franco, and Giuseppe Compagno. Experimental recovery of quantum correlations in absence of system-environment back-action. *Nature communications*, 4(1):1–7, 2013.

[144] Yoav Lahini, Mor Verbin, Sebastian D Huber, Yaron Bromberg, Rami Pugatch, and Yaron Silberberg. Quantum walk of two interacting bosons. *Physical Review A*, 86(1):011603, 2012.

[145] Konstantinos Poulios, Robert Keil, Daniel Fry, Jasmin DA Meinecke, Jonathan CF Matthews, Alberto Politi, Mirko Lobino, Markus Gräfe, Matthias

Heinrich, Stefan Nolte, et al. Quantum walks of correlated photon pairs in two-dimensional waveguide arrays. *Physical Review Letters*, 112(14):143604, 2014.

[146] J. I. Cirac and P. Zoller. Quantum computations with cold trapped ions. *Phys. Rev. Lett.*, 74:4091–4094, May 1995.

[147] Daniel Loss and David P. DiVincenzo. Quantum computation with quantum dots. *Phys. Rev. A*, 57:120–126, Jan 1998.

[148] Adeline Orieux, Antonio d'Arrigo, Giacomo Ferranti, Rosario Lo Franco, Giuliano Benenti, Elisabetta Paladino, Giuseppe Falci, Fabio Sciarrino, and Paolo Mataloni. Experimental on-demand recovery of entanglement by local operations within non-markovian dynamics. *Scientific reports*, 5:8575, 2015.

[149] Bi-Heng Liu, Li Li, Yun-Feng Huang, Chuan-Feng Li, Guang-Can Guo, Elsi-Mari Laine, Heinz-Peter Breuer, and Jyrki Piilo. Experimental control of the transition from markovian to non-markovian dynamics of open quantum systems. *Nature Physics*, 7(12):931, 2011.

[150] Chang-Ling Zou, Xiang-Dong Chen, Xiao Xiong, Fang-Wen Sun, Xu-Bo Zou, Zheng-Fu Han, and Guang-Can Guo. Photonic simulation of system-environment interaction: Non-markovian processes and dynamical decoupling. *Phys. Rev. A*, 88:063806, Dec 2013.

[151] Zhao-Di Liu, Henri Lyyra, Yong-Nan Sun, Bi-Heng Liu, Chuan-Feng Li, Guang-Can Guo, Sabrina Maniscalco, and Jyrki Piilo. Experimental implementation of fully controlled dephasing dynamics and synthetic spectral densities. *Nature Communications*, 9(1):3453, 2018.

[152] Inés de Vega and Daniel Alonso. Dynamics of non-markovian open quantum systems. *Rev. Mod. Phys.*, 89:015001, Jan 2017.

[153] A Rosario, E Massoni, and F De Zela. On the relationship between non-markovianity and entanglement protection. *Journal of Physics B: Atomic, Molecular and Optical Physics*, 45(9):095501, 2012.

[154] Barbara M. Terhal and Guido Burkard. Fault-tolerant quantum computation for local non-markovian noise. *Phys. Rev. A*, 71:012336, Jan 2005.

[155] Jian-Shun Tang, Chuan-Feng Li, Yu-Long Li, Xu-Bo Zou, Guang-Can Guo, Heinz-Peter Breuer, Elsi-Mari Laine, and Jyrki Piilo. Measuring non-markovianity of processes with controllable system-environment interaction. *EPL (Europhysics Letters)*, 97(1):10002, 2012.

[156] Bi-Heng Liu, Dong-Yang Cao, Yun-Feng Huang, Chuan-Feng Li, Guang-Can Guo, Elsi-Mari Laine, Heinz-Peter Breuer, and Jyrki Piilo. Photonic realization of nonlocal memory effects and non-markovian quantum probes. *Sci Rep*, 3:1781, May 2013.

[157] Dariusz Chruściński and Andrzej Kossakowski. Witnessing non-markovianity of quantum evolution. *The European Physical Journal D*, 68(1):7, Jan 2014.

[158] Carole Addis, Bogna Bylicka, Dariusz Chruściński, and Sabrina Maniscalco. Comparative study of non-markovianity measures in exactly solvable one- and two-qubit models. *Phys. Rev. A*, 90:052103, Nov 2014.

[159] A Romanelli, AC Sicardi Schifino, R Siri, G Abal, A Auyuanet, and R Donangelo. Quantum random walk on the line as a markovian process. *Physica A: Statistical Mechanics and its Applications*, 338(3-4):395–405, 2004.

[160] Man-Duen Choi. Completely positive linear maps on complex matrices. *Linear algebra and its applications*, 10(3):285–290, 1975.

[161] Vittorio Gorini, Andrzej Kossakowski, and Ennackal Chandy George Sudarshan. Completely positive dynamical semigroups of n-level systems. *Journal of Mathematical Physics*, 17(5):821–825, 1976.

[162] Steffen Wißmann, Heinz-Peter Breuer, and Bassano Vacchini. Generalized trace-distance measure connecting quantum and classical non-markovianity. *Physical Review A*, 92(4):042108, 2015.

[163] Dariusz Chruściński and Sabrina Maniscalco. Degree of non-markovianity of quantum evolution. *Physical Review Letters*, 112(12):120404, 2014.

[164] SC Hou, SL Liang, and XX Yi. Non-markovianity and memory effects in quantum open systems. *Physical Review A*, 91(1):012109, 2015.

[165] Ángel Rivas, Susana F Huelga, and Martin B Plenio. Quantum non-markovianity: characterization, quantification and detection. *Reports on Progress in Physics*, 77(9):094001, 2014.

[166] Heinz-Peter Breuer, Elsi-Mari Laine, Jyrki Piilo, and Bassano Vacchini. Colloquium: Non-markovian dynamics in open quantum systems. *Rev. Mod. Phys.*, 88:021002, Apr 2016.

[167] Heinz-Peter Breuer, Elsi-Mari Laine, and Jyrki Piilo. Measure for the degree of non-markovian behavior of quantum processes in open systems. *Phys. Rev. Lett.*, 103:210401, Nov 2009.

[168] Elsi-Mari Laine, Jyrki Piilo, and Heinz-Peter Breuer. Measure for the non-markovianity of quantum processes. *Phys. Rev. A*, 81:062115, Jun 2010.

[169] F. F. Fanchini, G. Karpat, B. Çakmak, L. K. Castelano, G. H. Aguilar, O. Jiménez Farías, S. P. Walborn, P. H. Souto Ribeiro, and M. C. de Oliveira. Non-markovianity through accessible information. *Phys. Rev. Lett.*, 112:210402, May 2014.

[170] Dariusz Chruściński, Chiara Macchiavello, and Sabrina Maniscalco. Detecting non-markovianity of quantum evolution via spectra of dynamical maps. *Phys. Rev. Lett.*, 118:080404, Feb 2017.

[171] Bruno Bellomo, Antonella De Pasquale, Giulia Gualdi, and Ugo Marzolino. A tomographic approach to non-markovian master equations. *Journal of Physics A: Mathematical and Theoretical*, 43(39):395303, 2010.

[172] Ángel Rivas, Susana F. Huelga, and Martin B. Plenio. Entanglement and non-markovianity of quantum evolutions. *Phys. Rev. Lett.*, 105:050403, Jul 2010.

[173] Jayaseetha Rau. Relaxation phenomena in spin and harmonic oscillator systems. *Phys. Rev.*, 129:1880–1888, Feb 1963.

[174] M. Ziman, P. Štelmachovič, V. Bužek, M. Hillery, V. Scarani, and N. Gisin. Diluting quantum information: An analysis of information transfer in system-reservoir interactions. *Phys. Rev. A*, 65:042105, Mar 2002.

[175] Bassano Vacchini. General structure of quantum collisional models. *International Journal of Quantum Information*, 12(02):1461011, 2014.

[176] Salvatore Lorenzo, Francesco Ciccarello, and G. Massimo Palma. Composite quantum collision models. *Phys. Rev. A*, 96:032107, Sep 2017.

[177] N. K. Bernardes, A. R. R. Carvalho, C. H. Monken, and M. F. Santos. Environmental correlations and markovian to non-markovian transitions in collisional models. *Phys. Rev. A*, 90:032111, Sep 2014.

[178] Ruari McCloskey and Mauro Paternostro. Non-markovianity and system-environment correlations in a microscopic collision model. *Phys. Rev. A*, 89:052120, May 2014.

[179] András Bodor, Lajos Diósi, Zsófia Kallus, and Thomas Konrad. Structural features of non-markovian open quantum systems using quantum chains. *Phys. Rev. A*, 87:052113, May 2013.

[180] F. Ciccarello, G. M. Palma, and V. Giovannetti. Collision-model-based approach to non-markovian quantum dynamics. *Phys. Rev. A*, 87:040103, Apr 2013.

[181] F Ciccarello and V Giovannetti. A quantum non-markovian collision model: incoherent swap case. *Physica Scripta*, 2013(T153):014010, 2013.

[182] Tomáš Rybár, Sergey N Filippov, Mário Ziman, and Vladimír Bužek. Simulation of indivisible qubit channels in collision models. *Journal of Physics B: Atomic, Molecular and Optical Physics*, 45(15):154006, 2012.

[183] Jiasen Jin and Chang shui Yu. Non-markovianity in the collision model with environmental block. *New Journal of Physics*, 20(5):053026, 2018.

[184] Andrea Chiuri, Chiara Greganti, Laura Mazzola, Mauro Paternostro, and Paolo Mataloni. Linear optics simulation of quantum non-markovian dynamics. *Scientific reports*, 2:968, 2012.

[185] Francesco Ciccarello. *Quantum Measurements and Quantum Metrology*, volume 4, chapter Collision models in quantum optics, page 53. 2017. 1.

[186] Jiasen Jin, Vittorio Giovannetti, Rosario Fazio, Fabio Sciarrino, Paolo Mataloni, Andrea Crespi, and Roberto Osellame. All-optical non-markovian stroboscopic quantum simulator. *Phys. Rev. A*, 91:012122, Jan 2015.

[187] Andrew G. White, Daniel F. V. James, Philippe H. Eberhard, and Paul G. Kwiat. Nonmaximally entangled states: Production, characterization, and utilization. *Phys. Rev. Lett.*, 83:3103–3107, Oct 1999.

[188] Salvatore Lorenzo, Francesco Plastina, and Mauro Paternostro. Geometrical characterization of non-markovianity. *Phys. Rev. A*, 88:020102, Aug 2013.

[189] William K. Wootters. Entanglement of formation of an arbitrary state of two qubits. *Phys. Rev. Lett.*, 80:2245–2248, Mar 1998.

[190] C. Herreño-Fierro and J. R. Luthra. Generalized concurrence and limits of separability for two qutrits. *eprint arXiv:quant-ph/0507223*, July 2005.

[191] Tohya Hiroshima and Satoshi Ishizaka. Local and nonlocal properties of werner states. *Phys. Rev. A*, 62:044302, Sep 2000.

[192] M. Barbieri, F. De Martini, G. Di Nepi, and P. Mataloni. Generation and characterization of werner states and maximally entangled mixed states by a universal source of entanglement. *Phys. Rev. Lett.*, 92:177901, Apr 2004.

[193] Álvaro Cuevas, Massimiliano Proietti, Mario Arnolfo Ciampini, Stefano Duranti, Paolo Mataloni, Massimiliano F. Sacchi, and Chiara Macchiavello. Experimental detection of quantum channel capacities. *Phys. Rev. Lett.*, 119:100502, Sep 2017.

[194] M B Plenio and S F Huelga. Dephasing-assisted transport: quantum networks and biomolecules. *New Journal of Physics*, 10(11):113019, 2008.

[195] F. Caruso, A. W. Chin, A. Datta, S. F. Huelga, and M. B. Plenio. Highly efficient energy excitation transfer in light-harvesting complexes: The fundamental role of noise-assisted transport. *The Journal of Chemical Physics*, 131(10):105106, 2009.

[196] Lorenza Viola and Seth Lloyd. Dynamical suppression of decoherence in two-state quantum systems. *Phys. Rev. A*, 58:2733–2744, Oct 1998.

[197] Bi-Heng Liu, Xiao-Min Hu, Yun-Feng Huang, Chuan-Feng Li, Guang-Can Guo, Antti Karlsson, Elsi-Mari Laine, Sabrina Maniscalco, Chiara Macchiavello, and Jyrki Piilo. Efficient superdense coding in the presence of non-markovian noise. *EPL (Europhysics Letters)*, 114(1):10005, 2016.

[198] Yang Dong, Yu Zheng, Shen Li, Cong-Cong Li, Xiang-Dong Chen, Guang-Can Guo, and Fang-Wen Sun. Non-markovianity-assisted high-fidelity deutsch–jozsa algorithm in diamond. *npj Quantum Information*, 4(1):3, 2018.

[199] Susana F. Huelga, Ángel Rivas, and Martin B. Plenio. Non-markovianity-assisted steady state entanglement. *Phys. Rev. Lett.*, 108:160402, Apr 2012.

[200] M. B. Plenio and S. F. Huelga. Entangled light from white noise. *Phys. Rev. Lett.*, 88:197901, Apr 2002.

[201] B. Kraus, H. P. Büchler, S. Diehl, A. Kantian, A. Micheli, and P. Zoller. Preparation of entangled states by quantum markov processes. *Phys. Rev. A*, 78:042307, Oct 2008.

Acknowledgments

This Ph.D. thesis is the result of many efforts on my side, but not only. There are many people to thank, without whom I would never have achieved my goal.
First of all, my supervisor Paolo. He has been a guide throughout my PhD: I could not have found a better supervisor. He was always available to talk about physics despite his endless amount of things to do. He always had the right word not only to make the experiment work but also to encourage me to do my best. Definitely, the best supervisor ever.
Of course, I have to thank Sabrina. I need few words to say the most important thing: thank you for your love and trust in me. Love you. Definitely, the best partner ever.
Thanks to Mauro, who is very stupid and always ready to do some nonsense when I talk about something serious, but is also very helpful when it comes to see things from another perspective. Definitely, the best goofy friend ever.
Thanks to Mattia, Riccardo and Stefano, a wonderful group of friends dissatisfied with life, whose only goal is to get to the weekend as soon as possible. Definitely the best company to laugh with.
Thanks to Alessandro, whose theoretical skills allowed me to conclude my PhD. Without his ideas I would have never done any of my research. Best CAPO ever.
Thanks to Davide, always available to solve computer problems, but not only. Without him my PhD would have been in quantum optics instead of quantum optics and information. Definitely the best hacker ever.
Thank to the entire G21 group: as I said in the acknowledgments of my master's thesis almost four years ago, you are a group that one is never bored of being a part of. Definitely, best research group ever.
A special mention is for the Paderborn group, in the persons of Christine, Jan, Syam, Sonja, Matteo and Marcello (but, of course, the others too!): you made me feel at home during the wonderful months I spent in your group. Thank you again for your support and help. Definitely, the best hosting group ever!
Thank to my family, Mom, Dad and my brother Alessandro, who always left me free to make my own decisions. Thank you for your support, I hope you are proud of me. Definitely, best family ever.
Well, I did it.
I achieved my goal.
I got my Ph.D.
I don't know what will happen now.
But as Forrest Gump said "I am pretty tired. I think I'll go home now."
See you.